IMPERIAL COLLEGE LONDON
DEPARTMENT OF EARTH SCIENCE AND ENGINEERING
DOCTOR OF PHILOSOPHY (Ph.D.) THESIS

Pore-Scale Imaging and Characterization of Three-Phase Flow in Porous Media Applied to Carbon Dioxide Storage in Hydrocarbon Reservoirs

By

Abdulla Ismaeil Abbas Haidar Alhosani

Supervisors

Prof. Martin J. Blunt
Dr. Branko Bijeljic

ACADEMIC YEAR 2022-2023

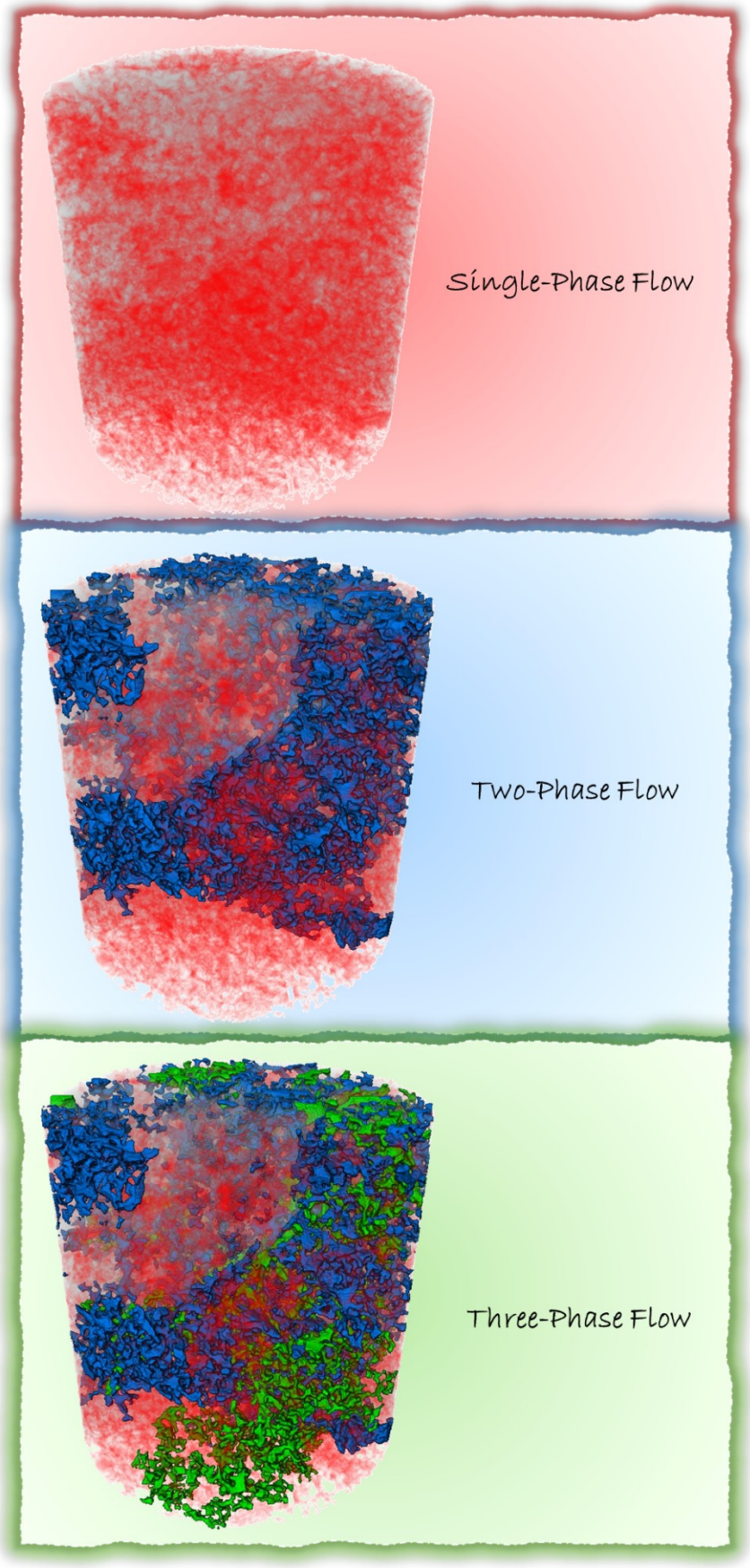
Single-Phase Flow
Two-Phase Flow
Three-Phase Flow

Contents

Abstract

Rapid implementation of large-scale carbon capture and storage is necessary to limit global warming this century. Amongst various CO_2 storage sites, depleted oilfields provide an immediate option since injection infrastructure is in place and there is an economic benefit from enhanced oil recovery. To design secure carbon storage in oilfields, we need to understand how the three fluid phases – CO_2, oil, and water – flow simultaneously in the microscopic pore spaces of the reservoir. In this PhD thesis, we present a novel methodology to study three-phase flow in porous media, at various wettability and gas-oil miscibility conditions, using X-ray microtomography. The use of X-ray imaging allows for a complete investigation of the pore-scale properties that control flow and trapping in three-phase flow, i.e., wettability order, spreading and wetting layers, and double/multiple displacement events. In addition, our advanced experimental and image analysis techniques permit access to key petrophysical properties including fluid saturations, capillary pressures, three-phase relative permeabilities and pore occupancy maps. The three-phase experiments we perform include unsteady-state and steady-state flow conditions and employ both laboratory-based and synchrotron X-ray sources. While laboratory-based scanners image the fluid configurations at the end of displacement or at steady-state equilibrium, synchrotron scanners allow us to capture the pore-scale dynamics during displacement.

First, we investigate unsteady-state three-phase flow under near-miscible gas-oil conditions – where the gas-oil interfacial tension is ≤ 1 mN/m – and show that fluids display a unique behavior compared to that seen at immiscible conditions where the interfacial tension is larger by one order of magnitude. In a water-wet system, at near-miscible conditions, gas and oil appear to become neutrally wetting to the surface. This prevents oil from spreading in layers sandwiched between gas and water; the strict wettability order – water-oil-gas, from most to least wetting – seen at immiscible conditions breaks down. This facilitates the flow of oil and gas along the same path in the pore space occupying the centre of the larger pores, while water remains connected in wetting layers in the corners. While this behaviour is desirable for oil recovery, it can impact the storage security as oil can no longer trap CO_2. In a weakly oil-wet system, the wettability order shifts from oil-water-gas to oil-gas-water as we move from immiscible to near-miscible conditions. As CO_2 becomes the intermediate-wet phase, at near-miscible conditions, it forms spreading layers in the corners of the pore space. The existence of CO_2 in spreading layers has huge implications on the storage design since its flow conductance is naturally restricted which implies that subsequent water injection is not necessary to prevent CO_2 migration and escape.

Next, we show that reservoir rocks can undergo severe wettability alterations rendering them strongly oil-wet. Under unsteady-state flow at immiscible conditions, we observe the predicted, but hitherto unreported, three-phase wettability order in strongly oil-wet rocks, where water occupies the largest pores, oil the smallest, while CO_2 occupies pores of intermediate size. Although this wettability order is the same as that seen in a weakly oil-wet rock at near-miscible conditions, the pore-scale fluid configurations are different. While CO_2, the intermediate-wet phase, spreads in layers at near-miscible conditions, at immiscible conditions, it exists in the pore space as disconnected ganglia. The existence of CO_2 in disconnected clusters, at immiscible conditions, allows for the capillary trapping of gas by oil in the centre of the pores which is not possible when CO_2 forms layers. However, capillary trapping of gas by water is still impossible at both miscibility conditions since gas is more wetting to the surface than water. This implies that water re-injection to disconnect the CO_2 in the reservoir is unnecessary in both cases.

Using a synchrotron X-ray source, we then investigate the invasion pattern during unsteady-state two- and three-phase flow – water injection followed by gas – in a strongly oil-wet reservoir rock at immiscible conditions. During water injection, we observe that the displacement of oil by water is a drainage-like process, where water advances as a connected front displacing oil in the centre of the pores, confining the oil to wetting layers. The displacement is an invasion percolation process, where throats, the restrictions between pores, fill in order of size, with the largest available throats filled first. Moreover, we observe drainage associated pore-filling dynamics including Haines jumps and snap-off events. Subsequently, during gas injection, a distinct invasion pattern is observed for three-phase flow, where gas progresses through the pore space in the form of disconnected clusters mediated by double and multiple displacement events. Gas advances in a process we name three-phase Haines jumps, during which gas re-arranges its configuration in the pore space, retracting from some regions to enable the rapid filling of multiple pores. The gas retraction leads to a permanent disconnection of gas ganglia, which do not reconnect as gas injection proceeds.

Lastly, we develop a novel experimental approach to investigate steady-state three-phase flow using pore-scale X-ray imaging. Our newly designed flow cell allows for the differential pressure across the system to be measured, enabling for the simultaneous determination of three-phase relative permeability and capillary pressure. We first investigate steady-state three-phase flow in a water-wet system at immiscible conditions, where the wettability order is water-oil-gas, from most to least wetting. We discover a unique flow dynamics where gas is disconnected across the system despite its continuous injection; gas flows by periodically opening critical flow pathways in intermediate-sized pores. We observe intermittent gas-oil and oil-water behaviour even under capillary-dominated conditions in three-phase flow. At steady-state conditions, it was impossible to displace the trapped gas in our water-wet system since it is double capillary trapped by spreading, oil, and wetting, water, layers. Gas has the lowest relative permeability in the pore space, while oil the highest. Next, we study steady-state three-phase flow in a mixed-wet system at immiscible conditions with an oil-water-gas wettability order. We observe that the gas flow is disconnected, similar to the water-wet system. However, intermittency was more pronounced in the mixed-wet system. The oil relative permeability was the highest in the pore space followed by water, then gas like the water-wet system. The impact of saturation history on gas and water relative permeabilities was larger than its impact on the oil relative permeability. Surprisingly, there was no gas trapping in the system due to its mixed-wet nature which prevents oil and water from completely surrounding the gas phase.

This thesis presents an effective and universal methodology to study three-phase flow in porous media at the pore-scale using X-ray microtomography. While the results were strictly discussed in the context of subsurface storage and recovery, it can have implications for many other engineering applications including microfluidic devices, packed bed chemical reactors and catalysis. The findings of this thesis can be used to advise on the design of the optimal conditions to store as much CO_2 as possible while maximizing oil production in CO_2-enhanced oil recovery projects.

Acknowledgments

Words cannot express my gratitude to my supervisors, *Prof. Martin J. Blunt* and *Dr. Branko Bijeljic*, whom without this endeavour would not have been possible. Your invaluable guidance and support through every step of the journey is greatly appreciated. I speak from my heart when I say, "I could not have asked for better supervisors".

I would also like to thank my examiners *Prof. Ken Sorbie* and *Prof. Peter King* for dedicating their time and expertise to assess my work and provide valuable feedback.

I am also grateful to my sponsors *Abu Dhabi National Oil Company* (ADNOC), who funded my research, for their generous contribution. I would like to extend my sincere thanks to *Dr. Djamel Ouzzane*, my industrial supervisor, *Mrs. Kenza Kheznadji*, my R&D focal point, and *Mrs. Lisa Nichols*, my scholarship officer, for their precious advice and guidance.

I am also extremely thankful for my Imperial College friends and colleagues whom I could not have undertaken this journey without, especially *Dr. Amer Alhammadi*, *Dr. Alessio Scanziani*, *Dr. Ahmed Selem*, *Dr. Qingyang Lin*, *Dr. Ali Raeini*, *Dr. Sajjad Foroughi* and *Dr. Mutluq Alarouj***.**

Finally, I would like to take this opportunity to thank my number one supporter, my *family*, especially my *dad* and *aunt***,** who inspired me to go down this path. Their belief in me kept my spirit and motivation high throughout my journey. Special thanks to my *sister* for helping me with the design of graphics. Lastly, I would like to thank my *brothers* and *cousins*, my biggest distraction, for all the entertainment and emotional support they provided, without you none of this would have been possible.

"This is by the grace of my lord" ~ Quran [27:40]

Dedication

This work is dedicated to my *family*, particularly to my *dad* and *aunt*. I hope I can continue making you proud.

Statement of Originality

I declare that this thesis *"Pore-Scale Imaging and Characterization of Three-Phase Flow in Porous Media Applied to Carbon Dioxide Storage in Hydrocarbon Reservoirs"* is a production of my own work, under the supervision of Prof. Martin J. Blunt and Dr. Branko Bijeljic in the Department of Earth Science and Engineering at Imperial College London. All published and unpublished material used in the thesis has been acknowledged. This thesis has not been previously submitted, in whole or in part, to any other academic institution for a degree, diploma, or any other qualification.

Copyright Declaration

List of Publications

Journal Articles

1. Akai, T., Lin, Q., **Alhosani, A**., Bijeljic, B. and Blunt, M.J., 2019. Quantification of uncertainty and best practice in computing interfacial curvature from complex pore space images. *Materials*, *12*(13), p.2138.
2. **Alhosani, A**., Scanziani, A., Lin, Q., Pan, Z., Bijeljic, B. and Blunt, M.J., 2019. In situ pore-scale analysis of oil recovery during three-phase near-miscible CO_2 injection in a water-wet carbonate rock. *Advances in Water Resources*, *134*, p.103432.
3. **Alhosani, A**., Scanziani, A., Lin, Q., Raeini, A.Q., Bijeljic, B. and Blunt, M.J., 2020. Pore-scale mechanisms of CO_2 storage in oilfields. *Scientific reports*, *10*(1), pp.1-9.
4. **Alhosani, A**., Scanziani, A., Lin, Q., Foroughi, S., Alhammadi, A.M., Blunt, M.J. and Bijeljic, B., 2020. Dynamics of water injection in an oil-wet reservoir rock at subsurface conditions: Invasion patterns and pore-filling events. *Physical Review E*, *102*(2), p.023110.
5. Scanziani, A., Lin, Q., **Alhosani, A.**, Blunt, M.J. and Bijeljic, B., 2020. Dynamics of fluid displacement in mixed-wet porous media. *Proceedings of the Royal Society A*, *476*(2240), p.20200040.
6. Scanziani, A., **Alhosani, A.**, Lin, Q., Spurin, C., Garfi, G., Blunt, M.J. and Bijeljic, B., 2020. In situ characterization of three-phase flow in mixed-wet porous media using synchrotron imaging. *Water Resources Research*, *56*(9), p.e2020WR027873.
7. **Alhosani, A**., Scanziani, A., Lin, Q., Selem, A., Pan, Z., Blunt, M.J. and Bijeljic, B., 2020. Three-phase flow displacement dynamics and Haines jumps in a hydrophobic porous medium. *Proceedings of the Royal Society A*, *476*(2244), p.20200671.
8. Blunt, M.J., **Alhosani, A**., Lin, Q., Scanziani, A. and Bijeljic, B., 2021. Determination of contact angles for three-phase flow in porous media using an energy balance. *Journal of Colloid and Interface Science*, *582*, pp.283-290.
9. **Alhosani, A**., Lin, Q., Scanziani, A., Andrews, E., Zhang, K., Bijeljic, B. and Blunt, M.J., 2021. Pore-scale characterization of carbon dioxide storage at immiscible and near-miscible conditions in altered-wettability reservoir rocks. *International Journal of Greenhouse Gas Control*, *105*, p.103232.
10. **Alhosani, A**., Bijeljic, B. and Blunt, M.J., 2021. Pore-scale imaging and analysis of wettability order, trapping and displacement in three-phase flow in porous media with various wettabilities. *Transport in Porous Media*, *140*(1), pp.59-84.
11. **Alhosani, A**., Selem, A.M., Lin, Q., Bijeljic, B. and Blunt, M.J., 2021. Disconnected Gas Transport in Steady-State Three-Phase Flow. *Water Resources Research*, *57*(12), p.e2021WR031147.

Conference Proceeding Papers

1. Blunt, M., Kearney, L., **Alhosani, A**., Lin, Q. and Bijeljic, B., 2021, September. Wettability Characterization from Pore-Scale Images Using Topology and Energy Balance with Implications for Recovery and Storage. In *SPE Annual Technical Conference and Exhibition*. OnePetro.
2. Bijeljic, B., **Alhosani, A**., Selem, A.M., Oliveira, R. and Blunt, M.J., 2021, December. Imaging and Modeling of Multiphase Flow and Reactive Transport in Geological Storage and Oil Recovery. In *AGU Fall Meeting 2021*. AGU.

Conferences and Consortium Meetings

1. **Alhosani. A.** Pore-scale Imaging and Analysis of Three-Phase Flow: Impact of Wettability and Miscibility. In *21st Imperial College Consortium on Pore-Scale Modelling and Imaging 2020*.
2. **Alhosani. A.,** Lin. Q., Scanziani. A., Bijeljic. B., Blunt. M.J. Optimizing Carbon Dioxide Storage in Oilfields at the Pore-Scale. In *Interpore 2020*.
3. **Alhosani. A.** Pore-scale Imaging and Analysis of Three-Phase Flow: Impact of Wettability and Miscibility. In *22nd Imperial College Consortium on Pore-Scale Modelling and Imaging 2021*.
4. **Alhosani. A**., Scanziani. A., Lin. Q., Selem. A., Alhammadi. A., Foroughi. S., Bijeljic. B., Blunt. M.J. Optimizing Carbon Dioxide Storage in Oilfields at the pore-scale. In *Interpore 2021*.
5. **Alhosani. A.** Carbon Dioxide Storage in Hydrocarbon Reservoirs: Effect of Wettability, Miscibility, Disconnected Gas Flow and Relative Permeability. In *23rd Imperial College Consortium on Pore-Scale Modelling and Imaging 2022*.
6. Goodarzi. S., **Alhosani. A.,** Bijeljic. B., Blunt. M.J. Hysteresis in Multiphase Flow and Application to Hydrogen Storage. In *Interpore 2022*.

List of Symbols

Symbol	Meaning	SI unit
q	Darcy velocity	$m.s^{-1}$
g	Acceleration due to gravity	$m.s^{-2}$
K	Absolute Permeability	m^2
μ	Viscosity	Pa.s
ρ	Density	$kg.m^{-3}$
Q	Volumetric flow rate	$m^3.s^{-1}$
A	Area	m^2
L	Length	m
x	Distance	m
σ	Interfacial tension	$N.m^{-1}$
P_c	Capillary pressure	Pa
κ	Total curvature	m^{-1}
κ_m	Mean curvature ($\kappa/2$)	m^{-1}
r	Radius of curvature	m
k_r	Relative permeability	
Ca	Capillary number	
I	Transmitted beam intensity	
I_o	Incident beam intensity	
μ_x	Linear attenuation coefficient	m^{-1}
t	Thickness	m
a	Specific surface area	m^{-1}
θ	Contact angle	Degrees
θ_g	Geometric contact angle	Degrees
θ_t	Thermodynamic contact angle	Degrees
f	Fractional flow	
ΔP	Pressure drop across the system	Pa
ϕ	Porosity	
S	Saturation	
Bo	Bond number	
l	Characteristic length	m
CT	Grey-scale peak value	
PV	Pore volume	mL
t	Time	s
T	Temperature	^oC
P	Pressure	Pa

List of Tables

List of Figures

Chapter 1

In this chapter, we will provide the reason behind selecting three-phase flow in porous media to be the topic of this PhD research. First, the introduction will address the worldwide increase in energy demand driven by the rapid growth in human population. Then, a description of the impact of harnessing fossil fuels, to supply this demand, on the climate and CO_2 concentrations will follow. Carbon capture, utilization, and storage (CCUS) is then proposed as a part of the solution to prevent dangerous climate change. Next, will discuss how coupling CCUS with enhanced oil recovery (EOR) is the way forward for rapid large-scale implementation of CO_2 storage. The chapter then highlights the importance of understanding three-phase flow in porous media for the optimization of CCUS and EOR in hydrocarbon reservoirs. Finally, the novel contributions of this PhD work to the three-phase flow literature, addressed using pore-scale X-ray imaging, and the structure of this thesis will be outlined.

1.1 Population Growth and Energy Demand

Today, there are 7.9 billion people on the planet and the number is projected to reach 10.9 billion by the end of the century according to the United Nations [1], see Fig. 1.1. This rapid growth in the world's population and economy has led to a substantial increase in global energy demand over the years. The current world's consumption of primary energy is 556 EJ with oil, coal, and gas holding the largest shares of the energy mix, 31.2%, 27.2% and 24.7% respectively [2], see Fig. 1.2. Renewables, nuclear energy, and hydroelectricity contribute to less than 17% of the world's primary energy. The fact that almost 83% of the world's energy supply comes from burning fossil fuels – i.e., oil, coal, and gas – cannot be ignored.

1.2 Climate Change and CO_2 Emissions

Fossil fuels release large quantities of carbon dioxide into the atmosphere when burned for energy. Greenhouse gases such as CO_2 trap heat in the atmosphere when emitted, raising the atmosphere's temperature, and causing global warming. Over time, global warming is changing weather patterns and disrupting the usual balance of nature which poses many risks to human beings and the environment. Examples of these risks include hotter temperatures, more severe storms, rising sea levels, increased drought, melting polar ice, ocean acidification and water scarcity.

Currently, almost 35 Gt of CO_2 are emitted annually into the atmosphere just from burning fossil fuels [3], see Fig. 1.3. These emissions are the main contributor to the continuous warming of the earth's surface, with global temperatures being the hottest in the past 2000-plus years [4]. Fig. 1.4 from NASA's Goddard Institute for Space Studies (GISS) illustrates that the year 2020 was the hottest year on record, since record keeping began in 1880, with an annual average temperature anomaly of 1.02 ^{o}C. With that said, immediate actions must be taken to limit anthropogenic CO_2 emissions. According to the Intergovernmental Panel on Climate Change (IPCC), temperature rises must be limited to 2 ^{o}C this century in order to prevent dangerous climate change consequences [5].

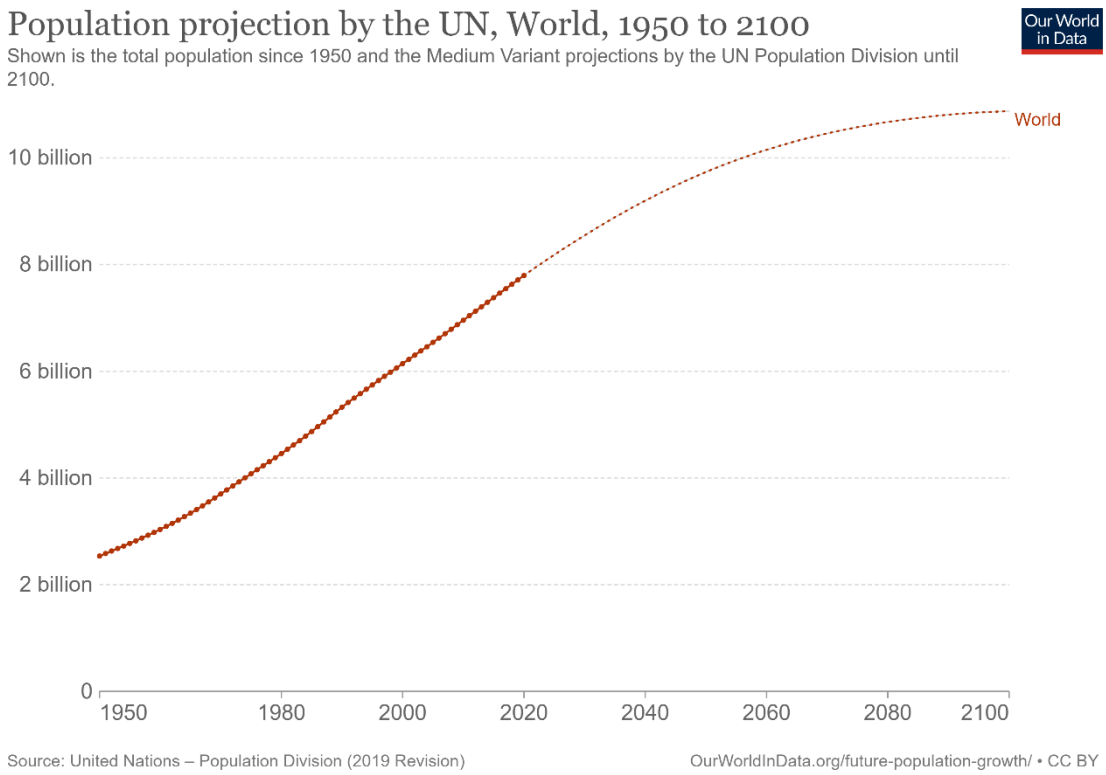

Figure 1. 1. The world's human population projection by the United Nations between the years 1950 and 2100. From Roser [1].

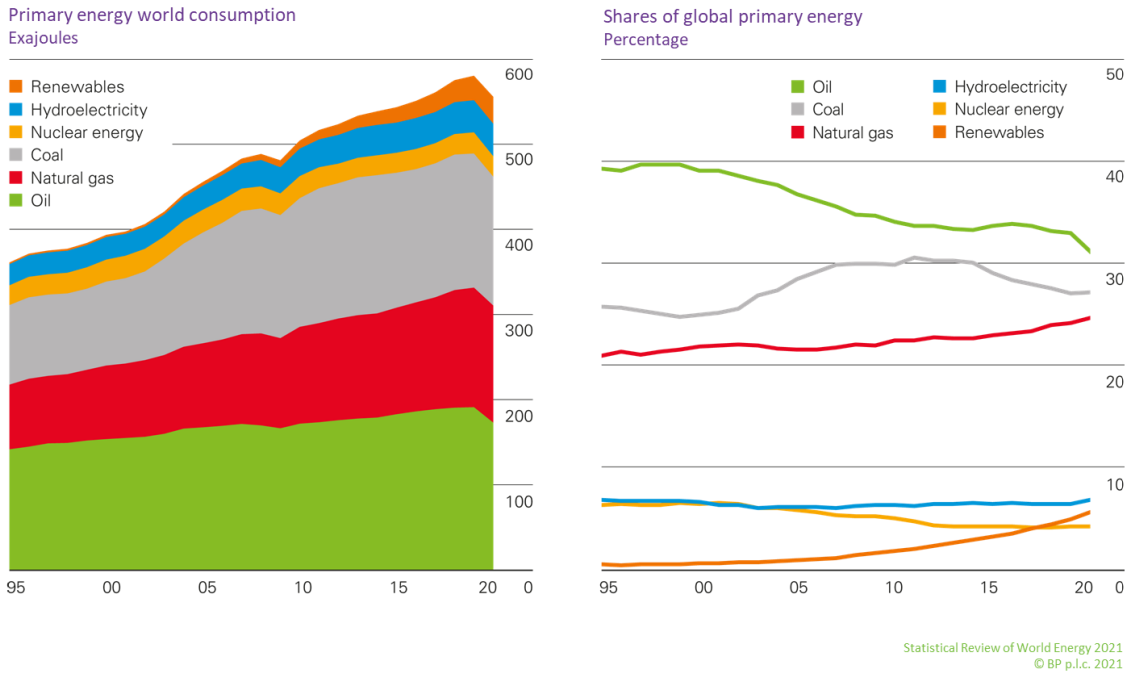

Figure 1. 2. (Left) World consumption of primary energy (EJ). (Right) Fuel shares of global primary energy (%). From BP Statistical Review of World Energy [2].

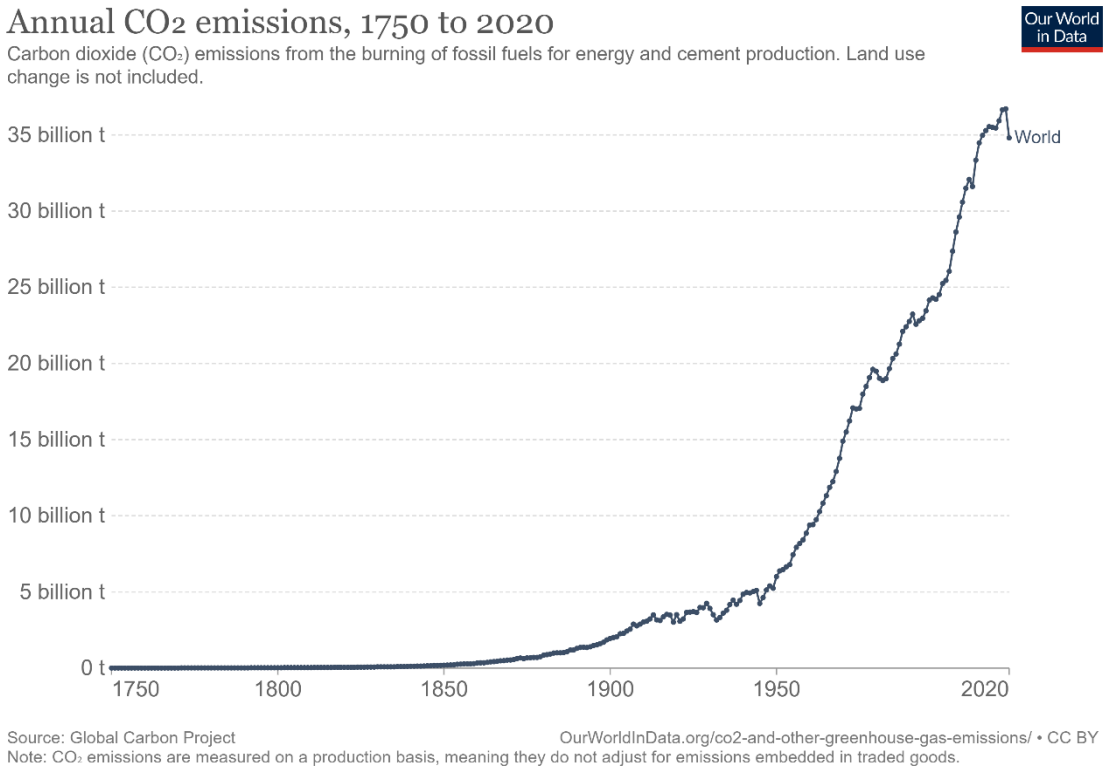

Figure 1. 3. Annual CO_2 emissions released into the atmosphere from burning fossil fuels for energy. From Ritchie and Roser [3].

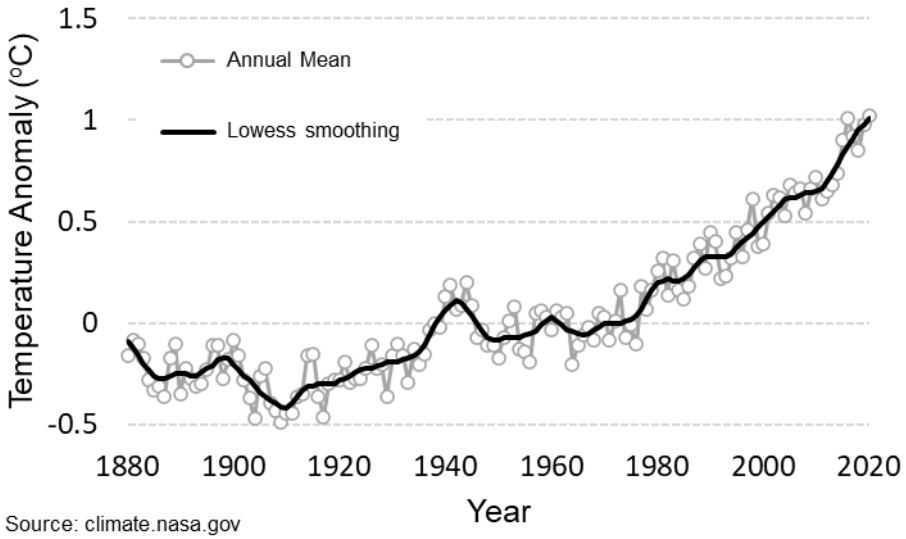

Figure 1. 4. The change in global surface temperature relative to 1951-1980 average temperatures. From NASA/GISS [4].

1.3 Carbon Capture, Utilization and Storage (CCUS)

With the continuous role of fossil fuels in providing most of the world's primary energy, nearly all the assessment scenarios compiled by the IPCC that limit climate change to less than 2 ^{o}C require the large-scale deployment of carbon capture, utilization and storage (CCUS) [5]. CCUS refers to the collection of carbon dioxide (CO_2) from power generation plants, and other large industrial sources, and its transportation to the storage site, where CO_2 is sequestered in deep geological formations. Capturing and storing CO_2 emissions can directly eliminate their impact on climate change.

Why is CCUS considered a vital component of the efforts to prevent dangerous climate change? Carbon capture and storage is thought of as a critical transitional technology, providing a short-term solution to mitigating climate change consistent with the continued use of fossil fuels while a more sustainable, low carbon energy system is developed in the long-term.

This PhD thesis will focus on the storage aspect of CCUS, more specifically the residual (or capillary) trapping mechanism of CO_2 that occurs inside the reservoir pore spaces. However, first, let us review all the potential methods by which CO_2 gets stored once it is injected in underground formations:

- **Structural trapping:** In this method, the upward movement and escape of CO_2 into the atmosphere is prevented by an impermeable rock layer, also known as cap rock. This is similar to the traps in hydrocarbon reservoirs which hold oil and gas underground for millions of years.
- **Dissolution:** Once CO_2 is injected it can dissolve in the formation brine forming a denser phase that sinks deep in the reservoir, storing the CO_2.
- **Mineralization (reaction):** One of the chemical products of CO_2 contact with brine is carbonic acid which can react with the host rock over thousands to millions of years forming solid calcium carbonates keeping the CO_2 underground.
- **Residual (or capillary) trapping:** In this last method, which is more rapid, the injected CO_2 gets segregated into disconnected clusters (or bubbles) in the pore space of the rock which hinders its flow potential in the reservoir. Thus, providing safe storage of CO_2 over geological times. An example of this method is shown in Fig. 1.5.

In order to optimize and improve the last CO_2 storage mechanism (residual trapping), a detailed investigation of the pore-scale physics is required, which will be the focus of this thesis. This will be facilitated through the use of X-ray microtomography which allows for the fluids inside the rock pore space to be imaged as shown in Fig. 1.5.

According to the International Energy Agency (IEA), 227 Gt of CO_2 must be stored safely in underground locations by 2060 to limit temperature rise to below 2 ^{o}C [6]. While there are abundant storage sites either in deep saline aquifers or in oil and gas hydrocarbon reservoirs – where the estimated storage capacity potential is 5000 and 1000 Gt of CO_2 respectively – the major challenge for carbon capture and storage technology is the cost. The deployment of CCUS is very expensive with costs widely varying dependent on the industrial capturing process, transportation type and distance, and storage prices [7].

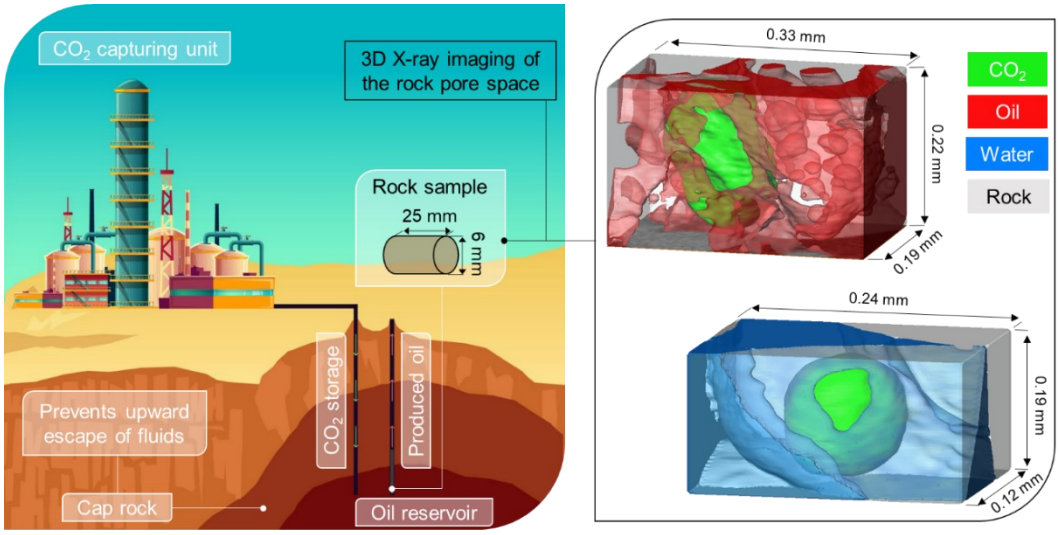

Figure 1. 5. Diagram showing the implementation of residual (or capillary) CO_2 storage trapping mechanism in an oil reservoir. In this method CO_2 is broken-down into disconnected clusters in the pore space of the rock, and capillary forces prevent its movement, providing safe storage.

1.4 CCUS in Enhanced Oil Recovery (EOR)

One of the viable solutions to reduce the costs of implementing CCUS involves the storage of CO_2 in oil and gas reservoirs. Injecting CO_2 in hydrocarbon reservoirs as part of enhanced oil recovery (EOR) processes results in additional hydrocarbon recovery, generating revenue to off-set the costs of capture and storage [8]. Carbon dioxide flooding is an effective and well-established oil recovery mechanism that uses the experience of the oil industry to extend the lifetime of many reservoirs. The combination of CO_2 storage with EOR offers immediate financial incentive as opposed to the storage of CO_2 in saline aquifers which is considered a huge investment without obvious economic return.

Furthermore, given the short time frame for the implementation of CCUS at a global scale, it is most practical in oil and gas reservoirs, where the infrastructure including facilities, pipelines, and injection wells, as well as detailed knowledge of the fields already exist.

In fact, almost 95% of the 31 Mt of CO_2 captured annually is injected in oil reservoirs as part of EOR projects [9]. Fig. 1.6 shows a map of the carbon capture and storage projects around the world illustrating that most of the captured CO_2 is injected for CO_2-EOR applications. Nonetheless, the goal of most CO_2-EOR projects is to solely improve oil recovery rather than store CO_2. Hence, the injected CO_2 is typically designed to be fully miscible with the resident oil, where CO_2 dissolves in oil forming a single phase, allowing for a complete oil displacement efficiency. However, this usually results in the recycling of the injected CO_2 in the reservoir – as CO_2 gets produced with oil – and therefore, does not mitigate the impact of CO_2 on climate change.

For the CO_2 to remain safely stored in CO_2-EOR applications, it must be injected at immiscible or near-miscible conditions, where CO_2 exists as a separate phase in the reservoir – does not mix with oil – minimizing its production back out of the reservoir. Although altering the CO_2 injection conditions in CO_2-EOR to maximize the amount of CO_2 trapping comes at a cost, it is not economically unfeasible. Especially that it is now clear that coupling CCUS with EOR is the way forward towards a future with net zero carbon dioxide emissions.

The storage of CO_2 in oil reservoirs as part of EOR processes will be the topic of this PhD thesis. The work will focus on investigating three-phase flow at the micro-scale – also called the pore-scale – to

discover the physics of displacement at immiscible and near-miscible gas-oil conditions, where water, oil, and CO_2 flow as distinct phases in the reservoir.

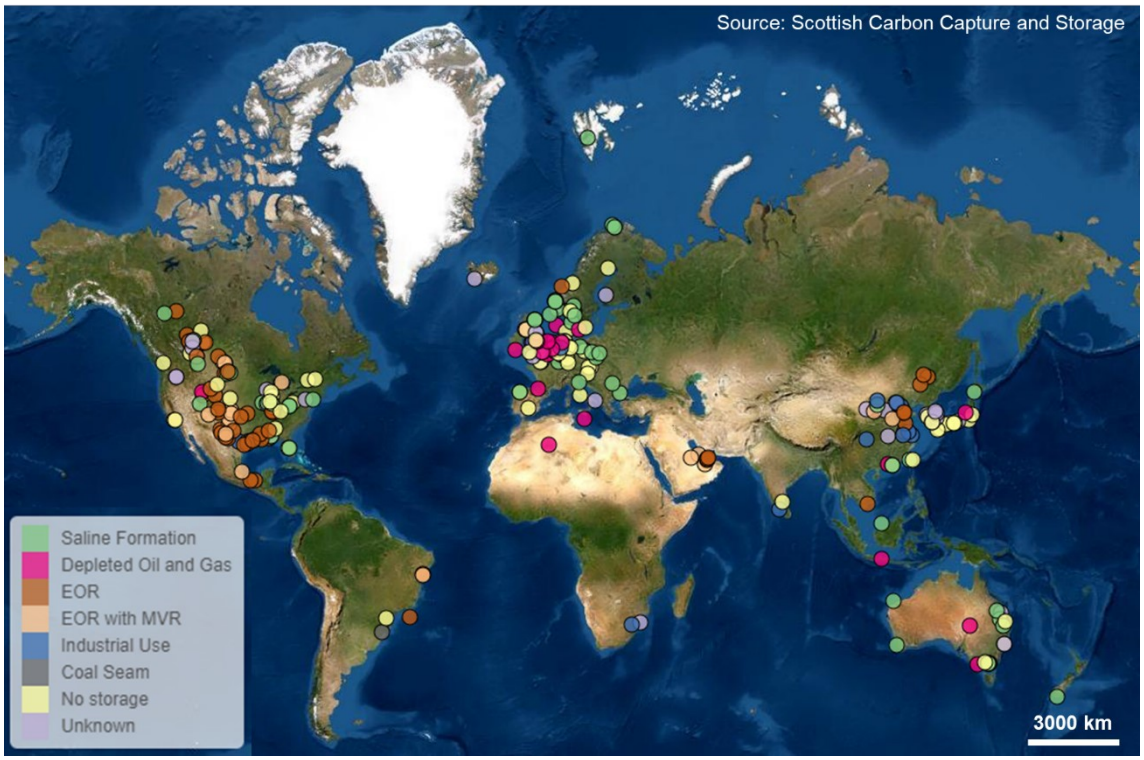

Figure 1. 6. A map showing the carbon capture and storage (CCS) projects around the world. The map includes both operating and planned projects which capture, transport and store at least 500,000 tonnes of CO_2 per year. The colours differentiate between the application and storage site of the projects. From SCCS [10].

1.5 The Role of Three-Phase Flow in Porous Media

During CCUS-EOR processes, there is a simultaneous flow of three fluid phases, oil, water, and CO_2, in the pore spaces of the reservoir rock. In order to optimize the local displacement efficiency, in terms of the amount of CO_2 stored and oil recovered, we need to accurately characterize the three-phase flow pore-scale physics. A thorough study of the behaviour of fluids in the pores at the micro-scale, where the characteristic size is of 100s of micro-metre or lower, is essential to understand the CO_2 trapping mechanism, especially residual (or capillary) trapping, and oil displacement processes, which will be the focus of this PhD work.

Nonetheless, for an optimal design of CO_2 storage in hydrocarbon reservoirs, an investigation of the macro-scale characteristics such as the spatial distribution of permeability and variable connectivity of the pore space – which occur at the scale of metres or centimetres – as well as locating fractures is also necessary, especially for the structural and dissolution trapping mechanisms. Furthermore, a comprehensive chemical characterization of the rock formation is crucial for an effective mineralization CO_2 trapping. However, these properties will not be a topic of discussion in this PhD thesis.

1.6 Research Motivation

Unlike two-phase flow in porous media, relatively few studies can be found in the literature on three-phase flow at the pore-scale. This is mainly ascribed to two reasons: (i) the increasing difficulty of performing three-phase flow experiments; and (ii) the complex physical pore-scale processes that underly three-phase flow, which make it hard to verify and interpret the outcomes. As a result, even in this day and age of advanced technology, we still do not have a complete predictive understanding of three-phase flow in porous media.

Nonetheless, with the recent development of three-dimensional X-ray microtomography, which allows for the *in situ* visualization of the fluids in the pore space, we finally have a tool to begin to understand the three-phase pore-scale processes [11, 12]. This non-invasive technology has been deployed extensively to investigate unsteady-state and steady-state two-phase flow [13-15]. However, in three-phase flow, its scope has been limited to investigate unsteady-state flow at immiscible gas-oil conditions [16, 17]. Hence, there is a clear gap in the literature. We plan to bridge this gap by developing approaches to extend the reach of this tool, in three-phase flow, to study unsteady-state flow at near-miscible conditions, and steady-state flow at immiscible conditions. As one of the pioneering works on three-phase flow X-ray imaging, we set the scene for future studies.

1.7 Thesis Aim, Objectives, Contributions and Structure

The aim of this PhD is to use X-ray microtomography to expand on the knowledge of the pore-scale physics that control three-phase flow in porous media at various wettability and miscibility conditions. We mainly focus on understudied three-phase flow topics such as **near-miscible conditions**, **oil-wet wettability states**, **flow dynamics**, and **steady-state conditions**, which will be investigated, for the first time, using X-ray imaging in this PhD thesis. The insights from this work are used to advise on the design of the optimal CO_2 injection strategy to maximize the amount of CO_2 trapped and oil recovered in CCUS-EOR projects.

We perform a total of **seven** three-phase flow experiments combined with pore-scale X-ray imaging. These experiments include unsteady-state and steady-state flow conditions with static and dynamic X-ray imaging. Dynamic imaging refers to fast synchrotron imaging, which allows to capture the flow dynamics, while static images are acquired using a laboratory X-ray machine at the end of the displacement. The novelty in each of the experiments is twofold: (i) the design of the experimental flow and imaging apparatus; and (ii) the new insights gained into three-phase flow pore-scale physics. The seven experiments are outlined in Table 1.1 with their respective contribution to the pore-scale three-phase flow literature.

This thesis is divided into **seven chapters**. The results are presented in chapters 3 – 6. Chapters 3 and 4 will present the unsteady-state work investigated with static and dynamic imaging at near-miscible and immiscible conditions. A review of all the unsteady-state three-phase flow insights gained with X-ray imaging will follow in chapter 5. Finally, chapter 6 will present the steady-state work at immiscible conditions.

The thesis will be structured as follows:

- **Chapter 2** will describe the fundamental equations and concepts that underly multiphase flow in porous media before providing a synthesized literature review on pore-scale three-phase flow studies. The importance of our work will be clearly highlighted in the literature review.
- **Chapter 3** will present the materials and methods, results, discussion, and conclusions of the near-miscible and immiscible unsteady-state experiments investigated with static imaging (*EXP1*, *EXP2* and *EXP3*).
- **Chapter 4** will present the materials and methods, results, discussion, and conclusions of the two- and three-phase flow immiscible unsteady-state experiments investigated with dynamic imaging (*EXP4* and *EXP5*).
- **Chapter 5** will provide a synthesized review of all the latest insights gained into unsteady-state three-phase flow using three-dimensional X-ray imaging; this will include work from this PhD and other studies in the literature. The analysis is then placed in a practical context by discussing implications for flow and trapping to suggest the optimum injection strategy to enhance the microscopic displacement efficiency for carbon storage and enhanced oil recovery projects.
- **Chapter 6** will present the materials and methods, results, discussion, and conclusions of the immiscible steady-state experiments investigated with static imaging (*EXP6* and *EXP7*).
- **Chapter 7** will highlight the final remarks of this research and suggest topics for future work

Table 1. 1. A list of the novel experiments performed in this PhD thesis with their respective contribution to the pore-scale three-phase flow literature. * Is a two-phase flow experiment with novel findings.

	Experiment	Flow Type	Miscibility	Wettability	Imaging
	EXP1	Unsteady-state	Near-miscible	Water-wet	Static
Novelty	Designing the first experimental apparatus that allows for the investigation of near-miscible gas-oil conditions using pore-scale X-ray imaging				
Major Findings	The strict wettability order in the system breaks down at near-miscible conditions – oil and water become neutrally wetting to the surface in a water-wet rock				
	Oil does not form layers sandwiched between gas and water despite having a positive spreading coefficient; instead, it exists in disconnected clusters				
	EXP2	Unsteady-state	Near-miscible	Weakly oil-wet	Static
Novelty	First pore-scale X-ray imaging investigation of a weakly oil-wet system at near-miscible conditions				
Major Findings	CO_2 becomes more wetting to the surface than water at near-miscible conditions; the altered wettability order is oil-CO_2-water, from most to least wetting				
	CO_2, the intermediate-wet phase, spreads in layers in the corners of the pore-space of a weakly oil-wet system at near-miscible conditions				
	The flow conductance of CO_2 in the reservoir is significantly reduced at these conditions; water injection to limit the CO_2 movement is unnecessary				
	EXP3	Unsteady-state	Immiscible	Strongly oil-wet	Static
Novelty	Providing, for the first time, an experimental evidence of strongly oil-wet rocks using pore-scale X-ray imaging,				
Major Findings	The wettability order is oil-CO_2-water, from most to least wetting, in strongly oil-wet rocks at immiscible conditions				
	CO_2, the intermediate-wet phase, exists in disconnected ganglia at immiscible conditions				
	Capillary trapping of CO_2 by water is not possible in strongly oil-wet rocks at immiscible conditions				
	*EXP4**	Unsteady-state	Immiscible	Strongly oil-wet	Dynamic
Novelty	Investigating, for the first time, two-phase flow dynamics during water injection in a strongly oil-wet reservoir rock using pore-scale X-ray imaging				
Major Findings	Water displaces oil in a drainage-like process, where water advances as a connected front displacing oil in the centre of the pores, confining it to wetting layers				
	The displacement is an invasion percolation process, where throats, the restrictions between pores, fill in order of size, with the largest available throats filled first				
	Drainage associated dynamics – Haines jumps and snap-off events – are observed during the displacement				
	EXP5	Unsteady-state	Immiscible	Strongly oil-wet	Dynamic
Novelty	Investigating, for the first time, three-phase flow dynamics during gas injection in a strongly oil-wet reservoir rock using pore-scale imaging				
Major Findings	Gas progresses through the pore space in the form of disconnected ganglia mediated by double and multiple displacement events in a strongly oil-wet rock				
	Gas advances in a process we name three-phase Haines jumps, during which gas retracts from some regions to enable the rapid filling of multiple pores				
	The gas retraction leads to a permanent disconnection of gas ganglia, which do not reconnect as gas injection proceeds				
	EXP6	Steady-state	Immiscible	Water-wet	Static
Novelty	Developing a novel experimental approach to combine steady-state three-phase flow techniques with pore-scale X-ray imaging for the first time				
	Designing a new flow cell that allows for the simultaneous injection of three fluid phases while recording the pressure drop across the system which enables for the simultaneous determination of three-phase relative permeability and capillary pressure on the same sample				

Major Findings	Gas is disconnected at steady-state conditions in a water-wet system; gas flows by periodically opening critical flow pathways in intermediate-sized pores
	Intermittent gas-oil and gas-water flow occurs in three-phase flow even under capillary-dominated displacement conditions
	As gas invades the pore centres it is impossible to displace it at steady-state conditions since it is double capillary trapped by both oil and water layers
	The gas relative permeability was the lowest since it was disconnected in the pore space and oil the highest as it was connected in medium-sized pores
	EXP7 Steady-state Immiscible Mixed-wet Dynamic
Novelty	Investigating, for the first time, three-phase steady-state flow conditions in a mixed-wet reservoir rock using pore-scale X-ray imaging
Major Findings	The wettability order in the mixed-wet system is oil-water-gas, from most to least wetting
	Intermittent gas-oil and oil-wet flow behaviour was observed under capillary dominated conditions; both intermittencies occurred in intermediate pores
	Gas advances in the form of disconnected ganglia mediated by double and multiple displacement processes
	Oil relative permeability was the highest in the pore space followed by water, then gas
	The impact of saturation history on gas and water relative permeabilities was larger than its impact on the oil relative permeability
	There was no gas trapping in the mixed-wet system

Chapter 2

This chapter will start by reviewing the physics controlling multiphase flow in porous media. A description of the pore-scale phenomena that are unique to three-phase flow will follow. Next, the chapter will briefly highlight the current state-of-the-art of the X-ray imaging technology and how it can be used to improve our understanding of multiphase flow processes. An in-depth, synthesized literature review of the published studies on the flow of three phases in porous media is then presented. In the later section, (2.2), we will highlight the gaps in the literature and link it to the experiments we perform to shed a light on the importance and novelty of our work. The chapter ends with a list of the research questions that will be answered in this PhD thesis.

2.1 Theory

2.1.1 Fluid Flow in Porous Media

2.1.1.1 Darcy's law and permeability

The ability of a porous medium to transmit fluids is controlled by a property known as permeability. The permeability of a medium is related to its porosity, pore structure and connectivity. This intrinsic property is primarily quantified using Darcy's Law. This law was first proposed by the French engineer Henry Darcy in 1865 for the flow of water in sand filters (single-phase flow) [18]:

$$q = -\frac{K}{\mu}\left(\frac{\partial P}{\partial x} - \rho g\right) \tag{2.1}$$

where q is the Darcy velocity, which is the volume of fluid flowing per unit area of the porous medium, $\partial P/\partial x$ is the macroscopic pressure gradient along the length of the core in direction x, μ is the fluid viscosity, g is the acceleration due to gravity, ρ is the density, and K is the permeability – also known as absolute permeability – which has units of length squared.

An illustration of Darcy's law parameters on a core plug – a piece of rock – is shown in Fig. 2.1. According to Darcy's law, the fluids in the pore space flow from higher to lower pressures.

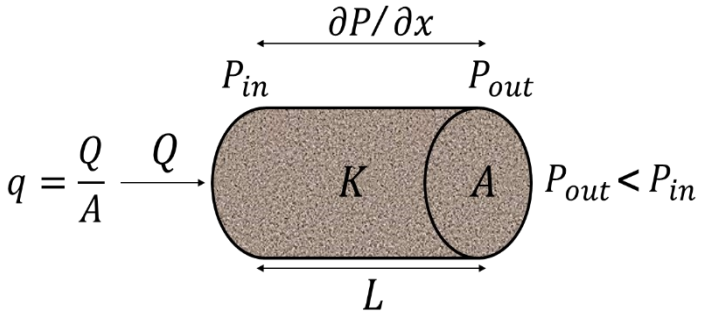

Figure 2. 1. An illustration of a cylindrical core plug showing the Darcy law parameters used to determine the absolute permeability of a rock. Where Q is the volumetric flow rate, A is the cross-sectional area, L is the length of the core, and P_{in} and P_{out} are the pressures at the inlet and outlet respectively. In a flow experiment Q, A and L are controlled, while P_{in} and P_{out} are measured externally to quantify the permeability.

Permeability is typically measured by recording the pressure drop across the sample while injecting a fluid through it. Permeability measurements can be performed on samples ranging from small core plugs to full diameter cores. Traditional permeability determination methods include steady-state,

unsteady-state and whole core methods. At the field-scale, permeability can be determined using well-test analysis techniques from field pressure and rate data.

2.1.1.2 Interfacial tension and capillary pressure

While the derivation of Darcy's law assumes the presence of a single phase in the porous medium, we typically encounter the existence of multiple fluids in the pore space, e.g., the simultaneous flow of oil-water, gas-water or gas-oil-water can occur in hydrocarbon reservoirs. The arrangement of these fluids with each other and the solid phase is locally controlled by an energy balance.

First, let us consider the case when two immiscible fluids are in contact with each other in a free space (no solid is present), e.g., a gas bubble in a water bath, as shown in Fig. 2.2. We observe that as the fluids come in contact, a distinct interface separating the two fluids is formed. The fluids will then re-arrange themselves to minimise the surface area of that interface, which is why gas forms a spherical shape in a water bath – a sphere has the lowest area per unit volume. From this we can define a property known as interfacial tension, σ, which is the energy per unit area of the interface between the fluids. In other words, it is the energy penalty of breaking the intermolecular forces between the two fluids and themselves.

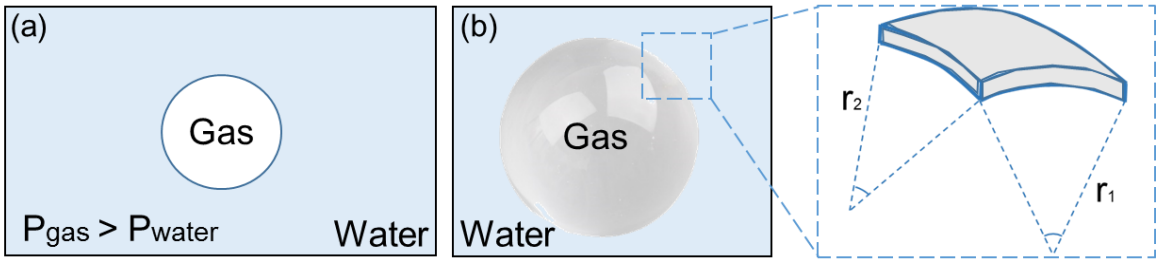

Figure 2. 2. (a) A schematic illustrating the arrangement of gas and liquid in free space. It indicates that when two immiscible fluids are in contact, a distinct interface separating the two fluids is formed. The fluids re-arrange themselves to minimise the area of that interface, which is why a gas bubble forms when it is in contact with water: this configuration has the lowest surface area per unit volume. **(b) A diagram illustrating a small expansion of the interface separating the gas and water phases in (a), where r_1 and r_2 are the principal radii of curvature of that interface**. P_{gas} and P_{water} refer to the pressures of gas and water respectively.

The existence of a curved interface between the fluids results in a different pressure within each fluid phase. Consider the gas bubble shown in Fig. 2.2 again. The phase that is bulging outwards, the gas phase, has higher pressure compared to the water phase. The pressure difference between the two phases is called the capillary pressure [18]:

$$P_c = P_1 - P_2 \tag{2.2}$$

where P_c is the capillary pressure, P_1 and P_2 are the pressures of the two phases in contact. By convention phase 2 is almost always the denser phase, in this case water.

Capillary pressure is usually quantified using the Young-Laplace equation [18, 19]. The equation relates the capillary pressure to the curvature of the interface between the two fluids through their interfacial tension:

$$P_c = \sigma\kappa = 2\sigma\kappa_m = \sigma\left(\frac{1}{r_1} + \frac{1}{r_2}\right) \tag{2.3}$$

where σ is the interfacial tension, κ is the total curvature of the interface, κ_m is the mean curvature, and r_1 and r_2 are the principal radii of curvature of the interface illustrated in Fig. 2.2b.

Given that the fluid arrangement in the pore space is controlled locally by an energy balance, positions of mechanical equilibrium will therefore represent a local energy minimum. Hence, for a displacement

to take a place, one fluid pushing out the other in the pore space, the process will have to be energetically favourable.

In order to have an energetically favourable displacement process, the pressure of the displacing fluid will have to exceed the capillary pressure between the fluids, i.e., a higher pressure than that existent already between the fluids is needed to disrupt the equilibrium position. The capillary pressure between two static fluids is also known as the capillary entry pressure. Therefore, it is evident that an accurate determination of the capillary pressure and consequently the interfacial tension between the fluids is essential to characterize displacement processes during multiphase flow in porous media.

In a hydrocarbon reservoir containing three fluid phases, we can define three capillary pressures between the fluid pairs: gas-oil, gas-water and oil-water capillary pressures.

Conventionally, capillary pressure is measured using various core flooding techniques. The three most widely used techniques are the porous plate method [20, 21], the mercury injection method [22], and the quasi steady-state flow method [23]. In this PhD thesis, we will characterize the local capillary pressure directly from measurements of curvature on pore-scale images: this method will be described in detail in section 3.1.3.2.5.2. In addition, the interfacial tension can be experimentally measured using the pendant drop and the capillary rise methods [24, 25].

2.1.1.3 Wettability and contact angle

In the previous section, we studied the existence of two fluids in contact with each other in free space; in this section will consider the introduction of a solid surface to the fluid-fluid system. Fig. 2.3 shows the typical arrangement in the presence of two fluids and a solid surface. One phase tends to spontaneously coat the surface, we denote this phase as the wetting phase. While the other phase has a lower tendency to coat or reside next to the solid surface, this phase is called the non-wetting phase.

This tendency of the solid surface to be preferentially coated by one fluid over the other is a surface property known as wettability. Wettability is typically determined using the contact angle θ. The contact angle is the angle between the solid surface and the tangent to the fluid-fluid interface at the point of three-phase contact; this is illustrated in Fig. 2.3a. By definition, the angle is measured from the solid surface to the tangent, passing through the denser phase – in this case, water, since it is denser than gas.

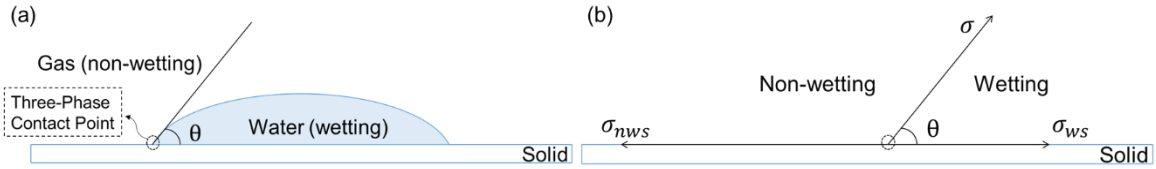

Figure 2. 3. (a) An illustration of fluid arrangements in contact with a solid surface. The angle between the solid surface and the tangent to the fluid-fluid interface at the point of three phase contact is the contact angle, θ, and is measured through the denser phase. **(b) An interpretation of the interfacial tensions between the fluid-fluid and the fluids and solid as balanced forces**. A horizontal force balance yields the Young equation, Eq. (2.4). σ, σ_{nws} and σ_{ws} are the interfacial tensions between the two fluid phases, the non-wetting phase and the solid, and the wetting phase and the solid.

In 1805, Thomas Young formulated an equation that expresses the contact angle in terms of the interfacial tension between the fluid-fluid interface and the interfacial tensions of the solid and the two fluid phases. He interpreted the interfacial tensions as forces acting along the interfaces and assumed that at equilibrium these forces balance out as shown in Fig. 2.3b [18]:

$$\sigma_{nws} = \sigma_{ws} + \sigma \cos\theta \qquad (2.4)$$

where σ_{nws} is the interfacial tension between the non-wetting phase and the solid, σ_{ws} is the interfacial tension between the wetting phase and the solid.

Eq. (2.4) can be re-arranged to find the contact angle:

$$cos\theta = \frac{\sigma_{nws} - \sigma_{ws}}{\sigma} \tag{2.5}$$

In the context of hydrocarbon reservoirs, the rock surfaces can have the affinity to either be coated by water or oil. In such systems the contact angle between oil and water can vary from 0° to 180°, ranging from a completely water-wet to a completely oil-wet system, respectively. Given that water is denser than oil, the contact angle is always characterized through the water phase. The presence of a gas phase does not alter the wettability of the mineral surfaces due to their composition lacking wettability alteration agents. Fig. 2.4 displays the various rock wettability states and their corresponding contact angles.

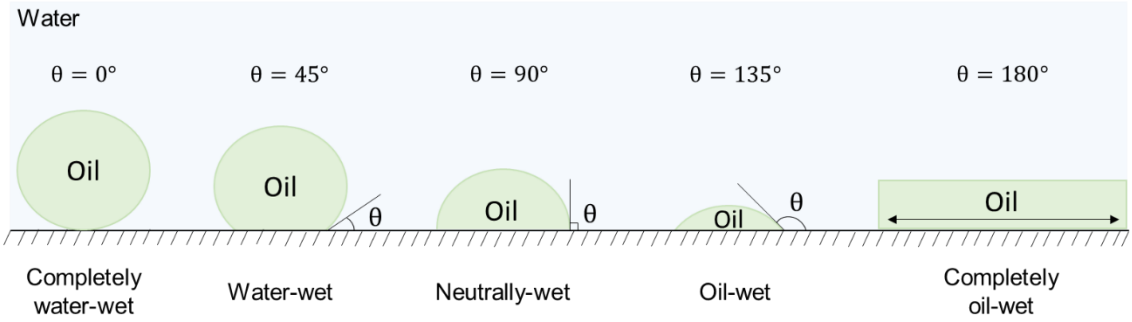

Figure 2. 4. An illustration of an oil droplet resting on a solid surface surrounded by water. The contact angle, θ, is measured through the water phase. Contact angles less than 90° represent a water-wet system, while angles higher than 90° represent an oil-wet system.

It is typically assumed that all hydrocarbon reservoirs are initially saturated with water, and therefore are strongly water-wet. However, it is the migration of oil into the reservoir that can alter its wetting behaviour through deposition and precipitation of asphaltenes from crude oil on the rock surfaces at conditions of high temperature and pressure. Subsequently, the reservoir may either remain water-wet, or become oil-wet, mixed-wet or neutrally-wet. A mixed wettability state refers to the case where parts of the pore space are water-wet, while the rest is oil-wet; the contact angle is distributed both above and below 90°. In contrast, neutrally-wet systems have no preference for either water or oil.

Conventionally, the wettability of a rock is characterized using both direct and indirect methods. Among the indirect methods, which infer wettability from macroscopic measurements of capillary pressure, the Amott wettability index [26] and the United States Bureau of Mines (USBM) wettability index [27] are the most popular. While the most effective direct technique is the contact angle goniometry technique [28] which measures the contact angle on an external surface but is difficult to apply inside a porous material.

However, with recent advances in pore-scale X-ray imaging allowing for the visualization of fluid configurations *in situ*, the contact angle can now be measured directly from three-dimensional images. This is known as the geometric contact angle and is measured between two vectors; one is tangential to the fluid-fluid interface and the other is to the rock surface [29-31]. Furthermore, advances in X-ray imaging also permitted for the calculation of the so-called thermodynamic contact angle, which defines the contact angle associated with the fluid displacement from an energy balance [32, 33]. These methods have significantly improved our pore-scale understanding of the physics in systems with complex wettabilities and therefore will be used to determine the contact angles in our experiments. The calculation of these angles is described in more detail in sections 4.1.3.5 and 4.2.3.5.

2.1.1.4 Multiphase Darcy law and relative permeability

As mentioned earlier, Darcy's law, Eq. (2.1), was derived for single-phase flow; however, it can be extended to account for the presence of multiple phases in the porous medium. The extension was first proposed by Muskat and Meres [34]: it assumes that the flow of each phase is governed by Darcy's law but with each parameter in the equation – e.g., pressure drop, viscosity and permeability – being specific to the phase itself:

$$q_i = -\frac{k_{ri}K}{\mu_i}\left(\frac{\partial P_i}{\partial x} - \rho_i g\right) \tag{2.6}$$

where q_i is the Darcy velocity of phase i and k_{ri} is its relative permeability. k_{ri} is a dimensionless parameter that represents how readily each phase will flow in the presence of other phases, and has values ranging between 0 and 1.

Relative permeability is typically considered a function of the phase saturation; if part of the pore space is occupied by water, then the ability of oil to flow through that pore is hindered and *vice versa*. Therefore, the relative permeability of a phase will be a monotonic function of its saturation and is typically plotted against it as shown in Fig. 2.5.

Nonetheless, relative permeability also depends on other properties such as wettability and saturation history.

In a porous medium, the wetting phase – the phase with a tendency to coat the surface – spreads over the solid in thin films as well as occupying small pores and corners of the pore space, while, the non-wetting phase, resides in the centres of large pores. This arrangement, which is controlled by the wettability of the surface, can directly impact the flow potential of the phases and therefore their relative permeability. For example, in a water-wet system, oil will flow more readily through the centre of the big pores compared to water which is confined to movement in the corners of the pore space. As a result, the oil relative permeability will be higher than that of water for the same saturation.

To observe the effect of saturation history on relative permeability, consider the case where only two fluids exist in the pore space, oil and water. The shape of the relative permeability curves for both fluids will differ depending on the process that is taking place, either during drainage, where the non-wetting phase displaces the wetting phase, or imbibition, where the wetting phase displaces the non-wetting phase. The drainage and imbibition relative permeabilities of water and oil in a water-wet system are shown in Fig. 2.5. The discrepancy in the shape of the relative permeability curves is termed hysteresis. It arises due to the differing pore-scale displacement mechanisms and fluid distribution during imbibition and drainage.

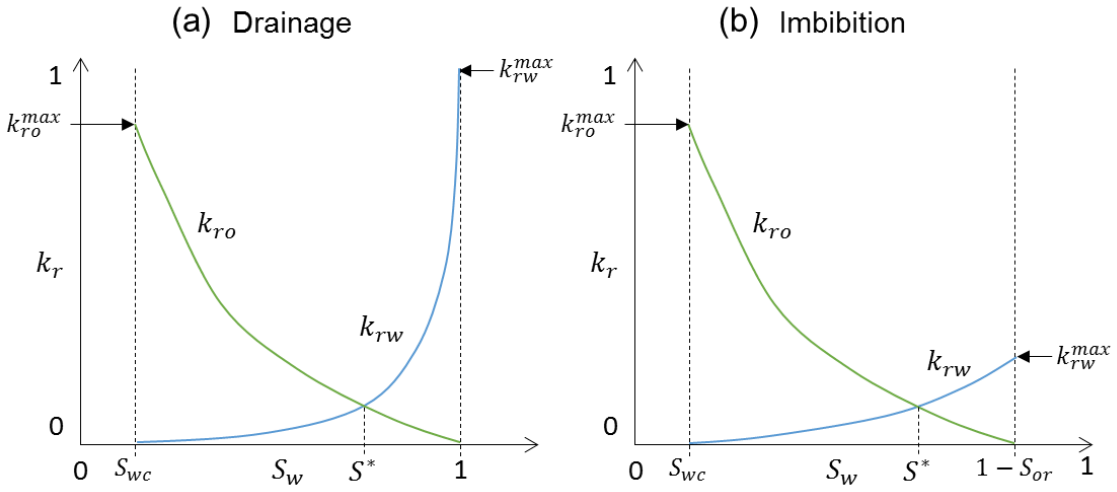

Figure 2. 5. Oil and water relative permeabilities in a water-wet system as a function of water saturation during (a) drainage and (b) imbibition. Blue lines represent the water relative permeability while green lines represent oil relative permeability. k_r is the relative permeability and S_w is the water saturation. Subscripts *w*, *o*, *c* and *r* refer to water, oil, connate and residual respectively, while superscript *max* refers to the maximum. * marks the cross-over saturation between oil and water relative permeabilities.

The impact of surface wettability on relative permeability is depicted in Fig. 2.6. The waterflood relative permeabilities for water-wet, oil-wet and mixed-wet systems are displayed. This occurs in hydrocarbon reservoirs when water is injected to boost oil and gas recovery. These relative permeabilities are labelled water injection rather than imbibition since water injection into oil-wet rocks or into oil-wet pores in a mixed-wet rock is in fact a drainage process, not an imbibition one.

The three most widely used experimental techniques to measure relative permeability are the steady-state, the unsteady-state, the centrifuge and gravity drainage methods [35]. In this PhD, we will develop, for the first time, an approach to combine steady-state relative permeability measurements with pore-scale X-ray imaging for three-phase flow. The purpose of this is to understand the impact of the pore-scale processes on three-phase relative permeability. At the moment, this has only been done for two-phase flow [14, 15]. Hence, this is a clear gap in the three-phase flow literature that we will fill in *EXPS* 6 and 7 (chapter 6), see Table 1.1.

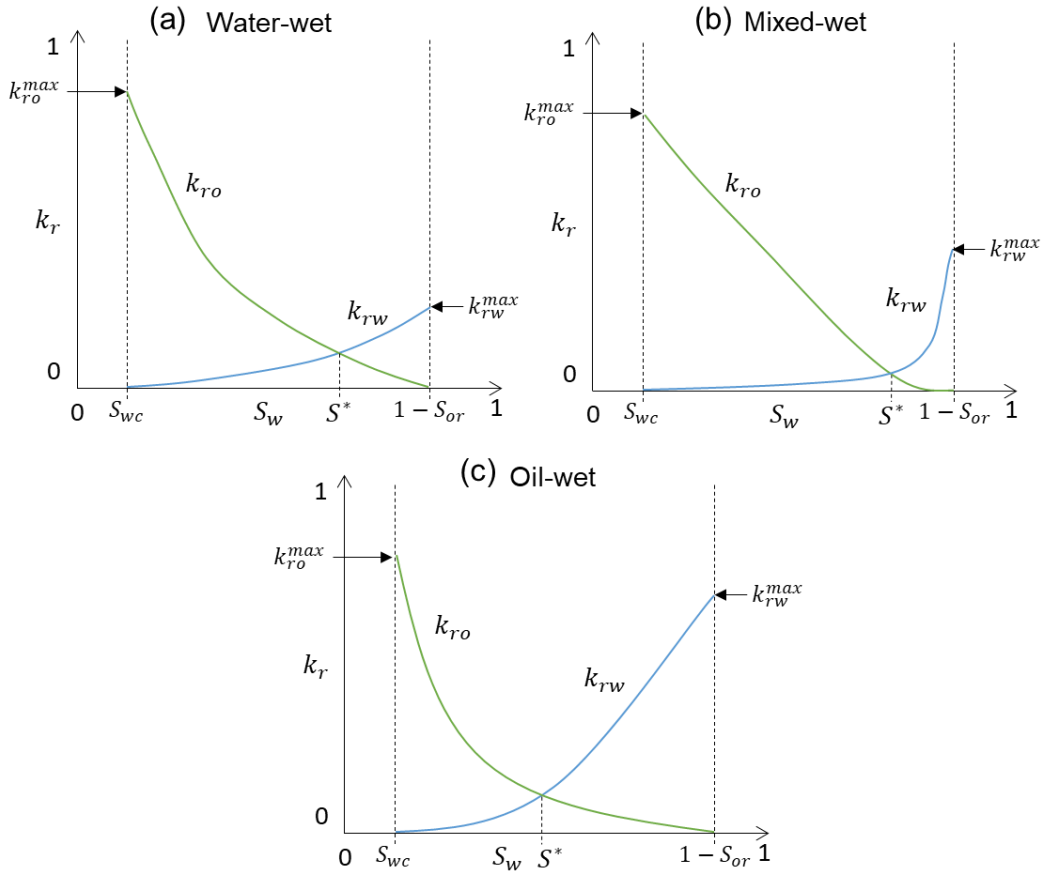

Figure 2. 6. Water injection relative permeability plotted as a function of water saturation in (a) water-wet, (b) mixed-wet and (c) oil-wet systems. Blue lines represent the water relative permeability while green lines represent oil relative permeability. k_r is the relative permeability and S is the saturation. Subscripts w, o, c and r refer to water, oil, connate and residual respectively, while superscript max refers to the maximum. * marks the cross-over saturation between oil and water relative permeabilities.

2.1.1.5 Layer flow, swelling and snap-off

It is evident from Fig. 2.6 that after injecting water to displace oil in the reservoir, the residual oil saturation (S_{or}) does not reach zero. Similarly, during primary drainage in hydrocarbon reservoirs, when oil and gas first migrate into the reservoir displacing water, the connate water saturation (S_{wc}) – or irreducible water saturation – also does not get to zero, see Fig. 2.5a. The fact that the fluids cannot be completely displaced from the pore space is intimately related to the heterogeneity of the reservoir – which can have an impact on both km- and µm-scales and is quantified by the sweep efficiency – and residual (or capillary) trapping which is a pore-scale phenomenon influenced by connectivity.

To understand this phenomenon, we need to closely examine a pore doublet model that incorporates some degree of heterogeneity and interconnectivity. A model example is shown in Fig. 2.7 in which a single pore branches off into two pores with different diameters and then re-merges into a single pore again. Initially, the pore space is saturated with water, see Fig. 2.7a. Let us first consider a primary drainage process, when oil first migrates into the pore space, pore 1 will be filled with oil, and assuming it is a water water-wet system, oil, as the non-wetting phase, will invade the centre of the pore, confining water, wetting, to layers in the corners and roughness of the pore space. The water wetting layers are assumed to be connected throughout the rock.

As oil further progresses into the pore space, it will fill pore 2 preferentially over pore 3 as it has a lower capillary entry pressure. The lower capillary entry pressure of pore 2 is attributed to its larger diameter from Eq. (2.3). The fluids distribution in pore 2, will be similar to that of pore 1, where oil resides in

the centre of the pore and water remains in the wetting layers. Oil will then continue to flow and fill pore 4 at the end of the model, and unless a driving pressure that exceeds the capillary entry pressure of pore 3 is imposed, the pore will remain saturated with water. The water in pore 3 is immobile and is called the irreducible water saturation in addition to the water confined to layers.

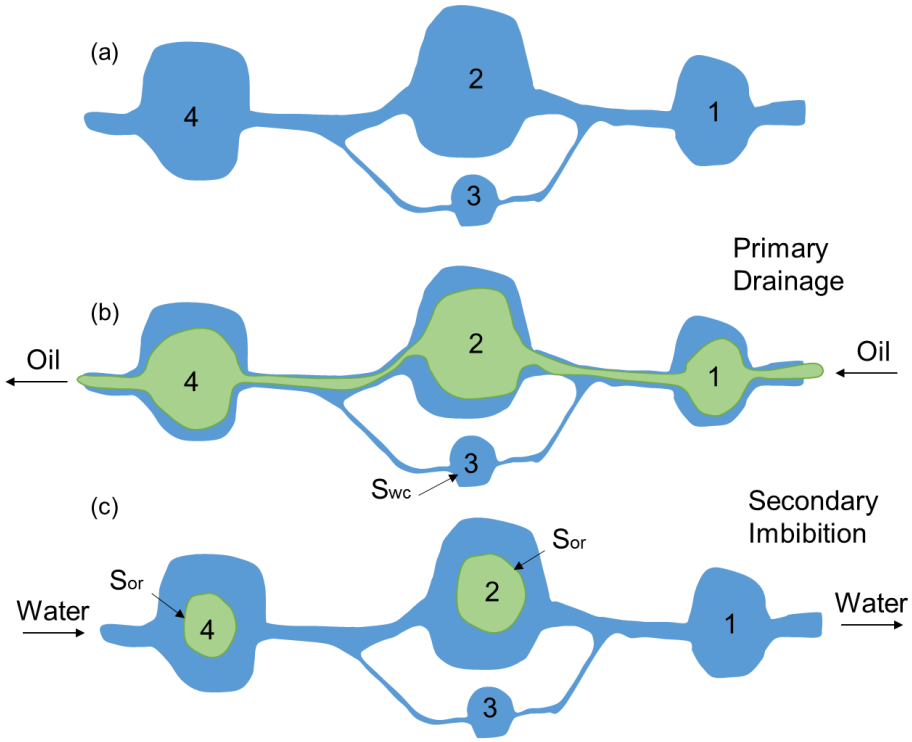

Figure 2. 7. An illustration of the fluid arrangements, displacement mechanism and residual saturations in a pore doublet model in (a) prior to primary drainage, (b) after primary drainage, and (c) after water injection (imbibition). The model is used to explain the phenomena of residual saturations. *S* is the saturation while subscripts *w*, *o*, *c* and *r* refer to water, oil, connate and residual respectively.

Now, let us consider the water injection process (imbibition) in the same system assuming that it remains water-wet after primary drainage, see Fig. 2.7c. As water moves into the pore space, from the other direction, the wetting layers will start to swell; this process is slow but allows for a uniform increase in the water saturation across the system. As these layers swell, their thickness increases until they meet, and the pore spontaneously fills with water, causing the remaining oil in the pore centre to snap-off and become isolated. In an imbibition process, the smaller pores are preferentially filled over the larger pores. Hence, pore number 3 will initially fill with water, and then water progresses to fill pore 1, and if pore 1 is filled with water before all the oil has drained from the larger pores (2 and 4), snap-off will occur in these pores and the oil becomes trapped. This oil is part of the residual oil saturation.

The snap-off process which leaves ganglia trapped as isolated droplets in the pore space is known as capillary trapping. Capillary trapping can occur in both water-wet and oil-wet media by the wetting phase which flows along the mineral surfaces. For oil recovery applications in oil-wet media, the theory is that the connectivity of the oil wetting layers throughout the rock results in a very low residual oil saturation, as oil can no longer get disconnected and trapped. However, in practice the rate of oil flow along these layers is very slow resulting in low oil recovery and smaller relative permeability. In contrast, capillary trapping is desired for gas storage applications either in aquifers, where water can trap the CO_2, or in oil reservoirs where CO_2 can be trapped by both oil and water if they are more wetting to the rock.

In this PhD, we will investigate, for the first time, the pore-scale dynamics during water injection in an oil-wet reservoir rock in *EXP* 4 (section 4.1), see Table 1.1. Despite this being a two-phase flow study, it is novel and can be of great value for the two-phase flow literature.

2.1.1.6 Flow pathways

Here, we will embark on a concept that is of significant importance for our steady-state three-phase flow work – in *EXPS* 6 and 7 – which will be presented in chapter 6. While the theoretical background provided in this chapter, (2), was not specific to certain flow conditions, the theory in this section, (2.1.1.6), is only pertinent to steady-state flow conditions. Steady-state conditions refer to the flow of one or more fluid phases simultaneously through the pore space at conditions of local equilibrium.

During two-phase flow in porous media at steady-state conditions, the fluid flow pathways are classified into three flow regimes: (i) connected flow pathways; (ii) ganglion dynamics; and (iii) intermittent flow pathways.

Most of the theory we have described falls in the connected flow pathway regime, which is also known as the Darcy or linear flow regime. In this regime, the relationship between the pressure gradient and flow rate is linear as per the Darcy law, Eq. (2.1). Here, each fluid phase has its own pathway, independent of the other fluid phases present [18]. The interface between fluids is static such that any disconnected phase in the pore space is considered trapped. The displacement in this regime is controlled by capillary forces.

In contrast, in a ganglion dynamics regime, where viscous forces are significant, the non-wetting phase is advected through the pore space in disconnected ganglia while the wetting phase is generally connected across the system [36]. Lastly, in the intermittent flow regime, the non-wetting phase exhibits a dynamic connectivity as it periodically gets connected and disconnected in the pore space [37]. The relationship between flow rate and pressure gradient is non-linear in the intermittent regime.

The determination of the flow regime is very important to explain and understand the pore-scale physics controlling the flow. This is usually achieved by calculating the capillary number, *Ca*, which is a dimensionless ratio of the viscous to capillary forces:

$$Ca = \frac{\mu q}{\sigma} \tag{2.7}$$

where q is the Darcy velocity of the displacing (injected) phase, while μ is its viscosity.

However, these flow regimes are specific to two-phase flow. In this PhD work we will observe a distinct flow behaviour in three-phase flow where the phases are intermittent in the Darcy flow regime (chapter 6).

2.1.2 Three-Phase Fluid Flow

This section will describe the key pore-scale physical processes that control fluid movement during three-phase flow, namely wettability order, spreading and wetting layers, and double/multiple displacement events [18]. These in turn control how each phase flows, its conductance, and how much is displaced or trapped.

In this thesis, we will consider immiscible gas-oil systems, defined here when the gas-oil interfacial tensions are around 10 mN/m or larger, and the oil and gas phases have distinct physical properties. We will also study near-miscible systems with gas-oil interfacial tensions of around 1 mN/m, which is an order of magnitude lower than the interfacial tension between the other fluid pairs. We will not discuss the fully-miscible gas case, since at these conditions only two phases exist (water and a hydrocarbon phase), or cases with ultra-low gas-oil interfacial tensions where viscous effects become significant at

the pore-scale in comparison to capillary forces, as again the behaviour is often similar – in terms of recovery and trapping – to a miscible displacement [8].

2.1.2.1 Wettability order and pore occupancy

In three-phase flow, it is wettability order that controls the arrangement of the fluid phases in the pore space [18]; it determines which phase preferentially wets the solid surface and which one instead occupies the centre of the pores. The wettability order, from most to least wetting, can be defined either directly by the contact angle θ at the interface of each fluid pair, or indirectly through pore occupancy. Pore occupancy refers to the size of the pores occupied by each fluid phase. The most wetting phase tends to occupy the smallest pores and throats as well as wetting layers. The most non-wetting phase preferentially resides in the centres of the larger pores, while the intermediate-wet phase occupies medium-sized pores and/or forms spreading layers sandwiched between the two other phases.

Conventionally, it is hypothesized that the wettability order is a function of surface wettability only [18]. However, through our investigations of different miscibility conditions – immiscible and near-miscible – we discover that the wettability order is also a function of gas-oil miscibility, see chapter 3.

For now, we will only outline the presumed wettability orders for different surface wettabilities at immiscible gas-oil conditions. These are presented in Fig. 2.8. For the water-wet system at immiscible conditions, in Fig. 2.8a, the wettability order is water-oil-gas from most to least wetting, where water, the most wetting phase, occupies the small-sized pores, gas, the most non-wetting phase, resides in the large-sized pores, while oil, the intermediate-wet phase, occupies the intermediate-sized pores. This wettability order is altered under immiscible weakly oil-wet conditions, as oil becomes the most wetting phase then water then gas (oil-water-gas), see Fig. 2.8b. For strongly oil-wet rocks, it is predicted that the wettability order changes, while oil remains the most wetting phase, gas becomes the intermediate-wet phase and water the most non-wetting phase.

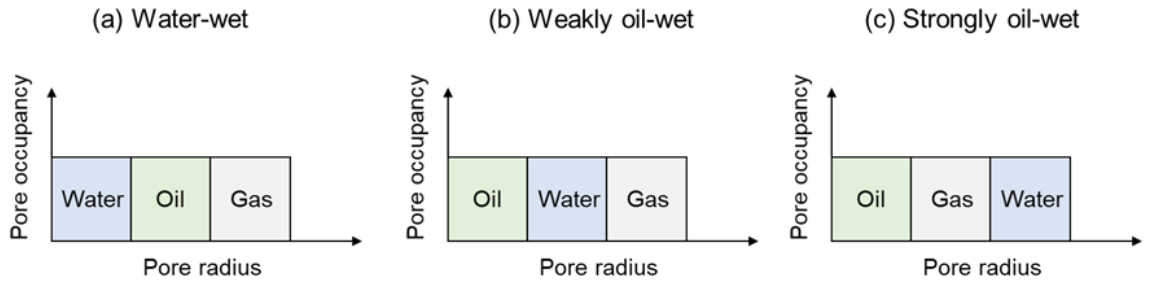

Figure 2. 8. Possible wettability orders in uniformly-wet systems at immiscible gas-oil conditions in (a) water-wet, (b) weakly oil-wet and (c) strongly oil-wet porous media. The complexities associated with pinned layers and filling are ignored here.

While the anticipated wettability orders for water-wet and weakly oil-wet systems at immiscible conditions have been observed directly inside rocks using pore-scale X-ray imaging [16, 17, 38], there has been no experimental evidence of the predicted wettability order for strongly oil-wet rocks, although it has been seen in micromodel experiments [39]. Therefore, there is a clear gap in the three-phase literature to determine if it is actually possible for the predicted wettability order in strongly oil-wet systems to occur in systems with rough surfaces, e.g., rocks. In this PhD, we plan to test this hypothesis by exposing a reservoir rock to severe wettability alterations and performing a three-phase flow experiment on it in *EXP* 3 (section 3.3), see Table 1.1.

2.1.2.2 Conductivity and trapping

The arrangement of the phases in the pore space, determined by wettability order, has consequences for their flow conductivity and trapping. If a phase occupies large and/or intermediate-sized pores, it will have a larger flow potential compared to if it occupies smaller pores. However, this assumes that the phases are connected through the pore space. Capillary trapping of a phase can occur when it exists as a disconnected bubble in the centre of the pores surrounded by another, more wetting, phase. Therefore, for a fluid phase to become trapped by another phase, in general, it must be less wetting than that phase. Hence, the most non-wetting phase has potentially the highest flow conductance when it is connected through the wide regions of the pore space but, conversely, can have the largest residual saturation if the flow pathways become blocked by more wetting phases.

2.1.2.3 Spreading and wetting layers

Fluid phases can form wetting and/or spreading layers in the pore space during three-phase flow [40]. The formation of layers maintains the hydraulic connectivity of the phase in the pore space which allows it to flow at very low saturations, while facilitating the trapping of the other phases – while wetting layers can trap the other two phases, spreading layers can only trap the most non-wetting phase [41]. The formation of wetting layers is dependent on the surface wettability, while the spreading coefficient C_s of each fluid phase determines whether or not it will form spreading layers sandwiched between the two other phases in the pore space [18]. The spreading coefficient of a phase i can be found using the interfacial tensions, σ, between the three fluid phases (i, j and k) [24, 42]:

$$C_{si} = \sigma_{jk} - \sigma_{ij} - \sigma_{ik} \tag{2.8}$$

Phase i can spread in layers sandwiched between phases j and k if its spreading coefficient is positive or close to zero. If the spreading coefficient is strongly negative, the formation of spreading layers is not favoured. In Eq. (2.8) we would normally refer to the interfacial tension values in thermodynamic equilibrium, where the spreading coefficient is either zero or negative [18].

Another necessary condition for the formation of spreading layers requires a certain balance between the fluid-fluid curvatures. We will explain this constraint in more detail in sections 3.1.3.2.5.1 and 3.3.3.5.1.

In most hydrocarbon reservoirs, at immiscible conditions, the equilibrium spreading coefficient of oil is positive or very close to zero; therefore, oil often spreads in layers sandwiched between gas and water regardless of the wettability of the rock.

While oil layers have been previously observed in micromodels [41, 43-45], it was not until recently that Scanziani et al. [16] managed to directly visualize them *in situ* using pore-scale X-ray imaging in a water-wet system. In this PhD work, we encounter examples of systems, where not only oil spreads in layers but also gas, at near-miscible conditions, as we will show in *EXP 2*, see section 3.2.

2.1.2.4 Double and multiple displacements

One unique characteristic of three-phase flow is double displacement which can occur under capillary dominated conditions [41, 44]. Double displacement refers to the displacement of one fluid phase by another, which in turn displaces another phase inside the porous medium [46]. Mathematically speaking, there are six possible double displacement events during three-phase flow: (*i*-*j*-*k*), (*i*-*k*-*j*), (*j*-*i*-*k*), (*j*-*k*-*i*), (*k*-*i*-*j*), (*k*-*j*-*i*) [18]. The dominant double displacement event depends on the injected phase, saturation history, wettability, and spreading and wetting layers. However, we will show in this PhD work that the gas-oil miscibility also plays a role in dictating double displacements.

Furthermore, it is also possible to have multiple displacements, with one phase displacing another and then another, with any number of intermediate steps [46]. Double and multiple displacements allow for both the mobilization of trapped fluid phases and their immobilization through displacement in wetting and spreading layers. Multiple displacement ensures that even in a capillary-controlled displacement, a phase can be displaced and advance through the pore space, even if it is disconnected and surrounded by other phases (apparently trapped).

Double and multiple displacements have been extensively studied previously in two-dimensional micromodels [43, 47, 48]. However, the question remains whether or not the same pore-scale behaviour will persist in three-dimensional natural porous systems. These displacements may occur less or more frequently in a complex, better connected pore space. In this PhD thesis, we will use, for the first time, fast synchrotron X-ray imaging – dynamic imaging – to capture double and multiple displacements *in situ* during three-phase flow in a strongly oil-wet reservoir rock in *EXP* 5 (section 4.2).

2.1.2.5 Mathematical and physical constraints

A three-phase displacement is normally simplified by breaking down events into a series of two-phase processes. There are three combinations of two phases: oil-water (*ow*), gas-water (*gw*) and gas-oil (*go*), where the phases water, oil and gas are labelled *w, o* and *g* respectively. There are also three fluid-fluid interfacial tensions, three contact angles, three saturations, three interfacial curvatures, and three capillary pressures. The capillary pressure equations, Eqs. (2.2) and (2.3), can be extended to for any number of fluid phases:

$$P_{cij} \equiv P_i - P_j = \sigma_{ij}\kappa_{ij} \tag{2.9}$$

for any combination of phases *i, j* and *k*. The curvature κ_{ij} is here defined to be positive if phase *i* bulges out into phase *j* (and, as a consequence, phase *i* is at a higher pressure than *j*).

However, there are constraints between the various three-phase parameters, as outlined below, so that only two contact angles, saturations and capillary pressures (or curvatures) are independent. The first constraint is easily derived from the definition of capillary pressure in Eq. (2.9) but is only valid for connected phases in capillary equilibrium:

$$\sigma_{ik}\kappa_{ik} = \sigma_{ij}\kappa_{ij} + \sigma_{jk}\kappa_{jk} \tag{2.10}$$

There is a similar constraint on contact angles, the Bartell-Osterhof relation [49, 50] under the same assumptions:

$$\sigma_{ik}\cos\theta_{ik} = \sigma_{ij}\cos\theta_{ij} + \sigma_{jk}\cos\theta_{jk} \tag{2.11}$$

where θ_{ij} is the contact angle between phases *i* and *j* at the solid surface measured through (traditionally the denser) phase *j*.

There are two other constraints, inherent in the definition of curvature and contact angle:

$$\kappa_{ij} = -\kappa_{ji} \tag{2.12}$$

and

$$\cos\theta_{ij} = -\cos\theta_{ji} \tag{2.13}$$

These constraints and equations will be heavily used in our work to explain the various three-phase flow pore-scale phenomena that we come across.

This marks the end of the theory section provided on two- and three-phase flow in porous media.

2.1.3 Pore-Scale X-ray Imaging

The use of X-ray microtomography to study multiphase flow in porous media, particularly in the pore spaces of rocks, has become a routine analysis in the oil and gas industry [18]; it is now known as digital core analysis. The ability of this non-destructive tool to image, in three dimensions, the processes and variables inside the pore space, has made it of central importance to multiphase flow studies in different systems, e.g., rocks, batteries, fuel cells, microfluidic devices, etc. Digital core analysis is typically conducted with micron resolution down to the pore-scale, which is well-suited for exploring rock properties and transport phenomenon at a representative elementary volume (REV) scale or millimetres to centimetres. This technology was first introduced to study rock systems by Flannery et al. [51] who used both laboratory and synchrotron X-ray sources to acquire micron-resolution images of a porous rock.

2.1.3.1 X-ray sources and applications

The current state-of-the-art in microtomographic imaging utilizes both synchrotron and laboratory-based facilities. Synchrotron sources emit X-rays from electrons by accelerating them around a circular ring at almost the speed of light. This allows for very high-resolution imaging and shorter acquisition times. Therefore, by using a synchrotron radiation source, time-resolved studies can be conducted down to a very high temporal resolution (~1s). With such rapid imaging systems, the pore-scale displacement dynamics can be captured during fluid invasion. However, access to these facilities is usually much more restricted than using the compact laboratory-based facilities. A synchrotron X-ray source will be used in *EXPS* 4 and 5, see chapter 4.

The ease of accessibility and use of laboratory-based X-ray microtomography makes it an attractive solution for the production of reliable three-dimensional images of the pore space. Despite the fact that longer times are needed to acquire the X-ray images, laboratory facilities can be used to investigate a wide range of pore-scale flow properties including micro and macro porosity, fluid saturations, interfacial areas, curvatures, pore occupancy, contact angles, layer formation, displacement processes, connectivity and trapping [11, 12, 52].

In this PhD work, we will use both synchrotron and lab X-ray microtomography in our experiments which will help provide a comprehensive understanding of three-phase flow. In the text, we will refer to synchrotron imaging as **dynamic imaging**, while the lab-based imaging will be called **static imaging**.

2.1.3.2 X-ray attenuation

When X-rays are incident on a rock saturated with fluids, there is a contrast between the rock and the fluids in the images. The contrast is a result of the materials having different attenuations due to their differing atomic numbers. The higher the atomic number of the material the higher is its absorption coefficient. As the X-ray beam passes through a material it loses its intensity and a fraction of the X-rays is attenuated, the attenuation of the X-rays follows Lambert-Beer's law [53]:

$$I = I_0 \times e^{-\mu x} \tag{2.14}$$

where I is the transmitted beam intensity, I_0 is the incident beam intensity, μ is the linear attenuation coefficient and x is the thickness of the material.

Depending on the transmitted beam intensity we can distinguish between the different materials in the X-ray image. Materials with higher attenuation coefficients will allow X-rays to penetrate a relatively short distance, hence it will have lower intensity compared to materials with lower attenuation

coefficients. Therefore, to be able to accurately identify/distinguish materials in the pore space image, we need sufficient variation in attenuation coefficients.

The attenuation contrast is typically increased by adding dopants to the fluids in the pore space. A dopant is an absorptive material used to produce a desired attenuation coefficient for a specific fluid. In our case, we have four phases in the X-ray images – rock and three fluids – and therefore, doping is necessary to distinguish the phases. Since it is difficult to dope the gas phase, we will dope both oil and water in our experiments. The doping percentage will depend on the rock type used in each experiment. Optimum doping percentages will be decided using phase contrast scans prior to performing the experiments.

2.2 Literature Review

This section will provide a synthesized literature review of all the relevant three-phase flow studies to our work. The sub-sections will be linked to the **seven** experiments listed in Table 1.1, in the same order as they are listed.

Just a reminder that *EXPS* 1 to 5 are performed at unsteady-state conditions, while *EXPS* 6 and 7 are at steady-state conditions. The fluids are injected consecutively at unsteady-state conditions, while at steady-state conditions they are injected simultaneously.

Sections 2.2.1 is concerned with the work previously performed at near-miscible gas-oil conditions. Section 2.2.2 looks at strongly oil-wet systems at immiscible conditions. The previous studies on two and three-phase pore-scale dynamics are described in section 2.2.3. Finally, the three-phase steady-state literature is reviewed in sections 2.2.4. Some definitions from the theory section, (2.1), maybe repeated for clarity and flow of text in this section.

2.2.1 Near-Miscibility

Here, we will review the three-phase flow literature on the pore-scale processes at near-miscible conditions. We will clearly identify the gap in the literature and how we plan to bridge it by performing X-ray imaging experiments at near-miscible conditions in a water-wet and a weakly oil-wet rock (*EXPS* 1 and 2, see Table 1.1).

Miscible flooding is an attractive option for many producing oil reservoirs that are experiencing a rapid decline in pressure and/or production from water injection. However, the achievement of miscibility may require high injection pressures, or enriched gases, both of which are expensive or operationally difficult; in contrast, near-miscible flooding may be cheaper and easier to implement [54]. Moreover, near-miscible conditions are more favourable for CO_2 storage. Near-miscible injection refers to the injection of gases at pressures slightly lower than the minimum miscibility pressure (MMP). Such conditions result in a low but not negligible interfacial tension between the gas and oil phases (~ 1 mN/m). Many laboratory studies and some field implementations suggest that near-miscible and miscible injection perform in a comparable manner [55].

Shyeh-Yung [54] conducted 33 near-miscible CO_2 core flooding experiments in both Berea sandstone and a Texas carbonate at reservoir conditions. The author reported that the change in tertiary oil recovery is minimal when switching from miscible to near-miscible conditions. They attributed the substantial oil recovery at near-miscible conditions to the low gas-oil interfacial tension which enhances the sweep efficiency and reduces pore level bypassing. These results contradict the severe decline in oil recovery the author observed from slim tube tests as the pressure dropped below the minimum miscibility pressure. These findings suggest that slim tube tests do not provide realistic data on recovery at near-miscible pressures, and whenever possible must be replaced with reservoir condition core floods.

Similarly, Schechter et al. [56] carried out extensive CO_2 core flooding experiments to optimize the performance of the EOR gas injection scheme in the Wellman unit. In their study, they considered dropping the reservoir pressure to reduce the injected volume of CO_2. In addition, they performed field scale simulations to characterize the sweep efficiency at lower pressures. They found out that maintaining the pressure slightly below the MMP did not reduce oil recovery; meanwhile the field scale simulations suggested optimum sweep efficiency at these conditions. Further experimental evidence provided by Grigg and Schechter [57] showed that oil recovery can still be quite high at pressures slightly below the MMP.

Near-miscible core flood tests were complemented by field-scale simulations to help justify the substantial oil recovery observed at these conditions [58-60]. Burger et al. [58] and Thomas et al. [60] simulated 2D miscible and near-miscible injection processes in heterogeneous reservoirs. Both authors reported a higher oil recovery for the near-miscible schemes which was attributed to their improved sweep efficiencies. Pande [59] demonstrated from a compositional simulation that the gravity and viscous cross-flow processes occurring at near-miscible conditions are the reasons behind the increased sweep efficiency. Overall, these studies indicate that a better sweep efficiency may be possible from near-miscible flooding, combined with operational cost savings. However, they do not address the impact of near-miscible conditions on local displacement efficiency.

In light of these promising results reported in near-miscible studies, many authors have investigated the microscopic mechanisms of oil recovery under these conditions [61-65]. While most authors focussed on understanding the phase behaviour of the fluids and quantifying the mass transfer mechanisms, only few tried to visualize the pore-scale dynamics. Understanding the pore-scale dynamics is essential to predict how the three-phases – oil, water and gas – flow simultaneously at equilibrium conditions, i.e., further away from the well.

Williams and Dawe [63] photographed near critical liquid-liquid mixtures in a transparent porous medium. They concluded that at very low interfacial tensions between gas and oil, the two phases can flow alongside each other in the same pore. Sohrabi et al. [61] imaged high pressure equilibrated gas-oil-water flow experiment in a 2D water-wet micromodel. They also observed the flow of oil and gas along the same path in a single pore. Their micromodel images indicate that as the gas front propagates through the porous medium, the oil recovery continues by cross-flow from the bypassed pores into the main flow stream which results in a high oil recovery.

The observations of Williams and Dawe [63] and Sohrabi et al. [61] indicate that in a water-wet medium, oil flows in the centre of the larger pores alongside the gas phase at near-miscible conditions. This contradicts the typical wettability order observed for water-wet media, where water occupies the smallest pores, gas the biggest, while oil spreads in layers occupying pores of intermediate size [18] as we have discussed in section 2.1.2.1. Hence, it appears that lowering the oil-gas interfacial tension at near-miscible conditions leads to a break-down in the strict wettability order in the system, as oil is no longer confined to movement in layers (oil does not spread in layers between gas and water) and is allowed to flow rapidly in the centre of the larger pores.

The impact that lowering the interfacial tension – at near-miscible conditions – has on relative permeability was highlighted in a study conducted by Longeron [66]. Longeron [66] measured two phase relative permeability in a vapour-liquid system and observed that lowering the interfacial tension between the fluids increased the relative permeability of the two phases. As the mixture approached miscibility, i.e., near-miscible conditions, the relative permeabilities approached a straight line. Intuitively, the displacement of oil by gas in the larger pores at near-miscible conditions will result in a higher oil relative permeability compared to the case where oil is displaced in layers in medium-sized pores. Furthermore, lowering the interfacial tension decreases the capillary pressure between the displacing and the displaced fluids. This suggests that gas can easily displace oil in the pore space at near-miscible conditions – improved microscopic displacement efficiency. The combination of oil

phase flowing in the larger pores and the improved gas displacement efficiency could justify the more favourable oil recovery observed at near-miscible conditions.

Nevertheless, before drawing any definitive conclusions, we must note that this phenomenon of oil flowing in the larger pores in the presence of gas was only observed in micromodels and there is no evidence of it occurring in real rock systems. Scanziani et al. [16] were the first to directly visualize the *in situ* wettability order at high temperature and pressure in a water-wet rock at immiscible conditions using three-dimensional pore-scale X-ray imaging. They demonstrated clearly the spreading of oil in layers sandwiched between gas and water in the pore space.

While pore-scale imaging of immiscible gas injection have been reported [16, 38, 67], there is a deficiency in the literature for near-miscible studies. This is attributed to the complexity of visualising the gas and oil phases at low interfacial tensions. At lower interfacial tensions, the gas and oil tend to have similar properties which makes it difficult to distinguish the two phases in the X-ray images. Therefore, the design of the experiment must be tailored to permit the visualisation of the pore-scale level mechanisms. This is a clear gap in the three-phase literature that we will fill in this PhD.

In *EXP* 1, (section 3.1), we will develop, for the first time, an experimental procedure that allows for the pore-scale X-ray imaging of near-miscible CO_2 injection in a water-wet rock. This will help directly visualize the hypothesized breakdown in the wettability order at near-miscible conditions, as well as confirm the absence of oil layers, which will indicate that the wettability order in a system is not only a function of wettability but also miscibility.

Furthermore, having investigated the pore-scale physics in a water-wet rock at near-miscible conditions in *EXP* 1, we will extend the scope of our near-miscible work to weakly oil-wet rocks in *EXP* 2 (section 3.2).

Studying rocks with altered surface wettability is particularly important for three-phase applications in oil reservoirs where the presence of crude oil in the pore space over geological times, at conditions of high temperature and pressure, changes the wettability. Both Scanziani et al. [38] and Qin et al. [17] studied weakly oil-wet rocks at immiscible conditions using X-ray microtomography. The authors confirmed the anticipated oil-water-gas wettability order, from most to least wetting, as we mentioned in section 2.1.2.1. However, weakly oil-wet systems have never been studied at near-miscible conditions.

2.2.2 Strongly Oil-Wet Surfaces

Here, we will provide the motivation for studying three-phase flow in strongly oil-wet rocks at immiscible conditions in *EXP* 3 (section 3.3).

In section 2.1.2.1 we mentioned that the theoretically anticipated wettability order for strongly oil-wet systems at immiscible conditions has never been observed inside rocks. In fact, for many years, it was believed that reservoir rocks cannot be rendered strongly oil-wet for a number of reasons which we outline below. Therefore, this wettability order, where gas becomes more wetting to the surface than water, was disregarded and long considered a myth in the oil industry which led to its exclusion from almost all three-phase flow models. Hence, we took it upon ourselves to prove whether or not reservoir rocks can be rendered strongly oil-wet in *EXP* 3.

It has been suggested that in natural rock systems it is not possible to strongly alter the wettability of the surface to the point where gas becomes the intermediate-wet phase [8, 68, 69]; it is generally assumed that gas will always remain as the most non-wetting phase. This is attributed to two reasons: (i) surface roughness, which retains water after primary drainage, may prevent the same strong wettability alteration as compared to micromodels where the surfaces are typically smooth [28, 70, 71]; and (ii) wettability in reservoir rocks is altered by being placed in contact with crude oil at high

temperatures and pressures for long periods of time, whereas in micromodels a synthetic chemical is used that guarantees a uniform hydrophobic coating [47, 72].

Nonetheless, we believe that the presence of crude oil in the pore space of the rocks under high temperature and pressure for millions of years exposes the rock surfaces to severe wettability alterations, possibly rendering the contacted surfaces strongly oil-wet. Therefore, in *EXP* 3 (section 3.3), we statically and dynamically age a reservoir rock for a period of eight months at 80 ºC and 10 MPa before using it in a three-phase flow experiment combined with pore-scale X-ray imaging. This work can have huge implications on the assumptions embedded in our current three-phase simulation models.

2.2.3 Pore-Scale Dynamics

2.2.3.1 Two-phase flow dynamics

In this section we will provide a detailed literature review on the pore-scale dynamics in two-phase flow. The gap in the literature and motivation behind performing the oil-wet two-phase synchrotron imaging experiment in *EXP 4* (section 4.1) will be highlighted.

Two-phase flow in porous structures occurs in many natural and industrial systems such as blood flow [73], the movement of food and water within the intestinal tract of the human body [74], transport in porous membranes [75], carbon dioxide storage in geological aquifers [76, 77], and oil recovery by water from reservoir rocks [8, 78]. To understand the dynamics of fluid flow in porous materials, we need to study the processes that control its movement, which occur at the pore-scale [18]. At the pore-scale, the physics underlying the flow is mainly governed by capillary forces that control the fluid-fluid displacement, which depends on the porous medium geometry and wettability.

According to the wettability of the invading and displaced fluids, the displacement processes are termed drainage or imbibition. This definition applies for strictly hydrophilic or hydrophobic systems. However, many of natural and manufactured porous media have a wettability that can be altered through contact with surface-active components of the fluids [70]. The resultant wettability controls a variety of processes from oil recovery to gas exchange in leaves, and the performance of fuel cells and batteries [18, 70, 79-82]. Hence, it is of great importance to study and quantify the dynamic nature of invasion patterns and the associated pore-scale events in porous media with an altered wettability. This is the main objective of our study; we now proceed with a review of the dynamics of two-phase flow in porous media.

When a porous medium is conceptualized, its void space is typically represented as a network composed of wide regions, the pores, that are connected together by narrower regions, the throats [18]. This network representation is sufficient to accurately characterize and track the filling sequence during displacement. When a non-wetting phase displaces the wetting phase, the process is called drainage: here, the non-wetting phase advances as a connected front through the pore space, displacing the wetting phase in the pore centres, and confining it to wetting layers in the corners of the pore space.

Drainage can be described as an invasion percolation process [83], where the non-wetting phase progresses from pore to pore through the widest available throats. Filling is only possible if the nearest-neighbour pore or throat is already filled. An available throat is a throat adjacent to a pore already filled with the invading phase [83, 84]. The capillary pressure for displacement, P_c, is defined through the Young-Laplace equation, for throats with a cylindrical cross-section of radius r, by:

$$P_c = \frac{2\sigma \cos\theta}{r} \tag{2.15}$$

In *EXP 4*, the displacement process we will investigate is water injection in an oil-filled system with altered wettability. In such systems, the contact angle, θ, is conventionally measured through the denser

phase, water, while the capillary pressure is the pressure difference between oil and water ($P_c = P_o - P_w$). During water injection, the water pressure increases with time and invasion proceeds in order of decreasing capillary pressure – the events with the largest capillary pressure occur first. We will define a drainage-like process for water injection as one represented by a contact angle greater than 90°, where $\cos\theta$ is negative, and hence the capillary pressure is also negative: the medium is water-repellent, and water has to have a higher pressure than oil to advance through the pore space. For a medium of constant wettability (contact angle), filling the largest available throats corresponds to a capillary-controlled displacement where the invading fluid progresses through the porous medium at the highest allowable capillary pressure (or lowest absolute value, since the capillary pressure is negative).

As the non-wetting phase (water) passes from a narrow throat into a wider pore, there is a sudden change in the local capillary pressure which results in rapid filling of the invaded pore, and possibly further filling of multiple pores and throats downstream of the invaded pore if they can also be invaded at the prevailing water pressure. This fast filling is known as a Haines jump [85]. To enable the displacement in multiple pores during a Haines jump, the non-wetting phase retracts from some throats, which we term Roof snap-off [18, 86, 87]. At the pore-scale, the retraction of the non-wetting phase is not a drainage process, but instead is an imbibition event, where now the wetting phase displaces the non-wetting phase. Snap-off can occur either in a pore that has just been invaded by the non-wetting phase, local snap-off, or in another region some distance way, distal snap-off [88].

Imbibition, where the contact angles are less than 90° and the capillary pressure is positive, is considered a more complex pore-scale process and its dynamics is often dominated by snap-off [89]. Snap-off occurs when the layers of the wetting phase start to swell in a throat, and if the wetting layers touch and coalesce, the throat spontaneously fills with the wetting phase leading to a disconnection and trapping of the non-wetting phase in the centres of the adjacent pore [89-92]. The trapping of the non-wetting phase by snap-off is favourable for CO_2 storage applications, where maximum trapping of CO_2 (non-wetting phase) is desired, whereas it is detrimental for oil recovery applications.

The early work of Lenormand et al. [90] provided information on the dynamics of pore-filling during drainage in two-dimensional micromodels. The same behaviour was also observed by Datta et al. [93] in three-dimensions, where drainage was investigated in a pack of sintered glass beads using confocal microscopy. However, it was not until recently that advances in X-ray micro-tomography have allowed for direct imaging of the rock pore space and the fluids within it [11, 12, 52, 94]. Many laboratory-based X-ray micro-tomography studies have provided detailed description of ganglia or disconnected non-wetting phase clusters at the end of imbibition and drainage processes [95-98]. However, these studies only report end point results at static conditions and hence do not capture the displacement or pore-filling sequence which occur on a much shorter timescale than that required for a single scan (which can take several minutes or hours).

To increase the temporal resolution of imaging, fast synchrotron X-ray micro-tomography can be used, which captures the pore-scale displacement dynamics on a timescale of seconds to around 1 minute [87, 88, 91, 92, 99-101]. Berg et al. [87] quantified the number of pores invaded by the non-wetting phase (*n*-decane) during a Haines jump in a water-wet Berea sandstone. Andrew et al. [88] further investigated interface retraction and snap-off during CO_2 injection, drainage, in a water-wet Ketton limestone. Moreover, Rücker et al. [92] characterized the impact of the pore-scale viscous effects on snap-off and coalescence events during imbibition in a sandstone rock. However, to date, all the reported dynamic studies were conducted in water-wet media. The displacement dynamics have not been investigated for water invasion in altered-wettability porous media. This is the gap in the literature we will target in *EXP* 4.

In *EXP* 4 (section 4.1), we use synchrotron X-ray micro-tomography to visualize the pore-scale dynamics during water injection in a reservoir rock with altered wettability. A previous study investigated the dynamics of water injection into a quarry limestone (Ketton) which had been in contact

with crude oil [102]. The experimental conditions, mineralogy (mainly calcite), fluids and wettability alteration protocol of the study conducted in Ketton are almost identical to our study in a reservoir rock. As we show later, although the geometric contact angles measured *in situ* are similar in the two cases, the macroscopic manifestation in terms of displacement sequence, energy balance and capillary pressure are different, emphasizing the importance of the interaction of pore geometry and wettability on displacement. In the Ketton rock, the behaviour revealed mixed-wet conditions, defined by the simultaneous filling of both small and large pores during water injection, indicating that the displacement was controlled by both pore geometry and wettability (local contact angles) – water invasion was not a drainage-like process [102]. However, reservoir rocks are likely to undergo a more significant wettability alteration when in contact with crude oil [103, 104], rendering the surfaces largely oil-wet. Moreover, the reservoir sample has a wider distribution of pore sizes than in a quarry Ketton sample. This means that pore size, rather than small changes in contact angle, control the displacement process.

2.2.3.2 Three-phase flow dynamics

Here, the work performed previously to understand the pore-scale dynamics during three-phase flow is reviewed. This section will clearly highlight the lack of dynamic studies in three-phase flow and therefore show the significance of our work. The main objective of *EXP* 5 (section 4.2) is to use fast synchrotron X-ray micro-tomography to characterize the key physical processes that control the pore-scale dynamics during three-phase flow in a strongly oil-wet porous medium, namely wettability order, spreading layers and double/multiple displacement events [18].

Most three-phase flow dynamic studies involved the use of two-dimensional, transparent micromodels to investigate the pore-scale fluid interactions. The spreading of fluids in layers was investigated by Oren et al. [41] who visualized the formation of spreading oil layers sandwiched between water and gas in a water-wet micromodel. The spreading layers maintained the hydraulic connectivity of oil in the pore space permitting its flow at low saturations.

Furthermore, previous micromodel studies have shown the occurrence of double displacement events in systems with variable wettability [39, 47, 48]. In a water-wet micromodel, at immiscible conditions, Keller et al. [45] observed the occurrence of double drainage (gas displacing oil displacing water) and double imbibition (water displacing oil displacing gas) events during gas injection and chase water re-injection respectively. Notice that the direct displacement of water by gas and gas by water is limited due to the formation of spreading of oil layers sandwiched between gas and water, preventing their direct contact in the pore space [48]. Multiple displacement events have also been observed in water-wet micromodels during cycles of gas and water injection; this behaviour was captured using pore network modelling [105]. Furthermore, Sohrabi et al. [39] visualized double displacement events in an oil-wet micromodel at immiscible conditions. They reported that the main double displacement event during gas injection was gas-oil-water with a modest amount of water-oil-gas displacement during chase water re-injection. The behaviour could also be reproduced using a pore-scale model that incorporated multiple displacement events [106].

Most of the research work conducted to visualize the displacement dynamics during multiphase flow has been on micromodels [90, 107, 108]. While 2D micromodels are useful for viewing pore-level events due to their visual clarity, they do not capture the flow behaviour of the fluids in three-dimensional porous media with complex structures, e.g., rocks and soils. In *EXP* 5, we use synchrotron X-ray microtomography to image the three-phase – gas, water, and oil – displacement dynamics during gas injection in a strongly oil-wet reservoir rock. Our ability to visualize the movement of the fluids and characterize the interactions at their interfaces inside the pore space will help provide an in-depth understanding of the physical processes involved.

While static imaging enables the wettability order and presence of spreading layers to be determined, double displacement events can only be inferred from these results [16, 38]. Scanziani et al. [16] performed three-phase flow experiments in water-wet carbonates, with static imaging, and confirmed, *in situ*, the spreading of oil layers and the anticipated wettability order: water-oil-gas from most to least wetting. Qin et al. [17] studied gas and water injection in weakly oil-wet rocks, where water was the intermediate-wet phase. They demonstrated that water does not form spreading layers in the pore space, and that gas was trapped by both oil and water during water injection.

To directly visualize double displacement events and obtain information about the evolution of the fluid arrangement in the pore space over time, fast synchrotron X-ray micro-tomography can be used, which allows for pore-scale images to be acquired at ~1 minute temporal resolution [87, 88, 96, 100, 109]. The use of synchrotron X-ray imaging helped provide valuable insights into the pore-scale dynamics of two-phase flow [87, 91, 92, 99, 102]; however, very few studies have used it to investigate the displacement events during three-phase flow [101, 110]. Scanziani et al. [101] was the first to use synchrotron imaging to study three-phase, water, oil and gas (nitrogen), displacement dynamics in a water-wet quarry limestone rock. The authors observed that gas moves in a connected front surrounded by oil spreading layers during gas injection. Moreover, they reported that during chase water re-injection, after gas injection, the dominant displacement event was water displacing oil displacing gas which resulted in double capillary trapping – gas trapping by oil layers and oil layers trapping by water wetting layers. This is favorable for gas storage applications, where immobilization of the gas phase is desired.

Furthermore, Scanziani et al. [110] employed synchrotron imaging to investigate the displacement dynamics in a rock with altered wettability, which displayed a mixed-wet behaviour with oil-water contact angles both above and below 90°. The gas remained largely connected during gas injection in the mixed-wet rock. The authors did not observe double displacement events during gas injection and chase water re-injection; both gas and water directly displaced oil in the pore space. This type of displacement can facilitate further oil recovery from petroleum reservoirs with limited gas recycling.

Nevertheless, to date, no three-phase flow synchrotron study has been performed in an oil-wet porous medium. To place the work in a more general context, an accurate characterization of three-phase flow in oil-wet systems is important since many natural and engineered surfaces are non-water-wet, or designed to be partially water-wet, from deep oil reservoirs to butterfly wings, human skin, textiles, medical devices and fuel cells [70, 79-82, 111].

In *EXP* 5 (section 4.2), we use synchrotron X-ray imaging, with high spatial and temporal resolutions, to investigate the pore-scale dynamics during immiscible gas injection in a strongly oil-wet reservoir rock at subsurface conditions. This is the three-phase extension of the analysis of the two-phase displacement in *EXP* 4 using the apparatus and experimental methodology applied to a quarry carbonate [110].

2.2.4 Steady-State Three-Phase Flow

This section will emphasize the need for the development of an experimental approach that combines pore-scale X-ray imaging with steady-state three-phase flow. The section will flag the shortcomings of the traditional steady-state methods and how pore-scale imaging will solve some of these issues, providing the motivation for our work in *EXPS* 6 and 7 (chapter 6). Our steady-state work will only investigate systems at immiscible gas-oil conditions.

The empirical extension of Darcy's law for flow in a porous medium to multiple phases, Eq. (2.6), proposed 85 years ago implicitly assumes that each phase flows – in steady-state – through a fixed subset of the pore space, and explicitly states that there is a linear relationship between pressure gradient and flow rate (the Darcy flux of each phase) [112]. While for two-phase flow it is now well-established

that a non-linear relationship between rate and pressure gradient emerges for fast flows, there is still a linear Darcy-like regime for capillary-controlled displacement, which is seen in most natural and engineered settings, where the fluids indeed flow through fixed pathways [37, 113, 114]. Therefore, the presumption is that in three-phase flow again there would be a capillary-dominated flow regime with fixed flow paths.

In *EXP* 6, we show that this is not the case and that three-phase flow appears to have a unique dynamics; even for capillary-controlled flow, the most non-wetting phase (gas in our experiments) is always disconnected across the system and is transported through the intermittent opening and closing of critical flow paths. This is facilitated by double and multiple displacement events, which are a unique feature of three-phase flow [39, 41, 115, 116].

At present, relative permeability – the saturation-dependent factor by which flow conductance is reduced in multiphase flow – can either be measured experimentally or predicted empirically [18]. However, our empirical models are currently incapable of predicting three-phase relative permeability to within an acceptable accuracy in many circumstances [35]. This is mainly attributed to the lack of understanding of the impact of complex pore-scale processes that occur during steady-state three-phase flow – namely wettability, layer flow, multiple displacements, and saturation history – on relative permeability. Indeed, as stated above, it is not even evident that a Darcy-like law to describe the flow is valid at all.

The steady-state method is considered to be the most reliable approach to measure relative permeability since it directly uses the multiphase Darcy law [35, 117]. Here, the fluids are simultaneously injected into the rock at a set of fixed fractional flows and the differential pressure drop and saturations are recorded when steady-state conditions are reached [117]. Nevertheless, laboratory measurements of three-phase relative permeability are complicated, expensive and time consuming. Therefore, rather than only relying on experimental measurements of macroscopic properties, we need to improve our models through a comprehensive analysis of the relationship between relative permeability and the underlying pore-scale phenomena. To do so, in this work, *EXP* 6, we develop a novel approach that combines the steady-state three-phase relative permeability measurement method with pore-scale X-ray imaging techniques.

Furthermore, pore-scale imaging can provide solutions to some of the challenges often faced during steady-state three-phase relative permeability measurements. With X-ray imaging, surface wettability can be directly assessed, especially to differentiate between weakly oil-wet and strongly oil-wet systems. Pore-scale imaging can also confirm *in situ* the existence of spreading layers, rather than relying on an empirical relationship between the interfacial tensions to determine whether or not a phase will spread, Eq. (2.8) [16, 42]. The use of imaging can help overcome a major drawback of the steady-state approach, which is the capillary end effect, by providing a direct assessment of the saturation profile along the sample [15]. This can help identify and/or eliminate the regions influenced by boundary effects, increasing the accuracy and reliability of steady-state relative permeability results.

Early work using X-ray imaging focussed on investigating unsteady-state two-phase displacements which helped in assessing trapping and recovery efficiency for CO_2 storage and oil recovery applications [13, 19, 29, 87, 91, 95, 97, 118]. The scope of the tool was then extended to study steady-state two-phase flow which enabled the simultaneous determination of relative permeability with capillary pressure in water-wet, oil-wet and mixed-wet rocks [14, 15, 113, 119-121]. The pore-scale insights gained from combining steady-state two-phase flow with pore-scale imaging have led to significant breakthroughs in the field, explaining the relative contribution of trapped phases, layers and micro-porosity to two-phase flow mechanisms, which helped in interpreting core-scale two-phase relative permeability data [14, 121].

In contrast, the use of pore-scale X-ray imaging in three-phase flow studies has been limited to unsteady-state experiments [16, 17, 38, 42, 101, 110, 122]; to date, there is not a single experiment that combines three-phase steady-state flow with pore-scale imaging. This is solely ascribed to the practical complications of the experiment as we will discuss later. To this end, we believe that developing an approach that combines three-phase steady-state flow with pore-scale imaging, where both relative permeability and capillary pressure can be measured simultaneously, as applied in two-phase flow [15, 113], can ultimately aid in the development of rigorously validated, physically-based pore-scale models and empirical correlations to predict three-phase relative permeabilities under various wettability and miscibility conditions. This is the gap in the literature that we will fill in *EXP* 6.

In *EXP* 6 (section 6.1), we will study three-phase flow in a water-wet porous medium. This system is well defined in the literature, with an unambiguous wettability order. In such systems, it is typically assumed that during steady-state flow all three fluid phases are connected in the pore space: gas is continuous in the larger pores, oil in spreading layers, and water in wetting layers. This assumption is embedded in models – including pore network models [123, 124] and empirical expressions for relative permeability [68, 125] – that predict three-phase relative permeability. However, in this study, *EXP* 6, using pore-scale imaging, we show that this assumption is incorrect and in fact, gas flows in disconnected ganglia surrounded by oil and water layers.

Furthermore, in *EXP* 7 (section 6.2), we will use the combined pore-scale X-ray imaging and steady-state three-phase flow approach developed in *EXP* 6 to study a mixed-wet reservoir rock sample. The motivation here is to extend our approach to investigate steady-state three-phase flow under various wettabilities.

2.3 Research Questions

The research questions that will be answered in this PhD thesis are listed below alongside the section it is addressed in:

- **Does oil spread in layers sandwiched between gas and water in a water-wet system at near-miscible conditions? Is wettability order a function of surface wettability only? Is the microscopic displacement efficiency improved under near-miscible conditions? What is the impact of lowering the gas-oil interfacial tension on double capillary trapping?** These questions will be answered by *EXP* 1 in section 3.1.
- **What is the wettability order in a weakly oil-wet system at near-miscible conditions? Is gas always the most non-wetting phase? Does gas form spreading layers if it is the intermediate-wetting phase? Is capillary trapping of gas by water possible if gas is more wetting? What is the flow potential of gas?** These questions will be answered by *EXP* 2 in section 3.2.
- **Is it possible to render rocks strongly oil-wet to the point where gas becomes more wetting than water at immiscible conditions? How is the pore-scale physics different than that in a weakly oil-wet system at near-miscible conditions, where the wettability order is the same? Does gas spread in layers at immiscible conditions? Is gas connected in the pore space? How does this wettability order influence capillary trapping?** These questions will be answered by *EXP* 3 in section 3.3.
- **Is water injection in an oil-filled, oil-wet system a drainage process? Is the displacement of oil by water an invasion percolation process? How does wettability influence the displacement? Are drainage associated dynamics – Haines jumps and snap-off events – observed? Are the phases well-connected in the pore space?** These questions will be answered by *EXP* 4 in section 4.1.
- **How does gas progress through the pore space, being the intermediate-wetting phase, in a strongly oil-wet system at immiscible conditions? What facilitates gas invasion if it exists in disconnected clusters? Does gas get reconnected as gas injection proceeds? What types of double displacement processes are observed? Do Haines jumps occur in three-phase flow?** These questions will be answered by *EXP* 5 in section 4.2.
- **What are the implications of the different pore-scale observations for CCUS-EOR projects? How should CO_2 injection be designed to maximize storage security and oil recovery?** These questions will be answered in a review of all the unsteady-state three-phase X-ray imaging experiments presented in section 5.
- **Are gas, oil, and water connected in the pore space at steady-state conditions in a water-wet system? Is it possible to observe intermittent phases under capillary-dominated conditions at immiscible conditions? How come gas, the most non-wetting phase, is disconnected at steady-state conditions? How does gas flow? What are the implications on three-phase relative permeability?** These questions will be answered by *EXP* 6 in section 6.1.
- **How do water, oil and gas flow at steady-state conditions in a mixed-wet system? What is the wettability order at immiscible conditions in a mixed-wet system? Is the gas flow disconnected? Why is the behaviour more intermittent compared to a water-wet system? What are the displacement processes in the pore space? Does gas get trapped in mixed-wet systems?** These questions will be answered by *EXP* 7 in section 6.2.

Chapter 3

In this chapter we will present the materials and methods, results, discussion, and conclusions of the unsteady-state experiments investigated with static imaging. Sections 3.1 and 3.2 will examine three-phase flow at near-miscible conditions in a water-wet and a weakly oil-wet rocks respectively (*EXP1* and *EXP2*, see Table 1.1). Then, the three-phase pore-scale physics in a strongly oil-wet rock at immiscible conditions (*EXP3*, see Table 1.1) will be investigated in section 3.3. The heading of each section is given the title of a published manuscript.

3.1 *In situ* pore-scale analysis of oil recovery during three-phase near-miscible CO_2 injection in a water-wet carbonate rock

3.1.1 Summary

In this section, we study *in situ* three-phase near-miscible CO_2 injection in a water-wet carbonate rock at elevated temperature and pressure using X-ray microtomography. We examine the recovery mechanisms, presence or absence of oil layers, pore occupancy and interfacial areas during a secondary gas injection process. In contrast to an equivalent immiscible system, we did not observe layers of oil sandwiched between gas in the centre of the pore space and water in the corners. At near-miscible conditions, the measured contact angle between oil and gas was approximately 73°, indicating only weak oil wettability in the presence of gas. Oil flows in the centres of large pores, rather than in layers for immiscible injection, when displaced by gas. This allows for a rapid production of oil since it is no longer confined to movement in thin layers. A significant recovery factor of 80% was obtained and the residual oil saturation existed as disconnected blobs in the corners of the pore space. At equilibrium, gas occupied the biggest pores, while oil and water occupied pores of varying sizes (small, medium and large). Again, this was different from an immiscible system, where water occupied only the smallest pores. We suggest that a double displacement mechanism, where gas displaces water that displaces oil is responsible for shuffling water into larger pores than that seen after initial oil injection. This is only possible since, in the absence of oil layers, gas can contact water directly. The gas-oil and oil-water interfacial areas are lower than in the immiscible case, since there are no oil layers and even water layers in the macro-pore space become disconnected; in contrast, there is a larger direct contact of oil to the solid.

3.1.2 Investigations

The motivation behind this study is outlined in section 2.2.1.

Here, in *EXP* 1, we will conduct a three-phase near-miscible flow experiment in a water-wet carbonate rock at elevated temperature and pressure – 70 °C and 10.85 MPa – combined with pore-scale imaging. We will examine (i) oil recovery mechanisms, (ii) whether or not oil layers are present, (iii) wettability order and pore occupancy, (iv) fluid-fluid interfacial areas, and (v) double displacement processes at near-miscible conditions. We compare the results to those obtained at immiscible conditions by

Scanziani et al. [16]. This will help directly visualize the predicted wettability order at near-miscible conditions, as well as confirm the presence or absence of oil layers.

3.1.3 Materials and Methods

3.1.3.1 Materials

The rock sample selected for the study was a Ketton limestone (composition: > 99% calcite), with a diameter of 5.9 mm and a length of 24.4 mm. The structure of Ketton is comprised of spherical grains with large pore spaces and micro-pores within the grains themselves. The size of micro-pores is typically smaller than that of an X-ray microtomography image resolution and therefore is impossible to capture using traditional segmentation methods [18, 126]. Therefore, in order to measure the total porosity of the sample, we use the differential imaging method proposed by Lin et al. [127]. In this method, the sub-resolution porosity is identified by subtracting a dry image of the sample from one where it is fully saturated with a high-contrast solution. The total porosity was measured to be 29%, with macro and sub-resolution porosities accounting for 15% and 14% respectively, see Fig. 3.1. Prior to performing the experiment, the water-wet sample was cleaned using methanol and dried in a vacuum oven at 90 °C for 72 hours.

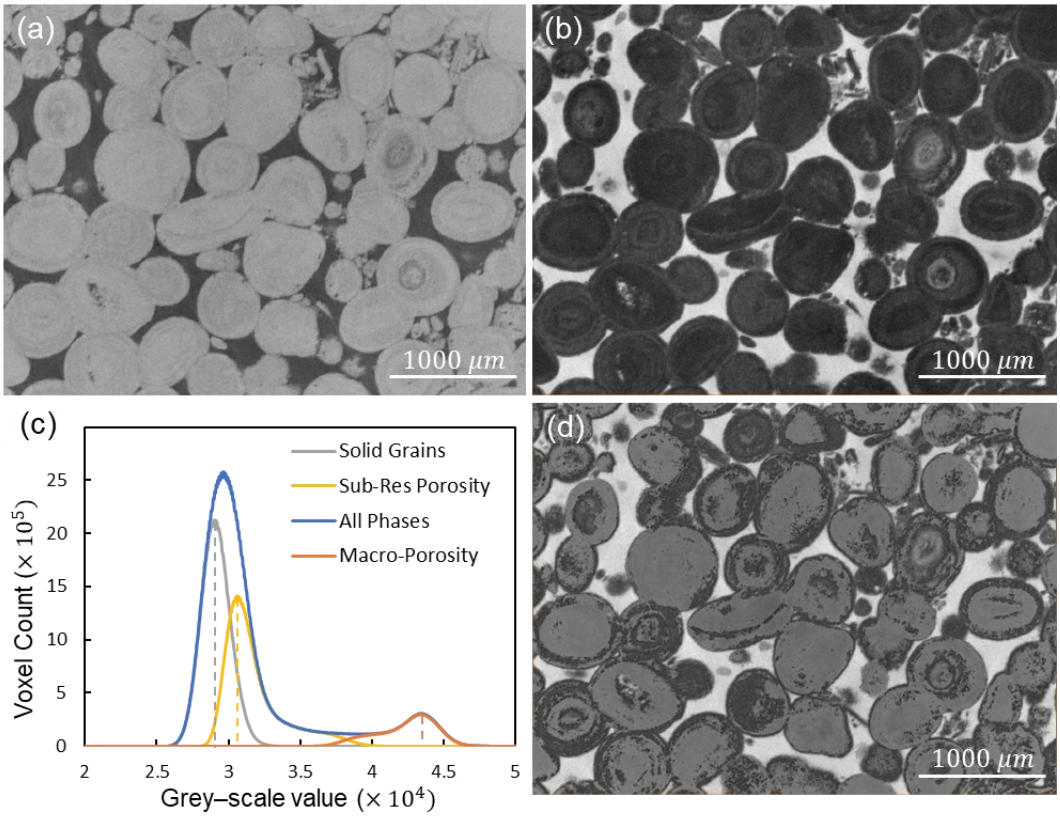

Figure 3. 1. (a) A two-dimensional cross-section of the dry scan of the Ketton sample acquired with a voxel size of 3.57 µm. (b) A two-dimensional cross-section of the differential image of the Ketton sample obtained by subtracting the grey-scale values of the high-contrast solution saturated scan from the dry scan in (a). (c) The histogram plot of the three-phases (macro-porosity, sub-resolution porosity and solid grains) in the saturated scan. The dashed lines represent the peak grey-scale value for each phase (CT). The sub-resolution porosity is calculated using $\phi_{sub} = (CT_{sub} - CT_{solid}) / (CT_{macro} - CT_{solid})$ to be 14%, while macro-porosity was found to be 15% giving a total sample porosity of 29%. (d) A segmented image of the Ketton sample showing in grey the solid grains, white the macro-porosity and black the sub-resolution porosity.

The three fluid phases selected to perform the near-miscible gas injection experiment were: (i) supercritical (sc) CO_2, (ii) decane as the oil phase and (iii) reservoir brine as the water phase. However, to enhance the contrast between the fluids in the pore-scale images, the water and oil phases were doped. The water phase was doped with a 30%wt sodium iodide, while decane was doped with a 20%wt iododecane solution. The optimum doping concentrations were judged with phase contrast scans and signal-to-noise ratio intensity histograms, see Fig. A1.1 in Appendix 1.

The interfacial tension between $scCO_2$ and the oil phase (80%wt decane and 20%wt iododecane mixture) was measured using the pendant drop method, with the two phases in thermodynamic equilibrium. The apparatus for performing the pendant drop interfacial tension measurements at high temperatures and high pressures is described elsewhere [128]. The pendant drop profile was digitized using the automated axisymmetric drop shape analysis (ADSA), which calculates the interfacial tension using the Young-Laplace equation. We measured the interfacial tensions between oil and sCO_2 phases at a temperature of 70 °C and pressures up to 6 MPa. The measured interfacial tension values are shown in Fig. 3.2. According to Georgiadis et al. [25], at a temperature of 70 °C, the relationship between the interfacial tension of a $scCO_2$ and decane system against pressure (ranging from 0 to 9 MPa) is given by a simple linear function: we were not able to measure directly the low interfacial tension at the experimental pressure, but had to use extrapolation. Hence, by fitting a linear regression line through the data, the interfacial tension measurements were extrapolated down to the minimum miscibility pressure (MMP). Therefore, to achieve near-miscible gas-oil conditions (~1 mN/m), our experiment was conducted at a temperature of 70 °C and a pressure of 10.85 MPa. The interfacial tensions, viscosities and densities of the three fluid phases are listed in Table 3.1.

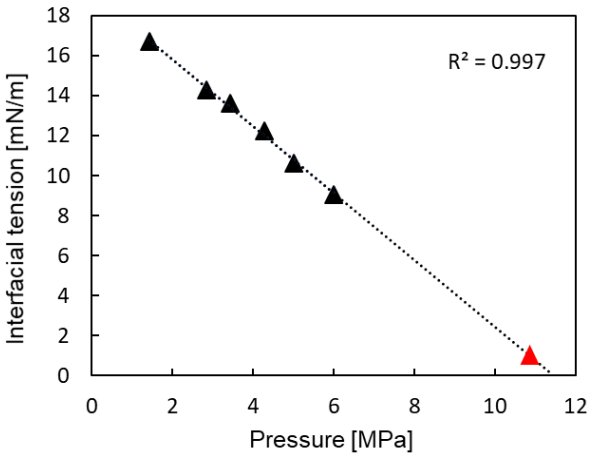

Figure 3. 2. Interfacial tension measurements between the $scCO_2$ phase and the oil phase (80%wt decane and 20%wt iododecane mixture) as a function of pressure at 70 °C. The black triangles represent the experimentally measured interfacial tension values, which can be found in Table A1.1 in Appendix 1, while the red triangle represents our selected near-miscible experimental conditions (10.85 MPa) based on the extrapolated data.

Table 3. 1. Thermophysical properties of the three fluid phases selected for the experiment. Data from Georgiadis et al. [25], Heidaryan et al. [129], and NIST [130]. *Densities measured at ambient conditions.

Fluid	Composition [%wt]	ρ [kg·m^{-3}]	μ [mPa·s]	σ [mN· m^{-1}]
Water	70% brine + 30% Sodium Iodide	1414.9*	-	σ_{gw}= 31
Oil	80% decane + 20% Iododecane	796.8*	1.12	σ_{ow}= 30
Gas	$scCO_2$	247.7	0.023	σ_{go}= 1

3.1.3.2 Methods

3.1.3.2.1 Flow loop

The experimental apparatus used to conduct the flow experiment is shown in Fig. 3.3. The apparatus consisted of four Teledyne Isco pumps, a Hassler type carbon fibre coreholder, an X-ray microtomography scanner and a Parr stirred reactor. The reactor was used to equilibrate the rock, brine and $scCO_2$ at the experimental conditions, 70 °C and 10.85 MPa, for 24 h prior to conducting the experiment. This step is essential to avoid the dissolution of the rock by the formation of acidic brine, a product of $scCO_2$ and brine mixing during the experiment. All the injected volumes of $scCO_2$ and brine in the rock were equilibrated.

The coreholder was placed inside the ZEISS Xradia 510 Versa 3D scanner for image acquisition. The rock sample was centred in the middle of the coreholder. The sample was connected to the flow lines by two steel end pieces placed at the inlet and outlet of the rock. Prior to inserting the sample in the coreholder, it was wrapped with a PTFE tape, then aluminium foil and placed in a Viton sleeve. All flow lines were made of thermoplastic 1/16th PEEK tubing which can withstand high pressures and temperatures.

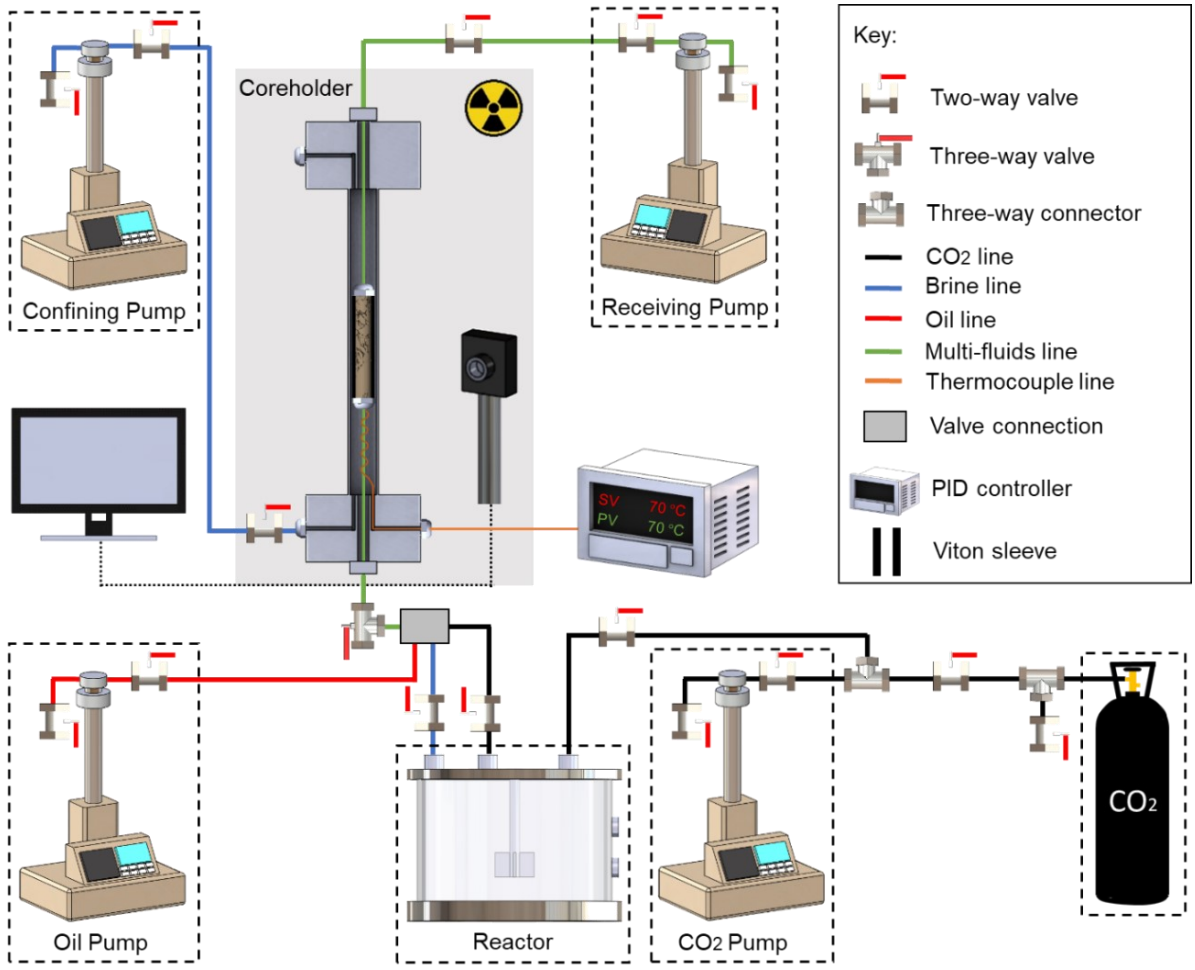

Figure 3. 3. The high-pressure, high-temperature flow apparatus used to perform the experiment. The apparatus consisted of four syringe pumps, stirred reactor, CO_2 cylinder, coreholder and a Zeiss X-ray microtomography scanner. The shaded area represents the scanner enclosure.

The sample was first flushed with non-equilibrated brine at 0.1 mL/min to displace the air and dissolve any pre-existing CO_2 in the system. The pressure of the non-equilibrated brine in the system was raised

gradually to the reactor pressure (10.85 MPa), and the confining pressure to 12.3 MPa. A confining pressure was applied to prevent fluid bypassing along the sample walls. The sample temperature was then raised to the reactor temperature (70 °C) using an Omega flexible heater connected to a PID controller. The electrical heater was wrapped around the carbon fibre coreholder with a separate thermocouple placed near the sample to monitor the temperature during the experiment.

3.1.3.2.2 Flooding sequence

The flooding sequence in the experiment follows an EOR secondary gas injection strategy: (i) water injection to start with a fully-saturated pore space, (ii) oil injection, representing primary oil migration, and (iii) gas injection, i.e., $scCO_2$. The secondary gas injection strategy was selected to maximise the number of interfaces between gas and oil phases to closely examine the near-miscible gas injection phenomenon. The experiments were performed under capillary dominated conditions to mimic the displacement mechanism in the subsurface. Firstly, 50 pore volumes (PV) of equilibrated brine were injected at a flowrate of 0.1 mL/min to displace the non-equilibrated brine and ensure 100% equilibrated brine saturation at the start of the experiment. Then, five PV of oil were injected into the sample at a flowrate of 0.008 mL/min for 100 mins to simulate a drainage process. Finally, equilibrated $scCO_2$ was injected into the sample at a rate of 0.008 mL/min, simulating a secondary recovery process, with a total volume corresponding to three PV. All injections were performed from the bottom of the sample. Injection details including capillary number values are provided in Table 3.2.

Table 3. 2. Details of the experimental injection sequence. PV stands for the pore volume of the sample. The capillary number was calculated using $Ca = \boldsymbol{\mu} q/\boldsymbol{\sigma}$, where $\boldsymbol{\sigma}$ is the interfacial tension between oil and water for oil injection and gas and oil for gas injection, $\boldsymbol{\mu}$ is the viscosity of the displacing fluid and q is the Darcy velocity. $\boldsymbol{\sigma}$ and $\boldsymbol{\mu}$ are shown in Table 3.1, while q is calculated by dividing the flow rate by the cross-sectional area of the sample.

Injection sequence	PV injected	Flow rate [mL/min]	Capillary number
Water	50	0.1	-
Oil	5	0.008	1.76×10^{-7}
Gas ($scCO_2$)	3	0.008	1.89×10^{-7}

3.1.3.2.3 Image acquisition

The ZEISS Xradia 510 Versa scanner was used to acquire three-dimensional images of the rock sample and the injected fluids. The photon energy range was set to (20 – 80) keV with a power of 7 W. A 3000 × 2000 (pixels) flat panel extension was employed at the detector to maximize the field of view while increasing the image resolution. Four scans with a resolution of 3.57 μm per voxel were acquired at different heights to image the whole sample after each injection step. The saturated scans required more projections and exposure time compared to the dry scan. Details regarding number of projections, exposure and scanning times are provided in Table 3.3.

Table 3. 3. The imaging parameters used in the Zeiss X-ray microtomography scanner. A large number of projections and longer exposure times were needed for the scans saturated with fluids to increase the image quality.

Scan	Projections	Exposure time [s]	Scanning time [min]
Dry	2400	1	76 × 4
Water injection	3201	1.75	142 × 4
Oil injection	3201	1.75	142 × 4
Gas injection	3201	1.75	142 × 4

3.1.3.2.4 Image processing

The images were reconstructed and a cylindrical mask equivalent in diameter to the rock sample was applied to discard any unwanted regions in the images including the Viton sleeve and the aluminium foil, see Fig. 3.4. The four scans, covering the whole sample, taken at each injection step were then stitched to build three-dimensional images of the whole rock sample (Fig. 3.4e). The stitched images containing fluids were then registered to the dry scan, to allow for a direct pore-by-pore comparison after each injection step.

A non-local means filter was applied to the pore-scale images to reduce the noise, allowing for a more accurate subsequent segmentation process. The segmentation was performed using the seeded watershed algorithm [131]. This allowed us to overcome misclassification at the fluid boundaries caused by the partial volume effect [132]. The seeded watershed algorithm relies on a gradient magnitude versus image intensity histogram. First, each phase is a assigned a grey-scale value range. Then, the intensity gradient for each phase is identified, at the boundaries, to demarcate the exact location of the fluid interfaces. The homogenous region of each phase (high certainty regions) is flooded with seeds, these seeds are then grown proportionally to a certain gradient value, and the two phases meet at the steepest intensity point 'hill slope' [133].

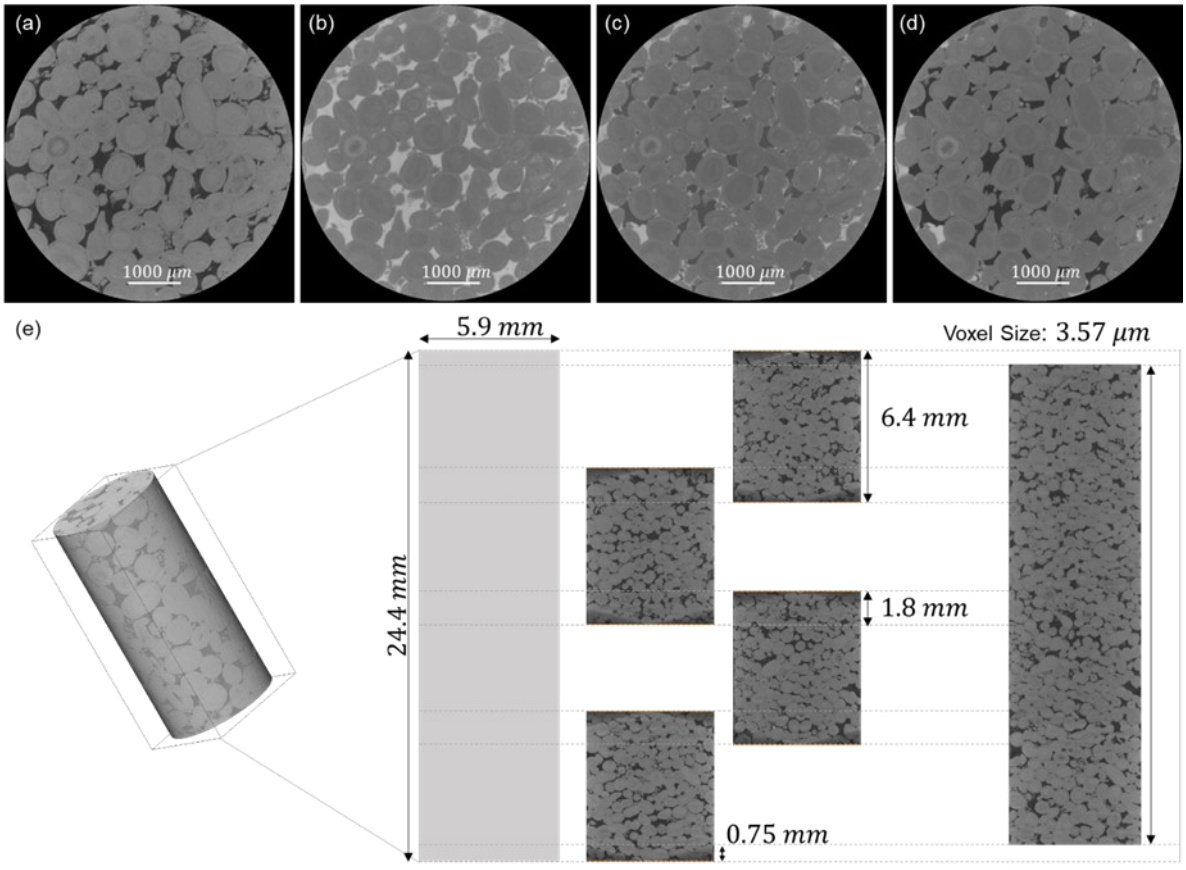

Figure 3. 4. A series of two-dimensional cross-sectional images with a voxel size of 3.57 µm of the Ketton sample acquired after (a) dry, (b) water injection, (c) oil injection and (d) gas ($scCO_2$) injection. (e) A schematic showing the location of the four scans taken to image the whole sample with the final stitched image.

3.1.3.2.5 Oil Layer formation analysis

3.1.3.2.5.1 Curvature constraint

From Table 3.1, we can see that the oil spreading coefficient ($C_s = \sigma_{gw} - \sigma_{ow} - \sigma_{go}$, Eq. (2.8)) is approximately zero. This suggests that oil layers can form, sandwiched between gas in the centres of the pores and water in the corners of the pore space [41]. Oil layers were indeed observed in three-phase imaging experiments performed at immiscible conditions [16] and no direct contact of gas and water was seen. However, the presence or absence of layers also depends on the curvatures of the fluid-fluid interfaces [134-136]. A necessary condition for the presence of oil layers in a corner of the pore space, as illustrated in Fig. 3.5, is [137]:

$$\kappa_{mgo} < \kappa_{mow} \tag{3.1}$$

where κ_m is the mean curvature of the interface, which in Fig. 3.5 is assumed approximately to be the inverse of the radius of curvature, while the other radius – out of the plane of the figure – is much larger. Using the Young-Laplace equation, (2.9), Eq. (3.1) can then be written as an inequality involving P_{cow} and P_{cgo}, the capillary pressures between oil-water and gas-oil phases respectively:

$$P_{cgo} < \frac{\sigma_{go}}{\sigma_{ow}} P_{cow} \tag{3.2}$$

The graphical representation of Eq. (3.2) is plotted in Fig. 3.5 using representative interfacial tension values. If the combination of P_{cow} and P_{cgo} falls above the critical line, oil layers cannot form. At near-miscible conditions, the ratio of σ_{go} to σ_{ow} is much lower compared to immiscible conditions. Therefore, the slope of the critical line is less steep and hence a much smaller P_{cgo} is sufficient to push oil layers out of the pore space.

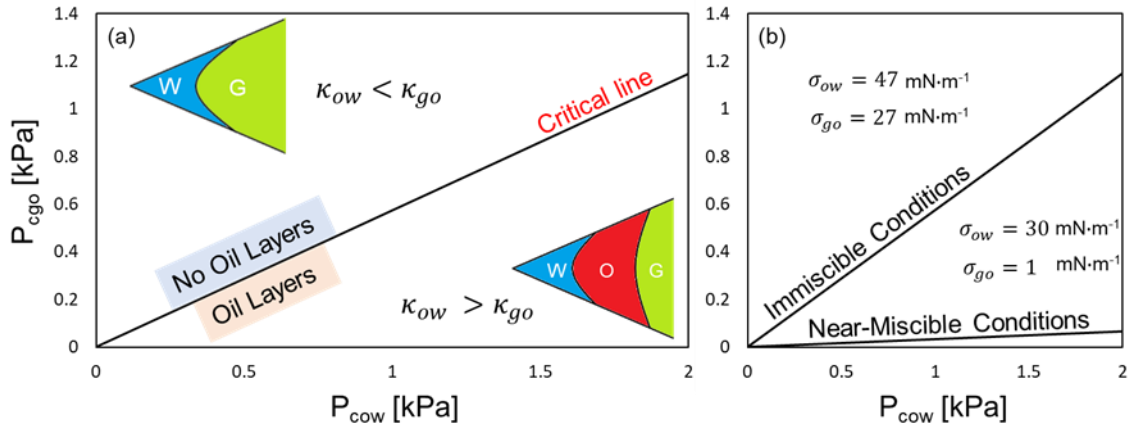

Figure 3. 5. A graphical representation of Eq. (3.2) that helps determine the likely presence or absence of oil layers in a spreading water-wet system depending on the microscopic oil-water and gas-oil capillary pressures. (a) The graph illustrates that if the ratio of P_{cgo} to P_{cow} falls above the critical line, oil layers cannot form as P_{cgo} will squeeze out the oil-water interface ($\kappa_{ow} < \kappa_{go}$) and *vice versa*. (b) The critical line for the immiscible conditions studied by Scanziani et al. [16] is much steeper compared to near-miscible conditions and therefore it is more likely for oil layers to form for the same gas-oil capillary pressure.

3.1.3.2.5.2 Curvature-based capillary pressure measurement

To perform the analysis detailed in the previous section, we used the curvature-based capillary pressure measurement approach [19]. The interfacial curvature between the fluids was measured from the segmented pore-scale images and then linked to the capillary pressure using the Young-Laplace equation, (2.9). We measured the curvatures of oil-water and gas-oil interfaces using a method previously presented in the literature [15, 19, 138-141]. First, a marching cube algorithm was used to

extract oil-water and gas-oil interfaces from segmented images. The less wetting phase, oil in the case of an oil-water interface and gas in the case of a gas-oil interface, was smoothed using the unconstrained smoothing method (kernel size = 5) to remove the staircase-like nature of the voxelized images. The smoothed interfaces are then modelled as a quadratic form:

$$ax^2 + by^2 + cz^2 + 2exy + 2fyz + 2gzx + 2lx + 2my + 2nz + d = 0 \quad (3.3)$$

The eigenvalues and eigenvectors of this quadratic form correspond to the principal curvatures of the interfaces and their directions, respectively. The mean of these curvatures was then substituted alongside representative interfacial tension values into the Young-Laplace equation to calculate the microscopic oil-water and gas-oil capillary pressures.

3.1.4 Results and Discussion

In section 3.1.4.1, we start by quantifying the fluid saturations after each injection step. Then, we list the measured oil-water, gas-water and oil-gas contact angles after near-miscible and immiscible gas injection in section 3.1.4.2. In section 3.1.4.3, the presence of oil layers and oil connectivity at near-miscible and immiscible conditions is investigated using the capillary pressure analysis described in section 3.1.3.2.5.1 followed by an examination of the local oil thickness maps. In sections 3.1.4.4 and 3.1.4.5, for near-miscible and immiscible conditions, we (i) quantify the interfacial area between the fluid phases and the fluid phases with the rock, and (ii) characterize the pore occupancy and visualize double displacement processes. For the comparisons in sections 3.1.4.2, 3.1.4.3, 3.1.4.4 and 3.1.4.5, the experimental dataset of Scanziani et al. [16] for water-wet Ketton limestone is used to represent immiscible conditions.

3.1.4.1 Saturation measurements

The saturation of each fluid phase in the macro-porosity only was measured on the segmented images after each injection step. We assume that the micro-porosity remained water-saturated throughout the experiment. In the results presented below we have, for simplicity, ignored the contribution of sub-resolution porosity to the saturation. The measured saturation end points are shown on the ternary diagram in Fig. 3.6. Initially, the sample was fully saturated with water (water saturation = 100%). Oil was then injected into the sample in a primary drainage process to form the initial reservoir conditions, with an oil saturation of 84% and 16% initial water saturation. Next, gas was injected in a secondary oil recovery process allowing for the production of both oil and water. At the end of the gas injection step, water, oil and gas saturations were 8%, 16% and 76% respectively. The injection of gas at near-miscible conditions resulted in an oil recovery factor of 80%; this is significantly higher than that seen in a previous immiscible gas injection study by Scanziani et al. [16], where only 41% of oil was recovered after gas injection. However, it must be noted that in the case of Scanziani et al. [16], gas was injected in a tertiary recovery process rather than a secondary one. According to Iglauer et al. [142], for a water-wet system, gas injection into a virgin oil reservoir leads to a lower residual oil saturation compared to the case where gas is injected after waterflooding. Nevertheless, the results show that the injection of gas in a secondary recovery process at near-miscible conditions can significantly improve oil recovery from the reservoir.

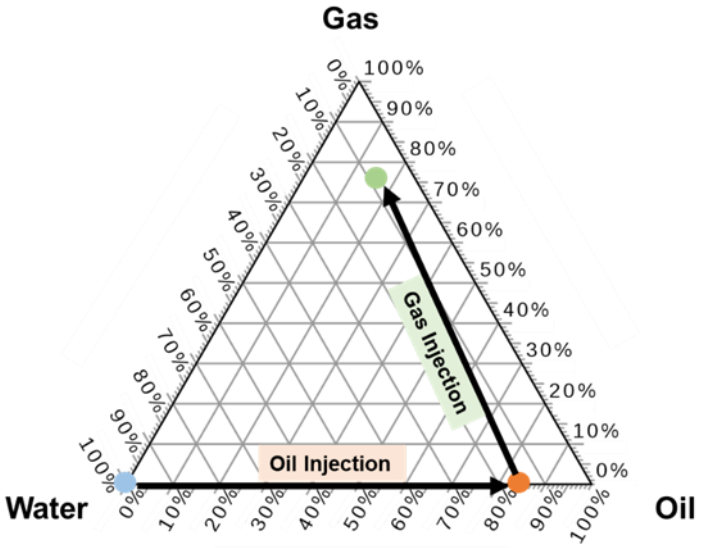

Figure 3. 6. A ternary diagram showing the end-point saturations of the three fluid phases after each injection step. Initially, the rock is fully saturated with water (blue point), then oil is injected in a primary drainage process until irreducible water saturation is reached (red point). Gas is then injected in a secondary recovery process resulting in the end-point saturations shown by the green point.

Given the large size of the stitched data, we selected the scan at the bottom of the sample for the subsequent analysis carried out in sections 3.1.4.2, 3.1.4.3, 3.1.4.4 and 3.1.4.5. The saturation profile of each fluid along the analysed region of the sample was measured after each injection step, see Fig. 3.7. The profiles of all three-phases were consistent and showed no sign of capillary end effects throughout the whole injection sequence.

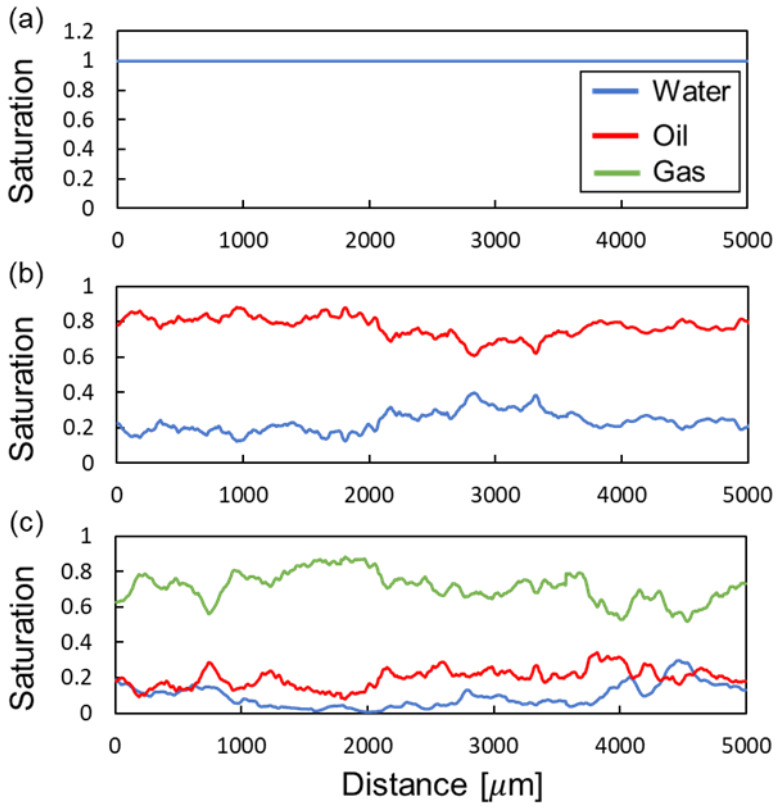

Figure 3. 7. The saturation profiles along the analysed region of the sample after (a) water injection, (b) oil injection, and (c) gas injection.

3.1.4.2 Contact angles

The effective geometric contact angles between oil and water (θ_{ow}), gas and oil (θ_{go}), and gas and water (θ_{gw}) were measured using the automated method developed by Scanziani et al. [31] at near-miscible and immiscible conditions. In this method, the contact angle is measured between two fluids *in situ* on a plane perpendicular to the local three-phase contact line constructed from the segmented images. The measured contact angles are listed in Table 3.4. The high standard deviations are ascribed to contact angle hysteresis and pore-scale surface heterogeneities, e.g., surface roughness and pore geometry [29].

The average oil-water contact angles at immiscible and near-miscible conditions, 48° and 52° respectively, indicate that the Ketton rock surfaces remained water-wet after oil and gas were injected into both systems. These measurements are in agreement with oil-water contact angles previously measured on similar rock-fluid systems [95]. Furthermore, no evidence of wettability alteration was found upon exposure to X-ray radiation as seen by Brown et al. [132].

In immiscible conditions, the effective gas-oil contact angle is assumed to be zero since oil forms layers surrounding the gas phase. Furthermore, the formation of oil layers sandwiched between gas in the centre of the pore space and water in the corners prevents the gas phase from directly contacting the water phase, which makes it impossible to determine a gas-water contact angle.

At low gas-oil interfacial tensions – i.e., near-miscible conditions – oil and gas become similar fluids as they approach miscibility. Since oil and gas become similar, the rock will no longer necessarily have a strong affinity to be coated preferentially by oil over gas. Therefore, the strict wettability order in the system breaks down and oil and gas are allowed to flow along the same path. This is evident from the large gas-oil contact angle measured at near-miscible conditions (73°), Table 3.4, which implies that the rock is neutrally wetting to oil and gas. It is further supported by the measured oil-water and gas-water contact angles at near-miscible conditions, Table 3.4, where both oil and gas formed the same effective contact angle, 52°, with water. The measured interfacial tensions and contact angles satisfy the Bartell-Osterhof contact angle constraint for multiple phases in thermodynamic equilibrium, Eq. (2.11), to within uncertainties in our measurements [49, 50]. This result – that the gas-oil contact angle increases under near-miscible conditions will be discussed further in section 5.

Table 3. 4. Measured oil-water (θ_{ow}), gas-oil (θ_{go}), and gas-water (θ_{gw}) contact angles after gas injection at immiscible and near-miscible conditions together with the standard deviation of the measured values. The contact angles were measured *in situ* through the denser phase: water in the case of oil-water and gas-water contact angles, and oil in the case of the gas-oil contact angle. The contact angles were measured using the automated method developed by Scanziani et al. [31]. Immiscible contact angles from Scanziani et al. [16].

Miscibility State	Oil-Water	Gas-Oil	Gas-Water
Immiscible	$\theta_{ow} = 48 \pm 19°$	$\theta_{go} = 0°$	N/A
Near-miscible	$\theta_{ow} = 52 \pm 22°$	$\theta_{go} = 73 \pm 17°$	$\theta_{gw} = 52 \pm 18°$

3.1.4.3 Oil layers and connectivity

Using the curvature constraint analysis described in section 3.1.3.2.5.1, the likely presence of oil layers was investigated for water-wet Ketton limestone at near-miscible and immiscible conditions. The gas-oil and oil-water capillary pressures were measured on segmented images using the curvature-based approach detailed in section 3.1.3.2.5.2. The results are shown in Fig. 3.8. At immiscible conditions, the ratio of P_{cgo} to P_{cow} lies below the critical line suggesting the formation of stable oil layers sandwiched between the gas and water phases, see Fig. 3.8a, and indeed oil layers were seen surrounding the gas phase and preventing direct contact of gas and water [16].

In contrast, during near-miscible gas injection, the P_{cgo} to P_{cow} ratio falls above the critical line suggesting that oil layers do not form (Fig. 3.8b): and indeed, we did not observe oil layers in the experiment – the gas, on injection, had sufficient pressure to push the oil from the pore space and oil layers were not seen. This confirms the micro-model observations of Williams and Dawe [63] that oil does not spread in layers at near-miscible conditions even if the spreading coefficient is close to zero.

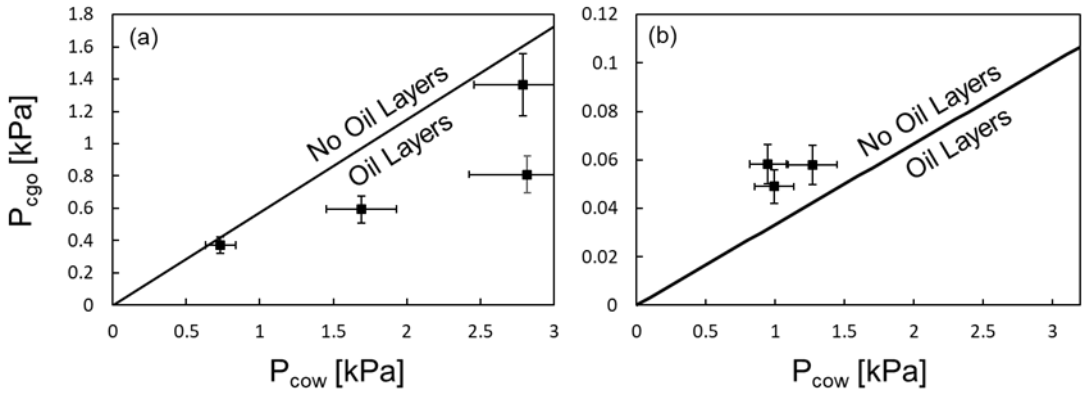

Figure 3. 8. Layer formation analysis conducted at (a) immiscible conditions and (b) near-miscible conditions. The graphs illustrate that under immiscible conditions oil layers are formed, while oil does not form layers under near-miscible conditions. Pressure data points in (a) from Scanziani et al. [16]. Error bars indicate uncertainty in the measurements.

Fig. 3.9 shows grey-scale images of the pore space illustrating the presence and absence of oil layers at immiscible and near-miscible gas injection conditions respectively.

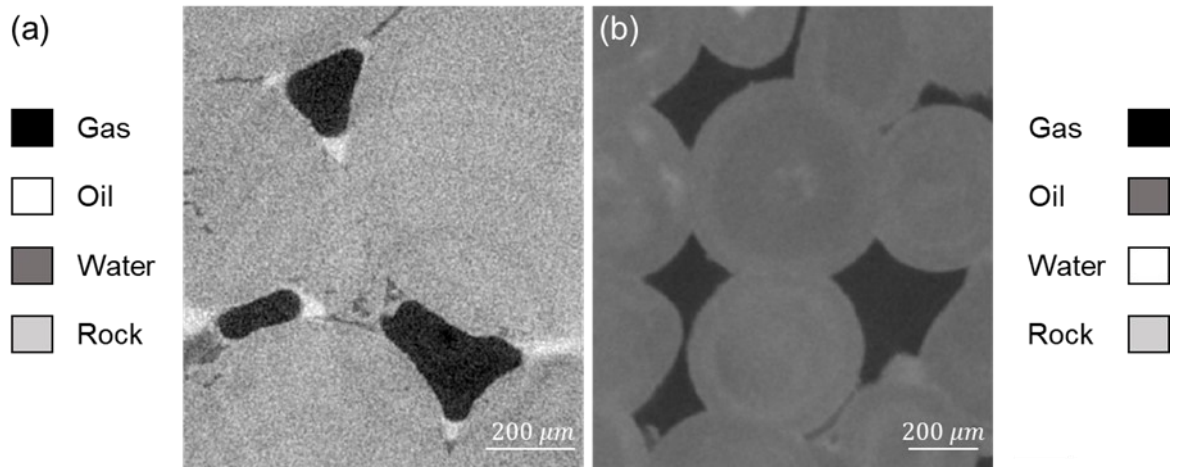

Figure 3. 9. (a) A 2 µm/voxel resolution image of a water-wet Ketton sample showing the presence of oil layers at immiscible conditions after gas injection [16]. (b) A 3.57 µm/voxel resolution image of a water-wet Ketton sample showing the absence of oil layers at near-miscible conditions after gas injection.

To examine the connectivity of the oil phase in the pore space, we obtained quantitative maps of the local oil phase thickness in three-dimensions using the approach developed by Hildebrand and Rüegsegger [143]. The three-dimensional oil thickness maps computed after gas injection at near-miscible and immiscible conditions are shown in Fig. 3.10. At near-miscible conditions, the residual oil phase existed as disconnected blobs residing in the corners of the pore space. However, for immiscible conditions, the oil phase was connected across the pore space by spreading layers with thicknesses that are of the order of 10 μm or larger. Furthermore, we computed thickness maps of the wetting water layers (Fig. A1.2 in Appendix 1). No evidence was found of connected water wetting layers in the macro-pore space in our near-miscible water-wet system, as opposed to the immiscible system. The absence of water layers will further be discussed in section 3.1.4.5.

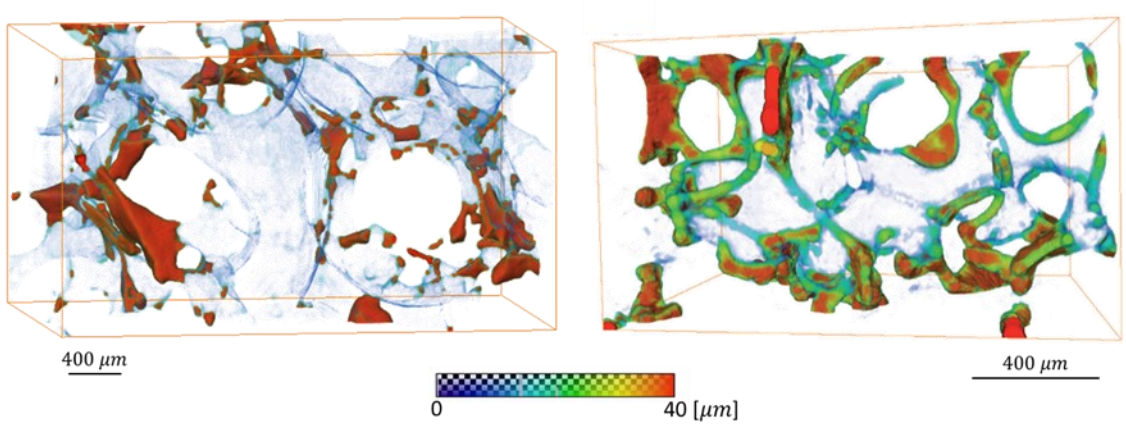

Figure 3. 10. The local thickness of the oil phase was computed at immiscible (right) and near-miscible (left) conditions. The oil phase was isolated and maximal balls were fitted to its structure to obtain the thickness maps at both conditions. Oil layer thickness map at immiscible conditions (right) from Scanziani et al. [16].

The results show that no oil layers are formed under near-miscible conditions in a spreading water-wet system. This suggests that the oil displacement mechanism in the reservoir at near-miscible conditions is different than that of an immiscible one, where oil is produced by slowly draining the oil layers sandwiched between water and gas phases.

3.1.4.4 Interfacial area

Since oil does not form layers at near-miscible conditions, gas can directly contact water in the pore space. To validate this assumption, we quantified the specific interfacial areas – area per unit volume – between: (i) the three fluid phases and (ii) each phase with the solid at near-miscible conditions and compared it to that at immiscible conditions, where there is no direct contact between gas and water. The measured interfacial areas are shown in Fig. 3.11. As expected, there is a rise in the area between gas and water at near-miscible conditions (Fig. 3.11a). However, there is a clear drop in the area between oil and water: this is caused by the absence of wetting layers which increase the oil-water interfacial area. The oil-gas specific area remains the highest at both injection conditions.

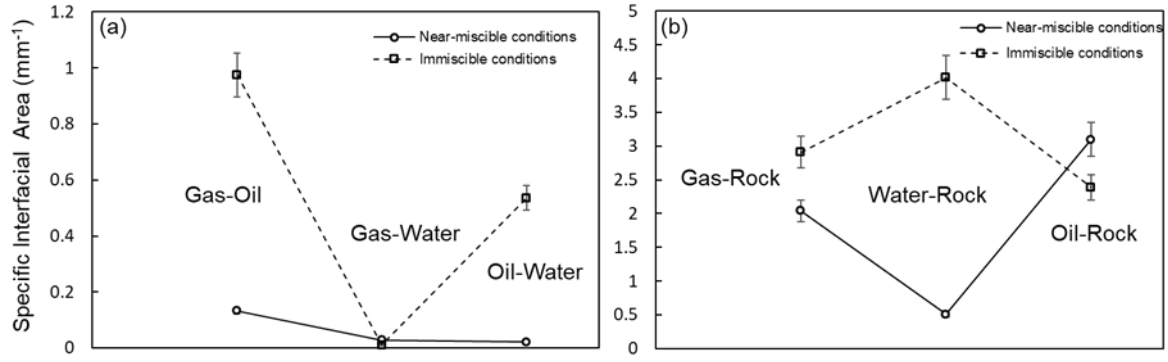

Figure 3. 11. Specific area measurements between (a) the three phases in the pore space and (b) each phase with the solid, at immiscible and near-miscible gas injection conditions. The specific area is calculated on extracted fluid-fluid and fluid-solid interfaces from segmented images. Error bars reflect uncertainties in the specific area measurement from one location to another. Gas, oil and water saturations at near-miscible conditions are S_g = 0.76, S_o = 0.16 and S_w = 0.08 respectively, while saturations at immiscible conditions are S_g = 0.64, S_o = 0.22 and S_w = 0.14. The different fluid saturations at both injection conditions might impact the measured interfacial areas.

3.1.4.5 Pore occupancy and double displacement

To characterize the pore occupancy, we adopted the procedure developed by Scanziani et al. [16] which relies on the maximal ball (MB) method [144]. First, the largest spheres that can occupy the pore space are found from the dry scan of the sample [145, 146]. The spheres are then imposed on the grey-scale images to find a relationship between the dimensions of the pore and the phase occupying it. The pore occupancies obtained during the near-miscible and immiscible experiments are shown in Fig. 3.12.

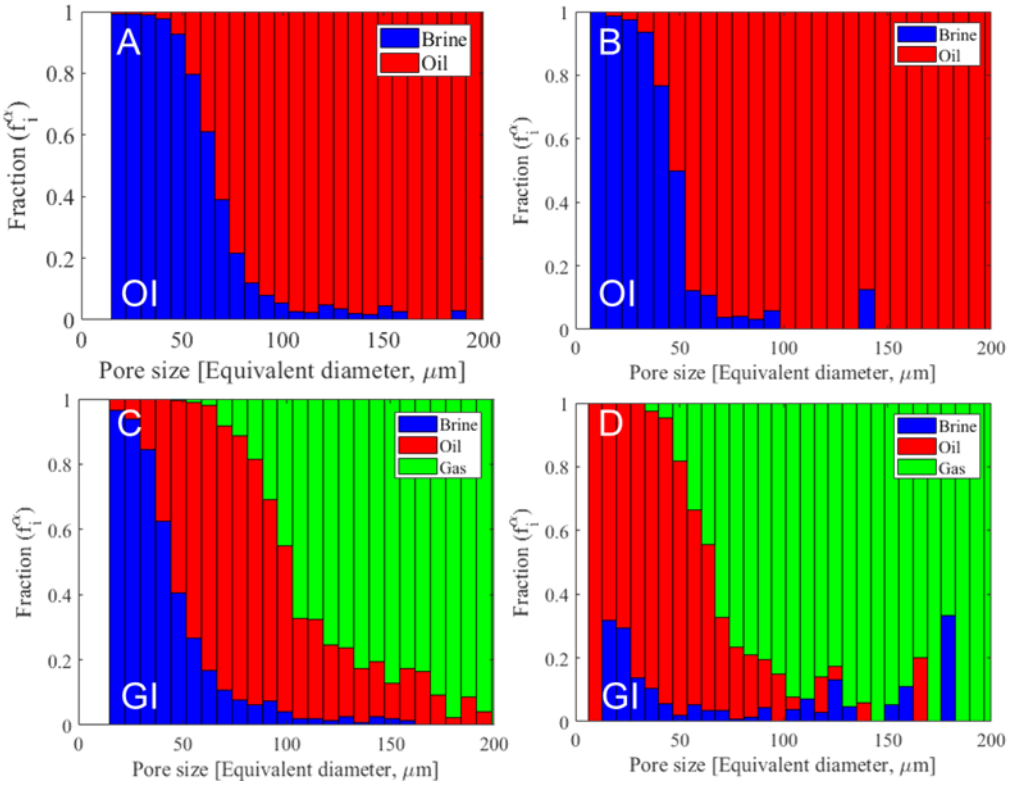

Figure 3. 12. Coloured bar charts representing the pore occupancy in the rock after oil injection at (A) immiscible conditions and (B) near-miscible conditions, and after gas injection at (C) immiscible conditions and (D) near-miscible conditions.

As anticipated, during oil injection in water-wet systems, oil invades the largest pores, confining water to the smaller ones (Figs. 3.12a and 3.12b). The pore occupancy after gas injection at immiscible and near-miscible conditions are shown in Figs. 3.12c and 3.12d respectively. At immiscible conditions, gas, being the most non-wetting phase, invaded the centre of the larger pores, pushing oil into medium-sized pores, while water was squeezed into smaller pores [16, 18], as expected based on the order of wettability.

The pore occupancy at near-miscible conditions is more intriguing, however: oil was displaced from large/medium-sized pores, replaced by gas and produced. Two noticeable movements happen during near-miscible gas injection: (i) oil is squeezed into a large fraction of the small-sized pores, and (ii) water is displaced from the smaller pores to occupy medium and large-sized pores. This results in a unique pore occupancy order at near-miscible conditions, where gas tends to reside in the largest pores, while oil and water occupy pores of varying sizes – small, medium and large.

The ability of oil and water to occupy pores of different sizes stems from several factors including: (i) oil does not form layers in the presence of gas and water; (ii) water is no longer confined in wetting layers; and (iii) double displacement processes.

In both experiments, the principal overall displacement is oil by gas. In the immiscible experiment, where oil surrounds the gas phase, this occurs exclusively by direct removal of oil by gas: gas replaces oil in the larger pores as evident in Fig. 3.12c. In contrast, in the near-miscible experiment, we can have gas displacing oil in a double displacement process [41, 45], where gas displaces water that displaces oil. The overall result is to increase the saturation of gas and displace oil, but here water changes its pore occupancy. It is evident from Fig. 3.12d, that gas displaces water in some of the smaller pore spaces – where it resides after oil injection – and then this water displaces oil in larger pores. The result is that water now appears, after gas injection, to reside in larger pores than it occupied after oil injection.

There is also a modest amount of displacement of water by gas in the immiscible experiment, here, gas directly displaces water from the larger water-filled elements. Furthermore, it is possible to have a double drainage process, where gas displaces oil that displaces water. In this case, it is the pore occupancy of oil that changes. For the immiscible experiment, see Fig. 3.12c, the tendency is for oil to be pushed out of the larger pores by gas and then displace water from smaller elements. However, for the near-miscible experiment, we see the same process, but where oil is pushed into some of the very smallest pores which tends to disconnect the water, as evident in Fig. 3.13.

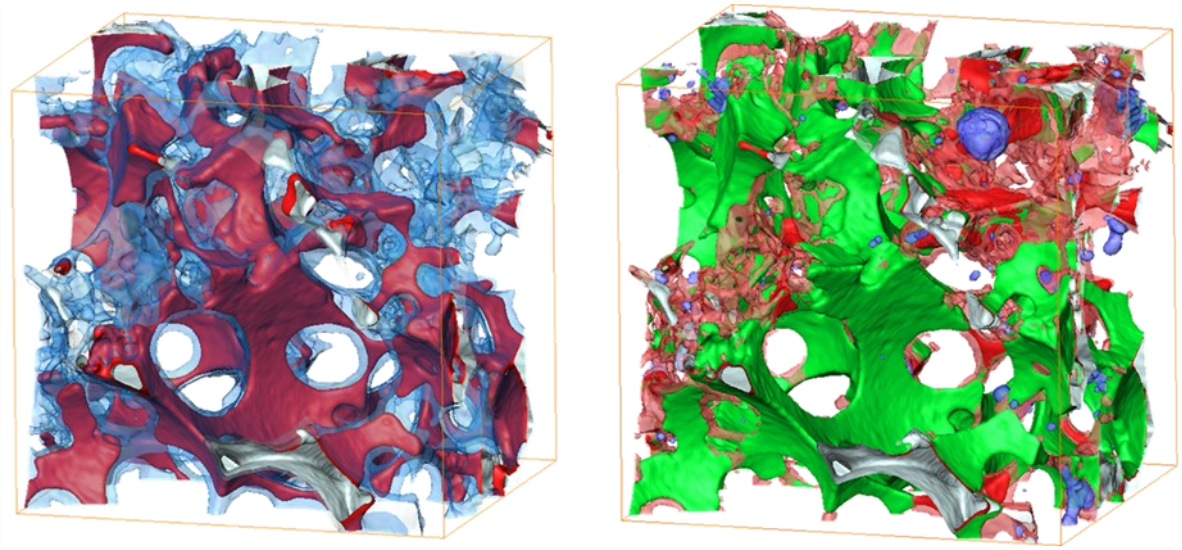

Figure 3. 13. A three-dimensional representation of a selected subvolume (1500 × 1500 × 1200 µm^3) of the pore space showing how oil residing in the centres of the pore space after oil injection (left) is pushed into the corners of the pore space after gas injection (right), occupying a large fraction of the smaller pores. This prevents the formation of connected water wetting layers in the corners of the pore space. Water is shown in blue, oil prior to gas injection in dark red, oil post gas injection in light red, and gas in green. The rock has been rendered transparent in both images.

The results show that the fluid pore occupancy in a water-wet system is altered when switching from immiscible to near-miscible conditions. This is likely to have a direct impact on the three-phase relative permeability of the system compared to the immiscible case with potentially lower oil and water relative permeability at low saturation, but a high oil relative permeability at intermediate saturation to facilitate the favourable recovery seen.

Furthermore, the most significant impact of oil layers is that they provide a mechanism for the displacement of waterflood residual oil, which enables the recovery of oil down to very low saturations. Therefore, if oil does not spread at near-miscible conditions, how is it recovered if gas is injected in a tertiary recovery process? Perhaps near-miscible gas injection is only more efficient if implemented as a secondary recovery process. Moreover, the presence of spreading oil layers enables efficient trapping of gas during subsequent water injections – in near-miscible systems there may be less gas trapping.

3.1.5 Final Remarks and Suggestions

We have provided a detailed three-dimensional *in situ* pore-scale analysis of near-miscible three-phase flow at elevated temperature and pressure in a water-wet carbonate rock. In particular, we investigated the (i) presence of oil and water layers, (ii) fluid-fluid and fluid-solid interfacial areas, (iii) pore occupancy, and (iv) double displacement processes at near-miscible conditions and compared these results to observations made at immiscible conditions by Scanziani et al. [16]. The three phases were injected in the rock in the following order: (i) water injection, (ii) primary oil drainage, and (iii) secondary gas injection. We observed distinct pore-scale phenomena at near-miscible conditions, suggesting that it is a unique displacement process and cannot be represented by models developed for immiscible displacement.

The main findings of the study can be summarized as follows:

1. A substantial amount of oil can be recovered by secondary gas injection at near miscible conditions (up to 80% recovery factor). This is attributed to two reasons: (i) gas displaces oil efficiently from the pores (100% microscopic displacement efficiency) due to the low gas-oil interfacial tension, and (ii) the displaced oil flows rapidly in the centre of the larger pores, as it is no longer confined to movement in layers, until it gets produced.
2. The rock becomes neutrally wetting to gas and oil as they become similar fluids at near-miscible conditions; the strict wettability order in the system breaks down. This facilitates the flow of gas and oil along the same path in the pore space. Oil and gas have similar contact angles with water.
3. Oil does not form layers between water and gas in a water-wet system at near-miscible conditions, despite having a spreading coefficient close to zero. The gas-oil capillary pressure is sufficiently high to squeeze oil out of layers, while oil itself is not strongly wetting to gas (point 2).
4. A series of gas-oil-water and gas-water-oil double displacement events were observed. Gas-water-oil displacement enables water to be pushed into larger pores.
5. The pore occupancy order is altered at near-miscible conditions, while gas tends to reside in the largest pores, oil and water occupy pores of varying sizes (small, medium and large).
6. Oil displaces water from the small-sized pores preventing the formation of a connected wetting layer throughout the macro-pore space.
7. The altered interfacial tensions at near-miscible conditions impact the fluid arrangement in the pore space, resulting in a high oil-gas relative interfacial area and lower, but similar, oil-water and gas-water interfacial areas in the pore space.

Having proved that the pore-scale physics are different under near-miscible conditions compared to immiscible conditions in a water-wet system, in the next section, (3.2), we will examine the near-miscible conditions in a weakly oil-wet system.

3.2 Pore-scale mechanisms of CO_2 storage in oilfields

3.2.1 Summary

We use high-resolution X-ray imaging to study the flow of oil, water and CO_2 in a weakly oil-wet rock at near-miscible conditions. We show that contrary to conventional understanding, CO_2 does not reside in the largest pores, which would facilitate its escape, but instead occupies smaller pores or is present in layers in the corners of the pore space. The wettability order is altered, from that seen at immiscible conditions, such that CO_2 becomes more wetting to the surface than water. It is estimated that the CO_2 flow is restricted by a factor of ten, compared to if it occupied the larger pores. This shows that CO_2 injection in oilfields, with weakly oil-wet wettability at near-miscible conditions, provides secure storage with limited recycling of gas; the injection of large amounts of water to capillary trap the CO_2 is unnecessary.

3.2.2 Investigations

In the previous section, (3.1), we examined near-miscible conditions in a water-wet system. Here, we extend our investigations to weakly oil-wet systems. Further motivation behind this study is provided in section 2.2.1.

In *EXP* 2, we use X-ray microtomography to image CO_2, oil and water in the pore space of a reservoir rock under weakly oil-wet near-miscible conditions at high temperature, 70 °C, and pressure, 10.85 MPa. We selected a water-alternating-gas (WAG) flooding scheme to mimic the typical displacement sequence encountered in oil reservoirs. We will demonstrate where and how readily CO_2 flows in the rock pore space by: (i) quantifying the configuration of the three phases; (ii) calculating the flow conductance of the phases; and (iii) measuring the amount of CO_2 trapping.

Given that we observed a breakdown in the strict wettability order at near-miscible conditions in a water-wet rock in *EXP* 1, we suspect that the wettability order will also change in weakly oil-wet rocks at near-miscible conditions. Based on our work here, in *EXP* 2, we challenge the assumption that CO_2 remains the most non-wetting phase in weakly oil-wet rocks at low gas-oil interfacial tensions of approximately 1 mN/m: oil and CO_2 have similar wetting properties and pore-scale configuration. The wettability order is different such that CO_2 is no longer the most non-wetting phase, instead it spreads in layers as the intermediate-wet phase, with significant implications for trapping, flow and storage. Once again proving that the wettability order is also a function of miscibility. The existence of CO_2 in layers substantially impedes its movement in the reservoir, and its possible escape through boreholes, which eliminates the need for water injection to restrict its flow, and hence more of the pore space can be occupied by CO_2, boosting storage capacity.

3.2.3 Materials and Methods

3.2.3.1 Rock and fluid properties

The rock sample used in this study was extracted from a large producing carbonate oil reservoir in the middle east which is mainly composed of calcite (96.5% wt), with small amounts of dolomite, kaolinite and quartz [13]. The sample was 5.9 mm in diameter and 24.9 mm in length with a total helium porosity of 0.26 and a segmented porosity, from the X-ray images, of 0.25. Sample pore volume was measured to be 0.708 mL based on the helium porosity. The absolute permeability was measured to be 2.7×10^{-13} m^2 on the larger rock (3.8 cm in diameter and 6.4 cm in length) from which our sample was drilled.

The fluids and experimental conditions, 70 ºC and 10.85 MPa, were kept the same as the previous study, in section 3.1, to achieve near-miscible gas-oil conditions. Fluid properties are listed in Table 3.1.

3.2.3.2 Wettability alteration protocol

The sample wettability was restored to the initial reservoir conditions prior to performing the experiment through a process known as ageing. Ageing is performed by exposing the rock surfaces to crude oil either dynamically and/or statically. Dynamic ageing refers to the continuous injection of the crude oil inside the rock sample, while static ageing means no flow (the sample is typically immersed in a crude oil bath): we used a combination of dynamic and static ageing. We have used a light crude oil from the same reservoir as the rock in the ageing process, see Table 3.5 for the crude oil properties.

Table 3. 5. Composition analysis of the reservoir crude oil. Data from Alhammadi et al. [13].

	Crude oil	Units
Density at 21 ºC	830 ± 5	kg/m^3
Saturates	55.25	wt%
Aromatics	38.07	wt%
Resins	6.22	wt%
Asphaltenes	0.46	wt%
Total Acid Number	0.24	mg KOH/g
Total Base Number	356	ppm

Prior to ageing the rock, it was cleaned using methanol and dried in an oven for 24 h. Reservoir conditions, 80 ºC and 10 MPa, were then established and the dry sample was saturated with formation brine (100% brine saturation): this formation brine was pre-equilibrated with carbonates to ensure that no chemical reactions occurred in the rock. The first step involved the injection of crude oil into the sample, where 40 pore volumes (1 pore volume = 0.708 mL) of crude oil were injected from the bottom of the sample, with a step wise increase in the flow rate from 0.001 mL/min to 0.1 mL/min. The same procedure was then repeated; however, crude oil was injected from the top of the sample this time. Once the sample was saturated with crude oil, the dynamic ageing procedure started, where five pore volumes of fresh crude oil were injected every day into the sample for a week. After that, the sample was kept at the same temperature and pressure for three weeks. This marked the end of the dynamic ageing process. Subsequently, the sample was aged statically by placing it inside a sealed crude oil bath for four months at 80 ºC.

3.2.3.3 Flow apparatus and experimental procedure

The flow loop was the same as the previous study in section 3.1.3.2.1, see Fig. 3.3. However, the experimental procedure was changed since a different flooding sequence was adopted. After inserting the coreholder in the scanner. The sample was first flushed with 50 pore volumes of doped decane (80% wt decane + 20% wt iododecane mixture) at a rate of 0.1 mL/min to displace all the crude oil in the sample. During this step, the temperature was set to 70 ºC and the pressure was raised gradually to the experimental pressure, 10.85 MPa and a confining pressure of 12.85 MPa was applied.

The flooding sequence in the experiment follows a water-alternating-gas (WAG) injection strategy to mimic the typical displacement sequence encountered in oilfields [8]. The fluids were injected from the bottom of the rock in this order: (i) first waterflooding [WF1]; (ii) gas injection [GI], (iii) second waterflooding [WF2]. All injections were performed under capillary dominated conditions to mimic subsurface flow conditions, as opposed to the displacement being controlled by viscous forces. At each injection, one pore volume of fluid was injected into the rock at a rate of 0.005 mL/min, see Table 3.6.

After the experiment, the rock was cleaned and dried at 60 ºC in vacuum for three days to prepare the sample for acquisition of a dry scan.

Table 3. 6. Details of the experimental injection sequence. PV stands for the pore volume of the sample. The capillary number was calculated using $Ca = \boldsymbol{\mu} q/\boldsymbol{\sigma}$, where $\boldsymbol{\sigma}$ is the interfacial tension between oil and water for water injection, and gas and oil for gas injection, $\boldsymbol{\mu}$ is the viscosity of the displacing (injected) fluid and q is the Darcy velocity. $\boldsymbol{\sigma}$ and $\boldsymbol{\mu}$ are shown in Table 3.1, while q is calculated by dividing the flow rate by the cross-sectional area of the sample (109 mm^2).

Injection sequence	PV injected	Flow rate (mL/min)	Capillary number
First waterflooding [WF1]	1	0.005	1.38×10^{-7}
Gas injection [GI]	1	0.005	1.18×10^{-7}
Second waterflooding [WF2]	1	0.005	1.38×10^{-7}

3.2.3.4 Image acquisition

The ZEISS scanner energy range and voltage were kept the same as the previous study, see section 3.1.3.2.3. In this study, scans with two resolutions were acquired after each injection: first, a lower resolution scan of 3.57 µm per voxel of the whole sample (1652×1652×6974 voxels) was acquired. Then, a scan of higher resolution, 1.82 µm voxel size, was acquired at the centre of the sample only (1483×1483×1758 voxels), see Fig. 3.14. The 3.57 µm scans were used to characterize fluid saturations and pore occupancy, while the 1.82 µm scans were used to determine connectivity; the flow simulations were performed on a subset of these images. Details regarding the imaging parameters used in the scanner are provided in Table 3.7.

Table 3. 7. X-ray imaging parameters for the 3.57 µm scan (LR) and the 1.82 µm scan (HR) after each injection step. IC stands for initial reservoir conditions

Scan	Projections (LR-HR)	Exposure time [s] (LR-HR)	Scanning time [min] (LR-HR)
Dry	3201 - 5001	1.54 – 4	146 × 4 – 540 × 1
IC	3201 - 5001	1.54 – 4	146 × 4 – 540 × 1
WF1	3201 - 5001	2.00 – 4	162 × 4 – 540 × 1
GI	3201 - 5001	2.00 – 4	162 × 4 – 540 × 1
WF2	3201 - 5001	2.00 – 4	162 × 4 – 540 × 1

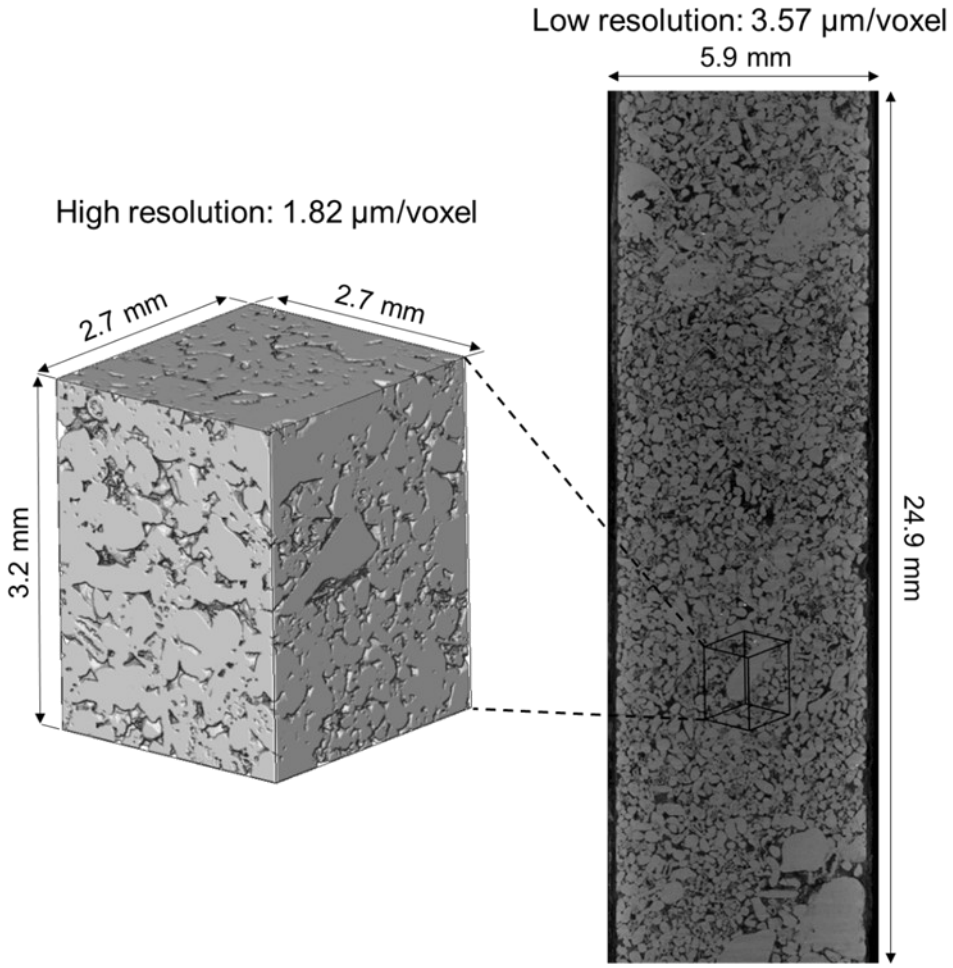

Figure 3. 14. A schematic showing the location of the high-resolution scan (1483×1483×1758 voxels), 1.82 µm voxel size, (left) relative to the lower-resolution scan (1652×1652×6974 voxels), 3.57 µm voxel size, (right) of the whole sample. The images shown are of the dry scan of the sample.

3.2.3.5 Image segmentation

The lower resolution images of the whole sample, 3.57 µm voxel size, were segmented using the seeded watershed algorithm [131] similar to the previous study, see section 3.1.3.2.4 for details. Watershed segmentation provides a rapid and accurate segmentation of pore-scale images; therefore, it was applied to the large 3.57 µm images of the whole rock.

The higher resolution images, 1.82 µm voxel size, were segmented using machine learning-based trainable WEKA segmentation method [147]. No filter was applied prior to segmenting the images to avoid averaging of voxel values especially at the fluid-fluid contacts to preserve the features of each phase. WEKA segmentation was chosen to segment the high-resolution images as it preserves the shape of the interface between the phases, facilitating more accurate characterization of flow properties and thicknesses of gas layers, as we will show later [148, 149]. The classifier was trained by manually selecting voxels that belong to the oil, rock, brine and gas phases from the raw images. During classifier training, the fast-random algorithm was used alongside the mean and variance texture filters. The trained classifier was then applied to the images to segment the oil, gas, rock and water phases. Fig. 3.15 shows raw and segmented images of the higher resolution scans, 1.82 µm. WEKA is very CPU intensive, hence, it was not possible to apply it to the large 3.57 µm images of the whole sample.

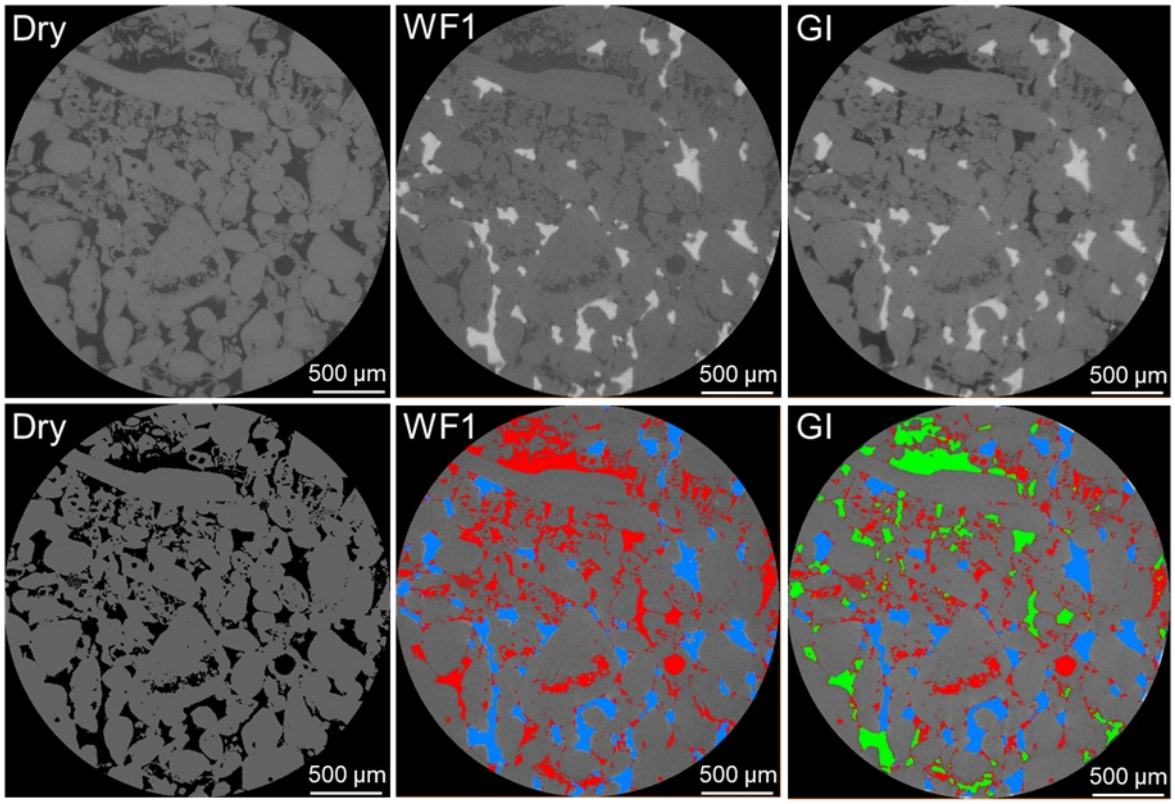

Figure 3. 15. Images of the higher resolution scans, 1.82 µm voxel size, showing (top row, from left to right) a raw dry scan of the rock, a raw image after the first waterflooding (WF1) and a raw image after gas injection (GI). (bottom row) shows the segmentation of the images in the top row, segmented using WEKA segmentation method. These images were selected to show the accuracy of segmentation for two, three and four phases. In the raw images, gas is shown in black, rock in light grey, oil in dark grey and water in white. In the segmented images, gas is shown in green, rock in grey, oil in red and water in blue.

3.2.3.6 Relative permeability simulations

In this study, we will estimate the relative permeability of each phase by running flow field simulations. Each phase was segmented independently, and the Navier-Stokes equations were solved for the flow field of each phase. We used the high-resolution images for the relative permeability calculations. We assumed no flow boundary conditions at the solid surface and the interfaces with other phases, and applied a constant pressure drop across the largest connected cluster in the images, see Fig. A2.1 in Appendix 2. We used OpenFoam, a finite element method, to solve for the flow, see [150] for more details. Then, using Darcy's law, the permeability of the phase was computed from the ratio of the total flow per unit area times the viscosity to the pressure gradient. This was compared to the absolute permeability, computed when all the pore space was assumed to be filled with one phase. The relative permeability is the ratio of the phase permeability to the absolute permeability.

Since the largest connected cluster of the gas phase after gas injection did not span the system, we cropped all the images to have the same size as the connected gas cluster in GI, indicated by the horizontal lines in Fig. A2.1 in Appendix 2, and computed flow on these cropped images of size 1483×1483×1000 voxels. This will tend to over-estimate the relative permeability for the gas phase after GI, since the phase may indeed be disconnected (relative permeability of zero), or only connected through regions that cannot be resolved in the scan.

3.2.4 Results and Discussion

3.2.4.1 Distribution of CO_2, oil, and water in the pore space

To understand flow and displacement we first quantify pore occupancy, see Fig. 3.16. We find that water is the most non-wetting phase since it occupies the largest pores, followed by gas, with oil most wetting in the smallest pores. This wettability order from most to least wetting – oil, gas, water – has been seen in micro-model experiments, but not inside reservoir rocks before [151], and contradicts previous studies where oil and gas were not near-miscible [16, 17].

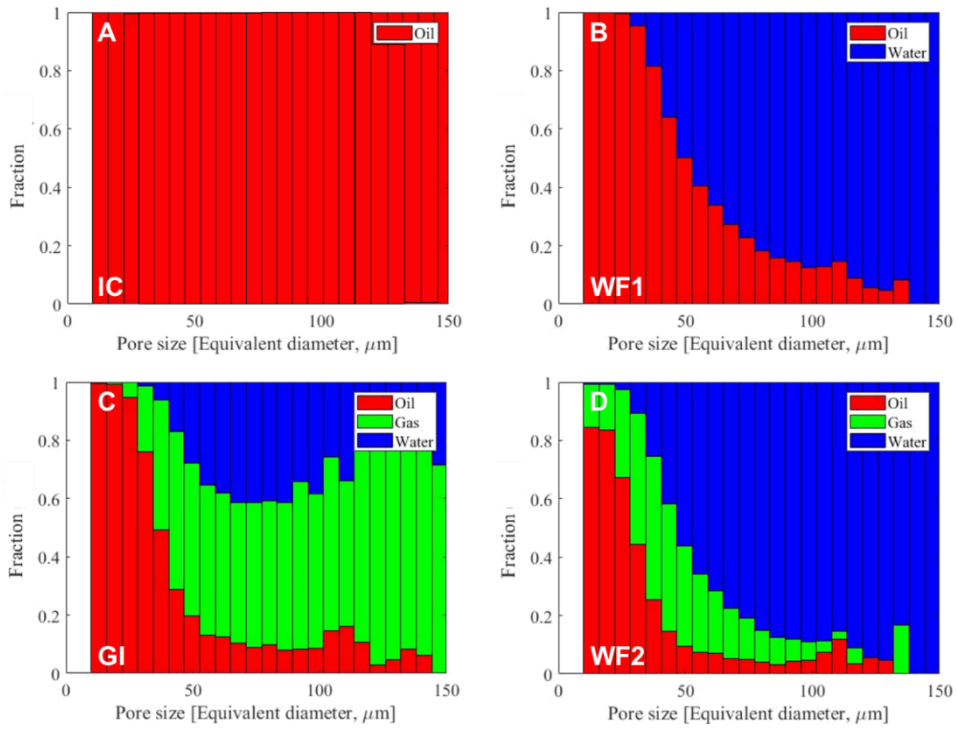

Figure 3. 16. Bar charts showing the fraction of the pores occupied by each phase as a function of pore diameter after each injection step. Pore occupancy is defined as the phase in the centre of the pore – this phase will also have the largest volume in the pore. (A) initial reservoir conditions (there is an initial water saturation of ~1% which is not evident from the bar chart) [IC], (B) first waterflooding [WF1], (C) gas injection [GI], and (D) second waterflooding [WF2]. Oil is shown in red, water in blue and gas, CO_2, in green.

Initially, the rock was saturated with oil to restore the initial reservoir conditions, see Fig. 3.16: at initial conditions (IC) some water was present in the pore space but at a very low saturation ~ 1%, which is why it is not evident on the bar chart (this excludes water in unresolved micro-porosity). As expected for oil-wet media, during the first waterflooding (WF1), water, the non-wetting phase, invaded the largest pores, while oil, the wetting phase, remained confined in the smaller ones. After gas injection (GI), water was trapped in the centres of the pore space as disconnected ganglia. In water-occupied pores, the gas can reside in layers next to the solid trapping water in the centre, see Fig. 3.19. The wettability order – oil, gas, water – is more apparent during the second waterflooding (WF2), where water invaded the centres of the larger pores confining gas and oil to intermediate and small sized pores respectively. This shows that the injection of water in WF2 limits the available storage capacity for CO_2 as the usable volume of the oilfield pore space occupied by CO_2 is restricted.

3.2.4.2 CO_2 flow conductivity

Fig. 3.17 shows the connectivity of the phases after each injection step. During water injection, water can form a connected path through the larger pores. In contrast, oil and gas tend to form thinner structures. Oil fills the smaller pores and is retained close to the solid surface, while CO_2 forms layers which follow a tortuous path through the pore space.

We computed the flow field, that is the velocity, of oil, gas and water on the images shown in Fig. 3.17. From these flow fields, the permeability of each phase can be computed. When the pore space is completely filled with one phase the absolute permeability is 3.7×10^{-13} m^2; this value is close to the directly-measured value of 2.7×10^{-13} m^2 through the whole sample. The relative permeability is defined as the ratio of the permeability of a phase that partially fills the pore space to the absolute permeability [18]. As indicated in Fig. 3.17, the relative permeability of gas is only 0.037 after gas injection despite having a saturation of 33 ± 2%, see Fig. 3.18 – the flow conductance is reduced by a factor of almost 30, while water in the larger pores has a higher relative permeability of 0.23. The oil has the lowest relative permeability of only 0.023 since it occupies the smallest pores. This reduction in oil and gas relative permeability under near-miscible oil-wet conditions has been observed in conventional flow tests on rock samples, but not explained using the wettability order [152]. After WF2, the gas and oil relative permeabilities are further reduced by one order of magnitude to 0.0054 and 0.0021 respectively, implying extremely restricted flow; however, less CO_2 is stored in the pore space with a saturation of only 21 ± 2%, see Fig. 3.18.

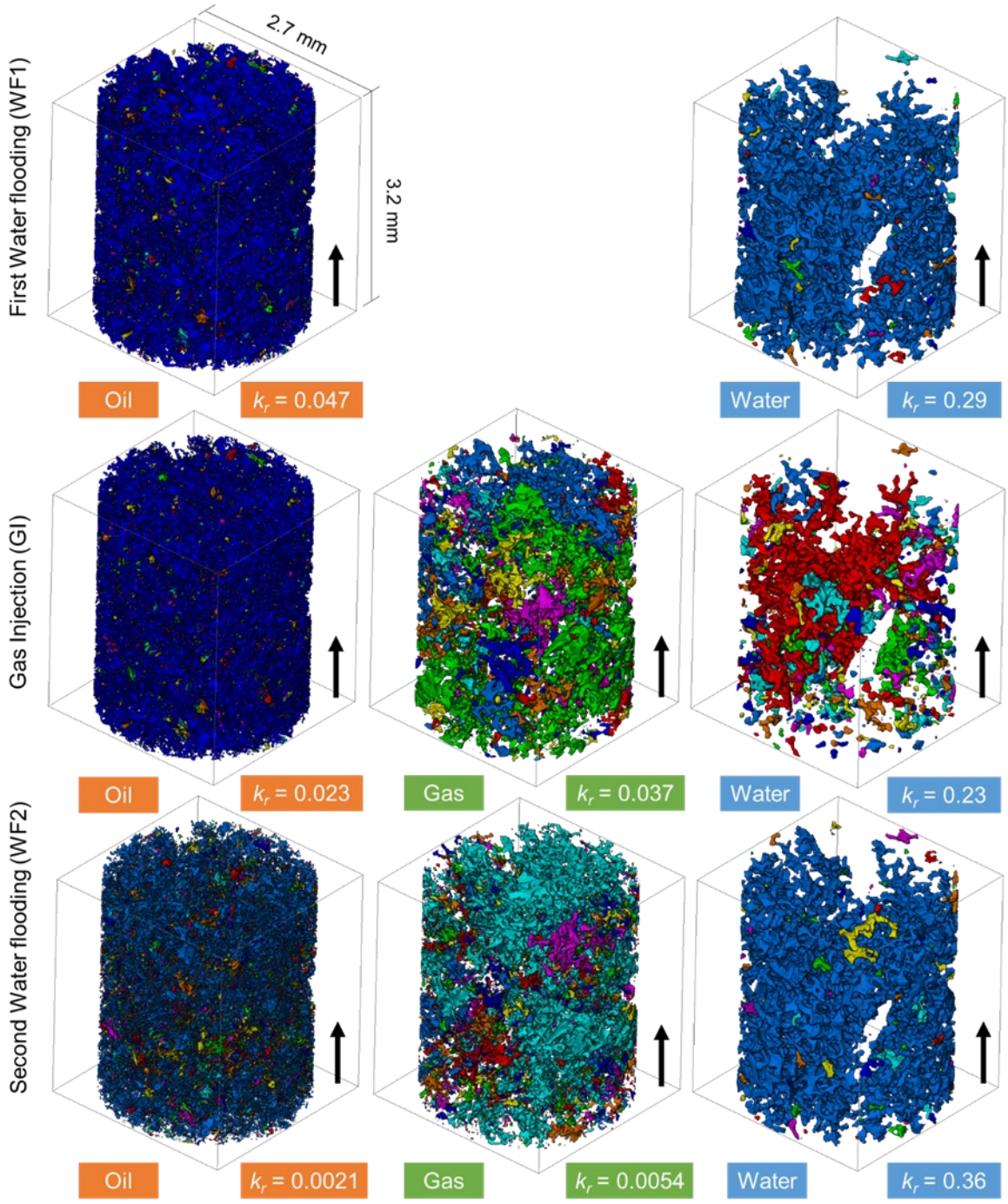

Figure 3. 17. Three-dimensional maps showing the connectivity of the phases during the displacement sequence. The colours indicate discrete clusters of each phase. The relative permeability, k_r, is shown in the boxes.

3.2.4.3 CO_2 saturation and trapping

The remaining saturation of CO_2, oil and water in the rock pore space after each injection was measured on segmented images of the whole rock. The change in fluid saturations throughout the flooding sequence is shown on the ternary diagram in Fig. 3.18. After the first waterflooding (WF1), only 30 ± 2% of the oil was recovered. This is ascribed to water invading the centres of the pores, while oil remains connected in the corners and small pores in wetting layers, Fig. 3.16. This is a common characteristic of oil-wet media [13, 95, 153]. During gas injection (GI), CO_2, the intermediate-wet phase, displaced some of the oil that was in the corners of the pore space leaving water stranded in the centres. This is

ideal from an oil recovery standpoint: the recovery factor increased to 53 ± 2%. Almost 33 ± 2% of the pore space remained saturated by CO_2 after gas injection (GI). WF2 displaced both oil and CO_2. Despite a substantial increase in the oil recovery during WF2 (68 ± 2%), as seen in other WAG experiments [17, 151], it results in a lower CO_2 saturation (21 ± 2%), i.e. a lower CO_2 storage capacity after water injection: less CO_2 is stored and indeed some of the injected CO_2 is produced with the oil. This is also a lower CO_2 saturation than is capillary trapped under water-wet conditions in similar rocks [154].

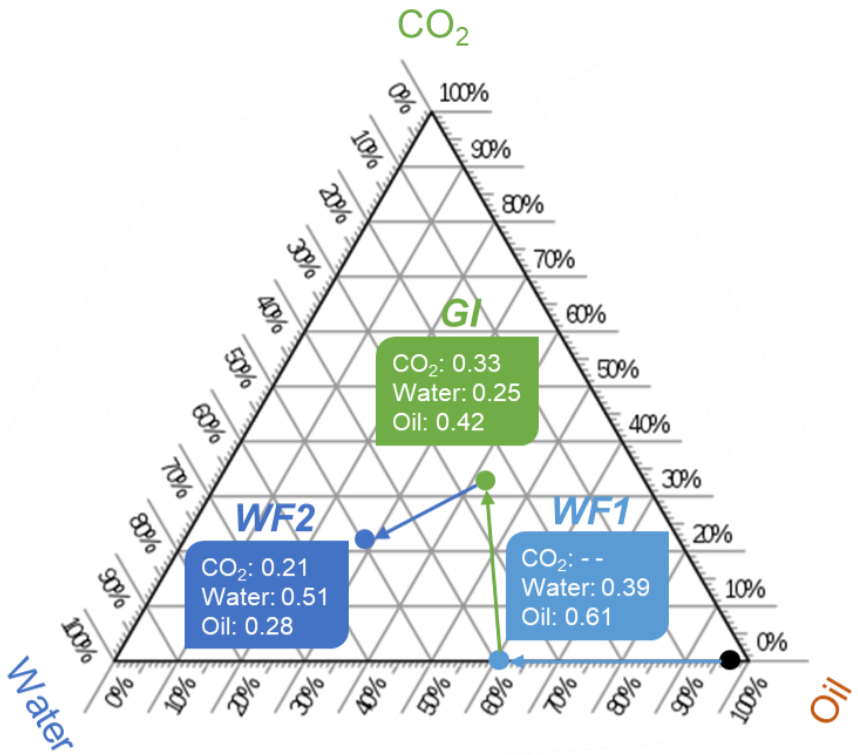

Figure 3. 18. A three-phase ternary diagram showing the end-point saturations during the flooding sequence. Saturation is defined as the volume of a phase divided by the total pore volume. At first (black point on the diagram), the rock is restored to its initial reservoir conditions (water saturation: 0.01 and oil saturation: 0.99). The coloured arrows point to the chronological order of injection events: (i) first waterflooding [WF1]; (ii) gas injection [GI; and (iii) second waterflooding [WF2]. The error in the saturation measurement is within ± 2%.

3.2.4.4 Gas layer thickness

Fig. 3.19 shows maps of the local thickness of the gas layers after gas injection (GI) and second waterflooding (WF2). The thickness of these gas layers was quantified on images with 746×491×600 voxels of size 1.82 µm: the thickness is defined as the diameter of the largest sphere that fits entirely in the gas phase at each location. Note that the thickness on both cases is much smaller than a typical pore size, see Fig. 3.16 where the x-axis of the bar chart shows the pore size distribution of the rock sample used, indicating that the gas resides principally in layers, as opposed to occupying the centres of larger pores.

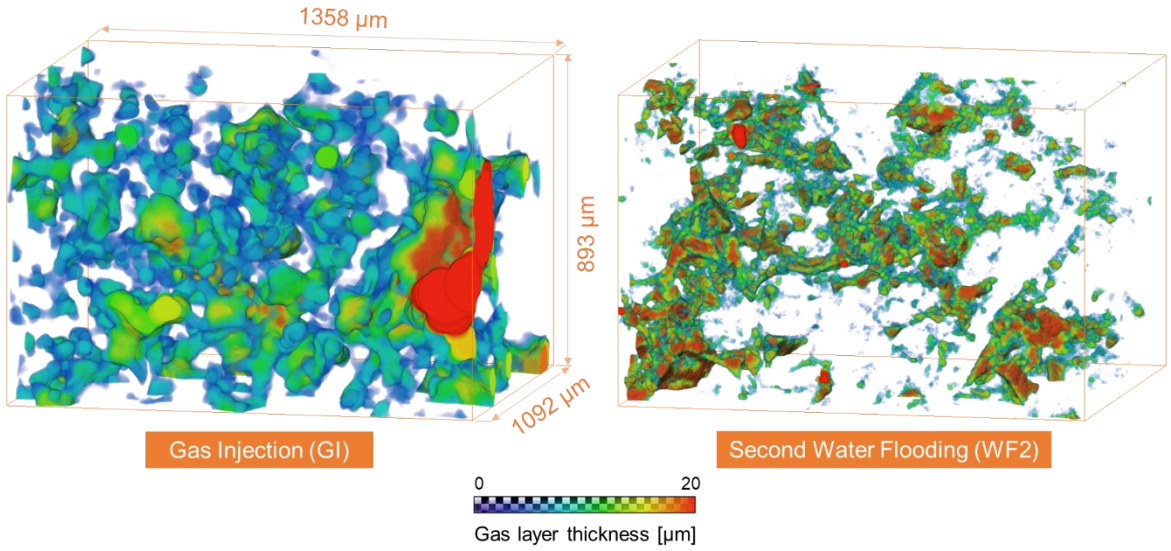

Figure 3. 19. Three-dimensional maps of the local thickness of gas layers computed after (left) gas injection (GI) and (right) second waterflooding (WF2). The thickness maps were quantified on images of voxel size of 1.82 µm with 746×491×600 voxels. The gas layers have an average thickness of approximately 15-20 µm.

It is common practice to inject alternate slugs of water and gas in oilfield operations for three reasons. Firstly, this saves money, as the gas is more expensive to collect and inject than water. Secondly, it is presumed that gas is the most non-wetting phase: injecting water helps to limit gas flow and production [8]. Thirdly, repeated flooding cycles lead to higher oil recovery, as we see here, Fig. 3.18. We have shown that for storage applications, CO_2 flow is restricted even when gas alone is injected. To maximize storage capacity, the CO_2 saturation should be as high as possible. This implies that an injection strategy of CO_2 injection only, or with limited amounts of water, is favourable, and that CO_2 is unlikely to be produced in significant quantities. Moreover, we have shown that CO_2 has very low relative permeability in the reservoir, which makes it harder – but not impossible – for the stored CO_2 to flow towards abandoned wells and escape through legacy boreholes. Therefore, after CO_2 injection, the wells must be closed in and the CO_2 should remain underground for thousands of years, since its upwards migration is prevented by cap rock [155].

3.2.5 Final Remarks and Suggestions

We have demonstrated that the wettability order is altered at near-miscible conditions in a weakly oil-wet rock. Our results prove that the traditional assumption that CO_2 is always the most non-wetting phase is incorrect. At near-miscible conditions, oil is the most wetting phase, occupying the smallest pores, as well as wetting layers, water is the most non-wetting phase, residing in the centres of the pores, while CO_2 is the intermediate-wet phase, forming layers between oil and water. This wettability order leads to the confinement of CO_2 in layers of low flow conductivity. Therefore, the injection of water is not required to constrain the gas flow. The migration of CO_2 beyond the oilfield is prevented by the cap rock, which has contained the hydrocarbons for millions of years.

We suggest that near-miscible conditions in reservoir rocks provide ideal conditions for recovery and storage: the wettability order oil-gas-water is likely to be seen in any oil-wet or mixed-wet rock, which comprise the majority of carbonate reservoirs [18]. On the other hand, if complete miscibility is achieved, the oil and gas flow together as one phase [156]. While this is favourable for oil recovery, it facilitates the flow of CO_2 and so is less favoured for secure storage.

An engineering assessment of CO_2 storage in oilfields will also involve a quantitative analysis of large-scale flow accounting for reservoir structure, variations in permeability and well placement. However,

one key input is the flow potential of the phases, controlled by pore-scale fluid configurations: we have shown that the flow of CO_2 is impeded by an order of magnitude or more compared to conventional models where it is the non-wetting phase. This finding implies that CO_2 can be injected alone, or with minimal amounts of water, to maximize storage capacity while still restricting the possibility of CO_2 escape.

In the next section, (3.3) we will investigate the three-phase pore-scale physics in a strongly oil-wet reservoir rock under immiscible conditions, where the wettability order is oil-gas-water from most to least wetting. Since the wettability order is similar to the one observed in this section, under weakly oil-wet near-miscible conditions, we will compare the results of the two experiments.

3.3 Pore-scale characterization of carbon dioxide storage at immiscible and near-miscible conditions in altered-wettability reservoir rocks

3.3.1 Summary

We study *in situ* immiscible CO_2 flooding in a strongly oil-wet reservoir rock at elevated temperature and pressure using X-ray microtomography. We observe the predicted, but hitherto unreported, three-phase wettability order in strongly oil-wet rocks, where water occupies the largest pores, oil the smallest, while CO_2 occupies pores of intermediate size. We investigate the pore occupancy, existence of CO_2 layers, oil recovery and CO_2 trapping in the strongly oil-wet rock at immiscible conditions and compare it to the results of the previous section, (3.2), obtained on the same rock type under weakly oil-wet near-miscible conditions, with the same wettability order. CO_2 spreads in connected layers at near-miscible conditions, while it exists as disconnected ganglia in medium-sized pores at immiscible conditions. Hence, capillary trapping of CO_2 by oil occurs at immiscible but not at near-miscible conditions. Moreover, capillary trapping of CO_2 by water is not possible in both cases since CO_2 is more wetting to the rock than water. The oil recovery by CO_2 injection alone is reduced at immiscible conditions compared to near-miscible conditions, where low gas-oil capillary pressure improves microscopic displacement efficiency. Based on these results, to maximize the amount of oil recovered and CO_2 stored at immiscible conditions, a water-alternating-gas injection strategy is suggested, while a strategy of continuous CO_2 injection is recommended at near-miscible conditions.

3.3.2 Investigations

In section 2.2.2, we provide the motivation for investigating three-phase flow in strongly oil-wet rocks.

Here, in *EXP 3*, we will provide the first experimental evidence of the anticipated three-phase wettability order in strongly oil-wet rocks at immiscible conditions – using microtomography X-ray imaging – and assess the implications it has on the safety of carbon dioxide storage in CO_2-EOR applications. We perform an immiscible water-alternating-gas (WAG) flow experiment in a carbonate reservoir rock at elevated temperature and pressure (60 °C and 8 MPa). We will examine, *in situ*, (i) fluid-fluid geometric contact angles, (ii) pore occupancy, (iii) fluid configurations and connectivity (Euler characteristic), (iv) three-phase capillary pressures, (v) presence or absence of gas layers, (vi) specific interfacial areas, (vii) fluid saturations, and (viii) CO_2 trapping mechanisms. We compare the results with those obtained in *EXP 2*, in section 3.2, on a weakly oil-wet reservoir rock under near-miscible conditions where the wettability order is the same, oil-gas-water, from most to least wetting.

3.3.3 Materials and Methods

3.3.3.1 Rock and fluid properties

A reservoir rock was selected for this study with a diameter of 6.1 mm and a length of 24.6 mm. The sample was drilled from the same larger piece of rock, and is of similar size, to the sample used in section 3.2 in the near-miscible study. The petrophysical properties of the sample are listed in Table 3.8. The segmented X-ray porosity was lower than the total helium porosity as it considers the macro-porosity only, leaving out the sub-resolution porosity within the rock grains which cannot be imaged.

Table 3. 8. Petrophysical properties of the reservoir sample.

Sample properties		
Diameter	6.1	mm
Length	24.6	mm
Total helium porosity	26.1	%
Segmented X-ray porosity	18.0	%
Pore volume (PV)	187	µL

The three fluid phases used in the experiment were: (i) light crude oil from the same reservoir as the rock (refer to Table 3.5 for the crude oil properties); (ii) brine solution prepared using the same salt composition as the reservoir brine; and (iii) supercritical (sc) CO_2. Both crude oil and brine were doped with contrast agents, 20 wt% iododecane ($C_{10}H_{21}I$) and 30 wt% sodium iodide (NaI) respectively.

The interfacial tensions between the selected experimental fluids, water (70% brine + 30% sodium iodide), oil (80% crude oil + 20% iododecane) and scCO_2, were measured using the pendant drop method at two-phase equilibrium. The apparatus for conducting the interfacial tension measurements at the experimental conditions (60 °C and 8 MPa) is detailed elsewhere [128]: it took approximately 10 minutes for the fluids to reach equilibrium. The thermophysical properties of the fluids used in this experiment are shown in Table 3.9.

Table 3. 9. Thermophysical properties of the three fluid phases selected for the experiment at 60ºC and 8 MPa. The gas spreading coefficient at the experimental conditions was calculated using $C_{sg} = \sigma_{ow} - \sigma_{gw} - \sigma_{go}$, where *o, w* and *g* label oil, water and gas respectively. Data from NIST [130], CDP [157] and Toolbox [158]. *Densities measured at ambient conditions, 20ºC and 0.1 MPa.

Fluid	Composition (%wt)	ρ (kg·m^{-3})	μ (mPa·s)	σ (mN· m^{-1})
Water	70% brine + 30% Sodium Iodide	1414.9*	0.468	σ_{gw} = 30.98
Oil	80% crude oil + 20% Iododecane	890.5*	0.305	σ_{ow} = 21.23
Gas	scCO_2	191.6	0.023	σ_{go} = 9.75
				C_{sg} = -19.5

3.3.3.2 Wettability alteration protocol

The same wettability alteration, ageing, protocol used in the near-miscible study was used in this experiment, see section 3.2.3.2. However, after dynamically ageing the sample for four weeks, the sample was immersed in a sealed crude oil bath and left to age statically at high temperature, 80 ºC, for eight months while it was aged statically for four months only in the near-miscible case.

3.3.3.3 Flow apparatus and flooding experiment

In this study, we used the same flow apparatus as the previous studies, see Fig. 3.3. Refer to section 3.1.3.2.1 for a detailed description of the apparatus.

The flooding sequence followed a water-alternating-gas (WAG) injection strategy, which is the same sequence used in the previous weakly oil-wet near-miscible study, refer to section 3.2.3.3. The injections were performed in the following order: (i) first waterflooding [WF1]; (ii) gas injection [GI]; and (iii) second waterflooding [WF2]. All injections were performed from the bottom of the sample under capillary dominated conditions to represent flow in the centre of the field away from the wellbore, see Table 3.10.

Table 3. 10. Details of the flooding experiment. The capillary number between the different fluids was calculated using $Ca = \mu q/\sigma$ where σ is the interfacial tension, μ is the viscosity of the displacing (injected) fluid and q is the Darcy velocity. μ and σ are shown in Table 3.9, while q is calculated by dividing the flow rate by the cross-sectional area of the sample (29.22 mm^2). Subscripts w, g and o stand for water, gas and oil phases respectively. Two pore volumes of fluid were injected in the sample during each flooding sequence.

Injection Sequence	Flow rate (mL/min)	Capillary number [Ca]	
First waterflooding [WF1]	0.005	$Ca_{[wo]} = 6.29\times10^{-8}$	
Gas Injection [GI]	0.005	$Ca_{[gw]} = 2.12\times10^{-9}$	$Ca_{[go]} = 6.73\times10^{-9}$
Second waterflooding [WF2]	0.005	$Ca_{[wg]} = 4.30\times10^{-8}$	$Ca_{[wo]} = 6.29\times10^{-8}$

The main distinction from the previous study at near-miscible conditions, in section 3.2, was that two pore volumes of fluid were injected at each flooding sequence in this study, while only one pore volume was injected previously. Furthermore, since the fluids and experimental conditions (60 °C and 8 MPa) were changed to achieve immiscible conditions in this study, we will briefly describe the steps followed to perform the experiment:

1. To initiate the experiment, 50 PV of doped crude oil (80% crude oil + 20% Iododecane) were flushed through the rock at a flow rate of 0.1 mL/min to replace the undoped crude oil in the aged sample.
2. The pressure in the sample was then raised gradually to the experimental pressure (8 MPa), and the confining pressure to 10 MPa.
3. The sample temperature was then elevated to the experimental conditions (60 °C) using the heating jacket.
4. The WAG flooding sequence was then started by injecting 2 PV of water into the rock at a rate of 0.005 mL/min for 75 mins, this was followed by the injection of 2 PV of $scCO_2$ and then 2 PV of water at the same flow rate.

3.3.3.4 Image acquisition and segmentation

The same image acquisition parameters and segmentation methods as the previous study, in section 3.2, were used here. Four 3.57 µm per voxel scans were taken at different locations to construct an image of the whole sample, and a zoomed in 1.82 µm per voxel scan was taken close to the centre of the sample after each flooding sequence, see Fig. 3.20. The 3.57 µm per voxel scans were segmented using the watershed algorithm, while machine learning-based trainable WEKA was used to segment the 1.82 µm per voxel scan. Refer to sections 3.2.3.4 and 3.2.3.5 for more details. Stitched images of whole sample after each injection step are shown in Fig. A3.1 in Appendix 3.

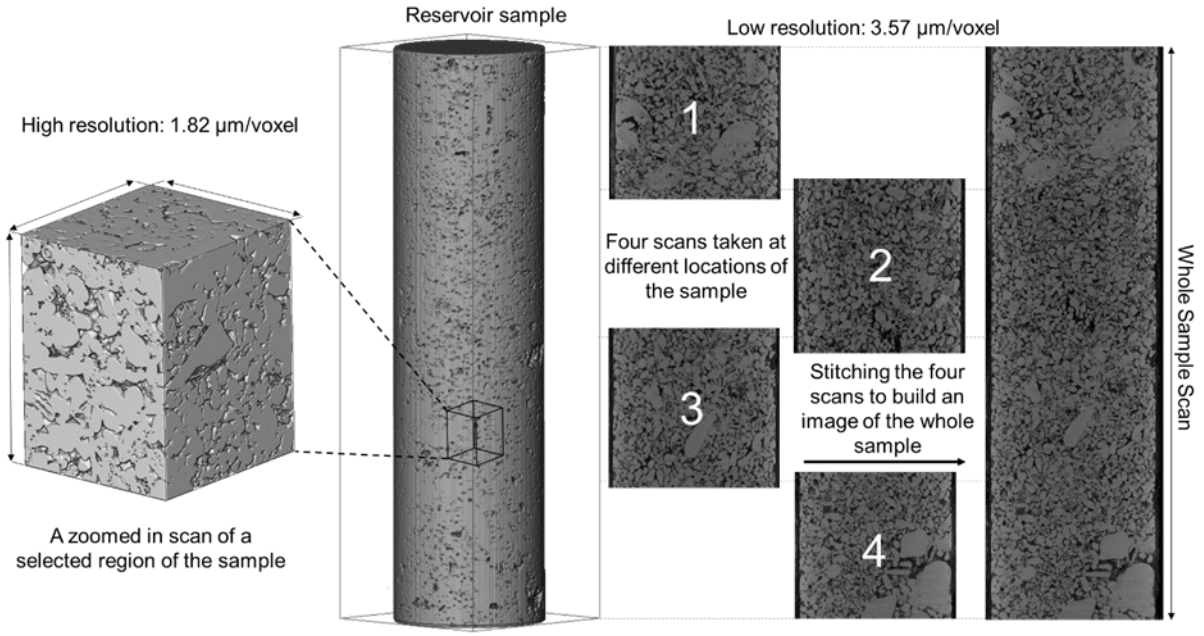

Figure 3. 20. A schematic showing the location of the four low-resolution scans, 3.57 µm voxel size, taken to construct an image of the whole sample (1157×1146×5517 voxels), and the high-resolution scan, 1.82 µm voxel size, taken almost at the centre of the sample (1381×1404×1689 voxels).

3.3.3.5 Gas layer formation analysis

In this section, we describe a curvature analysis that allows us to investigate whether spreading gas ($scCO_2$) layers can be present in the pore spaces of the rock or not. This analysis is similar to the one described in section 3.1.3.2.5 for the formation of oil layers. Given that CO_2 is predicted to be the intermediate phase, it may spread in pore-sized (microns) layers separating oil in the corner and water in the centre of the pore space. The existence of CO_2 in layers will have an impact on its relative permeability and thence its flow conductance in the reservoir.

3.3.3.5.1 Curvature constraint

There are two necessary criteria for spreading gas layers to form in an oil-wet system with an oil-gas-water wettability order. (i) The first is that the gas spreading coefficient ($C_{sg} = \sigma_{ow} - \sigma_{gw} - \sigma_{go}$, where *o, w* and *g* label oil, water and gas, CO_2, respectively) must be close to zero. From Table 3.1, we find that C_{sg} = -2 mN/m for near-miscible conditions. This value is sufficiently close to zero to allow layers to form. However, for immiscible flooding C_{sg} = -19.5 mN/m, Table 3.9, which prohibits the formation of layers. (ii) The second criterion is that the values of gas-oil and gas-water interfacial curvatures must satisfy the following inequality, as illustrated in Fig. 3.21:

$$\kappa_{mgo} > \kappa_{mgw} \tag{3.3}$$

where κ_m is the mean curvature of the fluid-fluid interface. In Fig. 3.21, the curvature of the fluid-fluid interface is assumed to be the inverse of the radius of curvature, while the other radius – out of the plane of the figure – is much larger. The mean curvature can be related to the capillary pressure through the Young-Laplace equation, (2.9). Hence, Eq. (3.3) can be written as an inequality involving P_{cgw} and P_{cgo}, the capillary pressures between gas-water and gas-oil phases respectively:

$$P_{cgo} > \frac{\sigma_{go}}{\sigma_{gw}} P_{cgw} \tag{3.4}$$

Using representative interfacial tension values, Tables 3.1 and 3.9, Eq. (3.4) can be plotted as shown in Fig. 3.21. The next section provides details on how the curvature is estimated. Fig. 3.21 (right) indicates that if the ratio of P_{cgo} to P_{cgw} falls above the critical line, the black line spanning the diagram, gas layers can form in a three-phase rock system with a wettability order of oil-gas-water. Furthermore, the interfacial tension between the fluids change when switching from immiscible to near-miscible gas-oil conditions, hence, by plotting Eq. (3.4) at the two conditions, we observe that the critical line is much steeper at immiscible conditions compared to the near-miscible case indicating again that it is much harder for gas layers to form at immiscible conditions. The capillary pressures between the phases will be determined using the curvature-based approach as described previously in section 3.1.3.2.5.2.

The overall conclusion of this analysis is that gas layers will not form under immiscible conditions but may be seen under the near-miscible conditions studied in our experiments.

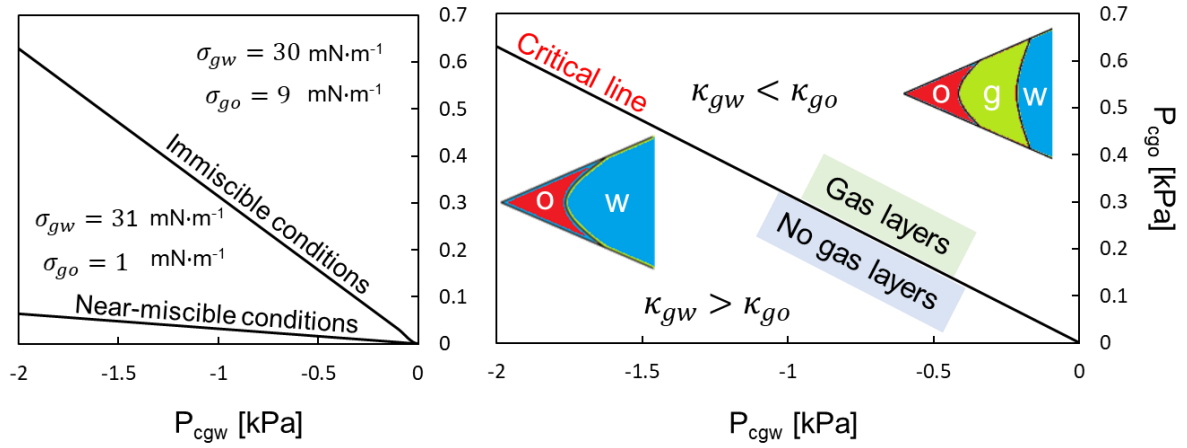

Figure 3. 21. A graphical representation of Eq. (3.4) that helps determine the likely formation of gas layers in an oil-wet system with a wettability order of oil-gas-water depending on the microscopic gas-water and gas-oil capillary pressures. (right) The graph illustrates that if the ratio of P_{cgo} to P_{cgw} falls above the critical line, gas layers will form as a much lower P_{cgo} will be needed to squeeze out the gas-oil interface ($\kappa_{gw} > \kappa_{go}$) and *vice versa*. (left) The critical line is less steep at near-miscible conditions, the study in section 3.2, compared to immiscible conditions and therefore it is more likely for gas layers to form at near-miscible conditions for the same gas-oil capillary pressure.

3.3.4 Results and Discussion

In this section, we quantify pore-scale properties that are relevant to carbon dioxide storage and oil recovery in our immiscible oil-wet experiment and compare the results to that of section 3.2 for near-miscible conditions. First, in section 3.3.4.1, we start by characterizing the rock surface wettability at immiscible and near-miscible conditions by: (i) measuring the geometric contact angle between the three fluid phases; and (ii) quantifying the pore occupancy of each phase. This allows us to verify the anticipated order of wettabilities in the two systems – oil-gas-water from most to least wetting. Next, we qualitatively and quantitatively confirm the presence of gas layers at near-miscible conditions and their absence at immiscible conditions by examining the fluid configurations and connectivity *in situ*, as well as measuring the Euler characteristic in section 3.3.4.2. In section 3.3.4.3, we use the capillary pressure measurements to conduct the curvature analysis detailed in section 3.3.3.5.1 to quantitively show that the necessary criteria for gas to spread in layers are fulfilled at near-miscible conditions in contrast to immiscible conditions. Finally, in sections 3.3.4.4 and 3.3.4.5, for immiscible and near-miscible conditions, we (i) measure the specific interfacial areas between the fluids and the fluids and rock; (ii) quantify the saturations of water, oil and CO_2 after each injection step; and (iii) examine the trapping mechanisms for both cases. We synthesize the results in section 3.3.4.6 by discussing the

implications of these results on CO_2 storage and oil recovery under each CO_2 injection condition (immiscible or near-miscible) in CCS-EOR projects.

3.3.4.1 Wettability characterization

3.3.4.1.1 Contact angles

The geometric contact angle between the fluids was measured after gas injection (GI) on a segmented high-resolution, 1.82 μm/voxel, subvolume (1500×1500×400 μm^3) of the pore space using the automated algorithm developed by AlRatrout et al. [30] at immiscible and near-miscible conditions. The distribution of the effective contact angles between oil-water (measured through water), CO_2-water (measured through water), and CO_2-oil (measured through oil) are shown in Fig. 3.22.

Fig. 3.22 depicts that both the immiscible and near-miscible systems are oil-wet with an average oil-water contact angle of 118° and 112° respectively. The reservoir rocks used in the two experiments were aged dynamically in the same coreholder; however, in the immiscible experiment the rock was left to statically age for eight months, while it was statically aged for four months only in the near-miscible experiment. This has resulted in the slightly more oil-wet surface in the immiscible experiment as shown by the higher average oil-water contact angle. From Fig. 3.22, it is also evident that the CO_2-water contact angle is higher than 90° in both immiscible and near-miscible experiments indicating that water is less wetting than CO_2 in the pore space, while the CO_2-oil contact angle is below 90° indicating that oil is more wetting than CO_2. This shows that the wettability order under both oil-wet immiscible and near-miscible conditions is oil-gas-water from most to least wetting. The oil-water contact angle was also measured after the first waterflooding (WF1) and the second waterflooding (WF2) for the immiscible system and showed a consistent distribution throughout the injection sequence, which confirms that there was no wettability alteration during the flooding experiment: see Fig. A3.2 in Appendix 3.

In equilibrium, the Bartell-Osterhof relationship, Eq. (2.11), can be used to determine the CO_2-water contact angle from the oil-water and CO_2-oil angles and interfacial tensions [49, 50]. The predicted values of θ_{gw} are shown in Table 3.11 together with the measured values, using the interfacial tensions in Tables 3.1 and 3.9. In the near-miscible case, since the gas-oil interfacial tension is low and the gas-water and oil-water interfacial tensions are similar, then from Eq. (2.11) we predict that $\theta_{gw} \approx \theta_{ow}$, which is consistent with our measurements.

On the other hand, we measure a larger gas-water contact angle under immiscible conditions than predicted from Eq. (2.11). The reason for this discrepancy is that the Bartell-Osterhof relationship holds at one location in equilibrium, while we are measuring the contact angles in different locations for different fluid pairs in a rock where the contact angle varies spatially. It appears that CO_2 (the gas phase) occupies the more oil-wet pores: the larger oil-wet pores are filled with water during waterflooding. During gas injection, CO_2 preferentially displaces water from the most oil-wet (and hence gas-wet) pores, since this is most favoured in an imbibition displacement. On the other hand, water remains in more water-wet pores. Hence for the gas-water angle the values are biased towards larger values of contact angle.

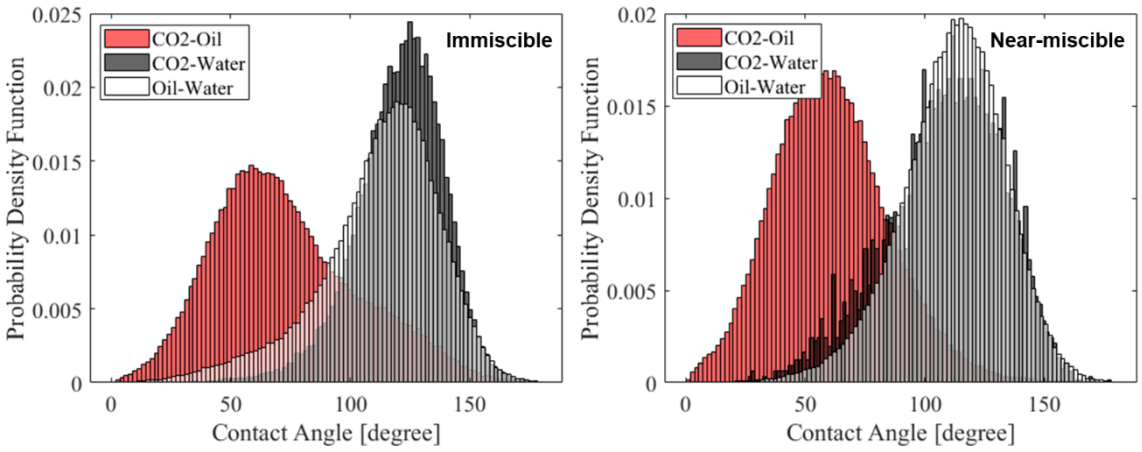

Figure 3. 22. Normalized histograms of the measured *in situ* contact angles between CO_2-water, oil-water and CO_2-oil in the aged rock at (left) immiscible and (right) near-miscible conditions. The contact angles were measured through the denser phase: water in the case of oil-water and CO_2-water contact angles, and oil in the case of the CO_2-oil contact angle. The contact angles were measured using the automated method developed by AlRatrout et al. [30].

Table 3. 11. Measured oil-water (θ_{ow}), gas-oil (θ_{go}), and gas-water (θ_{gw}) contact angles after gas injection (GI) at immiscible and near-miscible conditions together with the predicted θ_{gw} using the Bartell-Osterhof relationship, Eq (2.11), using the mean values. The measured mean values and standard deviations are of the contact angle distributions shown in Fig. 3.22.

Miscibility state	Measured θ_{ow}	Measured θ_{go}	Measured θ_{gw}	Predicted θ_{gw}
Near-miscible	112 ± 21°	67 ± 22°	108 ± 18°	110°
Immiscible	118 ± 25°	60 ± 24°	124 ± 24°	103°

3.3.4.1.2 Pore occupancy

Pore occupancy was quantified on pore-scale images of the whole sample (4,000×4,000×20,000 μm^3). The pore occupancies after the first waterflooding (WF1), gas injection (GI) and second waterflooding (WF2) at immiscible and near-miscible conditions are shown in Fig. 3.23. As expected for the oil-wet rocks in the immiscible and near-miscible experiments, the injection of water during WF1 displaces oil, the wetting phase, from the larger pores confining it into smaller ones; water resides in the biggest pores, Figs 3.23a and d.

The pore occupancies after GI and WF2 at both conditions confirm that the wettability order is oil-gas-water from most to least wetting. As shown in Fig. 3.23, water is the most non-wetting phase with a tendency to occupy the largest pores, CO_2 is the intermediate-wet phase occupying the medium-sized pores, while oil is the most wetting phase occupying the smallest pores.

The injection of CO_2 principally displaces water in both cases: this is because the CO_2 is wetting to water, see Table 3.11, and hence this represents a favourable imbibition process. CO_2 will preferentially fill the more oil-wet pores (which from Eq. 2.11 will be more gas-wet); this is evident from the contact angle distributions after gas injection shown in Fig. 3.22. There is also some displacement of oil, which is a less favoured drainage process, as gas is non-wetting to oil. More oil is displaced at near-miscible conditions, see Figs. 3.23b and e. This is attributed to the low gas-oil interfacial tension (1 mN/m) compared to immiscible conditions (9.8 mN/m) which results in a lower gas-oil capillary pressure; see section 3.3.4.3 for capillary pressure values. A low gas-oil capillary entry pressure allows CO_2 to invade a larger fraction of the smaller pores resulting in an efficient displacement of oil by gas at near-miscible conditions. Moreover, during gas injection (GI) at immiscible and near-miscible conditions, water gets

trapped in the centres of the pore space as disconnected ganglia since it is the most non-wetting phase, as described in the next section.

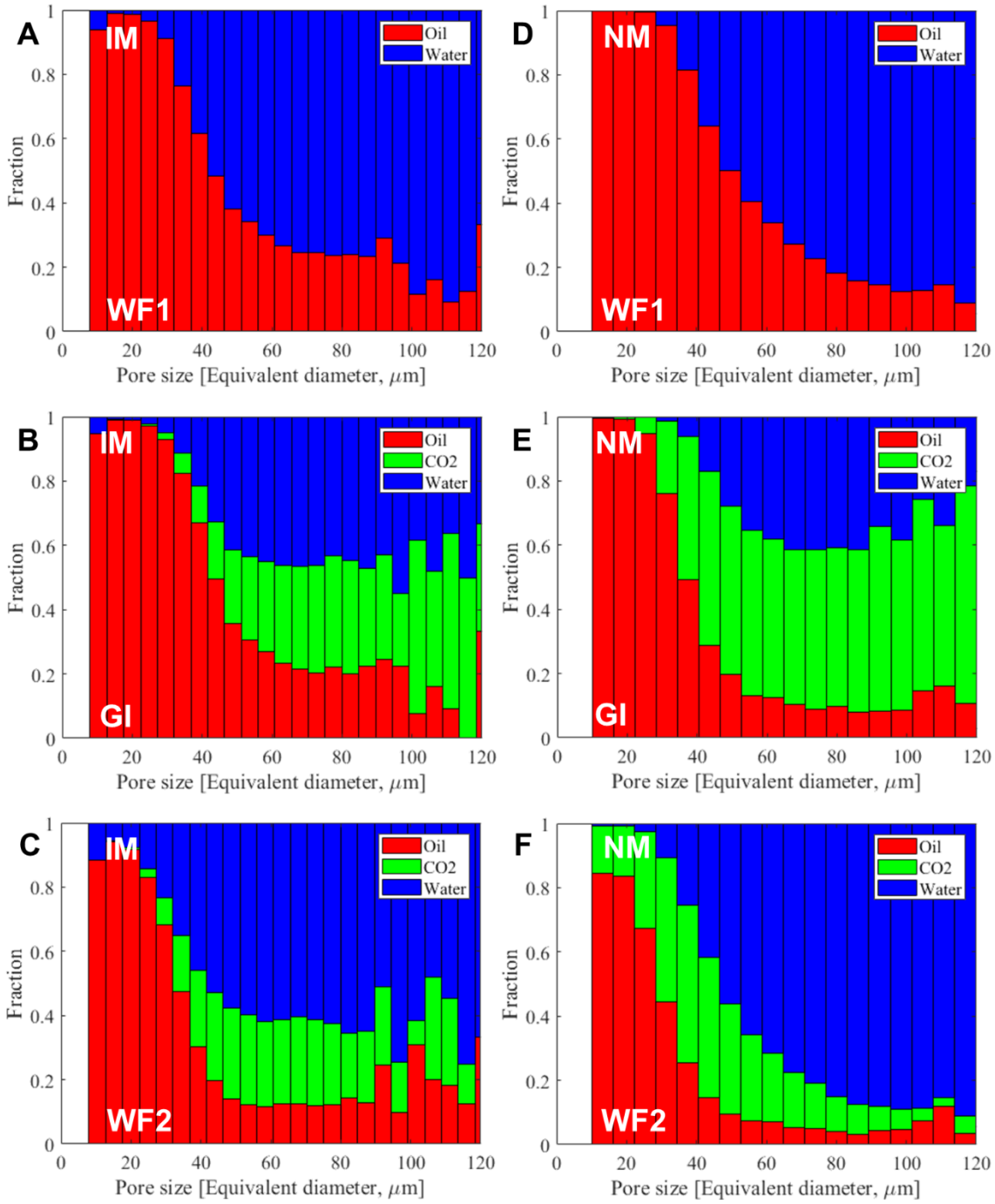

Figure 3. 23. Coloured bar charts showing the pore occupancy of each fluid phase in the pore space after gas injection [GI] at (B) immiscible and (E) near-miscible conditions, and after second waterflooding [WF2] at (C) immiscible and (F) near-miscible conditions. Pore occupancy is defined as the phase occupying the centre of the pore – this phase will also have the largest volume in the pore. Pore occupancy was quantified on pore-scale images of the whole sample (4,000×4,000×20,000 μm^3). Oil is shown in red, water in blue and gas, CO_2, in green.

During the second waterflooding (WF2), at near-miscible conditions, water invades the centres of the larger pores confining CO_2 and oil to smaller sized pores: CO_2 is forced to occupy smaller pores than those filled during GI, see Fig. 3.23f. On the other hand, during second waterflooding (WF2) at

immiscible conditions, the injection of water causes CO_2 to displace more oil out of the intermediate sized pores, shuffling it into some of the larger pores by a double displacement process [159], where water displaces gas that displaces oil: this is a double drainage event [41], see Fig. 3.23c. This behaviour is explained further in section 3.3.4.2 when we analyse gas layers.

3.3.4.2 Fluid configurations and connectivity

Fig. 3.24 shows example two- and three-dimensional images of a trapped water ganglion in a single pore during gas injection (GI) at both immiscible and near-miscible conditions. We observe that at near-miscible conditions, CO_2, the intermediate-wet phase, spreads in layers surrounding water, the most non-wetting phase. CO_2 exists in sheet-like layer structures at near-miscible conditions as shown in section 3.2. However, no evidence was found of oil residing in the corners when CO_2 invaded the pore (at this resolution); CO_2 layers are not sandwiched between oil in the corners and water in the centre. Because of the lower gas-oil interfacial tension (1 mN/m) compared to the gas-water interfacial tension (31 mN/m), Table 3.1, at near-miscible conditions, the gas front efficiently displaces all the oil in the corners, leaving water stranded in the centres of the pore space. CO_2 layers do not appear to coexist with oil in the same pore at near-miscible conditions. A similar behaviour was observed in section 3.1 in the water-wet system, where the injection of CO_2, the most non-wetting phase, at near-miscible conditions displaced all the oil, the intermediate-wet phase, in the pore space preventing it from spreading in layers.

At immiscible conditions however, CO_2 does not form layers but instead exists as disconnected ganglia in the pore space, see Fig. 3.24. This is consistent with the very negative gas spreading coefficient in this case, see Table 3.9 and Fig. 3.21. This means that CO_2, water and oil cannot reside in the same pore under immiscible conditions. CO_2 can either be present with water or oil in the same pore, occupying the corners of the pore in the case of water, and the centres in the case of oil. This limitation means that during water injection, one of the principal displacement processes is likely to be double drainage where water displaces CO_2 which then displaces oil in some of the larger pores, as discussed in the context of the pore occupancy, Fig. 3.23c. Unlike near-miscible conditions, CO_2 does not displace all the oil it contacts due to the higher gas-oil interfacial tension (9.8 mN/m), Table 3.9.

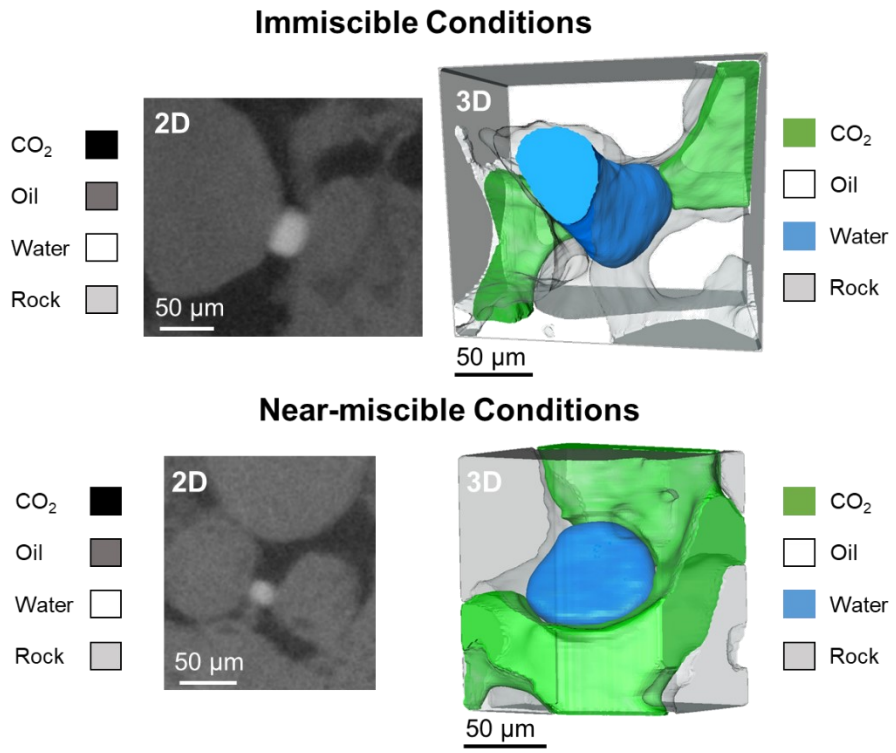

Figure 3. 24. Two-dimensional raw images and three-dimensional segmented images of a trapped water ganglion in a single pore after gas injection (GI) at immiscible and near-miscible conditions. CO_2 spreads in layers at near-miscible conditions, while it exists as disconnected clusters at immiscible conditions. The size of the 3D subvolumes shown at immiscible and near-miscible conditions are 185×209×121 μm^3 and 109×134×152 μm^3 respectively. The pore-scale images were acquired by X-ray microtomography at a resolution of 1.82 µm per voxel.

To examine the connectivity of the water and CO_2 phases in the macro pore space, we plotted 3D coloured volume maps identifying the size of each disconnected phase cluster – a large range of colours represents a poorly connected phase, while a narrow colour distribution indicates better connectivity. The connectivity of the water and CO_2 phases after gas injection (GI) and second waterflooding (WF2) are shown in Fig. 3.25 at immiscible and near-miscible conditions. In general, although not very well connected, the connectivity of CO_2 is slightly improved at near-miscible conditions. This is attributed to the existence of CO_2 in sheet-like layers at near-miscible conditions, while CO_2 forms disconnected ganglia and no layers at immiscible conditions, see Fig. 3.24. Nevertheless, at immiscible conditions, the CO_2 has a tendency to occupy some of the larger pores, Fig. 3.23, so that, for the same saturation, it is likely to have a larger flow conductance than under near-miscible conditions. The CO_2 follows a tortuous path through the pore space in both cases, however.

There is more water trapping (water is highly disconnected) during gas injection (GI) at immiscible conditions compared to near-miscible conditions. This is because, since CO_2 cannot form layers, both phases essentially compete to occupy some of the larger and medium-sized pores, blocking each other's flow. During the second waterflooding (WF2), water forms a connected path through the larger pores at both conditions. While not shown in Fig. 3.25, oil exists in highly connected thick wetting layers close to the rock surface: the oil wetting layer becomes thinner as more oil gets produced throughout the flooding experiment.

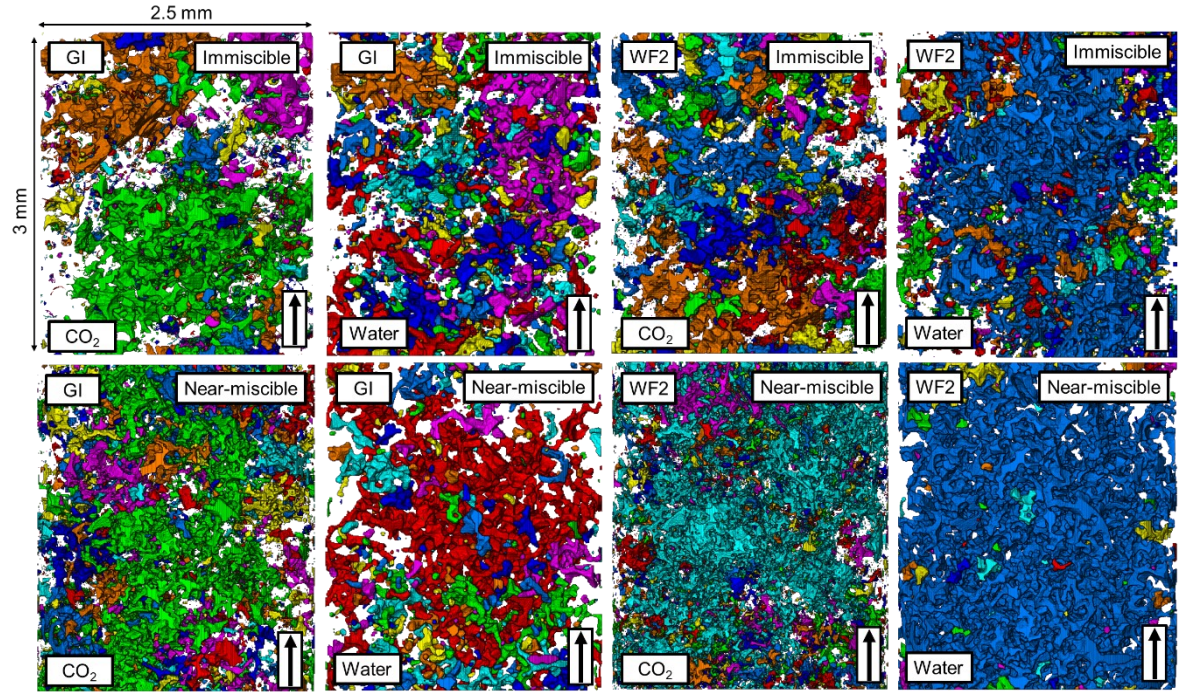

Figure 3. 25. Three-dimensional maps showing the connectivity of water and CO_2 phases during gas injection (GI) and second waterflooding (WF2) at immiscible and near-miscible conditions. The colours indicate discrete clusters of each phase. Each subvolume is of 2,500×2,500×3,000 μm^3 size and 1.82 µm/voxel size. The vertical arrow points in the flow direction.

To quantitatively assess the connectivity of oil, water and CO_2, we measured the Euler characteristic which quantifies the topology of the fluid phases within the pore space [160-164], see Table 3.12. A large negative Euler characteristic indicates that the fluid phase is interconnected with many redundant loops, while a phase that is trapped into many discrete ganglia exhibits a large positive Euler characterstic [165]. The fluid phases in the high-resolution, 1.82 µm/voxel, subvolumes, size 2,500×2,500×3,000 μm^3, were isolated and the small features (below 10 voxels) were filtered out prior to measuring the Euler characteristic of each phase, consistent with previous work [165].

The results in Table 3.12 confirm the qualitative observations made based on Fig. 3.25. Water has a positive Euler characteristic after gas injection at both immiscible and near-miscible conditions confirming its existence in disconnected clusters in the centre of the pores, see Fig. 3.24, consistent with water being the most non-wetting phase. The water phase Euler characteristic decreases, as expected, after waterflooding. Under immiscible conditions water is still trapped in some of the larger pores giving a characteristic that remains positive, as evident in Fig. 3.25. After gas injection at both miscibility conditions, CO_2 has a smaller negative Euler characteristic compared to oil which is well-connected in wetting layers. The CO_2 Euler characteristic is smaller at near-miscible conditions, -634 mm^{-3}, compared to immiscible conditions, -102 mm^{-3}, after WF2, confirming the enhanced CO_2 connectivity at near-miscible conditions due to its existence in spreading layers.

Table 3. 12. Euler characteristic of water, CO_2 and oil measured after gas injection [GI] and second waterflooding [WF2] at immiscible and near-miscible conditions. The Euler characteristic was measured on high resolution images, 1.82 µm/voxel, and normalized to the total volume in both cases.

Miscibility state	Normalized Euler Characteristic (mm^{-3})					
	Gas Injection [GI]			Second waterflooding [WF2]		
	Water	CO_2	Oil	Water	CO_2	Oil
Immiscible	125	-504	-5055	21	-102	-17298
Near-miscible	90	-499	-17851	-2318	-634	-24027

3.3.4.3 Capillary pressure and curvature analysis

Using the curvature-based approach described in section 3.1.3.2.5.2, the capillary pressure between the fluids was measured after each injection step at immiscible and near-miscible conditions, see Fig. 3.26. The capillary pressure measurements were performed on high-resolution, 1.82 μm/voxel, subvolumes of size 2,500×2,500×3,000 μm^3. The saturations, see section 3.3.4.5, only consider phases in the resolvable macro pore space.

At both immiscible and near-miscible conditions, the capillary pressure between oil and water was negative, indicating that the pressure in the water phase is higher than oil, which is a characteristic of predominantly oil-wet media. The oil-water capillary pressure is more negative at near-miscible conditions, ranging from -1.3 kPa to -2.4 kPa, compared to immiscible conditions, ranging from -0.5 kPa to -1 kPa, see Fig. 3.26. This is partially attributed to the higher oil-water interfacial tension in the near-miscible experiment (30 mN/m) compared to the immiscible experiment (21 mN/m), see Tables 3.1 and 3.9. In addition, under near-miscible conditions, as shown in Fig. 3.23, oil tends to reside in smaller pores, which again would give a larger (more negative) capillary pressure. The fact that the average oil-water contact angles are higher in the immiscible case does not result in a more negative capillary pressure. As expected, the oil-water capillary pressure decreased with increasing water saturation at near-miscible conditions. However, in the immiscible experiment, the oil-water capillary pressure is more negative during gas injection (GI) at a lower water saturation. At the beginning of gas injection, after the first waterflood, the capillary pressure is likely to be large and negative, as the water displaces oil from increasingly small and oil-wet regions of the pore space. During gas injection, since the principal displacement is gas displacing water as an imbibition process, with a lower gas pressure than water, then P_{cow} can continue to have a large negative value while the gas pressure increases before gas is able to displace oil. During waterflooding, Fig. 3.23c, double displacement moves oil into larger pores, as discussed above, with a less negative capillary pressure.

The measured gas-water capillary pressure ranged from -0.5 kPa to -2.5 kPa at both immiscible and near-miscible conditions. A negative gas-water capillary pressure indicates that gas is more wetting to the rock surface than water. This confirms the reported wettability order of oil-gas-water from most to least wetting in section 3.3.4.1. Under immiscible conditions, we again see that the capillary pressure is less negative (higher) during WF2. Again, this is due to double displacement, and the fact that water displaces gas from the larger pores, see Fig. 3.23c. Note that this leads to a trend of capillary pressure with saturation which is counter-intuitive: an increase with increasing water saturation. This shows that in three-phase flow the capillary pressure is a function of both saturation and displacement path [134, 135, 166].

The gas-oil capillary pressure was positive at both immiscible and near-miscible conditions, indicating that oil is more wetting than gas, Table 3.11. As expected, the capillary pressure between gas and oil is higher at immiscible conditions (0.26 kPa to 0.38 kPa) compared to near-miscible conditions (0.04 kPa to 0.08 kPa) due to the higher gas-oil interfacial tension, see Tables 3.1 and 3.9.

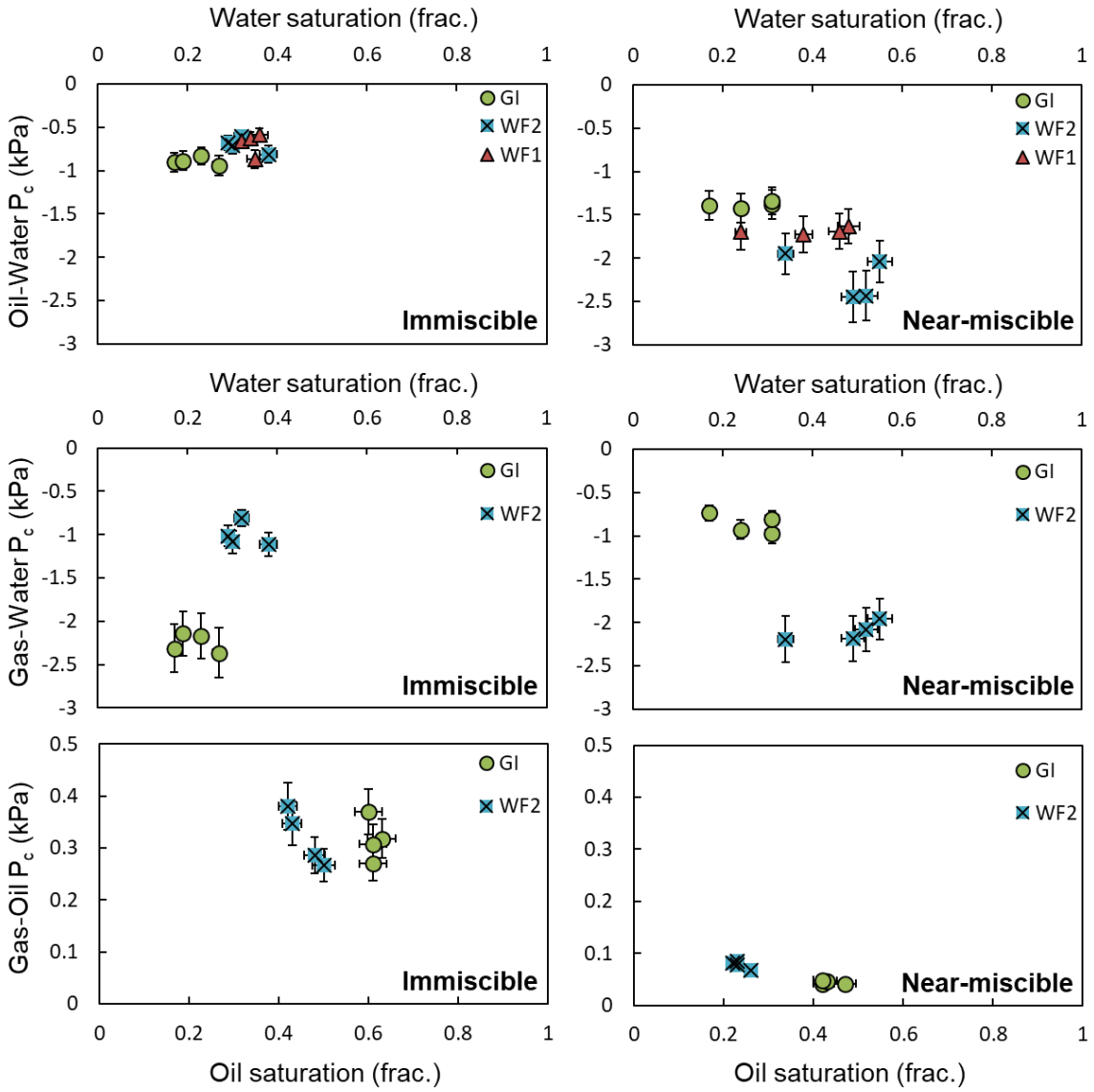

Figure 3. 26. Capillary pressures estimated from the average curvature of the fluid-fluid interfaces plotted as a function of water saturation in the case of oil-water and gas-water capillary pressures and as a function of oil saturation in the case of the gas-oil capillary pressure. Capillary pressure measurements after first waterflooding (WF1), gas injection (GI) and second waterflooding (WF2) are shown (left column) at immiscible conditions and (right column) at near-miscible conditions. Error bars indicate the uncertainty in the measurements.

The gas-water and gas-oil capillary pressure values in Fig. 3.26 were used to conduct the curvature analysis described in section 3.3.3.5.1, see Fig. 3.21, to quantitatively confirm that the gas layer spreading criteria are met at near-miscible conditions and that gas does not form layers at immiscible conditions. The results are shown in Fig. 3.27. At immiscible conditions, during gas injection (GI), the ratio of P_{cgo} to P_{cgw} falls below the critical line, suggesting that gas layers do not form, see Fig. 3.27 (left). During WF2, the curvature analysis indicates that layers are possible, but the large negative spreading coefficient of -19.5 mN/m, Table 3.9, in this case prevents their formation. In contrast, at near-miscible conditions, the P_{cgo} to P_{cgw} ratio lies above the critical line suggesting the formation of stable gas layers, see Fig. 3.27 (right). The formation of gas layers is also supported by a gas spreading coefficient close to zero at near-miscible conditions (C_{sg} = -2 mN/m, Table 3.1).

The existence of CO_2 in layers at near-miscible conditions substantially impedes its movement in the reservoir. While these layers maintain connectivity, they have low relative permeability (low flow conductivity) in the pore space of the rock. This was shown in section 3.2 where the relative

permeability of these layers on pore-space images was computed. On the other hand, we predict a higher CO_2 relative permeability at immiscible conditions, where CO_2 occupies some of the larger pores, Fig. 3.23, and exists in blobby structures; its flow is not confined to movement in layers.

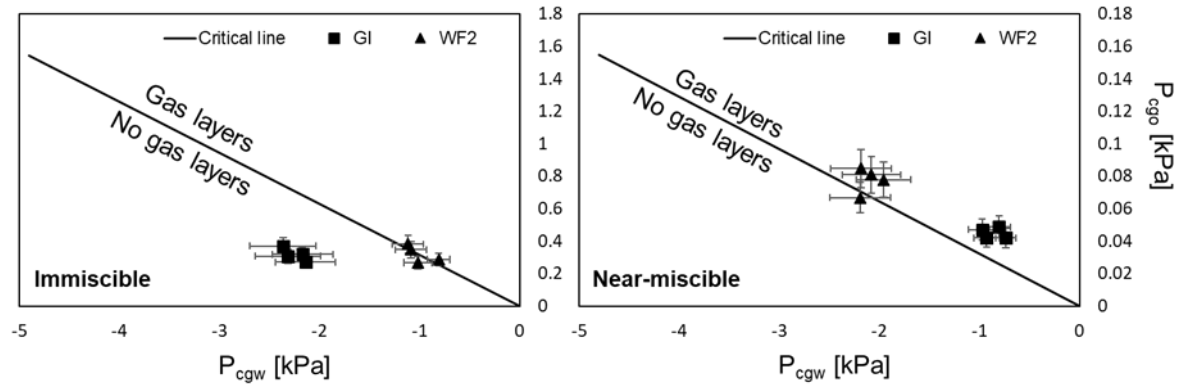

Figure 3. 27. Curvature gas layer analysis conducted at (left) immiscible conditions and (right) near-miscible conditions. The graphs illustrate that under immiscible conditions gas layers do not form, while gas can form layers under near-miscible conditions. Error bars indicate the uncertainty in the measurements.

3.3.4.4 Interfacial area

We also quantified the specific interfacial areas – area per unit volume (total volume of rock and pore space) – between each fluid pair and between the fluids and the rock surface (solid) at both conditions, see Fig. 3.28. From Fig. 3.28a and b, we observe that the CO_2-water interfacial area is higher at near-miscible conditions compared to immiscible conditions: this is caused by the presence of CO_2 layers which surround the water phase increasing their direct contact in the pore space. Moreover, the CO_2-water interfacial area increases during WF2 at both conditions since more water is present, allowing more contact between the two phases. As expected, the oil-water interfacial area decreases as oil is produced under both immiscible and near-miscible conditions. This also explains why the oil-solid interfacial area decreases throughout the flooding experiment, see Fig. 3.28c and d.

The CO_2-oil interfacial area is higher at immiscible conditions compared to near-miscible conditions (Fig. 3.28a and b): this is an initially surprising result as one would expect a higher gas-oil interfacial area at near-miscible conditions given the low gas-oil interfacial tension which makes a gas-oil interface more energetically favorable to form in the pore space, combined with the presence of gas layers. This behaviour, however, can be ascribed to the low gas-oil capillary entry pressure at near-miscible conditions: gas will almost always have sufficient pressure to displace oil efficiently out of the pores minimizing their direct contact in the pore space. This is similar to the efficient displacement of oil that was also observed in the near-miscible water-wet system in section 3.1. This interpretation is supported by the higher CO_2-solid interfacial area at near-miscible conditions compared to immiscible conditions, see Fig. 3.28c and d.

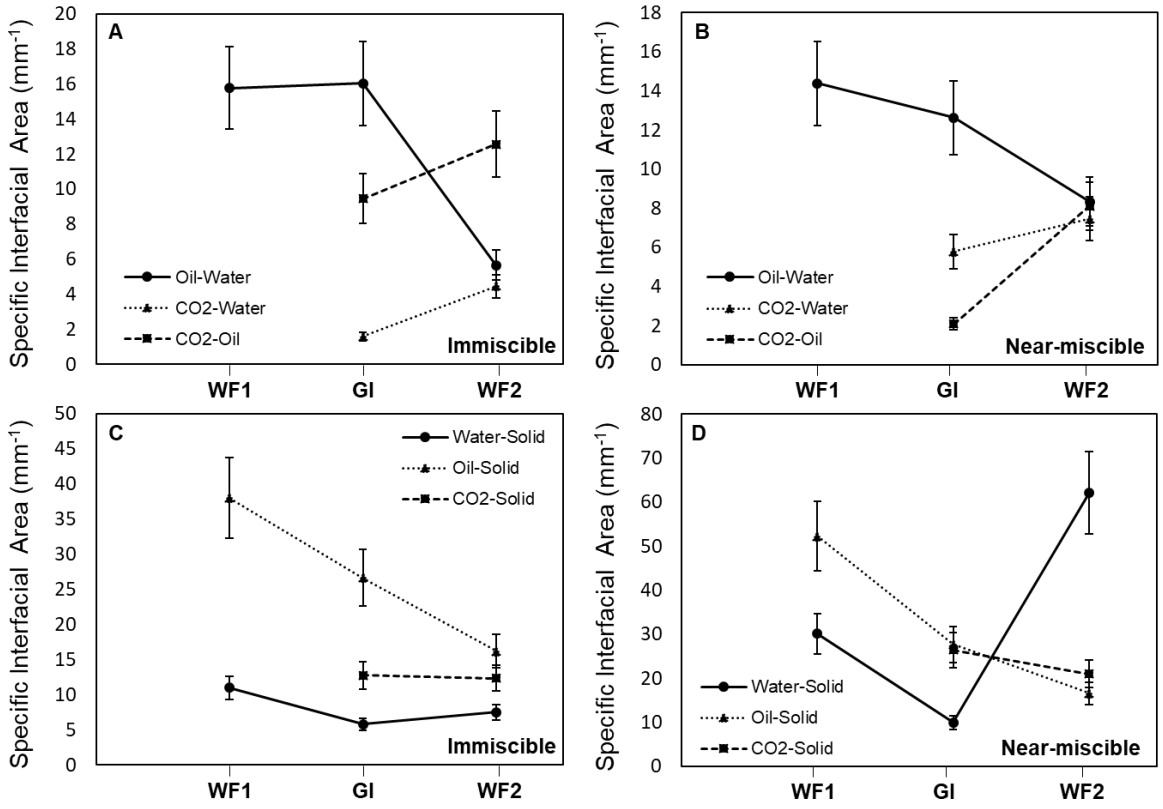

Figure 3. 28. Specific interfacial area measurements between each fluid pair in the pore space at (A) immiscible conditions and (B) near-miscible conditions, and between the fluids and the rock surface (solid) at (C) immiscible conditions and (D) near-miscible conditions. The specific area is calculated on extracted fluid-fluid and fluid-solid interfaces from segmented images. The measurements were performed on high-resolution, 1.82 μm/voxel, subvolumes of size 2,500×2,500×3,000 μm^3. Error bars reflect uncertainties in the specific area measurements.

3.3.4.5 Saturation and trapping

The saturation of water, oil and CO_2 in the macro pores was quantified after each injection step for both sets of experiments. The fluid saturations in Fig. 3.29 were measured on segmented images of the whole sample (4,000×4,000×20,000 μm^3). After the first waterflooding (WF1), 46 ± 2% of the oil was recovered at immiscible conditions, while only 39 ± 2% was recovered for the near-miscible experiment. The discrepancy in the oil recovered through water injection in the two experiments is attributed to many reasons including the use of different rock samples, different fluids, and different temperatures and pressures, rather than the wetting state of the rock. However, the low oil recovery observed during WF1 in the two experiments is ascribed to water invading the centres of the pores, bypassing oil which resides in wetting layers in the corners and small pores. This is a common characteristic of oil-wet media [72].

Next, CO_2 was injected in a tertiary recovery process allowing the production of both oil and water. At immiscible conditions, this resulted in a CO_2 saturation of only 24 ± 2%, while, at near-miscible conditions, the CO_2 saturation reached 33%; the injection of CO_2 at near-miscible conditions resulted in an additional oil recovery of 19 ± 2%, while at immiscible conditions only 9 ± 2% of extra oil was recovered. The higher oil recovery at near-miscible conditions is attributed to the negligible (low) gas-oil capillary pressure: as CO_2 invades the pore space it efficiently displaces all the oil it contacts (almost 100% microscopic displacement efficiency). The same favourable recovery has also been observed under near-miscible conditions in the water-wet rock in section 3.1.

Water injection during WF2 further reduces the oil and CO_2 saturations. At immiscible conditions, the subsequent injection of water is necessary to increase the oil production, an additional 14 ± 2% of oil was recovered during WF2; the injection of CO_2 alone is not sufficient to produce significant amounts of oil. Furthermore, water injection displaced only 5 ± 2% of the CO_2 saturation at immiscible conditions, while at near-miscible conditions the CO_2 saturation decreased by 12 ± 2%. The low CO_2 production at immiscible conditions is ascribed to the low connectivity of CO_2, CO_2 can form disconnected ganglia in the pore space, whereas, at near-miscible conditions, CO_2 exists in connected layers which allows the gas to be produced directly. This is also consistent with our interpretation that the principal displacement in immiscible conditions is double drainage: water displaces disconnected CO_2, but rather than being displaced, this CO_2 displaces oil in some of the larger pores, as discussed previously, see Fig. 3.23.

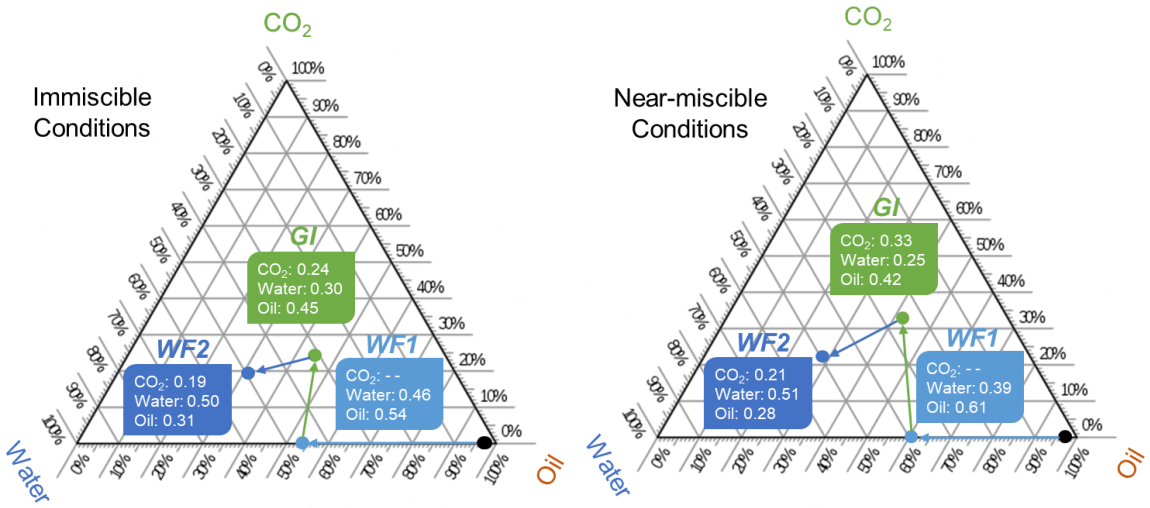

Figure 3. 29. Three-phase ternary diagrams showing the water, oil and CO_2 end-point saturations after each injection step at (left) immiscible conditions and (right) near-miscible conditions. At first (black point on the diagram), the rock is restored to its initial reservoir conditions (water saturation in macro pores: 0.01 and oil saturation: 0.99). The colored arrows point to the chronological order of injection events: (i) first waterflooding [WF1]; (ii) gas injection [GI], and (iii) second waterflooding [WF2].

To recall, for CO_2 to become capillary trapped by another fluid phase in the centres of the pore space, in general it must be less wetting than that phase. Therefore, since CO_2 is more wetting to the rock than water at both immiscible and near-miscible conditions, this means that it cannot be capillary trapped by water. However, at immiscible conditions, CO_2 can coexist with oil in the same pore and it is less wetting than oil; hence, CO_2 can be capillary trapped by oil at these conditions. An example of this is illustrated in Fig. 3.30, where the injection of water during WF2 at immiscible conditions resulted in capillary trapping of CO_2 by oil. The CO_2 snap-off was caused by oil that was displaced by water [39, 89]. In contrast, capillary trapping of CO_2 by oil is not possible at near-miscible conditions due to the low oil-gas capillary pressure, which prevents their direct contact in the pore space. This is confirmed by the lower Euler characteristic, see Table 3.12, after WF2, implying better connectivity.

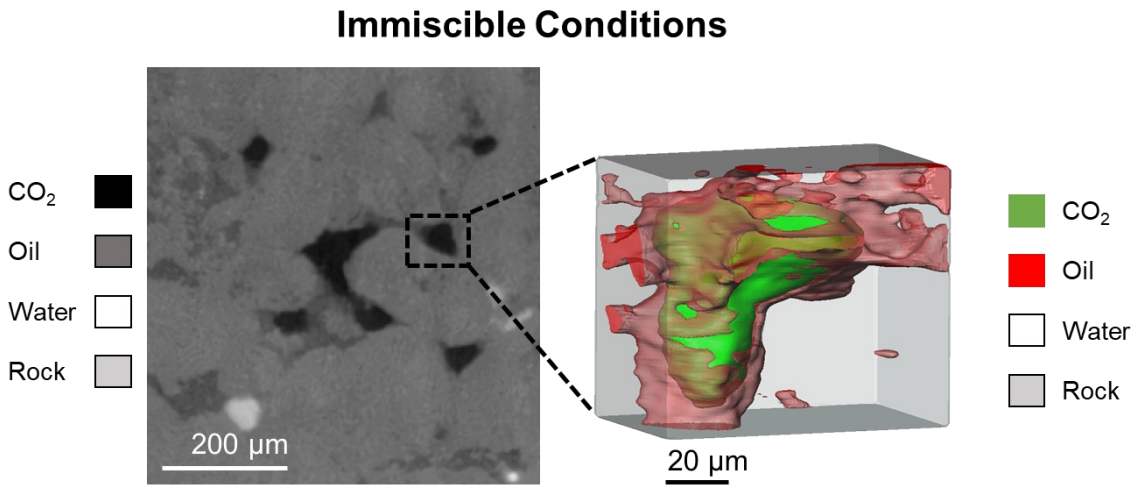

Figure 3. 30. (left) A 2D 1.82 µm resolution pore-scale image showing capillary trapping of CO_2 by oil under strongly oil-wet immiscible conditions in a carbonate rock after the second waterflooding (WF2). (right) A selected 3D subvolume (193×126×166 µm^3) from (left) showing a trapped CO_2 ganglion surrounded by oil in a single pore.

3.3.4.6 Implications for recovery and storage

So far, we have demonstrated that although the wettability order, oil-gas-water from most to least wetting, is the same under immiscible conditions and near-miscible conditions, the pore-scale fluid configurations and trapping mechanisms remain different. Accordingly, we presume that the selected injection conditions (immiscible or near-miscible conditions) will have different implications on oil recovery and the safety of carbon dioxide storage in CO_2-EOR projects. In our discussion of the results, the emphasis will be the on local displacement efficiency – that is the amount of recovery and storage in parts of the pore space contacted by the injected fluids. Overall recovery will also, of course, be controlled by well placement and large-scale reservoir heterogeneity.

We suggest that at near-miscible conditions, an injection of strategy of CO_2 injection only should be implemented for three reasons. (i) At near-miscible conditions, the flow of CO_2 in the pore space is restricted even when injected alone due to its existence in layers of low conductivity. This means that it is difficult for the stored CO_2 to solely flow towards abandoned boreholes and escape through them. (ii) Significant amounts of oil can be recovered by CO_2 injection only at near-miscible conditions; the low gas-oil interfacial tension results in a high microscopic or local displacement efficiency. (iii) The subsequent injection of water produces significant quantities of the stored CO_2, reducing the storage capacity; CO_2 exists in connected layers which allows the gas to be produced directly when displaced by water, albeit slowly. Water injection does not help to trap the CO_2 and simply facilitates its displacement. Therefore, a continuous CO_2 injection only strategy is recommended at near-miscible conditions, or with minimal amounts of water – CO_2 is unlikely to be produced in significant quantities.

In contrast, to aid oil recovery and CO_2 storage during CCS-EOR at immiscible conditions, a WAG injection strategy is suggested. This is ascribed to two reasons. (i) CO_2 exists as disconnected ganglia in the pore space of the reservoir rocks; hence, the subsequent injection of water does not produce a large quantity of the stored CO_2. Furthermore, at immiscible conditions, the injection of water can cause capillary trapping of CO_2 by oil in the centres of the pore space which is not possible at near-miscible conditions. Capillary trapping of CO_2 by oil ensures the safety of carbon storage. (ii) The injection of CO_2 alone at immiscible conditions is not sufficient to produce significant amounts of oil; subsequent water injection is necessary to increase the oil recovery.

3.3.5 Final Remarks and Suggestions

We have provided the first experimental evidence of three-phase displacement in strongly oil-wet reservoir rocks, where the wettability order in the system is altered such that water is the most non-wetting phase occupying the largest pores, oil is the most wetting phase occupying the smallest pores, while gas is the intermediate-wet phase occupying medium-sized pores. In our strongly oil-wet rock, at immiscible conditions, we use X-ray imaging to (i) characterize *in situ* contact angles and pore occupancy; (ii) examine fluid configurations and connectivity (Euler characteristic), (iii) investigate the formation of gas layers, (iv) quantify fluid-fluid/fluid-solid interfacial areas; (v) measure fluid saturations during a WAG flooding strategy; and (vi) determine the optimum carbon dioxide storage mechanism. We performed the same analysis on the near-miscible dataset presented in section 3.2, where the rock is slightly less oil-wet, but has the same wettability order in the pore space, oil-gas-water from most to least wetting. Despite having the same wettability order, we observed distinct pore-scale phenomena at immiscible and near-miscible conditions. Our main conclusions and implications from this work are:

- **CO_2 layers**. CO_2 as the intermediate-wet phase forms layers surrounding water at near-miscible conditions, while, at immiscible conditions, it exists as disconnected ganglia in the pore space. This is mainly due to the large negative gas spreading coefficient at immiscible conditions (C_{sg} = -19.5 mN/m) which prevents it from spreading in layers compared to the near-miscible case (C_{sg} = -2 mN/m). CO_2 can flow more readily in the pore space at immiscible conditions, when connected, as opposed to being confined to movement in layers at near-miscible conditions.

- **Capillary pressure**. As expected, the capillary pressure measurements displayed (-) negative oil-water and gas-water pressures and a (+) positive gas-oil pressure confirming the anticipated wettability order, oil-gas-water from most to least wetting, at both immiscible and near-miscible conditions. Despite having a similar gas-water capillary pressure in the two systems, the gas-oil capillary pressure was much higher at immiscible conditions due to its higher gas-oil interfacial tension.

- **Interfacial area**. The CO_2-water specific interfacial area is higher at near-miscible conditions because of the spreading of CO_2 layers surrounding the water phase, whereas the CO_2-oil interfacial area is higher at immiscible conditions due to the trapping of CO_2 in the centres of the pore space by the oil wetting layers.

- **Trapping**. Water, the most non-wetting phase, gets trapped in the centres of the pore space when CO_2 is injected at both conditions, with slightly higher water trapping at immiscible conditions. CO_2 is more connected at near-miscible conditions, albeit with a low flow conductance. Oil exists in thick wetting layers close to the rock surface at both conditions. It is not possible to capillary trap CO_2 by water in the centres of the pore space at both immiscible and near-miscible conditions since CO_2 is more wetting to the rock than water. However, capillary trapping of CO_2 by oil is possible at immiscible conditions.

- **Oil recovery**. Near-miscible gas injection conditions are more favourable for oil recovery due to the low gas-oil interfacial tension which allows gas to displace oil efficiently from the pores (almost 100% microscopic displacement efficiency).

- **Implications for CO_2 storage**. Our results suggest that for favorable oil recovery coupled with effective CO_2 storage at near-miscible conditions during CCS-EOR, an injection strategy of CO_2 injection only should be implemented, while a WAG injection strategy (injection of CO_2 and water alternately) is recommended at immiscible conditions.

Future work should primarily focus on quantifying the relative permeabilities of water, oil and CO_2 in the pore spaces of water-wet, oil-wet and mixed-wet rocks at immiscible and near-miscible conditions; we show measurements of relative permeability at immiscible conditions in chapter 6. Moreover, a time-resolved synchrotron experiment can be conducted to better characterize the pore-scale dynamics of three-phase flow in oil-wet rocks which will be the topic of chapter 4. Furthermore, these results could be used to study energy balance and connectivity to help develop improved theories of three-phase flow in porous media

Having investigated the pore-scale physics in a strongly oil-wet system using static imaging in this section, in the next sections, 4.1 and 4.2, we will use synchrotron dynamic imaging to study the pore-scale invasion dynamics during water and gas injection in a strongly oil-wet rock.

Chapter 4

In this chapter we will present the materials and methods, results, discussion, and conclusions of the dynamic two- and three-phase studies (*EXP4* and *EXP5*, see Table 1.1). The pore-scale invasion dynamics during water and gas injection in a strongly oil-wet rock are investigated using synchrotron X-ray imaging in sections 4.1 and 4.2 respectively. The two experiments were performed consecutively on the same reservoir sample. In section 4.1, only the area where dynamic images were acquired was analysed, while the whole sample – including the dynamic area – was analysed in section 4.2. Again, the heading of each section is given the title of the published manuscript.

4.1 Dynamics of water injection in an oil-wet reservoir rock at subsurface conditions: Invasion patterns and pore-filling events

4.1.1 Summary

We use fast synchrotron X-ray microtomography to investigate the pore-scale dynamics of water injection in an oil-wet carbonate reservoir rock at subsurface conditions. We measure, *in situ*, the geometric contact angles to confirm the oil-wet nature of the rock and define the displacement contact angles using an energy-balance-based approach. We observe that the displacement of oil by water is a drainage-like process, where water advances as a connected front displacing oil in the centre of the pores, confining the oil to wetting layers. The displacement is an invasion percolation process, where throats, the restrictions between pores, fill in order of size, with the largest available throats filled first. In our heterogeneous carbonate rock, the displacement is predominantly size controlled; wettability has a smaller effect, due to the wide range of pore and throat sizes, as well as largely oil-wet surfaces. Wettability only has an impact early in the displacement, where the less oil-wet pores fill by water first. We observe drainage associated pore-filling dynamics including Haines jumps and snap-off events. Haines jumps occur on single- and/or multiple-pore levels accompanied by the rearrangement of water in the pore space to allow the rapid filling. Snap-off events are observed both locally and distally and the capillary pressure of the trapped water ganglia is shown to reach a new capillary equilibrium state. We measure the curvature of the oil-water interface. We find that the total curvature, the sum of the curvatures in orthogonal directions, is negative, giving a negative capillary pressure, consistent with oil-wet conditions, where displacement occurs as the water pressure exceeds that of the oil. However, the product of the principal curvatures, the Gaussian curvature, is generally negative, meaning that water bulges into oil in one direction, while oil bulges into water in the other. A negative Gaussian curvature provides a topological quantification of the good connectivity of the phases throughout the displacement.

4.1.2 Investigations

The motivation behind performing this dynamic two-phase flow experiment is highlighted in section 2.2.3.1.

In *EXP* 4, we examine, *in situ*: (i) wettability and displacement contact angles; (ii) invasion patterns (pore-filling order); (iii) Haines jumps; (iv) snap-off events; (v) fluid saturations; (vi) specific interfacial areas; and (vii) oil-water capillary pressure. We test the hypothesis that in a highly heterogenous porous

medium with a significant wettability alteration from an original water-wet state, the pore space becomes largely water-repellent, and that water invasion is a drainage-type invasion percolation process. We compare some of the results with a similar study conducted on a Ketton limestone rock [102]. This work is important since non-water-wet surfaces are ubiquitous in nature, e.g. in deep oil reservoirs, rice leaves, butterfly wings, and human skin, as well as the fact that many surfaces are designed to be fully or partially water-repellent to improve their performance, e.g. textiles, medical and cosmetic devices including surgical masks, fuel cells and catalysts [18, 70, 79-82, 111, 167-169]. Moreover, this time-dependent data is vital for the validation of pore-scale models of multiphase flow.

4.1.3 Materials and Methods

In this section, we provide details regarding the rock and fluid properties, the methodology followed to establish the reservoir wettability, flow apparatus, image acquisition and processing. The sample was initially prepared in-house before transporting it to the synchrotron facility for imaging the flooding experiment. All imaging was conducted at the Diamond imaging beamline I13-2 (Diamond Light Source, Harwell campus, Didcot, UK).

4.1.3.1 Rock and fluid properties

The experiment was conducted on a 3.85 mm diameter and 13.8 mm long reservoir sample cut from the same large piece of rock used in sections 3.2 and 3.3, refer to section 3.2.3.1 for more details on the rock type. The reservoir rock is very heterogenous with a wide distribution of pore sizes varying from 3.5 to 120 μm; see Fig. A4.1 in Appendix 1 for the pore size distribution. The measured helium porosity of the sample was 26%, with the macro- and sub-resolution porosities accounting for 16% and 10% respectively. The pore volume (PV) of the sample corresponding to the total helium porosity was 0.0416 mL.

The experimental fluids used to represent the water and oil phases were doped deionized water (20% by weight potassium iodide) and doped *n*-decane (15% by weight 1-iododecane) respectively. The thermophysical properties of the two fluids are listed in Table 4.1.

Table 4. 1. Thermophysical properties of the oil and water phases at the experimental conditions (8 MPa and 60 ºC). The interfacial tension between oil and water was measured at 8 MPa and 60 ºC using the pendant drop method. Data from NIST [130], Toolbox [158], Jianhua [170].

Fluid	Composition (%wt)	ρ (kg·m^{-3})	μ (mPa·s)	σ (mN· m^{-1})
Water	80% deionized + 20% potassium iodide	1145.0	0.547	σ_{ow} = 52.1
Oil	85% *n*-decane + 15% 1-iododecane	715.2	1.088	

4.1.3.2 Wettability alteration

The surface wettability of the rock sample was altered oil-wet prior to conducting the experiment. We used the ageing protocol detailed in section 3.2.3.2, where the rock undergoes both dynamic and static ageing. Ageing was performed in-house before transporting the sample to the synchrotron light source facility.

4.1.3.3 Flow experiment and synchrotron imaging

The experimental apparatus used to conduct the flow experiment in the synchrotron light source facility is shown in Fig. 4.1. The sample-coreholder assembly is similar to that detailed in section 3.1.3.2. The flow cell was then placed in front of the synchrotron beamline to start the experiment.

The flow experiment was initiated by flushing 20 pore volumes of the oil phase (doped *n*-decane) through the sample at a flow rate of 0.1 mL/min to replace the crude oil used to alter the wettability. This step is essential to avoid the formation of emulsions during the experiment [109]. The system was then pressurized to the experimental conditions (8 MPa) and the confining pressure to 10 MPa. The temperature in the system was then raised to the experimental temperature (60 °C) using an Omega flexible heater. At this point, a single high-quality scan of the oil saturated rock was acquired (hereafter called the reference oil scan). While oil initially occupied almost 99% of the macro-pore space before water injection (measured on the reference oil scan), water was also initially present in the sub-resolution porosity and in the corners of the pore space.

The dynamic experiment was then started by injecting water into the oil saturated rock at a very low flow rate, 0.15 µL/min, achieving a capillary number ($Ca = \mu q/\sigma$, where σ is the oil-water interfacial tension, μ is the viscosity of water and q is the Darcy velocity of water) of 2.09×10^{-9} which resulted in capillary dominated flow conditions. Furthermore, the low flow rate enabled the flow dynamics to be captured with a temporal resolution of 70 s. During water injection, the centre of the sample was continuously scanned (hereafter called dynamic water injection scans). No, or minimal, displacement dynamics were observed after 92.1 minutes of water injection, and hence water injection was terminated.

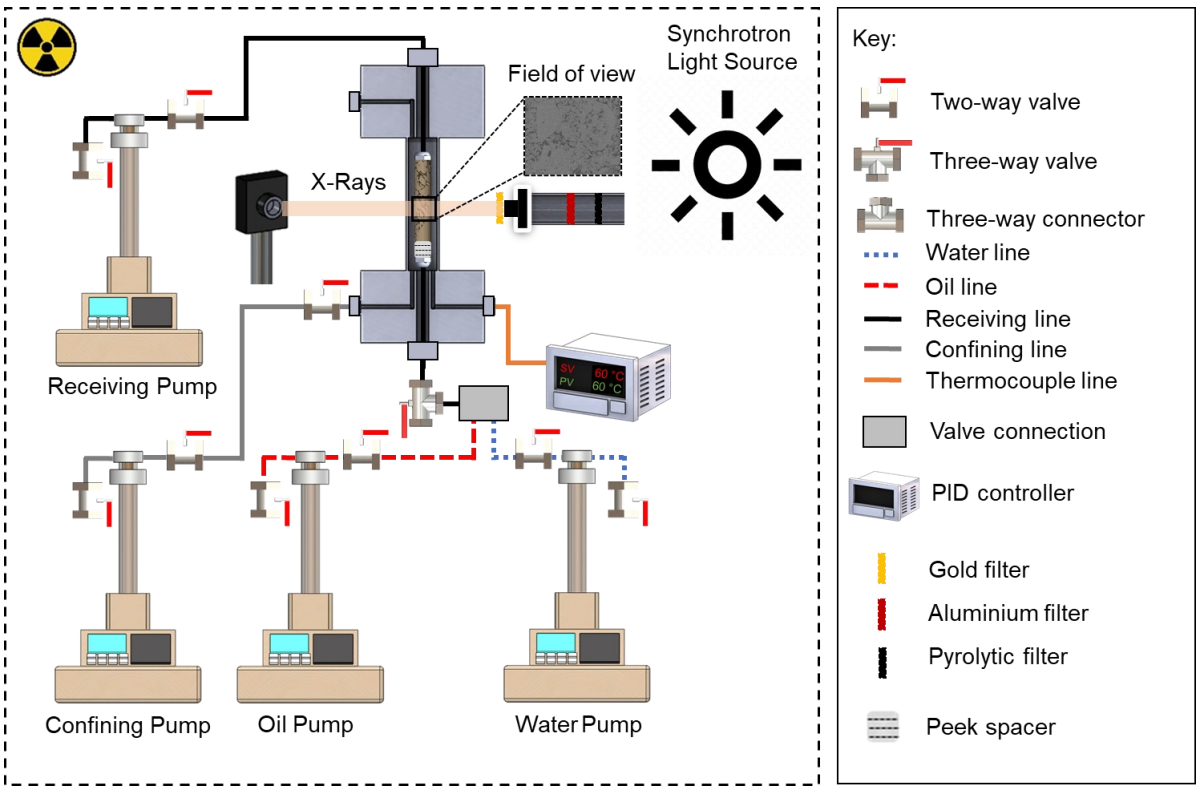

Figure 4. 1. The high pressure, high temperature flow apparatus used to conduct the water injection experiment. The apparatus consisted of four syringe pumps, a carbon fibre flow cell, flexible heating jacket connected to a PID controller, a PCO edge camera and a synchrotron light source.

The fast time-resolved synchrotron imaging was performed using a high photon flux pink beam with a peak photon energy of 15 keV. The X-rays were filtered by placing a 1.3 mm pyrolytic carbon filter, a 3.2 mm aluminium filter and a 10 µm gold filter in the beam line. In this section, (4.1), we will only analyze the dynamic images taken at the centre of the sample giving a $4.5\times4.5\times3.8$ mm^3 field of view with a pore volume (PV) of 0.02 mL as shown in Fig. 4.1. The imaged field of view covered the whole cross-sectional area of the sample. Imaging started when water was detected in the peek spacer. The size of the images was $1280\times1280\times1080$ voxels, with a voxel size of 3.5 µm. The high-quality oil scan

was acquired with a total of 2000 projections and 0.15 s exposure time. During water injection a total of 76 tomograms were acquired over a period of 92.1 minutes, with 700 projections and 0.065 s exposure time. The lower number of projections and exposure time allowed for the dynamic images to be acquired with a high temporal resolution (a complete tomogram was acquired every 70 s).

4.1.3.4 Image processing

The tomograms were then reconstructed to build three-dimensional pore-scale images of the rock and fluids within it. Fig. 4.2 shows 2D slices of the 3D pore-scale images taken after oil injection, Fig. 4.2a, and at the end of water injection, Fig. 4.2b. All images were segmented using the machine learning based trainable WEKA segmentation method [147, 171]. No filtering was applied to the images prior to segmentation as it can have an adverse effect on the quality of WEKA segmentation [13]. Two approaches were adopted to segment the reference oil scan and the water injection scans. In the case of the high-quality oil scan, the classifier was trained by manually selecting voxels that belong to the oil and rock phases, which was then applied to segment the whole image, see Fig. 4.2d.

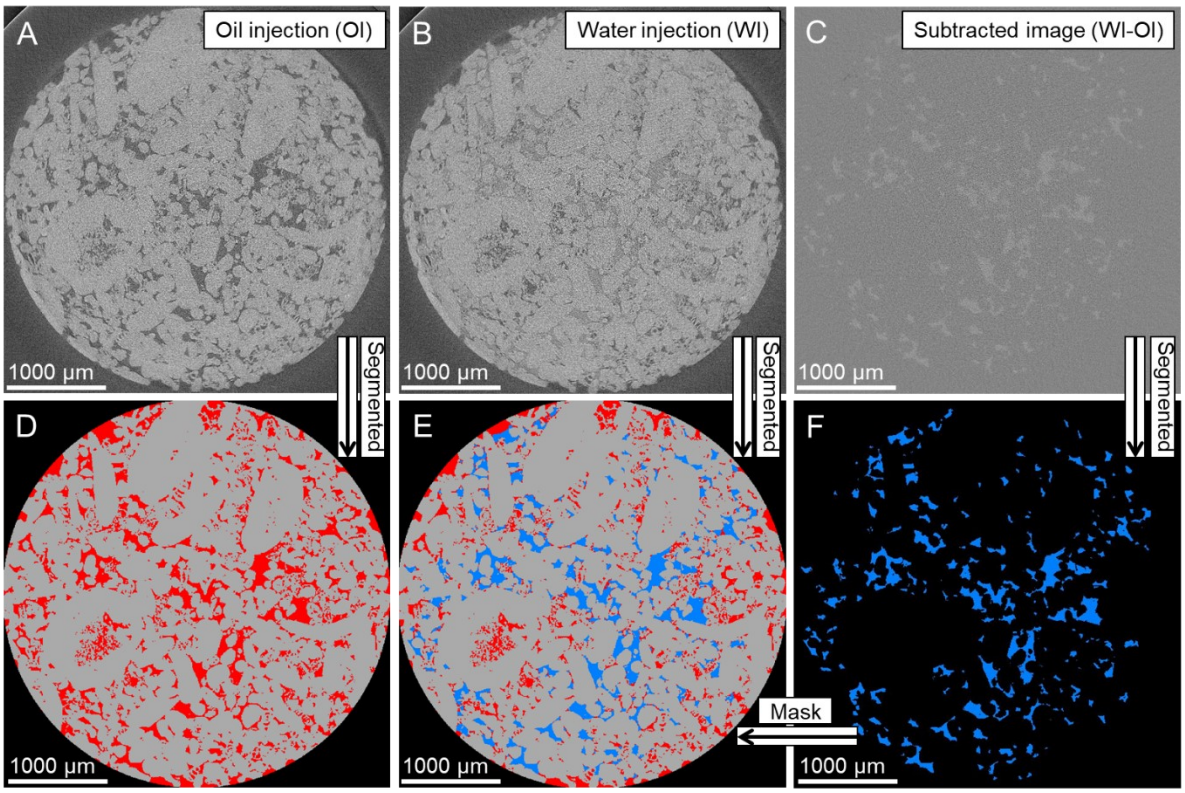

Figure 4. 2. Image segmentation workflow. The raw reference oil scan, 3.5 µm/voxel, in (A) was segmented directly using WEKA segmentation, see (D). To segment the water injection scan, 3.5 µm/voxel, in (B), it was first subtracted from the reference oil scan, in (A), to clearly distinguish the water phase, as shown in light grey in (C). The water phase in (C) was then segmented using WEKA, as shown in (F), and then masked on the segmented oil scan in (D) to give the final segmentation of the water injection scan, see (E). The mean and variance texture filters were used during WEKA segmentation.

The segmentation of the dynamic water injection scans was performed in four steps. (i) First, all the 76 time-series raw water injection images were registered to the raw oil reference scan. (ii) Each water injection scan containing three-phases (water, oil and rock) was then subtracted from the oil reference scan, which contains mainly two phases (oil and rock), creating a subtracted image where the water phase can be clearly distinguished, see Fig. 4.2c. (ii) Water was then segmented using WEKA by training the classifier to identify the voxels that belong to the water phase, see Fig. 4.2f. (iv) The segmented water phase was then masked on the segmented oil reference scan resulting in the final segmented water injection image, see Fig. 4.2e. A cylindrical mask was then applied on the segmented

images to remove the unwanted regions, e.g. the Viton sleeve. The fast-random algorithm was employed during all WEKA segmentations alongside the mean and variance texture filters**.**

4.1.3.5 Wettability characterization methods

Wettability can be inferred from the measured spatial distribution of contact angles between the fluids within the pore space, also known as the geometric contact angle (θ_g) [30, 31, 172-174], as demonstrated in sections 3.1, 3.2 and 3.3. While the geometric contact angle provides useful information on wettability on a pore-by-pore basis, its value is measured at rest and hence it does not necessarily represent the actual value encountered during displacement because of contact angle hysteresis [175]. Moreover, it has been shown that the use of spatially distributed geometric contact angle values were insufficient to reproduce the waterflooding behaviour in altered-wettability media [176].

Therefore, we also use an alternative approach to define the contact angle associated with the fluid displacement in our system, known as the thermodynamic contact angle, θ_t. θ_t is computed from an energy balance, and considers the changes in saturation and interfacial areas from two consecutive water injection images (time-steps) [32]:

$$\cos\theta_t = \frac{\kappa\phi\Delta S_w + \Delta a_{wo}}{\Delta a_{ws}} \tag{4.1}$$

where ΔS_w, Δa_{wo}, and Δa_{ws} are the differences, between two time-steps, in water saturation, and specific interfacial areas between water and oil, and water and solid measured on the macro-porosity. $\kappa = 2\kappa_m$ is the total curvature of the oil-water interface and ϕ is the imaged-based macro-porosity.

In our dynamic water injection images, we compute the thermodynamic contact angle between all the time-steps and compare its value to the distribution of geometric contact angle.

4.1.3.6 Pore-filling analysis

To quantitatively assess the order of pore-filling during water injection, we developed an in-house algorithm that detects the size of the filled elements as the water front progresses through the pore space. For each time-step, (i), the algorithm identifies the pores occupied by the advancing water front and measures the size of the throats connected to it, also known as available throats for invasion, using the maximal ball network extraction code [145, 146]. A throat is considered available whenever two pores connected to it are occupied by different phases (oil and water). Subsequently, the algorithm records the inscribed radius of the available throats, in (i), that become invaded by water in the next time-step (i+1). An available throat is considered invaded when both pores connected to it are filled with water and its centre is also occupied by water. Finally, the algorithm generates a plot showing the size of the invaded available throats at time-step (i+1) against the size of the available throats at time (i) to illustrate the order of filling during water injection. This approach is different from a conventional occupancy analysis that depicts the size of the invaded pores or throats at each time-step against the size of all the pores or throats in the rock. Here we only consider the throats available for invasion, which are adjacent to the advancing water front.

If the rock has become uniformly oil-wet (water-repellent), we expect water injection to be a drainage process. If displacement proceeds by invasion percolation then we expect at every time step the largest available throats to be filled [83].

4.1.3.7 Minkowski functionals

In addition to characterizing the *in situ* wettability and order of pore filling, the segmented pore-scale images can be used to compute the four Minkowski functionals, which are morphological measures that provide a complete geometrical characterization of the fluids within the pore space [177-179]. The zeroth order Minkowski functional (M_0), is the volume. In two-phase flow, this can be defined as the volume of each phase, which we obtained to calculate the saturation of the oil and water phases:

$$S = \frac{v}{\phi V} \tag{4.2}$$

where S is the fluid phase saturation defined here only in the macro-porosity, v is the volume of the fluid phase in the pore space, ϕ is the macro-porosity, and V is the image size (total volume).

Interfacial area is the first order Minkowski functional (M_1), from which we can define the specific interfacial area (a) between the fluids and the fluids and the solid (a has units of 1/length) [180]:

$$a = \frac{M_1}{V} \tag{4.3}$$

We computed the specific interfacial area between water and oil (a_{wo}), oil and solid (a_{os}), and water and solid (a_{ws}) from the segmented images.

The second order Minkowski functional (M_2) is the total curvature (the sum of the two principal curvatures) of the interface between two phases (κ) which can be related to the capillary pressure (P_c) through the interfacial tension (σ) using the Young-Laplace equation, (2.9) [19].

The third, and last, Minkowski functional (M_3) is the surface integral of the Gaussian curvature, or the product of the two principal curvatures ($\kappa_g = \kappa_1 \times \kappa_2$) [179]. The Gaussian curvature of the fluid-fluid interface can be used as a measure of the connectedness of the fluid phases in the pore space.

4.1.4 Results and Discussion

In this section, we will analyse the segmented images to investigate the pore-scale dynamics during water injection in the reservoir rock. First, in section 4.1.4.1, we compute the geometric and thermodynamic contact angles for each time-step to characterize the wettability of the rock; we suggest that the thermodynamic angles provide a better quantification of the wettability during displacement. In section 4.1.4.2, we examine the pore-filling events by qualitatively and quantitatively assessing: (i) the invasion patterns; (ii) Haines jumps; and (iii) snap-off events. We demonstrate that the water advance is an invasion percolation process. Finally, in section 4.1.4.3, for each water injection time-step, we quantify the Minkowski functionals describing: (i) fluid saturations; (ii) specific interfacial areas between the fluids and the fluids and rock; (iii) oil-water capillary pressure; and (iv) Gaussian curvatures. We compare the results with a previous study conducted on a Ketton sample [102].

4.1.4.1 Geometric and thermodynamic contact angles

The distribution of *in situ* geometric contact angles, θ_g, between oil and water was measured in a subvolume of size 1.75×1.75×1.75 mm^3, located in the centre of the field of view, during water injection using the automated method developed by AlRatrout et al. [30]. Fig. 4.3 shows the distribution of the geometric oil-water contact angles in our reservoir rock compared to that measured on Ketton limestone by Scanziani et al. [102]. The mean of the geometric contact angle distribution in the reservoir rock is 110° with a standard deviation of ± 20°. This indicates that the rock surfaces are predominately oil-wet, such that it prefers to be in contact with oil; water, the non-wetting phase, resides in the centres of the pores surrounded by oil wetting layers, see Figs. 4.4 and 4.5. Given the oil-wet nature of the rock, we

expect the displacement of oil by water to be drainage-like. Moreover, the wide range of pore sizes in the heterogenous reservoir sample, Fig. A4.1 in Appendix 4, suggests that the control on displacement is more likely to be governed by radius than contact angle, which is discussed further in section 4.1.4.2.1. The average geometric contact angle distribution in the reservoir rock is similar to that obtained on a Ketton limestone sample, 109 ± 19°, where the same wettability alteration protocol was employed [102], Fig. 4.3a. However, as we will show later, the displacement behaviour is very different. Furthermore, we observe that the mean geometric contact angle remains constant throughout the waterflooding experiment in the reservoir rock, see Fig. 4.3b.

Nevertheless, as mentioned earlier, the geometric contact angle is measured on a fixed oil-water interface. Many of the contacts between oil, water and the solid are pinned and have a hinging contact angle between the low, water-wet value when oil first entered the rock, and a higher value needed for water to advance across an altered wettability surface. Hence, the geometric values do not necessarily represent the oil-water contact angles encountered during displacement, with a tendency to underestimate the values [32, 175]. We therefore used Eq. (4.1) to calculate a thermodynamically consistent contact angle, θ_t, for each time-step. The calculated thermodynamic contact angles are shown in Fig. 4.3c: this represents the average oil-water contact angle for displacement consistent with the change in surface energy estimated from the images. Fig. 4.3c indicates that the thermodynamic contact angle in the reservoir rock has a stable trend during water injection, with an average value of approximately 135 ± 10°. A lower θ_t was observed early on in the displacement, 103 ± 10° and 105 ± 10°, indicating that, initially, water preferentially fills the less oil-wet pores, followed by the filling of increasingly oil-wet regions of the pore space. In the previous study on Ketton, the thermodynamic angle increased from 110° to 130°, shown in red in Fig. 4.3c, throughout the displacement; however, it was still lower than the thermodynamic angle for the reservoir rock [102]. Hence, we observe that the thermodynamic angle provides a better discrimination between the two cases than the geometric angle which displayed a similar distribution. Although the difference in wettability captured by the thermodynamic angle is relatively modest, combined with a more heterogenous pore-size distribution, it leads to a distinct displacement behaviour, as presented next.

Furthermore, a recent modelling study has shown that to match experiments of waterflooding in rocks with altered wettability, it is insufficient to use the geometric contact angle: instead, a larger contact angle should be used to account for contact angle hysteresis in the more oil-wet regions [176]. This implies that the thermodynamic contact angle better captures the displacement in a model.

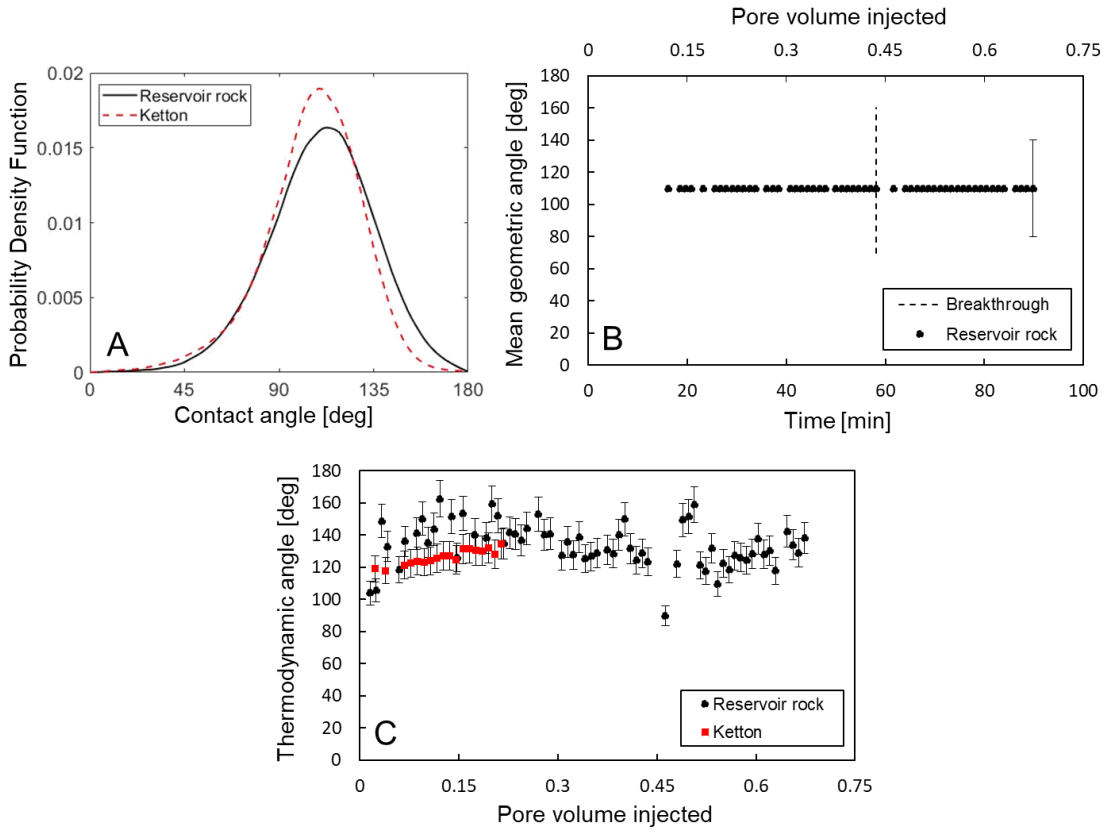

Figure 4. 3. (A) Normalized histograms of the measured *in situ* contact angles between oil-water in the reservoir sample (black) and in the Ketton limestone sample (red) at the end of waterflooding. (B) The mean of the calculated geometric contact angle distributions in the reservoir sample plotted as a function of time and pore volume injected. (C) The calculated average value of the thermodynamic contact angle, using Eq. (4.1), with pore volumes injected in the reservoir sample (black) and in the Ketton sample (red). Error bars in (B) show the standard deviation, while in (C) it indicates the uncertainty in the measurements. The geometric and thermodynamic contact angles measured on Ketton from Scanziani et al. [102].

4.1.4.2 Pore-filling events

The pore-scale dynamics of waterflooding were imaged for a total of 92.1 minutes, after which there was no significant change in the oil and water configurations in the pore space. Water breakthrough in the imaged field of view, which is 3.62 mm in length, occurred after 58.2 minutes, which corresponds to an injection of 0.45 PV of water. Fig. 4.4, show images of the advancing water phase acquired at different time-steps – each colour represents a different water cluster.

We observe that water advances as a connected front displacing the oil phase in the pore space which indicates that water injection in our oil-wet reservoir rock is a drainage process. Layer flow was inferred during displacement as oil, the wetting phase, was observed in the corners and roughness of the pore space, see Fig. A4.2 in Appendix 4, as well as in the pore centres. Furthermore, water invasion was accompanied by drainage dynamics associated with interface advancing and retraction, e.g., Haines jumps and Roof snap-off, see Fig. 4.4; this further confirms that drainage was the displacement process in the experiment. Drainage and its associated dynamics were previously imaged in water-wet systems [87, 100] but not in oil-wet systems. Fig. 4.4 shows that drainage dynamics continued even after breakthrough as water displaced more oil out of the pore space. This contrasts with the experiment on Ketton limestone where no displacement was observed after breakthrough [102].

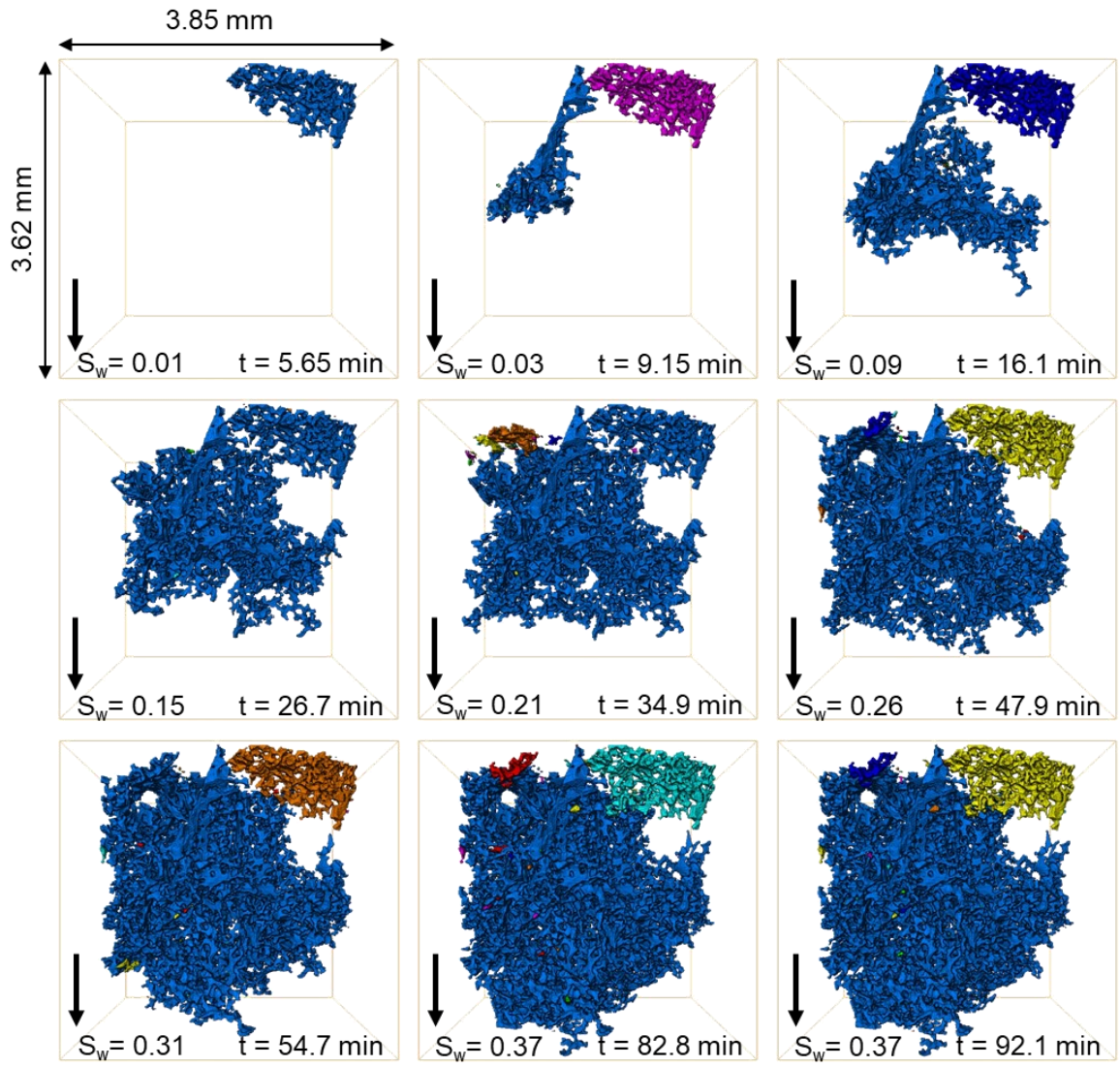

Figure 4. 4. Three-dimensional maps of the water phase connectivity during water injection shown at different time-steps. During invasion, water advanced as a connected front displacing oil in the pore space. This displacement was accompanied by apparent drainage dynamic events, including Haines jumps (t = 9.15 min) and Roof snap-off (t = 16.1, 47.9, 54.7, 82.8 and 92.1 min). The black arrow points towards the direction of flow.

4.1.4.2.1 Invasion percolation

The time-series segmented images were analysed to characterize the pore-filling order during water injection. First, we qualitatively assess the order of filling in a single pore occupied by oil and water, see Fig. 4.5. Fig. 4.5a illustrates that water resides in the centres of the pore space confining oil to wetting layers and small corners, which is a common characteristic of predominantly oil-wet media [72]. At time = 2.13 min, Fig. 4.5a, there are 5 available throats for water to pass through to progress to the next pores. These available throats are labelled from 1 to 5 in a decreasing order of size in Fig. 4.5c, where the oil phase was rendered transparent to make it possible to visualize the available throats. At time = 3.30 min, Figs 4.5b and 4.5d, we observe that water invaded the centres of the largest available throats (1, 2 and 3) to pass through, as they required the lowest absolute capillary entry pressures. We presume that as water pressure increases during water injection, water first had sufficient pressure to invade the largest throat (1), and then progressively filled the smaller throats (2 and 3). However, this happens on a much shorter time-scale than that required for a single scan, and hence was not captured

in the experiment. Overall, the throats were filled in order of size, with the largest filled first, which indicates that water injection in this rock is an invasion percolation process.

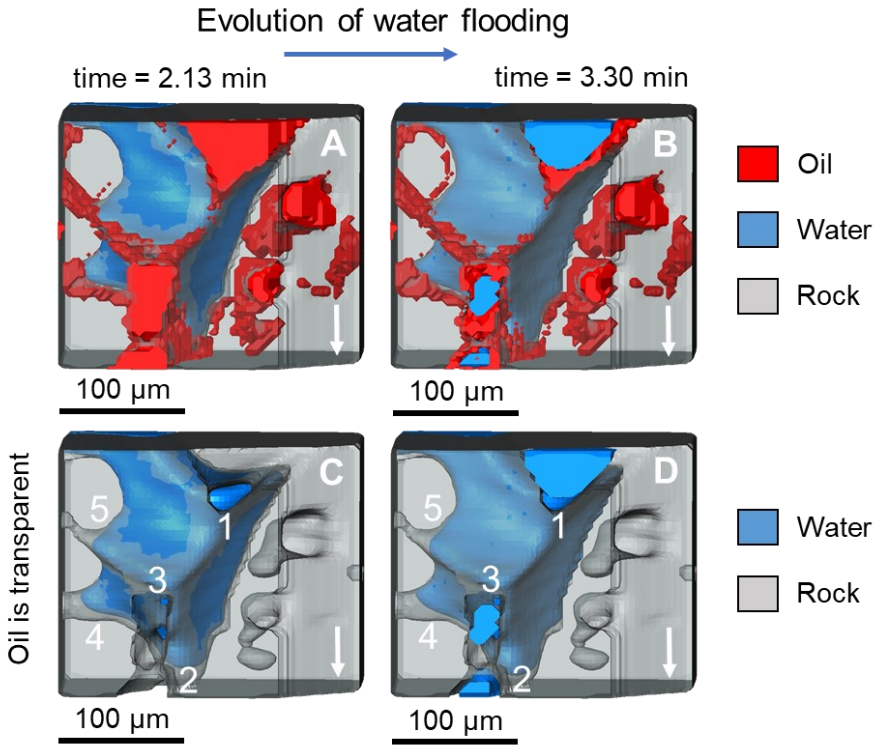

Figure 4. 5. Three-dimensional pore-scale images of a single pore (210×123×175 µm^3) showing the invasion pattern of water. (A) At time = 2.13 min, there are 5 throats connected to the pore that are available for subsequent water invasion. These throats are labelled from 1 to 5 in a decreasing order of size in (C), where oil was rendered transparent to make it possible to visualize the throats. (B) and (D) At time = 3.30 min, the largest throats 1, 2 and 3 get invaded by water which indicates that water injection in an oil-wet medium is an invasion percolation process. The white arrow points towards the direction of flow, while the blue arrow refers to the evolution of water invasion.

Using the pore-filling analysis described in section 4.1.3.6, the filling sequence was quantified in all the pores adjacent to the advancing water front in the dynamic images during water injection. For each time-step, the size of the invaded throats is plotted against all the available throats for invasion, see Fig. 4.6. Figs. 4.6a and 6b, show that the advancing water front invades the largest available throats at time-steps 2.13 min and 12.6 min respectively, which again confirms that water injection in oil-wet media is an invasion percolation process. This behaviour is further inferred from the cumulative result of all the 76 time-steps shown in Fig. 4.6c, indicating that water almost always invades the largest throats during displacement.

To show the significance of invasion percolation in our oil-wet rock, we generated a box plot for the invaded throats against the available throats for every 5 time-steps, see Fig. 4.6d. Fig. 4.6d shows that the portion of the available throats invaded by water always lies within the largest 5% of the available throats for invasion. This indicates that the displacement in our heterogenous oil-wet system is mainly size-controlled, as filling larger throats requires a lower absolute value of the oil-water capillary pressure, and that wettability has a little effect. This is attributed to the wide pore size distribution of the rock sample selected (Fig. A4.1 in Appendix 4). The impact of wettability on displacement is marked early on, where the less oil-wet pores were filled by water first, see Fig. 4.3. It is also unlikely that the later filling sequence is determined by a correlation between contact angle and throat radius, where the larger throats also have a smaller contact angle (favoring filling): previous work on a similar

reservoir rock has shown that there is weak tendency for larger pores and throats to be more oil-wet [70].

Wettability is expected to play a greater role in displacement in systems with a more uniform pore and throat size distributions. More specifically, it has been previously observed in the Ketton limestone sample with similar wettability conditions but a narrower pore size distribution, where both geometry and wettability controlled the displacement sequence and pores of all size were filled during water injection [102].

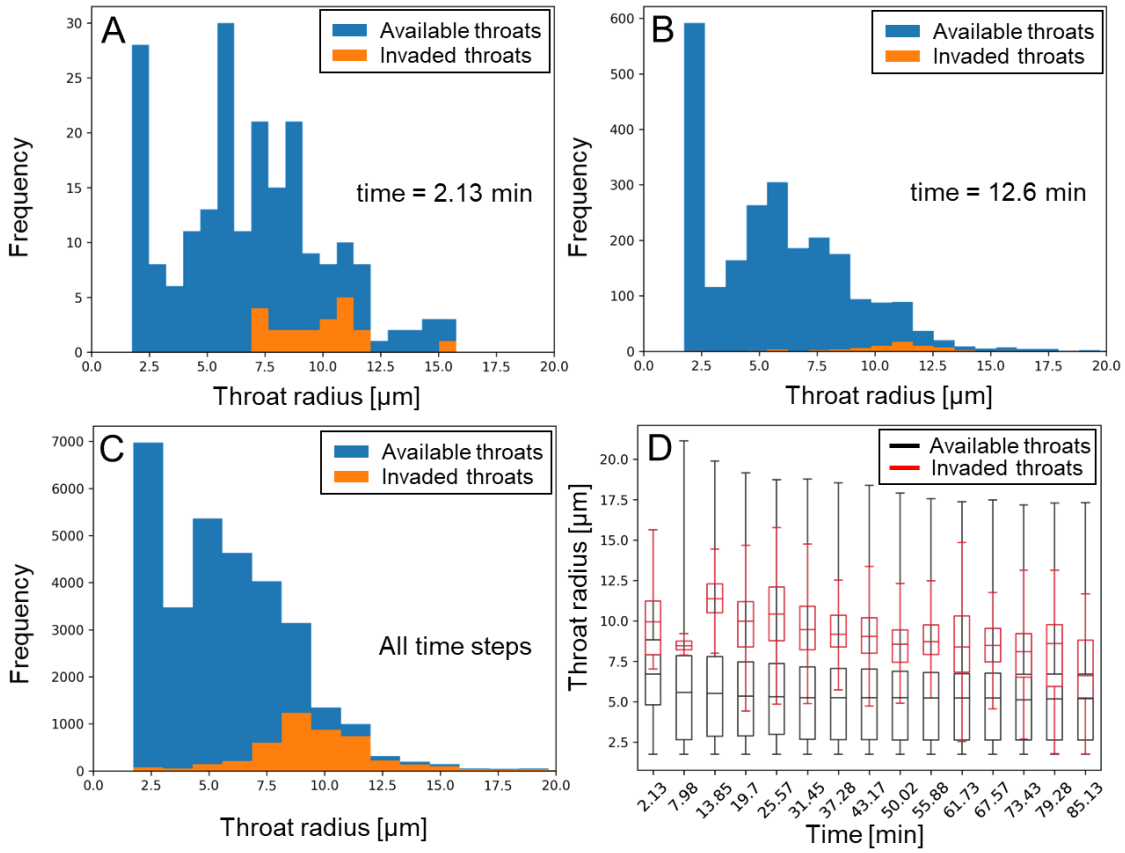

Figure 4. 6. Pore-filling analysis conducted by plotting the size of invaded throats against the size of all the available throats for water invasion. (A) and (B) The sizes of throats filled at time = 2.13 min and 12.6 min respectively. (C) A cumulative of the pore-filling analysis results at all the time-steps. (D) A box plot of the cumulative pore-filling results in (C) shown as a function of time.

4.1.4.2.2 Haines jumps

Haines jumps were observed on single and multiple pores level during water injection. Fig. 4.7 shows the rapid filling of multiple pores during a Haines jump, and quantifies the specific interfacial area of water before and after its retraction from the narrower regions. First, we notice a slow increase in the water saturation between time-steps 3.30 and 7.98 minutes, Figs. 4.7a and 4.7b respectively. However, as soon as the Haines jump occurs at time = 9.15 min, water rapidly fills multiple pores resulting in a large increase in the water saturation, see Fig. 4.7c. The movement of the advancing water interface during a Haines jump is very rapid and cannot be captured with the temporal resolution of this experiment (70 s); micromodel studies have shown that the pores drain on a millisecond timescale [181].

Furthermore, we observe a re-arrangement of the water phase in the pore space associated with the Haines jump, where water retracts from the high-pressure regions (throats) and flows towards regions of lower water pressure to supply the rapid filling. This is shown in Fig. 4.7d, where water has a lower specific interfacial area of 1.89 mm^{-1} at time = 9.15 min after the Haines jump compared to time = 7.98

min, where water had a specific interfacial area of 1.94 mm^{-1}. We noticed that water, shown in blue, has retracted from the throats, shown in orange, in the region marked with a dashed line. The effect of multiple pore filling during Haines jumps is more marked early in the waterflooding experiment, when most pores are occupied by oil only.

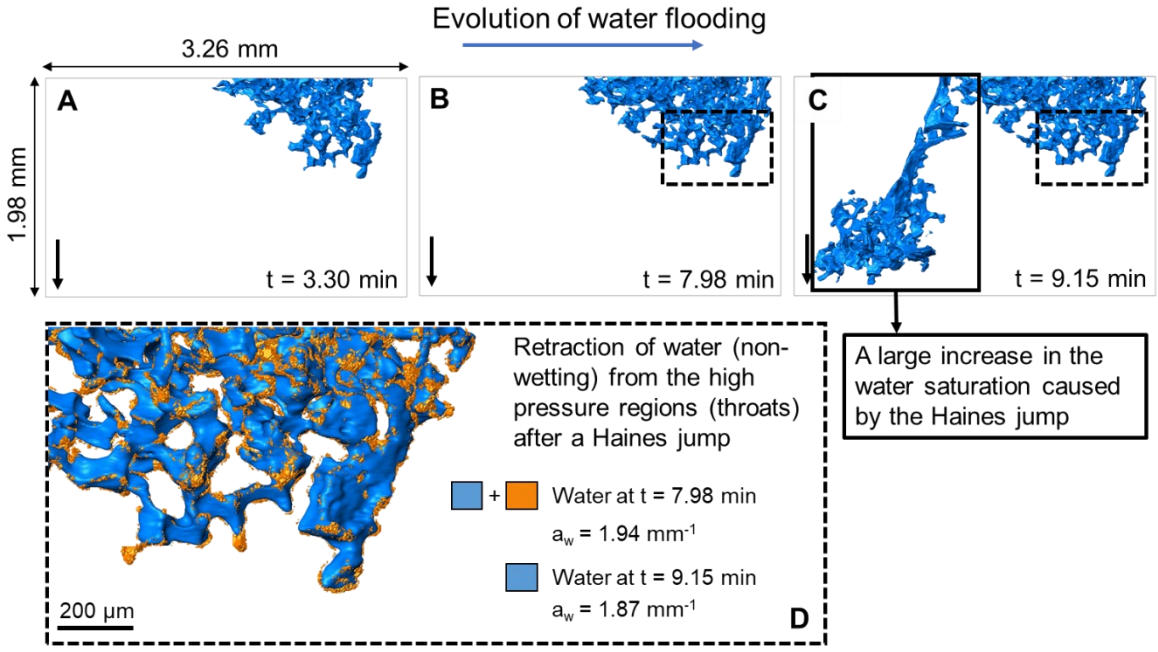

Figure 4. 7. Three-dimensional images of the water phase at different time-steps illustrating the rapid filling of multiple pores during a Haines jump. (A) and (B) show a slow increase in the water saturation, which was followed by a large increase in the water saturation caused by the Haines jump in (C). (D) The specific interfacial area of water is lower in the high-pressure region, marked by the dashed line, after the Haines jump due to water retraction. The black arrow points towards the direction of flow, while the blue arrow refers to the evolution of water invasion.

4.1.4.2.3 Local and distal snap-off

We observed the two types of snap-off, local and distal, during the waterflooding experiment, see Fig. 4.8. Distal snap-off occurs due to the retraction of water, the non-wetting phase, from the narrower regions of the pore space during a Haines jump, Fig. 4.7, some distance away from the jump itself. The retraction of water is an imbibition process, which can result in snap-off and disconnection of the water phase as shown in Fig. 4.8a. Next, we measured the capillary pressure in the system using the curvature-based method described in section 3.1.3.2.5.2. The measurements show a lower absolute value of the local capillary pressure for the disconnected water ganglion (-2.41 kPa) compared to the connected water cluster (-3.26 kPa); this indicates that the trapped water ganglion reaches a new state of capillary equilibrium in the pore space. Furthermore, as water invasion proceeds, its local capillary pressure decreases (higher water pressure) allowing it to re-access the throat where snap-off occurred, and hence it will reconnect with the stranded ganglion as shown in Fig. 4.8b.

Local snap-off occurs in the newly filled pores by the invading water front as shown in Fig. 4.8b. As water passes through a narrow throat into the adjoining pore, the local capillary pressure will suddenly change allowing the oil wetting layers in the throat to swell. If the capillary pressure reaches the threshold for snap-off, the throat will spontaneously fill with oil, trapping water as a disconnected ganglion in the centre of the pore [182]. Again, the snapped-off ganglion attains a new position of equilibrium with a lower absolute value of capillary pressure (-3.12 kPa) compared to the connected water phase (-3.36 kPa). As water progresses through the pore space, the trapped ganglion is

reconnected, see Fig. 4.8c. These snap-off events have been previously observed using fast synchrotron studies in water-wet media during oil invasion but not in oil-wet media [87, 88].

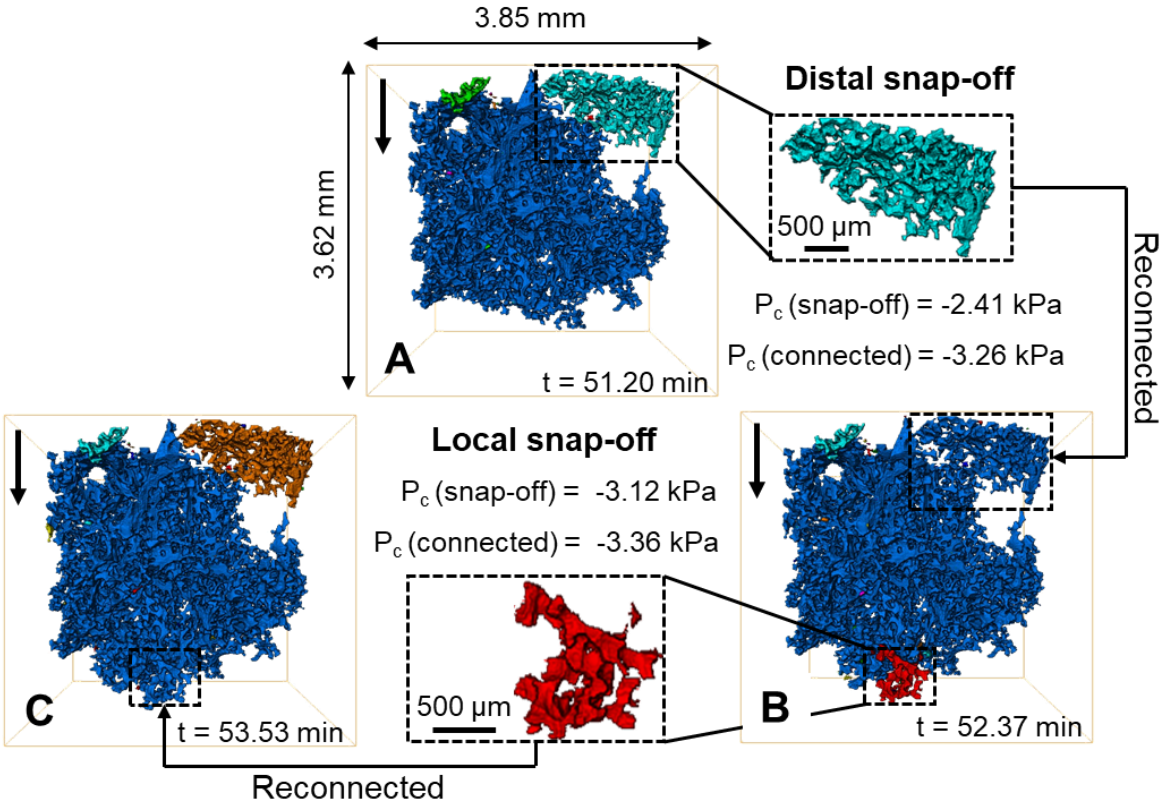

Figure 4. 8. Three-dimensional images illustrating the occurrence of local and distal snap-off during water injection. Only the water phase is shown – each colour represents a disconnected water phase cluster. The black arrow points towards the direction of flow.

4.1.4.3 Saturation, interfacial area, and capillary pressure

The saturation of oil and water in the macro pores was computed using Eq. (4.2) on the segmented water injection images, see Fig. 4.9a. Fig. 4.9a in shows that the water saturation linearly increased with time even after the observed breakthrough in the imaged field of view (58.2 minutes). A noticeable increase in the water saturation was recorded at 9.15 minutes, corresponding to the rapid filling of multiple pores caused by the Haines jump event shown in Fig. 4.7. The water and oil saturations stabilise to 38 ± 2% and 62 ± 2% respectively after 78.1 minutes, which corresponds to an injection of 0.58 PV of water: further injection of water does not displace oil out of the pore space. The low oil recovery factor seen is attributed to water invading the centres of the pores, leaving oil connected in thick wetting layers in the corners and crevices of the pore space. This behaviour was observed in previous waterflooding static experiments conducted on the same rock type in sections 3.2 and 3.3.

The oil-water and water-rock interfaces were extracted and smoothed [140], to measure their specific interfacial areas, Eq. (4.3). Fig. 4.9b shows that the water-rock and oil-water specific interfacial areas increase with time during water injection.

Furthermore, the interfacial curvature of the extracted oil-water interface was measured and substituted in Eq. (2.9) alongside the interfacial tension, 52.1 mN/m, Table 4.1, to characterize the capillary pressure of the system, see Fig. 4.9c. A strongly negative capillary pressure, -3.5 kPa, indicates that the macro pores are indeed oil-wet such that on average water bulges into oil with a higher pressure. This capillary pressure is higher than the value of -2.4 kPa measured for a Ketton sample which, as previously

discussed, displayed more mixed-wet behaviour [102]. The dashed square in Fig. 4.9c at 9.15 minutes shows the sudden change in the local capillary pressure that caused the Haines jump in Fig. 4.7.

The Gaussian curvature of the oil-water interface was computed and plotted as a function of time and pore volumes of water injected in Fig. 4.9d. While the sum of the curvatures is negative, in most cases one curvature is negative and the other positive, giving a negative Gaussian curvature. This indicates that the phases are well-connected in the pore space, implying that oil and water flow simultaneously, albeit oil flow is slow since it is confined to movement in wetting layers. Furthermore, we plotted, at three time-steps (9.15, 58.2, and 92.1 min), the two principal curvatures (κ_1 and κ_2, where we define $\kappa_1 > \kappa_2$), see Fig. 4.10. We observe that although the two curvatures have similar distributions, the negative curvature (κ_2) is more shifted to the left which results in the negative mean curvature, represented by the capillary pressure in Fig. 4.9c, and the negative Gaussian curvature shown in Fig. 4.9d. Forming negative and positive principal curvatures is a necessary condition for the oil and water phases to remain continuous in the pore space, implying a structure with many redundant loops.

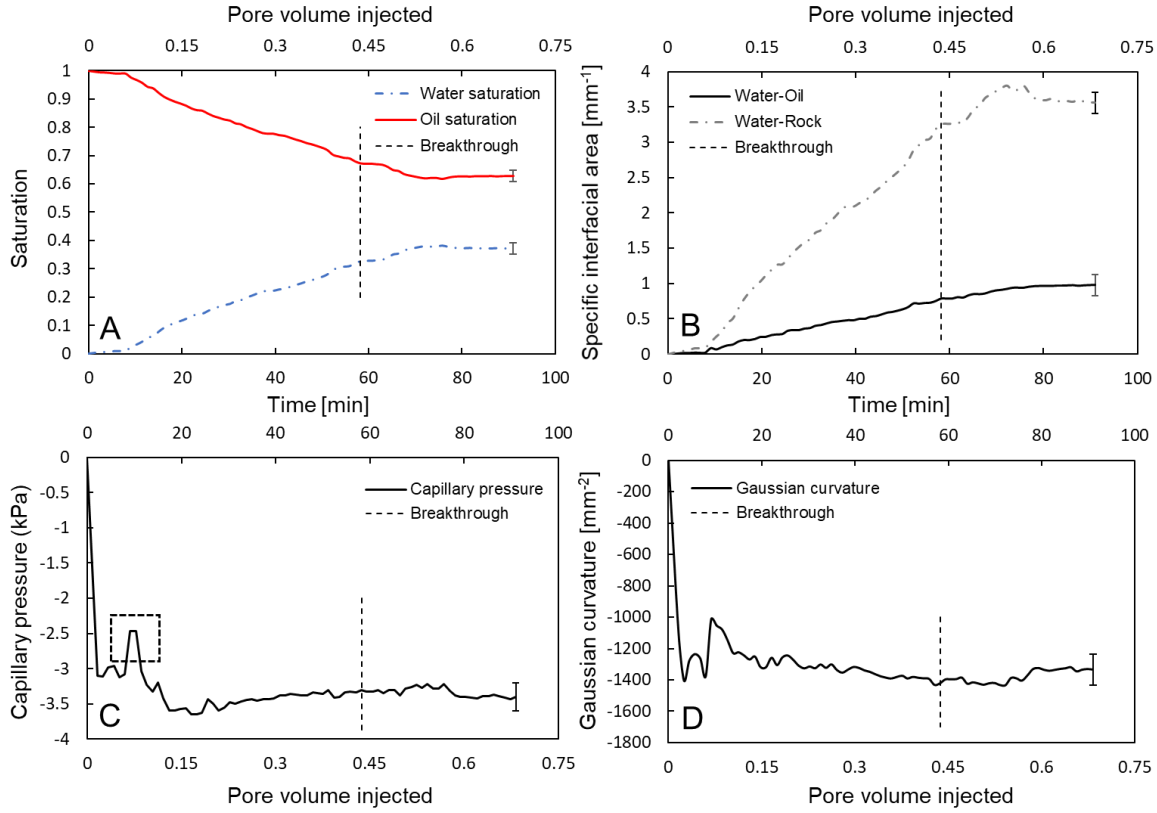

Figure 4. 9. Minkowski functionals. (A) Oil and water saturation profiles as a function of time and pore volume injected. (B) Change in specific interfacial areas of oil and water, and water and rock interfaces with time and pore volume injected. (C) Oil-water capillary pressure plotted as a function of time and pore volume injected. (D) Change in Gaussian curvature of the oil and water interface with time and pore volume injected. The dashed line represents the time of water breakthrough in the imaged field of view. The dashed square, in (C), shows a sudden change in the local capillary pressure which corresponds to the filling of multiple pores during a Haines jump, illustrated in Fig. 4.7. Error bars indicate the uncertainty in the measurements.

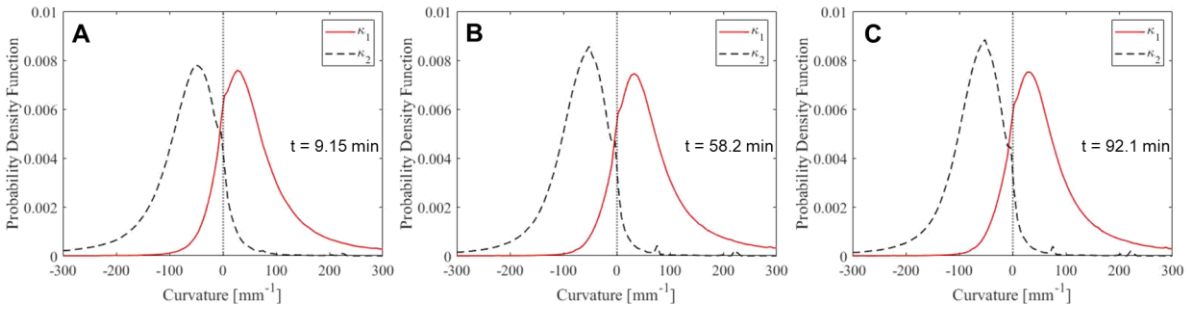

Figure 4. 10. Normalized histograms of the two principal curvatures, κ_1 and κ_2, of the oil-water interface at three time-steps, (A) t = 9.15 min, (B) t = 58.2 min and (C) t = 92.1 min. κ_1 is defined to be the larger curvature.

4.1.5 Final Remarks and Suggestions

This work provides pore-scale insights into the dynamics of two-phase fluid flow during water injection in an oil-wet reservoir rock. We have used fast synchrotron X-ray micro-tomography to visualize the displacement of oil by water, and investigate the pore-scale dynamics by examining: (i) *in situ* wettability and displacement contact angles; (ii) pore-filling order; (iii) Haines jumps; (iv) snap-off events; (v) fluid saturations; (vi) specific interfacial areas; (vii) oil-water capillary pressure; and (vii) Gaussian curvature.

We observe that the displacement of oil by water is a drainage-like process. Measurements of local contact angle, and the estimation of a value based on energy balance during the displacement, confirmed that the medium was oil-wet (water-repellent). Hence, the order of pore-filling followed an invasion percolation pattern, where throats filled in order of size, with the largest filled first. This is akin to drainage processes in water-wet systems. Water, the non-wetting phase, advances as a connected front displacing oil in the centres of the pore space; oil is confined to movement in wetting layers.

We observed drainage associated dynamics, e.g. Haines jumps and snap-off, before and after water breakthrough in the imaged rock section. Haines jumps were observed in single and multiple pores, alongside the re-arrangement of the non-wetting phase, water, to supply this rapid filling; water retracts from the high-pressure regions (throats) and flows towards regions of low water pressure. Furthermore, the two types of snap-off in drainage processes, local and distal snap-off, were also observed. In both snap-off events, the trapped (disconnected) water ganglion reaches a new position of capillary equilibrium in the pore space; the water ganglion has a lower absolute capillary pressure than that of the connected water cluster.

The water saturation stabilized to 38 ± 2% after the injection of only 0.58 pore volumes of water; further injection of water did not produce more oil. This was ascribed to the existence of oil in thick connected wetting layers in the corners of the pore space, where the access of water is limited. The oil-wet nature of the surface results in a negative capillary pressure; the Gaussian curvature is also negative which leads to well-connected oil and water phases in the pore space.

Overall, we have elucidated the invasion patterns and pore-filling events during water injection in a reservoir rock which manifests an oil-wet behaviour. The same methods and analysis can be used to characterise signature of two-phase flow dynamics and help design carbon storage, subsurface contaminant transport, fuel cells, batteries and chemical reactors for instance, as well as providing benchmark data for the validation and calibration of pore-scale models.

In the next section, (4.2), we will investigate the three-phase invasion dynamics when gas is introduced into the system after the water injection dynamics ended.

4.2 Three-phase flow displacement dynamics and Haines jumps in a hydrophobic porous medium

4.2.1 Summary

This section describes the three-phase extension of the two-phase dynamic imaging study presented in the previous section. We use synchrotron X-ray microtomography to investigate the displacement dynamics during three-phase—oil, water, and gas—flow in a hydrophobic porous medium. We observe a distinct gas invasion pattern, where gas progresses through the pore space in the form of disconnected clusters mediated by double and multiple displacement events. Gas advances in a process we name three-phase Haines jumps, during which gas re-arranges its configuration in the pore space, retracting from some regions to enable the rapid filling of multiple pores. The gas retraction leads to a permanent disconnection of gas ganglia, which do not reconnect as gas injection proceeds. We observe, *in situ*, the direct displacement of oil and water by gas as well as gas–oil–water double displacement. The use of local *in situ* measurements and an energy balance approach to determine fluid–fluid contact angles alongside the quantification of capillary pressures and pore occupancy indicate that the wettability order is oil–gas–water from most to least wetting. Furthermore, quantifying the evolution of Minkowski functionals implied well-connected oil and water, while the gas connectivity decreased as gas was broken up into discrete clusters during injection. This work can be used to design CO_2 storage, improved oil recovery and microfluidic devices.

4.2.2 Investigations

In the previous section, (4.1), we examined the dynamics during water injection in a strongly oil-wet system. Here, in *EXP* 5, we look at the pore-scale invasion patterns when gas is introduced into the system after water. In this section, we analyze not only the section of the rock where the dynamics were captured but also the whole sample. The motivation for this study is provided in section 2.2.3.2.

First, we characterize the fluid-fluid contact angles and pore occupancy to confirm the hydrophobic nature of the rock surfaces and infer the wettability order of the system. Then, we use fast imaging to examine, *in situ*, during gas injection, the evolution of: (i) gas connectivity; (ii) direct, double and multiple displacement events; (iii) water connectivity and trapping; and (iv) spreading layers. Finally, we quantify the change in Minkowski functionals – fluid saturations, interfacial areas and curvatures – with time to provide a complete description of the fluid topology in the pore space, i.e., fluid-fluid connectivity and trapping.

We observe that gas, the intermediate-wet phase, progresses through the pore space in the form of disconnected clusters. This behaviour is attributed to the pore-scale events, made possible by double and multiple displacements, that govern the gas movement in the porous medium, which we name three-phase Haines jumps. As gas displaces either oil or water, it rapidly progresses to fill several pores, which causes it to retract from regions further away to enable this fast filling. This retraction leads to a permanent disconnection of gas ganglia, which fail to get reconnected as gas injection proceeds. The disconnected gas ganglia reach a new position of capillary equilibrium in the pore space and can only be displaced through double or multiple displacement events.

The significant new observation is that gas is able to progress through the pore space, under capillary-dominated flow conditions, as disconnected ganglia. This is a process unique to three-phase flow and

distinct from ganglion dynamics in two-phase flow [183], where a disconnected phase can advect through the pore space when viscous forces are significant.

4.2.3 Materials and Methods

4.2.3.1 Rock and fluid properties

The experiment was performed on the same oil-wet reservoir sample that was described in section 4.1.3. Moreover, the methods and apparatus used are the same to those applied in section, (4.1.3), during waterflooding in the same sample. However, nitrogen was introduced to the system as the gas phase which required an additional pump as shown in Fig. 4.11. The thermophysical properties of the three fluid phases are listed in Table 4.2.

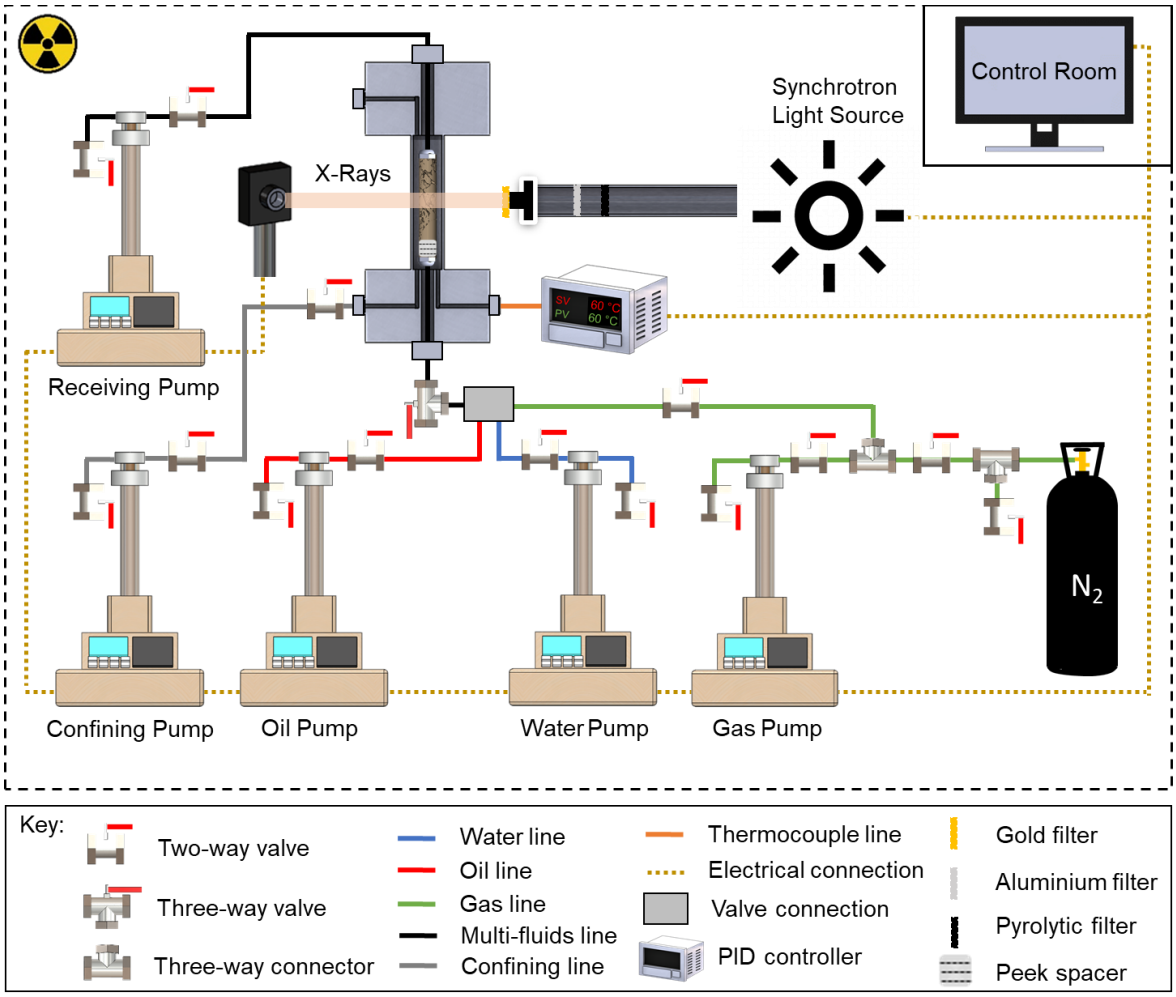

Figure 4. 11. The flooding and imaging apparatus used to conduct the three-phase flow experiment in the oil-wet reservoir rock at 8 MPa and 60 ºC. The rock was inserted in a flow cell placed in front of the synchrotron light source to image the movement of water, oil and gas in the pore space. The three fluid phases were injected at a very low flow rate using syringe pumps to capture the pore-scale displacement dynamics.

The interfacial tensions between the fluids, water (80 wt% H_2O + 20 wt% KI), oil (85 wt% $C_{10}H_{22}$ + 15 wt% $C_{10}H_{21}I$) and nitrogen were measured at the experimental conditions, 8 MPa and 60 ºC, using the pendant drop method. The apparatus for conducting the interfacial tension measurements is described elsewhere [128]. Using the values in Table 4.2, the spreading coefficients of the three fluid phases were calculated to be C_{sw} = -104.6 mN/m, C_{so} = +0.4 mN/m and C_{sg} = -22.8 mN/m. This indicates that it is only possible for oil to form spreading layers in the pore space since its spreading coefficient is close

to zero; water and gas do not spread in layers. Gas indeed did not form layers in these experiments, unlike in the near-miscible system in section 3.2 where the spreading coefficient is closer to zero and gas layers can be seen.

Table 4. 2. Densities, viscosities, interfacial tensions and spreading coefficients of the three fluid phases used in the three-phase flow experiment conducted at 8 MPa and 60 ºC. The spreading coefficient of each phase, *i*, was calculated using $C_{si} = \sigma_{jk} - \sigma_{ij} - \sigma_{ik}$, where σ is the interfacial tension and subscripts *i*, *j* and *k* denote the three fluid phases. The interfacial tensions were measured using the pendant drop method at the experimental conditions (8 MPa and 60 ºC) [128]. Densities were measured at 40 ºC and 7.6 MPa. The viscosity of *n*-decane is provided at ambient conditions [130], and of water and nitrogen at 50 ºC and 10 MPa [25].

Fluid	Composition (%wt)	ρ (kg·m^{-3})	μ (mPa·s)	σ (mN· m^{-1})	C_s (mN· m^{-1})
Water	0.80 H_20 + 0.20 KI	1154.1	0.547	σ_{gw} = 63.7	-104.6
Oil	0.85 $C_{10}H_{22}$ + 0.15 $C_{10}H_{21}I$	715.2	1.088	σ_{ow} = 52.1	+0.4
Gas	N_2	83.9	0.018	σ_{go} = 11.2	-22.8

4.2.3.2 Flow experiment

For completeness we will describe the full flow experiment including both water and gas injection, despite the waterflooding being described earlier in section 4.1.3.

A series of fluid injections: (i) oil injection [OI]; (ii) waterflooding [WF] and (iii) gas injection [GI], were performed in the aged reservoir rock, during which the pore space was continuously imaged to capture the dynamics of displacement. All injections were performed from the bottom of the sample under capillary dominated conditions, see Table 4.3. Fig. 4.12 shows two-dimensional raw pore-scale images of a cross-section of the rock acquired after each injection step.

First, 20 pore volumes of oil (doped *n*-decane) were injected into the sample at a flow rate of 0.1 mL/min to replace all the crude oil used to alter the wettability of the sample, see Fig. 4.12a. The temperature and pressure of the system were then raised to the experimental conditions (60 °C and 8 MPa), and a confining pressure of 10 MPa was applied. Water injection (WF) was then started at a very low flow rate, 0.15 µL/min, corresponding to a capillary number $Ca_{[wo]}$ of 2.09×10^{-9} defined by $Ca = \mu q/\sigma$, where σ is the interfacial tension, μ is the viscosity of the displacing fluid and q is the Darcy velocity (Table 1). Water was injected over a period of 92.1 minutes which corresponded to the injection of 0.69 PV of water, see Fig. 4.12b. Gas injection (GI) was then performed at the same flow rate for 32.2 minutes, corresponding to the injection of 0.24 PV of gas, with a gas-water $Ca_{[gw]} = 6.39\times10^{-11}$ and gas-oil $Ca_{[go]} = 3.64\times10^{-10}$. Waterflooding and gas injection were stopped when no significant change in the fluid configurations in the pore space had been observed for at least 15 minutes.

Table 4. 3. Details of the fluid injections performed during the three-phase flow experiment at 8 MPa and 60 ºC. Pore volumes (PV) injected correspond to the total porosity of the rock sample. WF and GI were stopped when no significant change in the fluid configurations in the pore space had been observed for at least 15 minutes. Capillary numbers were calculated using $Ca = \mu q/\sigma$, where σ is the interfacial tension, μ is the viscosity of the injected fluid and q is the Darcy velocity. Subscripts w, g and o stand for water, gas and oil phases respectively. σ and μ are shown in Table 4.2, while q is calculated by dividing the flow rate by the cross-sectional area of the sample (11.34 mm^2).

Injection Step	Flow rate (mL/min)	PV	Total Time (mins)	Capillary number
Oil injection (OI)	0.1	20.0	8.32	-
Waterflooding (WF)	0.00015	0.69	92.1	$Ca_{[wo]} = 2.09\times10^{-9}$
Gas injection (GI)	0.00015	0.24	32.2	$Ca_{[go]} = 3.64\times10^{-10}$ $Ca_{[gw]} = 6.39\times10^{-11}$

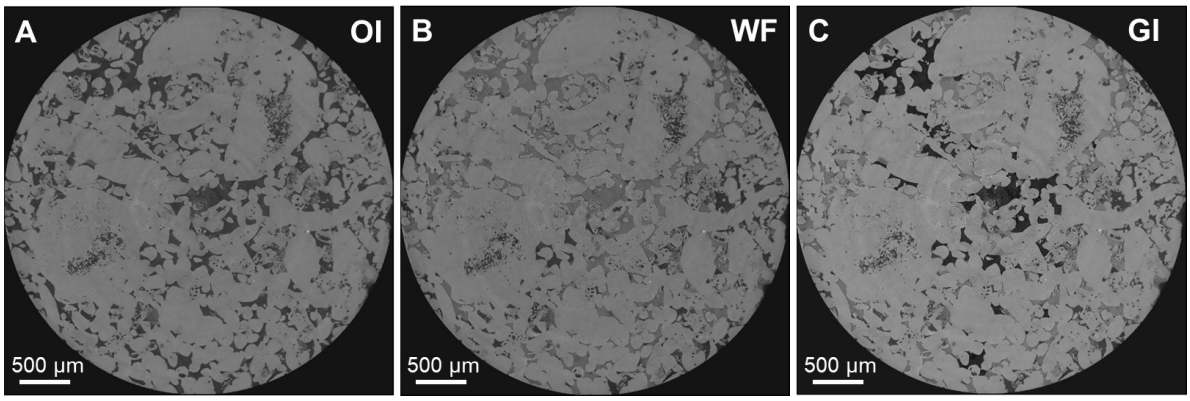

Figure 4. 12. Raw two-dimensional pore-scale images of a cross-section of the rock acquired after: (a) oil injection [OI]; (b) waterflooding [WF]; and (c) gas injection [GI], with a voxel size of 3.5 µm. In (a), rock is the light phase and oil is the dark phase. In (b) and (c), the order from darkest to brightest phase is oil-water-rock and gas-oil-water-rock respectively.

4.2.3.3 Synchrotron X-ray imaging

Static and dynamic scans were collected during the experiment with a voxel size of 3.5 µm. The dynamic scans were acquired during the injection of fluids, whereas static scans were acquired at the end of each injection. Dynamic imaging was performed at the middle of the sample, in the vertical direction, while static imaging of the whole sample was performed. The location of the dynamic scans relative to the static scans is shown in Fig. 4.13. The centre of the sample was selected for dynamic imaging since it does not contain large vugs and mineral grains. The macro-porosity is 16% in the static scans and 12% in the dynamic scans.

The dynamic images were 1280×1280×1080 voxels in size. During dynamic imaging of water injection, a total of 76 tomograms were acquired, every 70 s, with 700 projections and 0.065 s exposure time. On the other hand, 25 tomograms were acquired, every 74 s, during gas injection with 750 projections and 0.07 s exposure time. The high spatial and temporal resolution of synchrotron imaging allowed for the pore-scale displacement dynamics to be captured during water and gas injection. The static scans of the whole sample were acquired after each injection, see Fig. A5.1 in Appendix 5, with 2000 projections and 0.15 s exposure time.

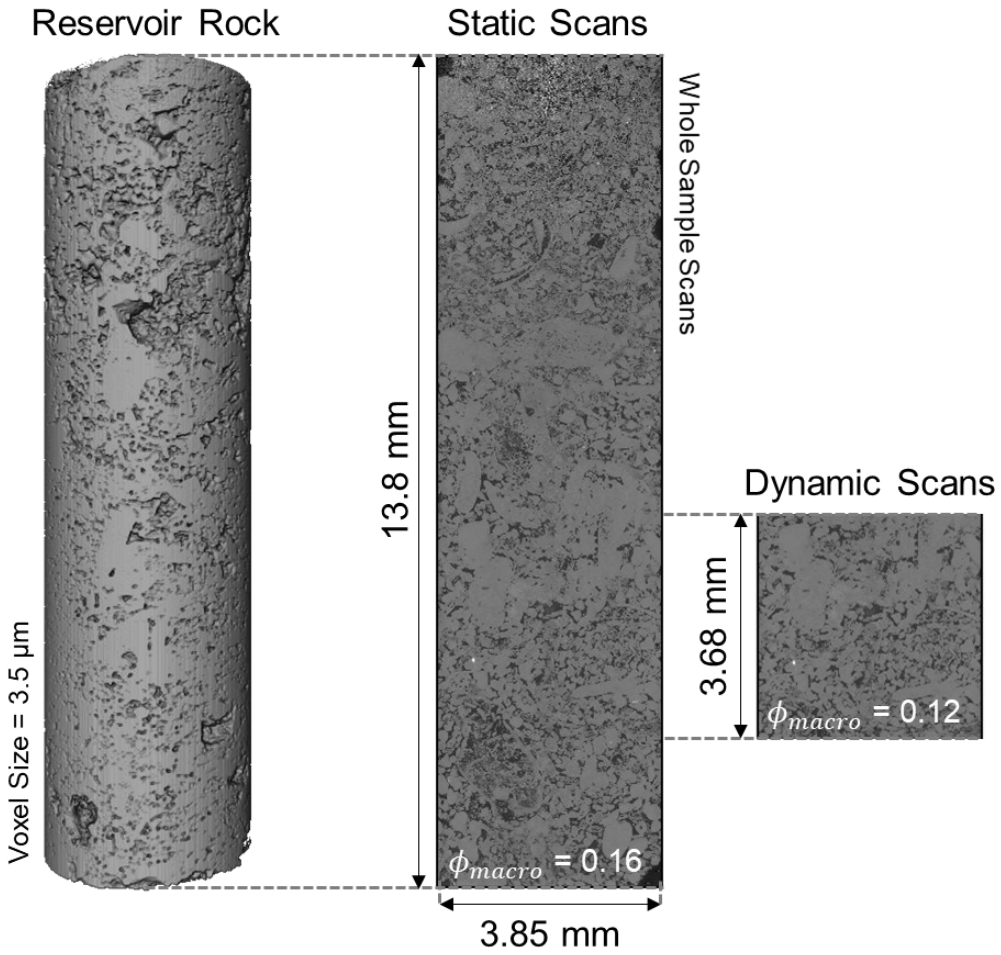

Figure 4. 13. Three-dimensional images showing the location of the dynamic scans (1280×1280×1080 voxels) relative to the static scans of the whole sample (1280×1280×3940 voxels). The spatial resolution of the images is 3.5 µm. The macro-porosities (ϕ_{macro}) of the static and dynamic scans are 16% and 12% respectively.

4.2.3.4 Image segmentation

The large static images were segmented using the seeded watershed algorithm [131], while the dynamic images were segmented using machine learning-based WEKA segmentation [147, 171] similar to the two-phase study, section 4.1.

Segmentation of the static images was performed in three steps. (i) The images acquired after OI, WF and GI were filtered using non-local means filter [184]. (ii) The filtered WF and GI images were then subtracted from the filtered OI image to clearly distinguish the water and gas phases in these images. (iii) The subtracted images were then filtered again with the non-local means filter and segmented using watershed algorithm. The same procedure was followed to segment the dynamic WF and GI images; however, WEKA was used instead of watershed since it provides a more accurate characterization of flow properties near fluid-fluid contacts [13]. During WEKA segmentation the fast-random algorithm was selected alongside the mean and variance texture filters. WEKA segmentation is shown in Fig. A5.2 in Appendix 5. WEKA is very CPU intensive, which explains why it was not applied to segment the large static images.

4.2.3.5 Wettability characterization methods

Just like we did in the two-phase study in section 4.1.3.5, we measure both geometric and thermodynamic contact angles on the dynamic gas injection images.

We use an energy balance approach to calculate fluid-fluid displacement contact angles, also known as three-phase thermodynamic contact angles (θ_t), between oil-water, gas-water, and gas-oil [18]. Thermodynamic contact angles have been proven to provide better estimates of displacement angles in two-phase flow compared to geometric values as shown in section 4.1. Assuming no change in Helmholtz free energy between two local states of equilibrium and ignoring viscous dissipation, the three-phase thermodynamic contact angles can be calculated using [185]:

$$\begin{aligned}&\left(\Delta a_{ws}\cos\theta_{t[ow]} - \Delta a_{ow} - \phi\kappa_{ow}\Delta S_w\right)\sigma_{ow}\\ &= \left(\Delta a_{gs}\cos\theta_{t[go]} + \Delta a_{go} - \phi\kappa_{go}\Delta S_g\right)\sigma_{go} + \Delta a_{gw}\sigma_{gw}\end{aligned} \tag{4.4}$$

where a is the interfacial area per unit volume, θ_t is the thermodynamic contact angle, ϕ is the dynamic image-based macro-porosity, S is the saturation (the fraction of the macro pore space occupied by each phase) and κ is the total curvature of the fluid-fluid interface. Subscripts s, w, g and o denote the solid, water, gas and oil phases respectively, while Δ is the change between two-consecutive time-steps.

The interfacial areas, curvatures and saturations were measured on the 25 dynamic pore-scale images obtained during gas injection (GI), and the values of $\theta_{t[ow]}$ and $\theta_{t[go]}$ that best fit Eq. (4.4) were found using the least squares approximation approach. The third contact angle, $\theta_{t[gw]}$, was found using the Bartell-Osterhof relationship, Eq. (2.11), for three-phases in thermodynamic equilibrium [49, 50].

4.2.4 Results and Discussion

First, in section 4.2.4.1, we use the geometric and thermodynamic contact angle measurements alongside pore occupancy to identify the wettability order of the system. Next, using static images of the whole sample, we show the end-state saturations of oil, water and gas after each injection in section 4.2.4.2. In section 4.2.4.3, we analyze the gas injection dynamics by examining the evolution of: (i) gas connectivity; (ii) direct, double and multiple displacement events; (iii) water connectivity and trapping; and (iv) oil layers. Finally, in section 4.2.4.4, we quantify the change in Minkowski functionals – saturations, interfacial areas and curvatures – with time to obtain a complete understanding of the fluid topology in the pore space.

4.2.4.1 Wettability characterization

4.2.4.1.1 Contact angles

The geometric fluid-fluid contact angles were measured at the end of waterflooding (WF) and gas injection (GI), in the same location, on a subvolume of size 0.5×0.5×0.5 mm^3. Fig. 4.14 shows the *in situ* spatial distribution of the effective oil-water, gas-water and gas-oil contact angles after WF and GI.

After waterflooding, the mean geometric oil-water contact angle was 110 ± 20°, indicating that oil is more wetting to the rock than water, and hence confirms that the ageing process rendered the rock surfaces oil-wet (hydrophobic), see Fig. 4.14a, as seen in section 4.1.

Furthermore, Fig. 4.14b shows that the mean oil-water contact angle decreases to 101 ± 22° after gas injection (Table 4.4). In three-phase flow, double displacement mechanisms allow for both water to displace oil, and oil to displace water in the pore space. In the latter process, water is receding, with a likely lower contact angle than the advancing angle during waterflooding, due to contact angle hysteresis. Therefore, the mean geometric contact angle decreases after gas injection, representing a position of equilibrium after events where water is both invading and receding.

The mean geometric gas-oil contact angle is 70 ± 27°, see Fig. 4.14b, once more indicating that oil is more wetting to the surface than gas, and therefore, it is the most wetting phase in the system. The measured mean of the gas-water geometric contact angle distribution is 87 ± 27°, suggesting that the rock surfaces are neutrally wetting to both gas and water. Hence, it is not possible to determine a clear

wettability order in the system using the geometric contact angle measurements only, which record values on hinging contact lines, rather than the angles during a displacement.

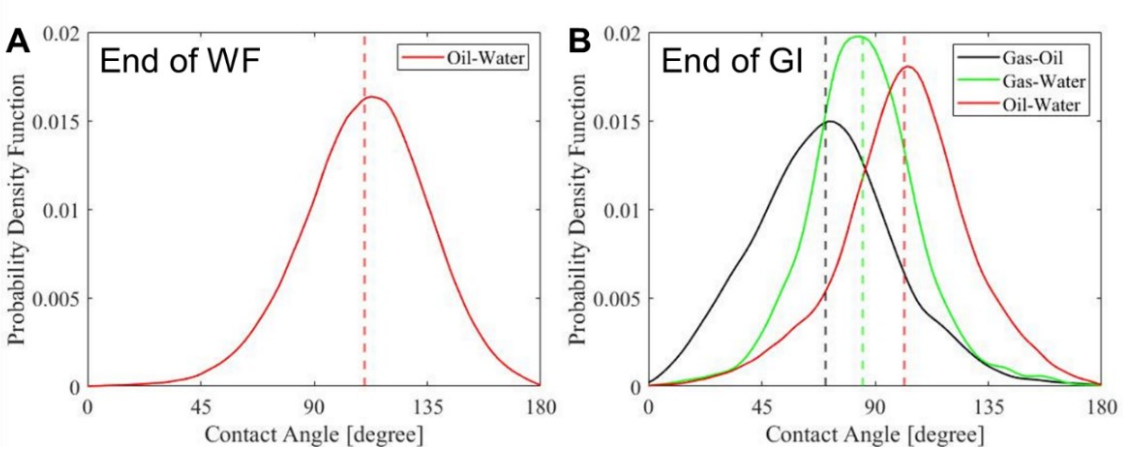

Figure 4. 14. Probability density function of the *in situ* measured distribution of fluid-fluid contact angles at the end of (a) waterflooding [WF] and (b) gas injection [GI]. The contact angles were measured using the automated method developed by AlRatrout et al. [30]. The angle was characterized through the denser phase: water in the case of oil and water and gas and water, and oil in the case of gas and oil.

To characterize the fluid-fluid contact angles encountered during displacement, we use Eq. (4.4) to find the gas-oil $\theta_{t[go]}$ and oil-water $\theta_{t[ow]}$ thermodynamic angles that best fit the data using the least squares approach, see Appendix 5. The thermodynamic contact angle calculations yield an oil-water angle of 125 ± 10^{o} and a gas-oil angle of 78 ± 10^{o}, see Table 4.4. The gas-water thermodynamic contact angle is determined using Eq. (2.11) as 115 ± 10^{o}. While the interpretations of the oil-water and gas-oil contact angles in this analysis are broadly consistent with those of the geometric contact angle measurements, the thermodynamic gas-water contact angle suggests that gas is, on average, more wetting to the rock than water. This allows us to establish a clear wettability order in the system, one in which oil is wetting to both water and gas, gas is non-wetting to oil and wetting to water, while water is non-wetting to both oil and gas. This implies that water will tend to occupy the larger pores and that the gas-water capillary pressure will be negative, as we will show later.

Table 4. 4. Measurements of the oil-water, gas-oil and gas-water mean geometric contact angles and thermodynamic contact angles after gas injection (GI). The error in the geometric contact angle represents the standard deviation of the distribution, while in the case of the thermodynamic contact angle it indicates the uncertainty in the measurements.

Method	θ_{ow}	θ_{go}	θ_{gw}
Geometric	$101^{o} \pm 22^{o}$	$70^{o} \pm 27^{o}$	$87^{o} \pm 25^{o}$
Thermodynamic	$125^{o} \pm 10^{o}$	$78^{o} \pm 10^{o}$	$115^{o} \pm 10^{o}$

From Table 4.4, we observe that the geometric contact angle tends to underestimate the displacement contact angles. This is further illustrated in Fig. 4.15 by visually inspecting gas-water contacts on static and dynamic raw pore-scale images. At rest, water forms contact angles with gas that are both lower and larger than 90°, indicating that the rock surfaces are neutrally wetting to gas and water. On the other hand, during the displacement of water by gas, we notice that the gas-water contact angle is almost always larger than 90°, implying that gas is wetting to water during flow (Fig. 4.15). Moreover, this behaviour was also seen in a recent modelling study, where the use of the geometric contact angle was insufficient to match experiments of waterflooding in rocks with altered wettability; instead a larger advancing contact angle was needed to match the results [176]. This analysis identifies a clear limitation with the geometric contact angle measurement and shows that it is not representative of displacement

contact angles in systems with altered wettability. In contrast, the gas-water thermodynamic contact angle measurement, Table 4.4, is in agreement with the angles observed during gas-water displacement, see Fig. 4.15, indicating that it is more representative of displacement angles compared to the direct geometric measurement.

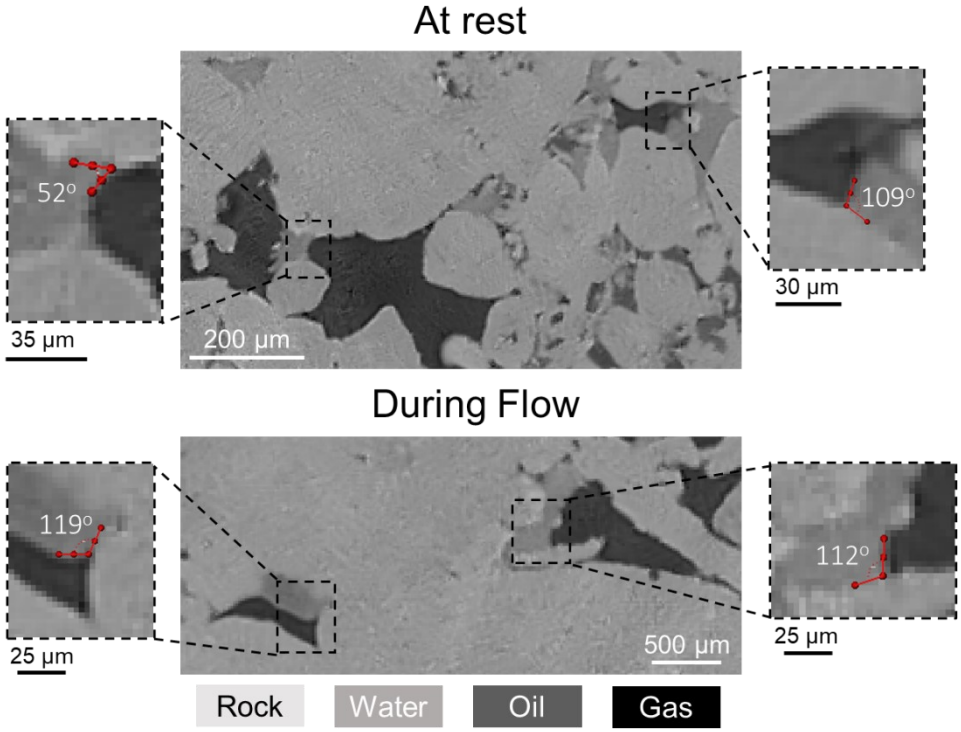

Figure 4. 15. Two-dimensional raw pore-scale images, with a voxel size of 3.5 µm, showing on (top) the contact angles formed between gas and water when the fluids are at rest and (bottom) the gas-water contact angles during the displacement of water by gas.

4.2.4.1.2 Pore occupancy

To further confirm the wettability order of the system, we quantified the pore occupancy on static images of the whole sample after waterflooding (WF) and gas injection (GI), see Fig. 4.16. As anticipated, during water injection in an oil-wet system, water displaces oil from the larger-sized pores confining it to smaller pores, Fig. 4.16a. Furthermore, Fig. 4.16b shows that after gas injection, water resides in the largest pores, oil the smallest, while gas occupies pores of intermediate size. This confirms that the wettability order of the system is oil-gas-water from most to least wetting. The wettability order inferred from pore occupancy is in agreement with the interpretations of the thermodynamic contact angle measurements. This wettability order has been previously observed in micromodels [47] and laboratory X-ray imaging experiments with CO_2 in the same reservoir rock, sections 3.2 and 3.3, but not before with nitrogen as the gas phase.

While in Fig. 4.16 there is a tendency for oil to reside in the smaller pores and water in the larger ones, we do still observe gas and water occupancy in pores of all size: there is not a strict segregation. We will discuss this further when we discuss the dynamics of gas invasion, but it is important to note that gas does not have a strong preference for either larger or smaller pores.

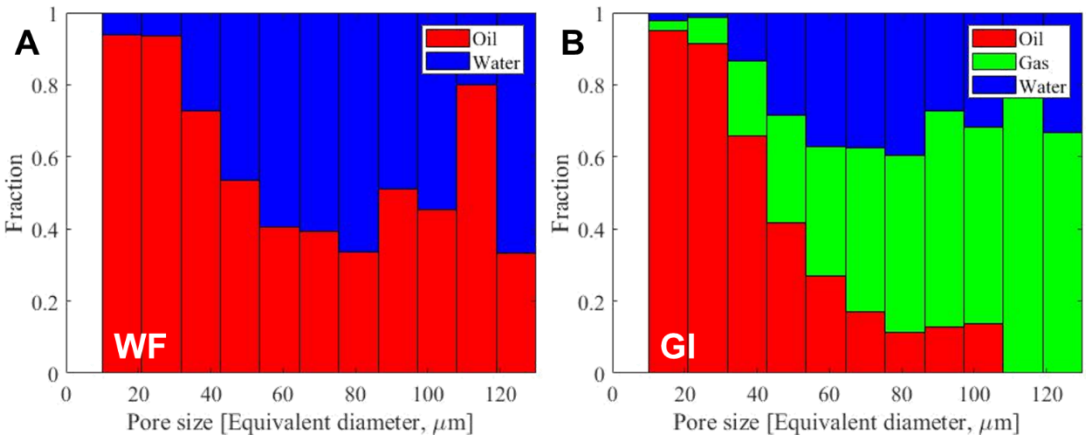

Figure 4. 16. Normalized bar charts showing the pore occupancy in the oil-wet rock, characterized on static images of the whole sample, after (a) waterflooding [WF] and (b) gas injection [GI].

4.2.4.2 Fluid saturations

The saturations of oil, gas and water in the macro pore space of the rock were measured on static images of the whole sample after water and gas injection, see Table 4.5 and Fig. A5.3 in Appendix 5. At initial conditions, the oil and water saturations were 99% and 1% respectively measured in the macro pore space; we presume that water is also initially present in the micro pores of the rock. After waterflooding, only 48 ± 5% of the oil was recovered. This is ascribed to the oil-wet nature of the rock, where water displaces oil in the centre of the pores only; oil remains connected in thick wetting layers. Gas injection displaces both oil and water out of the pore space; gas displaces 30 ± 5% of the resident oil, while only 16 ± 5% of water is displaced out of the system. A high remaining water saturation indicates that water gets trapped in the pore space of the rock. This is attributed to: (i) water being the most non-wetting phase, and hence it remains preferentially in the larger pores, Fig. 4.16; and (ii) the preferential displacement of oil by gas in the smaller-sized pores. The gas saturation reaches only 24 ± 5%, which is similar to saturation values observed on the same reservoir rock previously during the unsteady-state experiments (sections 3.2 and 3.3).

Table 4. 5. Water, oil and gas saturation in the macro pore space of the rock after each flooding step. Saturations were measured on static images of the whole sample. The error in the measurements is ± 5%.

Injection sequence	Water saturation	Oil saturation	Gas saturation
Oil injection (OI)	0.10	0.99	-
Waterflooding (WF)	0.48	0.52	-
Gas injection (GI)	0.40	0.36	0.24

4.2.4.3 Three-phase flow dynamics

In this section, we examine the various pore-scale dynamics observed during gas injection in our oil-wet rock, where the wettability order is oil-gas-water from most to least wetting. The two-phase displacement dynamics encountered during waterflooding (WF) will be briefly described to set the scene for the discussion of gas injection (GI) dynamics. A complete description of WF dynamics is provided in section 4.1. The pore-scale dynamics were investigated by imaging the rock section shown in Fig. 4.17, with a high temporal resolution during WF and GI.

The main finding of this section is that gas moves through the pore space as disconnected clusters through double and multiple displacement; this is a distinct dynamics not seen in two-phase flow, where the injected phase needs to remain connected to progress through the porous medium.

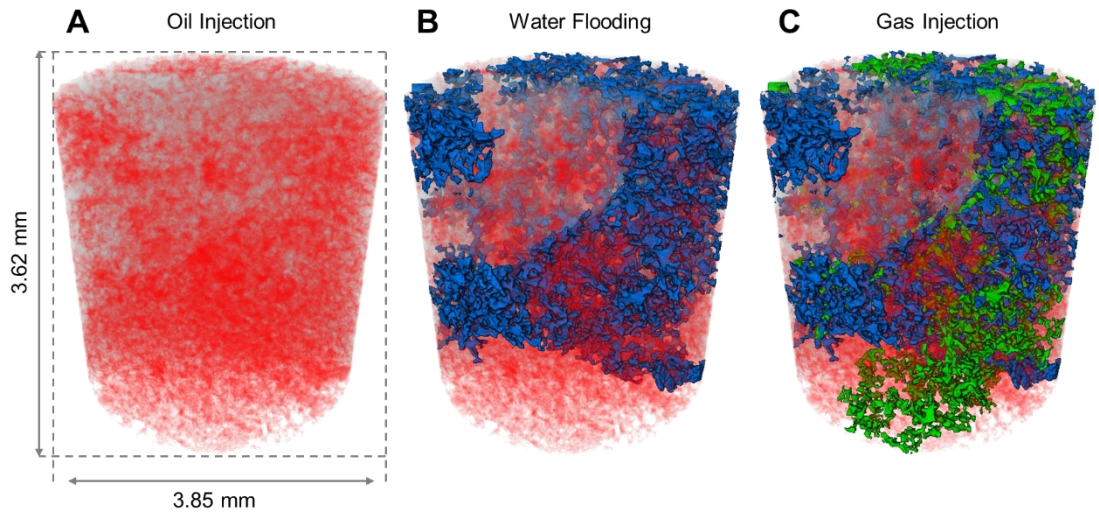

Figure 4. 17. A 3D volume rendering of the fluid configurations in the section of the rock imaged dynamically during (a) oil injection [OI], (b) waterflooding [WF], and (c) gas injection [GI]. Oil is shown in red, water in blue and gas in green.

4.2.4.3.1 Waterflooding

During waterflooding (WF), the displacement of oil by water is all piston-like. Water advances as a connected front in an invasion percolation process, where throats, the restrictions between pores, fill in order of size, with the largest available throats filled first; displacement is predominantly size-controlled. This is attributed to the wide pore size distribution of the heterogenous rock selected. Furthermore, we observe drainage associated pore-filling dynamics including Haines jumps and snap-off events.

Fig. 4.17b shows the fluid configurations in the oil-wet rock at the end of waterflooding – water is shown in blue and oil in red. As anticipated, there is a high remaining oil saturation due to the strongly oil-wet nature of the rock; oil not only remains connected in thick wetting layers but also many oil-filled pores have been completely bypassed by the incoming water front as a result of inadequate water pressure to overcome the high oil-water capillary pressure. This is in contrast with observations made in water-wet porous media, where water spontaneously imbibes through wetting layers and corners of the pore space trapping oil in the centres; no oil-filled pores were bypassed [48]. The dynamics of waterflooding stopped after the injection of 0.58 PV of water (78.1 minutes).

4.2.4.3.2 Gas injection

4.2.4.3.2.1 Invasion pattern and displacement events

We observe a distinct three-phase invasion pattern during gas injection in the oil-wet pore space. Gas, the intermediate-wet phase, advances through the porous medium in disconnected clusters; gas is not connected during GI. The connectivity of gas during GI is captured using dynamic imaging, see Fig. 4.18 – each color represents a different gas cluster. This is different to the invasion pattern observed during the two-phase waterflooding in section 4.1.

In two-phase flow, when a non-wetting phase displaces the wetting phase, Haines jumps are observed, which involve the rapid filling of multiple pores followed by retraction and disconnection of the non-wetting phase and the phases come to a new position of equilibrium [87, 88]. However, as injection proceeds, the non-wetting phase gets reconnected in the pore space: for capillary-dominated flow, the gas has to reconnect to progress further through the pore space. Haines jumps have been seen during two-phase flow in both water-wet and oil-wet rocks.

We observe a similar phenomenon during gas injection under three-phase conditions, namely the filling of several pores by gas, accompanied by the retraction of gas from other regions, leading to disconnection of gas ganglia in the pore space. Nevertheless, unlike two-phase flow, the occurrence of this phenomenon in our three-phase system leads to the permanent disconnection of gas; gas does not reconnect as gas injection proceeds. The disconnected gas ganglia reach a new position of equilibrium in the pore space; gas can only be further mobilized through double and multiple displacement events. This pore-scale phenomenon, which we name a three-phase Haines jump, controls the movement of gas in the pore space; gas displaces oil and water in a sequence of three-phase Haines jumps. The other distinction with two-phase flow is that the gas is intermediate-wet – it is non-wetting to oil but wetting to water.

This phenomenon, three-phase Haines jumps, has not been seen before during three-phase flow in porous media. Previous three-phase synchrotron studies in water-wet and mixed-wet rocks observed that gas progresses in a connected front maintaining its connectivity in the pore space [101, 186]. In these experiments, the gas was either the most non-wetting phase, or almost neutrally-wet with respect to water. However, in the study in section 3.3 conducted using static imaging, performed in the same reservoir rock and under immiscible oil-wet conditions, we observed that gas was highly disconnected at the end of gas injection. Using dynamic imaging we deduce that the origin of the poor connectivity is the advance of gas through three-phase Haines jumps.

A similar behaviour to three-phase Haines jump was seen during gas injection in an oil-wet micromodel [47] that was successfully modeled by considering multiple displacement events [106]. The behaviour was attributed to water blocking. In some cases, the progress of the advancing gas front was blocked if faced with a water occupied throat (restriction in the pore space). However, as the gas pressure built up, exceeding that of the gas-water capillary pressure, the throat would momentarily open, allowing gas to escape towards the next oil-filled pore. As gas pressure dropped, after displacement, the throat would again be filled by water, disconnecting the gas phase.

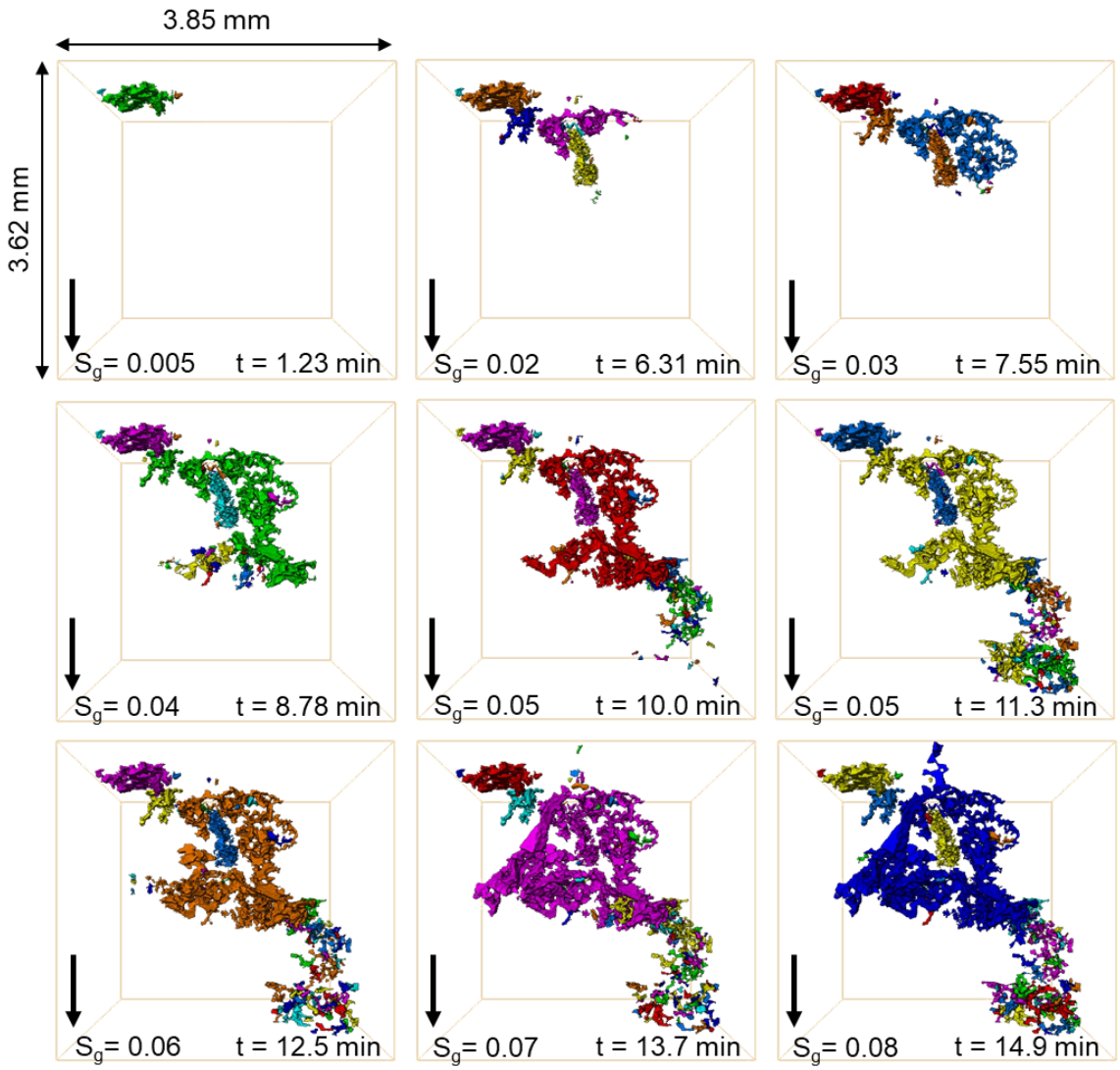

Figure 4. 18. Three-dimensional maps of the gas connectivity in the pore space during GI shown at different time-steps. Each disconnected gas cluster is labeled with a different colour. The black arrow points towards the direction of flow. S_g is the gas saturation in the imaged section, while t is time.

Three types of displacement were observed during gas injection: (i) direct gas-oil displacement; (ii) direct gas-water displacement; and (iii) gas-oil-water double and multiple displacement. Fig. 4.19 shows images of the various displacement events occurring at different time-steps – green represents the displacement of oil by gas, blue is water by gas, while red is water by oil. As discussed above, double and multiple displacements [46, 105, 106] are necessary to allow gas to propagate in disconnected clusters: in particular, for gas to remain disconnected there must be multiple displacement events of the form gas-oil-gas-water, where the second gas displacement in the sequence involves a trapped cluster. We suspect that there is a thin oil layer surrounding the gas phase during the direct gas-water displacement due to the positive initial oil spreading coefficient (+0.4 mN/m, Table 4.2); however, it is not visible at the given spatial resolution of the experiment (3.5 μm).

Notice that gas directly displaces oil and water in the pore space, and there is no strong preferential displacement of oil over water as seen in the carbonate rock study with a mixed-wet behaviour [186], where gas only displaced oil in a piston-like displacement during gas injection; there was no displacement of water by gas. Furthermore, this is different to water-wet systems, where gas only

initially displaces water until it comes in contact with oil which spreads in layers between gas and water preventing their direct contact in the pore space [101].

Initially, direct, double and multiple displacement events occur close to the advancing gas front; however, after gas breakthrough in the imaged rock section (11.3 mins), the pore-scale displacement dynamics continue to occur but at locations throughout the sample. The gas injection dynamics stop after the injection of 0.18 PV of gas (19.8 minutes); the gas pressure is insufficient for additional displacement.

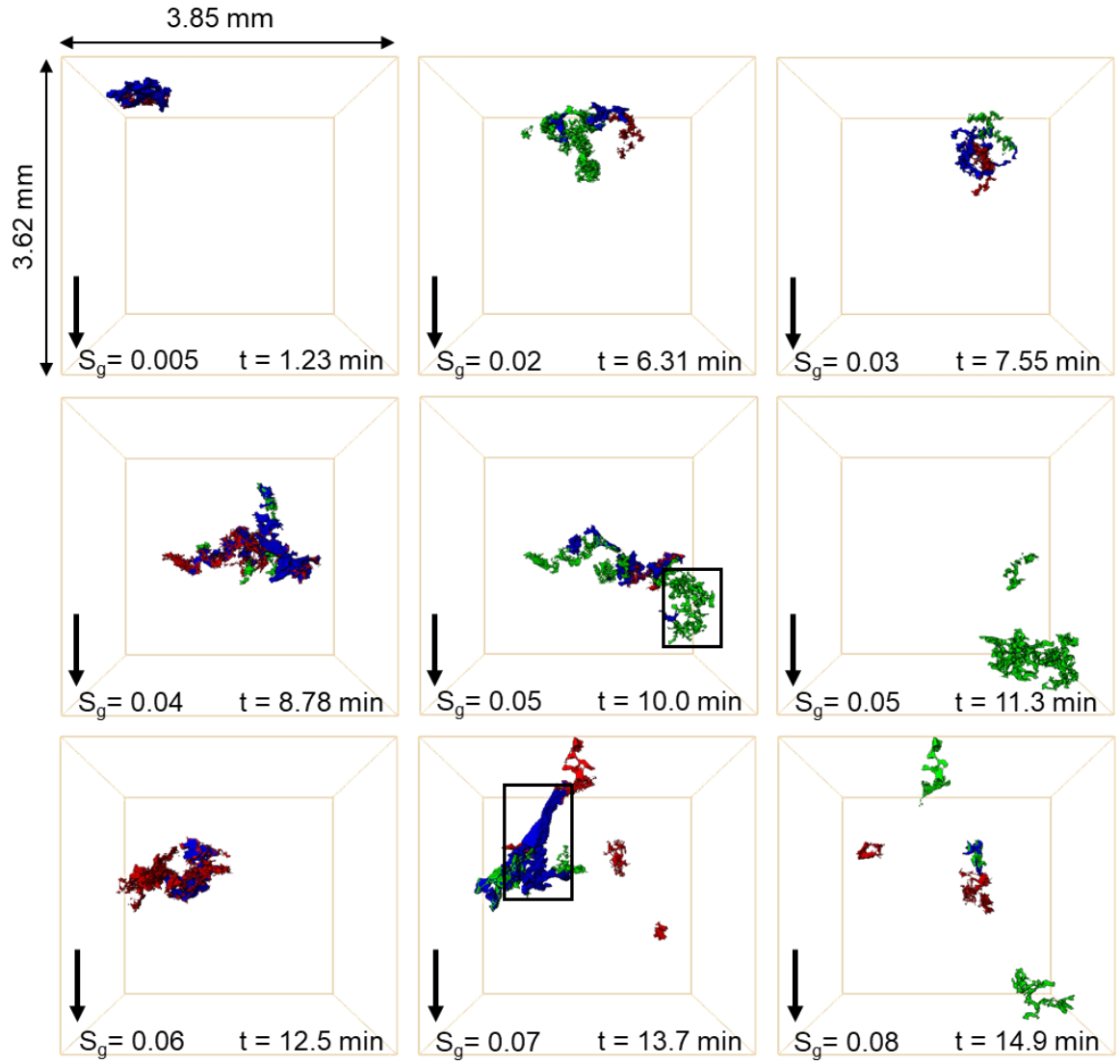

Figure 4. 19. Three-dimensional images of direct and multiple displacement events occurring at different time-steps during gas injection in the oil-wet rock. Displacement of oil by gas is shown in green, water by gas in blue and water by oil in red. The black arrow points towards the direction of flow. S_g is the gas saturation in the imaged section, while t is time.

To illustrate the displacement dynamics in more detail, Fig. 4.20 shows the rapid filling of multiple pores during a gas-oil three-phase Haines jump, where gas displaces oil overall – this displacement is marked by the black square in Fig. 4.19 at time = 10 min – and we have quantified the specific interfacial area between gas and the other phases (water, oil and solid) before and after its retraction from the narrower regions of the pore space. We notice, in Fig. 4.20b, that there is a large increase in the gas saturation caused by the three-phase Haines jump at time = 10 min – shown by the red square. Gas re-

arranges itself in the pore space during the three-phase Haines jump, flowing towards regions of low gas pressure to enable the rapid filling, which causes it to retract from the high-pressure regions (throats), disconnecting the gas phase. This is shown in Fig. 4.20c, where gas has a lower specific interfacial area with the other phases of 6.7 mm^{-1} at time = 10 min after the three-phase Haines jump compared to time = 8.78 min, where gas had a specific interfacial area of 6.9 mm^{-1} – gas specific interfacial area is quantified in the region marked with the black dashed line.

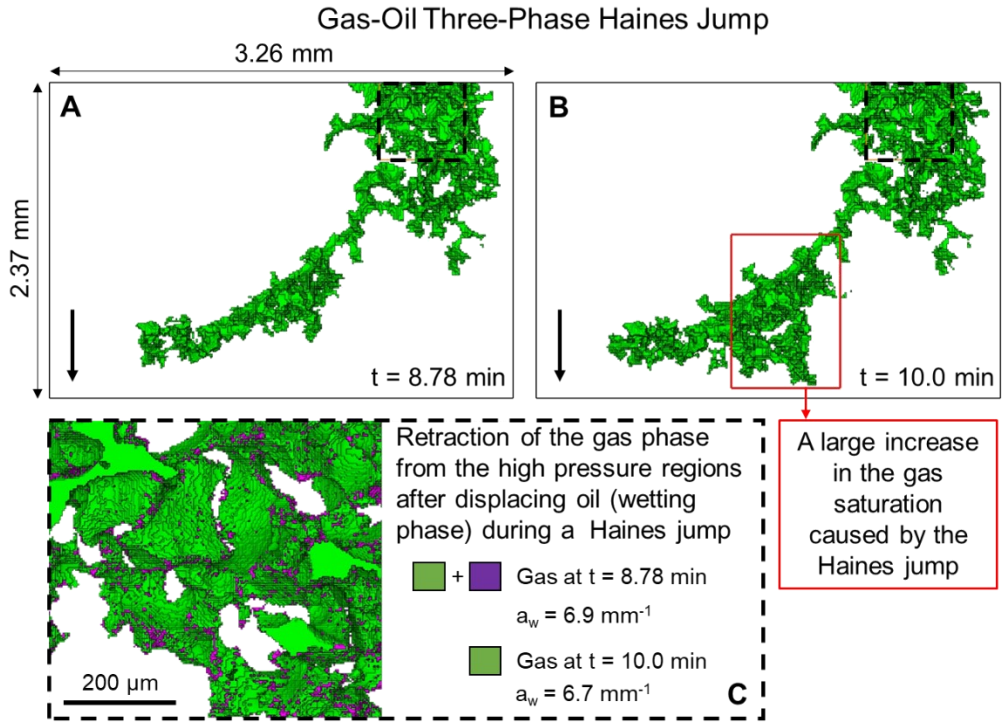

Figure 4. 20. Three dimensional images of the gas phase at different time-steps illustrating the occurrence of three-phase Haines jump during the displacement of oil by gas in the oil-wet pore space. (A) and (B) show the difference in gas saturation before and after the three-phase Haines jump. (C) The specific interfacial area between gas and the rest of the phases (water, oil and solid) is lower in the high-pressure region, marked by the dashed line, after the three-phase Haines jump due to gas retraction. The black arrow points towards the direction of flow.

The occurrence of a three-phase Haines jump during the displacement of water by gas is shown in Fig. 4.21 – this displacement event is shown by the black square in Fig. 4.19 at time = 13.7 min. Again, we observe that multiple pores were filled during the displacement resulting in a large increase in the gas saturation at time = 13.7 min. Similarly, gas has retracted from the high-pressure regions reducing its specific interfacial area with the other phases – in the dashed box – from 14.8 mm^{-1} at time = 12.5 min to 13.9 mm^{-1} at time = 13.7 min. In this case, gas retraction is more pronounced during the gas-water Haines jump (0.9 mm^{-1}) compared to the gas-oil one (0.2 mm^{-1}). Since neither gas nor water form layers, all the displacements are piston-like. However, gas is wetting to water, and so the initial advance is an imbibition process.

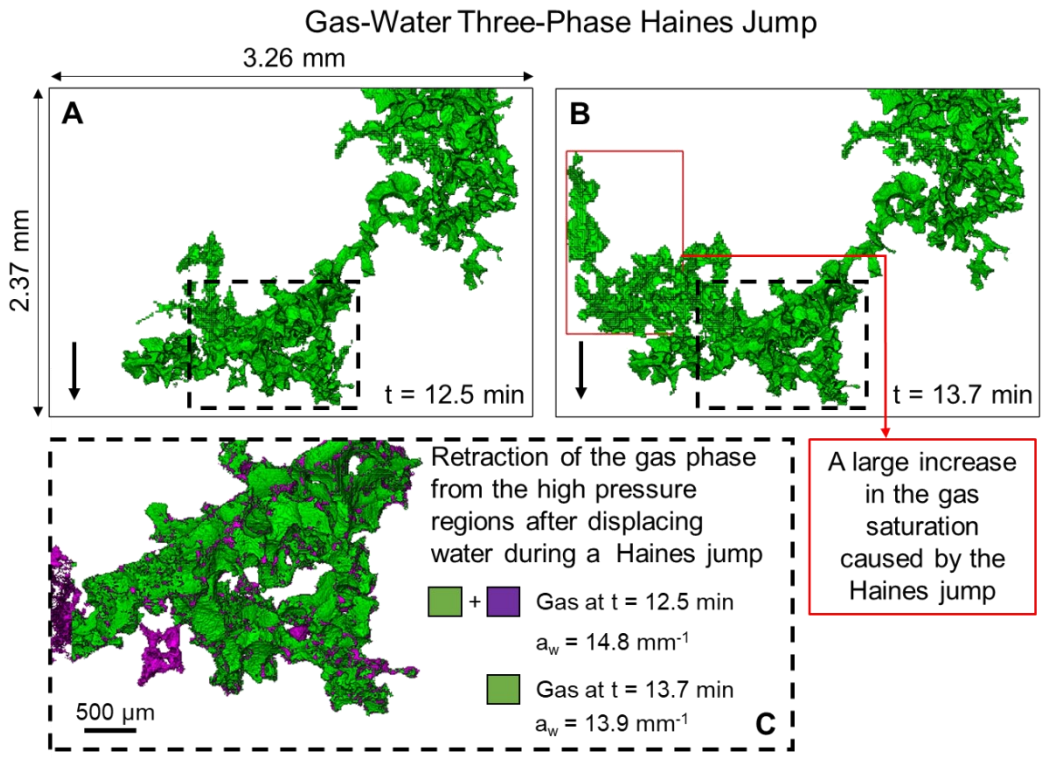

Figure 4. 21. Three dimensional images of the gas phase at different time-steps illustrating the occurrence of three-phase Haines jump during the displacement of water by gas in the oil-wet pore space. (A) and (B) show the difference in gas saturation before and after the three-phase Haines jump. (C) The specific interfacial area between gas and the rest of the phases (water, oil and solid) is lower in the high-pressure region, marked by the dashed line, after the three-phase Haines jump due to gas retraction. The black arrow points towards the direction of flow.

4.2.4.3.2.2 Water connectivity and trapping

Water, the most non-wetting phase, can become locally disconnected in the pore space during gas injection. Since gas, intermediate-wet, does not form spreading layers due to its large and negative spreading coefficient (C_{sg} = -22.8 mN/m, Table 4.2), water is principally trapped by oil, the most wetting phase, rather than gas. An illustration of this is shown in Fig. A5.4 in Appendix 5, where the incoming gas front only displaces some of the resident water, disconnecting it from the main water body; the trapped water cluster is surrounded by both oil and gas. Nevertheless, we observe that, in general, there is a single connected cluster across the system that contains most of the water throughout gas injection, see Fig. A5.5 in Appendix 5, since gas, although more wetting than water, cannot trap water by snap-off, which is the principal capillary trapping process, as it does not spread in layers [90]. This is different to oil-wet micromodel and laboratory micro-CT studies, where the injection of gas disconnected the water phase in the pore space, see section 3.3. However, in section 3.2, the gas was near-miscible with the oil, and could form spreading layers to trap water by snap-off.

4.2.4.3.2.3 Oil layers

As mentioned in section 4.2.3.1, the large and negative spreading coefficients of gas and water (C_{sg} = -22.8 mN/m and C_{sw} = -104.6 mN/m, Table 4.2), prevent them from forming spreading layers in the pore space. Oil not only spreads in layers sandwiched between gas and water, C_{so} = 0.4 mN/m (Table 4.2), but also exists in wetting layers close to the solid surface with gas or water occupying the centre of the pore space. Due to the lack of spreading water and gas layers, oil is the only phase that is always hydraulically connected from the inlet to the outlet of the porous medium. This increases its connectivity

in the pore space allowing it to flow even at very low oil saturations. This is in contrast with water-wet systems, where both oil and water are connected in the pore space; water is hydraulically connected through wetting layers and oil through spreading layers [41].

Fig. A5.6 in Appendix 5 shows 3D thickness maps of oil layers visualized at the end of waterflooding and gas injection on a subset of size 1.4×1.4×1.4 mm^3. The thickness was defined as the diameter of the largest sphere (maximal ball) that could fit entirely within the oil phase [143]. The average oil layer thicknesses after waterflooding and gas injection were 17 and 14 μm respectively. As one would expect, there were fewer and thinner oil layers in the pore space after gas injection due to the efficient displacement of oil by gas and/or drainage of oil through wetting layers. This is different to observations made on a mixed-wet system, where more oil layers were observed after gas injection [186]: in these experiments, gas-oil-water double displacement allowed oil to push water out of the pore space, increasing the thickness of wetting and spreading layers and there was little direct displacement of water by gas. In our experiment, gas displaces water directly, as well as oil, removing both phases out of the pore space.

4.2.4.4 Minkowski functionals

To obtain a complete characterization of the dynamics of three-phase flow, we quantified the evolution of the 3D Minkowski functionals – saturations, interfacial areas and curvatures – during gas injection (GI). In Fig. 4.22, measured on the dynamic images, we plot fluid saturations, fluid-fluid specific interfacial areas, fluid-solid specific interfacial areas and fluid-fluid capillary pressures against time and the corresponding pore volume (PV) of gas injected.

Note that the fluid saturations depicted in Fig. 4.22a are measured on the dynamically imaged section of the rock and are different from the saturations quantified on the whole sample in section 4.2.4.2. At the start of gas injection, the gas saturation increases very slowly until time = 5 min, where gas displaces oil and large amounts of water out of the dynamically imaged pore space. There is a slightly larger drop in water saturation compared to oil saturation during GI. However, it is important to note that the favoured displacement of water by gas over oil by gas is only seen in the dynamically imaged section, as saturation measurements on the whole sample, section 4.2.4.2, show that gas injection recovers 30 ± 5% of the resident oil, while only 16 ± 5% of water is produced. Moreover, we observe that the gas saturation further increases after gas breakthrough in the imaged section.

Figs. 4.22b and 4.22c show the evolution of fluid-fluid and fluid-solid specific interfacial areas respectively with time. At the beginning of gas injection, at low gas saturations, the interfacial area between gas and oil is very small. As the gas saturation increases, the gas-oil specific interfacial area rises linearly with time since oil is wetting to gas in the pore space; oil wetting and spreading layers surround gas in the centres of the intermediate-sized pores. However, the gas-oil specific interfacial area remains smaller than that between oil-water since the gas saturation is much lower than the water saturation. There is an abrupt increase in the gas-water interfacial area at the start of GI, which then remains constant throughout the displacement. This is attributed to spreading of oil layers sandwiched between gas and water, preventing their direct contact in the pore space. Furthermore, the low gas saturation results in a very low gas-solid interfacial area in the pore space. The oil-solid interfacial area is the highest due to oil being the most-wetting phase; oil resides in thick wetting layers next to the solid surface.

The two principal curvatures (κ_1 and κ_2) of the oil-water, gas-water and gas-oil interfaces were quantified during the displacement, see Fig. 4.23. The sum of the two curvatures – the total curvature (κ) – was then calculated and substituted in the Young-Laplace equation, (2.9), to obtain the fluid-fluid capillary pressures during gas injection. The results are shown in Fig. 4.22d. The oil-water capillary pressure remains approximately constant throughout the displacement with an average value of -3.0 kPa. A negative capillary pressure between oil and water indicates that the macro pores are indeed oil-

wet such that, on average, water bulges into oil with a higher pressure. The measured gas-water capillary pressure decreases during the displacement reaching a value of -2.0 kPa at the end of gas injection. A negative gas-water capillary pressure indicates that gas is more wetting to the rock surface than water. This confirms the reported wettability order of oil-gas-water from most to least wetting in section 4.2.4.1. Moreover, once gas is injected, the capillary pressure between gas and oil reaches a threshold value after which it remains constant during the displacement. The gas-oil capillary pressure is positive, since gas is less wetting than oil.

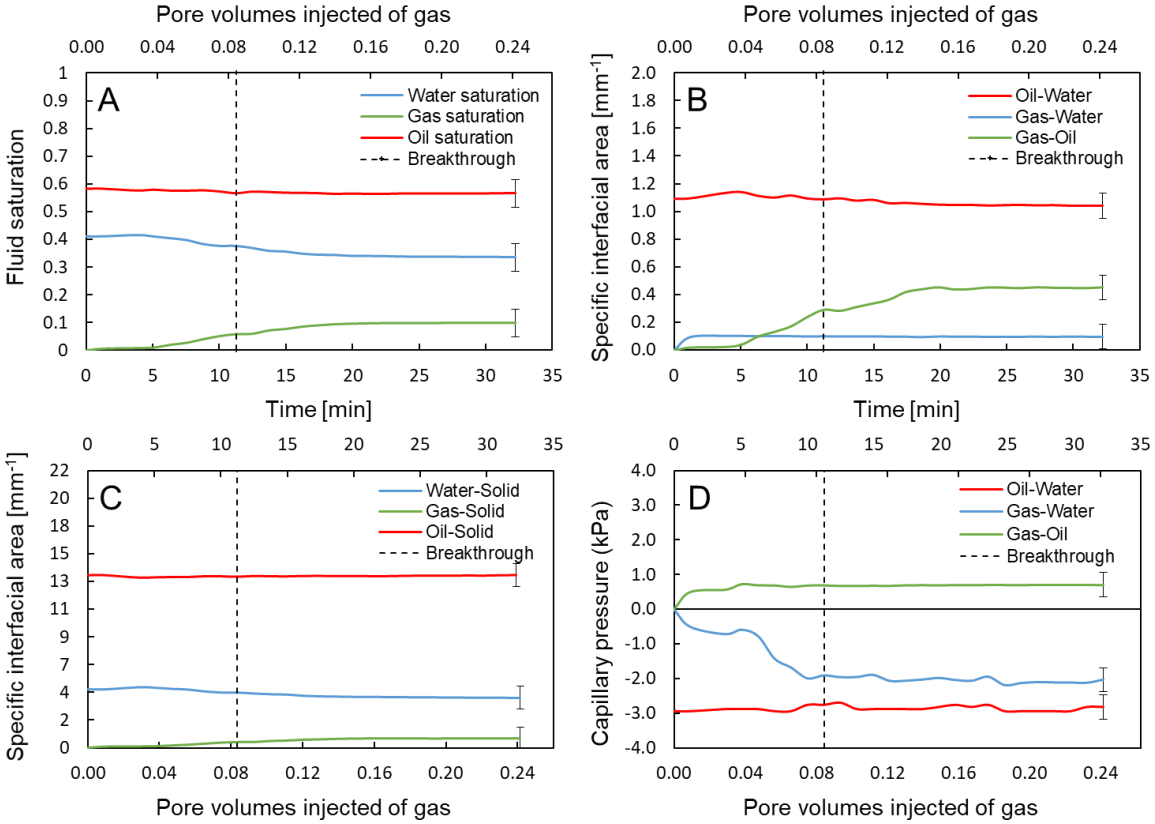

Figure 4. 22. The evolution of Minkowski functionals – (a) saturation, (b) fluid-fluid specific interfacial area, (c) fluid-solid specific interfacial area and (d) capillary pressure – during gas injection in the dynamically imaged section of the oil-wet rock. The vertical dashed line represents the time of gas breakthrough in the imaged field of view. Error bars indicate uncertainty in the measurement.

As mentioned previously, in section 4.1.3.7, the two principal curvatures of the fluid-fluid interface can be used to study the connectedness of the fluid phases in the pore space. The fluid-fluid connectivity can be characterized by investigating the product of the principal curvatures ($\kappa_1 \times \kappa_2$), also known as the Gaussian curvature [179]. A negative Gaussian curvature is an indicative of well-connected phases in the pore space, while a positive value indicates that the two phases form trapped clusters.

Figs. 4.23a, 4.23b and 4.23c show that κ_1 and κ_2 of the gas-oil interface have opposite signs, resulting in a very negative Gaussian curvature between gas and oil during gas injection. This indicates that oil is well connected in the pore space when in contact with gas, in wetting and spreading layers. Similarly, κ_1 and κ_2 of the oil-water interface have opposite signs, see Figs. 4.23d, 4.23e and 4.23f, indicating that oil and water are well connected, especially that water remains highly connected in the larger pores surrounded by oil layers during gas injection (see section 4.2.4.3.2.3 and Fig. A5.5 in Appendix 5).

Observations on the dynamic behaviour of κ_1 and κ_2 between gas and water are the most interesting (Figs. 4.23g, 4.23h, and 4.23i). There are two important points to make. (i) It is evident from the distribution of κ_1 and κ_2 that the gas-water interface has a less negative Gaussian curvature compared to gas-oil and oil-water interfaces, implying that gas and water are less connected in the pore space. This makes sense since neither water nor gas form spreading layers due to their large and negative spreading coefficients (C_{sg} = -22.8 mN/m and C_{sw} = -104.6 mN/m, Table 4.2); the spreading of a fluid phase in layers enhances its connectivity in the pore space. Furthermore, as illustrated in Figs. 4.18 and 4.19, the gas is disconnected throughout GI. (ii) We observe that as gas injection proceeds, κ_1 gets smaller with time, consistent with there being more gas clusters as injection proceeds – see Fig. 4.18.

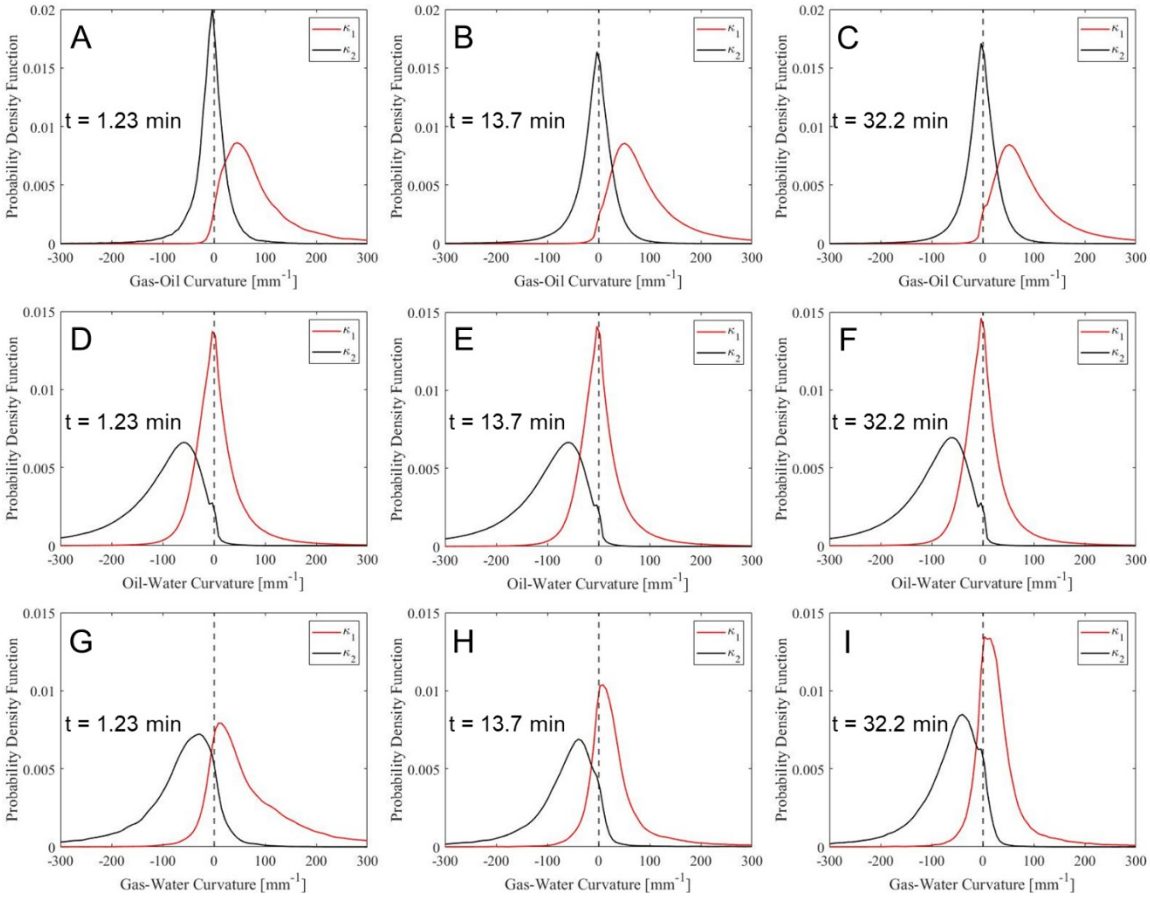

Figure 4. 23. Probability distributions of the two principal curvatures, κ_1 and κ_2, at the (a-c) gas-oil interface, (d-f) oil-water interface and (g-i) gas-water interface plotted at different time-steps during gas injection in the oil-wet porous medium. κ_1 is defined to be the larger curvature.

4.2.5 Final Remarks and Suggestions

We investigated the pore-scale dynamics of three-phase flow in a hydrophobic porous medium. Synchrotron X-ray imaging, with high spatial and temporal resolutions (3.5 μm and 74 s), was used to visualize the displacement of fluids inside the pore space during immiscible gas injection in an oil-wet reservoir rock. Subsequent to altering the wettability of the rock surfaces, water was injected into the oil saturated pore space, which was then followed by gas injection. The use of a synchrotron light source allowed us to characterize, *in situ*, wettability order, pore occupancy, fluids saturations, connectivity, direct and double displacement events, and Minkowski functionals which provided insights into fluid-fluid connectivity and trapping.

Measurements of geometric and thermodynamic contact angles confirmed that the medium was oil-wet (hydrophobic), with oil-water contact angles greater than 90°. The characterization of geometric contact

angles, measured locally, was insufficient to determine the wettability order in the system as it indicated that gas and water are neutrally wetting to the rock surface. In contrast, the estimation of thermodynamic contact angles, calculated during displacement using energy balance, demonstrated that the wettability order is oil-gas-water from most to least wetting. This was further supported by pore occupancy – where oil occupied the smallest pores, gas, the intermediate pores, and water the largest pores – and capillary pressure measurements which displayed (-) negative oil-water and gas-water pressures and a (+) positive gas-oil pressure. Overall, this analysis showed that geometric contact angles, measured on static interfaces, tend to underestimate the contact angles encountered during displacement, measured through the advancing angle, but that using an energy balance can correctly capture a representative wettability in three-phase flow.

We imaged the fluid configurations during gas injection, which illustrated that gas invades the porous medium in the form of disconnected clusters; gas being the intermediate-wet phase is not connected in the pore space. When gas displaced either oil or water, it rapidly filled multiple pores, significantly increasing the gas saturation in the pore space. This rapid filling was accompanied by retraction of gas from some of the further regions which disconnected the gas ganglia permanently in the pore space; the disconnected gas ganglia do not reconnect as gas injection continued. We call this phenomenon a three-phase Haines jump. Unlike in two-phase flow, the injected phase remained disconnected with displacement facilitated by double and multiple displacements. This dynamics is unique to three-phase flow, and is distinct from ganglion movement in two-phase flow, which only occurs under viscous-dominated flow conditions.

As gas invaded the pore space, it displaced oil and water in direct gas-water and gas-oil displacements, as well as double and multiple gas-oil-water displacement. No evidence of significant gas-water-oil double displacement was observed; as water is displaced by gas, water follows the easiest path to escape the pore space, which is its own path since it resides in the largest pores being the most non-wetting phase, and therefore, does not displace oil. During gas injection, water maintains its connectivity through the larger pores, while oil remains hydraulically connected through wetting layers and spreading oil layers. Some water gets trapped in the porous medium during gas injection.

We quantified the Minkowski functionals – saturations, interfacial areas and curvatures – during gas injection to provide a complete description of the topology of fluids in the pore space, fluid-fluid connectivity and trapping. The oil-water specific interfacial area was the highest, while the gas-water area was the lowest due to the spreading of oil in layers sandwiched between gas and water, and hence preventing their direct contact in the pore space. Quantification of the two principal curvatures of the oil-water, gas-water and gas-oil interfaces provided details on the connectivity of the phases. The results indicated that oil has a good connectivity with gas and water in the pore space. This was attributed to the oil-wet nature of the rock, since oil is confined in wetting layers close to the solid surface surrounding the gas and water phases in the centre of the pores. The analysis further confirmed the poor connectivity of the gas, which is broken up into discrete clusters as injection proceeds. This has big implications for the design of safe gas storage, improved oil recovery, contaminant removal in soils and three-phase flow in microfluidic devices.

This work can be used to validate three-phase flow pore-scale network models and to develop three-phase flow numerical simulators. Experiments on additional samples could test the reproducibility of the results presented here. Future work should focus on quantifying the relative permeability of the phases in oil-wet rocks by measuring the pressure drop across the sample to confirm the low gas mobility anticipated as a result of gas advancing in disconnected clusters. Furthermore, future work can study the dynamics of three-phase flow at near-miscible gas–oil conditions in water-wet and oil-wet porous media. This will help to assess the impact of (i) the absence of oil layers in water-wet systems and (ii) the formation of gas spreading layers in oil-wet systems, on the pore-scale displacement events. The experimental and image analysis methodology presented in this work can be used to design the

flow and trapping of three fluid phases in microfluidic devices, fuel cells, carbon storage and contaminant remediation in soils.

With this experiment, we conclude our work on unsteady-state three-phase flow in porous media. In the chapter, (5), we will summarize the findings of our work and other studies in the literature on unsteady-state three-phase flow and discuss the implications it has on the design of efficient CO_2 storage and oil recovery in oil reservoirs. Then, in chapter 6, we study the steady-state flow and measure relative permeability.

Chapter 5

In this chapter we provide a synthesized review of the latest insights into the key pore-scale physical processes that control the fluid movement during unsteady-state three-phase flow in porous media achieved with three-dimensional pore-scale imaging. The review will include unsteady state three-phase flow insights obtained with pore-scale imaging from this work, sections 3.1, 3.2, 3.3 and 4.2, and from other imaging studies in the literature. We end by placing the analysis in a practical context by discussing implications for carbon dioxide storage combined with enhanced oil recovery.

5.1 Pore-scale imaging and analysis of wettability order, trapping and displacement in three-phase flow in porous media with various wettabilities

5.1.1 Synthesis

This section describes the key pore-scale processes that control flow and trapping in a three-phase system, namely wettability order, spreading and wetting layers, and double/multiple displacement events. In a porous medium containing water, oil and gas, the behaviour is controlled by wettability, which can either be water-wet, weakly oil-wet or strongly oil-wet, and by gas-oil miscibility. We emphasize our earlier findings, in sections 3.1 and 3.2, that, for the same wettability state, the three-phase pore-scale events are different under near-miscible conditions – where the gas-oil interfacial tension is ≤ 1 mN/m – compared to immiscible conditions.

In a water-wet system, at immiscible conditions, water is the most-wetting phase residing in the corners of the pore space, gas is the most non-wetting phase occupying the centres, while oil is the intermediate-wet phase spreading in layers sandwiched between water and gas. This fluid configuration allows for double capillary trapping, which can result in more gas trapping than for two-phase flow. At near-miscible conditions, oil and gas appear to become neutrally wetting to each other, preventing oil from spreading in layers; instead, gas and oil compete to occupy the centre of the larger pores, while water remains connected in wetting layers in the corners. This allows for the rapid production of oil since it is no longer confined to movement in thin layers. In a weakly oil-wet system, at immiscible conditions, the wettability order is oil-water-gas, from most to least wetting, promoting capillary trapping of gas in the pore centres by oil and water during water-alternating-gas injection. This wettability order is altered under near-miscible conditions as gas becomes the intermediate-wet phase, spreading in layers between water in the centres and oil in the corners. This fluid configuration allows for a high oil recovery factor while restricting gas flow in the reservoir. Moreover, we show evidence of the order in strongly oil-wet systems at immiscible conditions, oil-gas-water, from most to least wetting. At these conditions, gas progresses through the pore space in disconnected clusters by double and multiple displacements; therefore, the injection of large amounts of water to disconnect the gas phase is unnecessary. We then place the analysis in a practical context by discussing implications for flow and trapping.

The emphasis of this work is on the three-dimensional pore-scale imaging of three-phase flow in natural systems. Rather than provide a comprehensive review of experimental and modelling studies we will instead focus our review on pore-scale imaging of three-phase flow in rock samples.

The synthesis of this work is shown in Fig. 5.1, which summarizes the main findings of the three-phase flow X-ray imaging experiments listed in Table 5.1. These experiments were either performed using laboratory X-rays (static imaging), which imaged fluid configurations at the end of a displacement, or synchrotron X-ray facilities (dynamic imaging), where images were acquired at approximately a time resolution of 1 minute throughout a displacement.

Wettability	Miscibility	Wettability order (most-least wetting)	Spreading and wetting layers	Displacement events		Gas trapping	Oil recovery
				Gas injection	Water flooding		
Water-wet	Immiscible	W O G	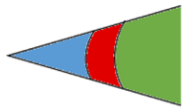	G O W	W O G		Good
	Near-miscible	W O G	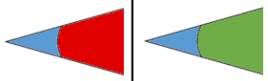	G O W G W O	No data		Excellent
Weakly oil-wet	Immiscible	O W G	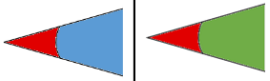	G W G O W	W O G	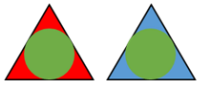	Good
	Near-miscible	G W O	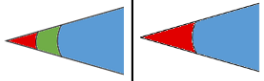	G W G O W	W O W G O	-	Excellent
Strongly oil-wet	Immiscible	O G W	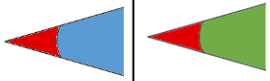	G W G O W	W O W G O		Very good
	Near-Miscible	G W O	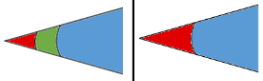	G W G O W	W O W G O	-	Excellent

Figure 5. 1. The wettability orders, spreading and wetting layers, and double displacement events for various wettability and miscibility conditions during three-phase flow in porous media under capillary dominated conditions. The content summarizes the main findings of the three-phase flow pore-scale imaging studies listed in Table 5.1 [16, 17, 38, 42, 101, 110, 122, 142].

Table 5. 1. Wettability, gas-oil miscibility, temperatures, pressures, interfacial tensions, and spreading coefficients of the three-phase flow pore-scale imaging studies discussed in this work. Shaded in grey are the experiments conducted using time-resolved synchrotron X-ray imaging.

Reference	Rock	Wettability	Miscibility	Pressure MPa	Temperature °C	σ_{go} mN/m	σ_{ow} mN/m	σ_{gw} mN/m	C_{so} mN/m	C_{sg} mN/m	C_{sw} mN/m
Scanziani et al. [16]	Ketton limestone	Water-wet	Immiscible	8	60	27	47	72	-2	-52	-92
Feali et al. [42]	Bentheimer sandstone	Water-wet	Immiscible	-	-	-	-	-	+5.9	-	-
Iglauer et al. [142]	Clashach sandstone	Water-wet	Immiscible	0.1	20	31	52	72	-11	-51	-93
Scanziani et al. [101]	Ketton limestone	Water-wet	Immiscible	8	60	27	47	72	-2	-52	-92
Section 3.1	Ketton limestone	Water-wet	Near-miscible	10.85	70	1	30	31	0	-2	-60
Qin et al. [17]	Fond du Lac carbonate	Weakly oil-wet	Immiscible	4.13	40 & 90	-	-	-	-	-	-
Scanziani et al. [38]	Reservoir carbonate	Weakly oil-wet	Immiscible	8	60	27	47	72	-2	-52	-92
Scanziani et al. [110]	Ketton limestone	Weakly oil-wet	Immiscible	8	60	11	52	64	0	-23	-105
Section 3.2	Reservoir carbonate	Weakly oil-wet	Near-miscible	10.85	70	1	30	31	0	-2	-60
Section 3.3	Reservoir carbonate	Strongly oil-wet	Immiscible	8	60	10	21	31	0	-20	-42
Iglauer et al. [122]	Bentheimer sandstone	Strongly oil-wet	Immiscible	10	50	3	23	40	+14	-20	-60
Section 4.2	Reservoir carbonate	Strongly oil-wet	Immiscible	8	60	11	52	64	0	-23	-105

A key feature of three-phase flow and the analysis in this work concerns wettability, or the local distribution of contact angles. Contact angle will be determined in two ways to assess the wettability order in three-phase flow: geometric and thermodynamic, see section 4.2.4.1.1 for more details.

The contact angles measured using both the geometric and thermodynamic approaches for the experiments discussed here are listed in Table 5.2 and plotted in Fig. 5.2, where $\cos\theta_{gw}$ is plotted as a function of $\cos\theta_{ow}$. The quadrants of the graph define different wettability orders: for $\cos\theta_{ow} > 0$ and $\cos\theta_{gw} > 0$ the wetting order, from most to least wetting, is water-oil-gas; for $\cos\theta_{ow} < 0$ and $\cos\theta_{gw} > 0$ the order is oil-water-gas, while for $\cos\theta_{ow} < 0$ and $\cos\theta_{gw} < 0$ we have an oil-gas-water wetting order.

We will now discuss the main findings of the three-phase flow pore-scale imaging studies summarized in Fig. 5.1. We will examine the wettability order, spreading and wetting layers, and multiple displacement events at each surface wettability and miscibility condition, and discuss their implications on oil recovery and gas storage applications.

Table 5. 2. Geometric and thermodynamic contact angle measurements between oil and water, gas and oil, and gas and water at different conditions of wettability and miscibility. The error in the geometric contact angle represents the standard deviation of the distribution, while in the case of the thermodynamic contact angle it indicates the uncertainty in the measurements. Data from [16, 38, 101, 110] and sections 3.1, 3.2, 3.3 and 4.2.

Wettability	Miscibility	Method	θ_{ow}	θ_{go}	θ_{gw}
Water-wet	Immiscible	Geometric	47° ± 5°	0°	N/A
		Thermodynamic	48° ± 10°	0°	44°± 10°
	Near-Miscible	Geometric	52° ± 22°	73° ± 17°	52° ± 18°
		Thermodynamic	-	-	-
Weakly oil-wet	Immiscible	Geometric	105° ± 27°	57° ± 25°	80° ± 23°
		Thermodynamic	-	-	-
	Near-Miscible	Geometric	112° ± 21°	67° ± 22°	108° ± 18°
		Thermodynamic	-	-	-
Strongly oil-wet	Immiscible	Geometric	118° ± 25°	60° ± 24°	124° ± 24°
		Thermodynamic	125° ± 10°	78° ± 10°	115° ± 10°

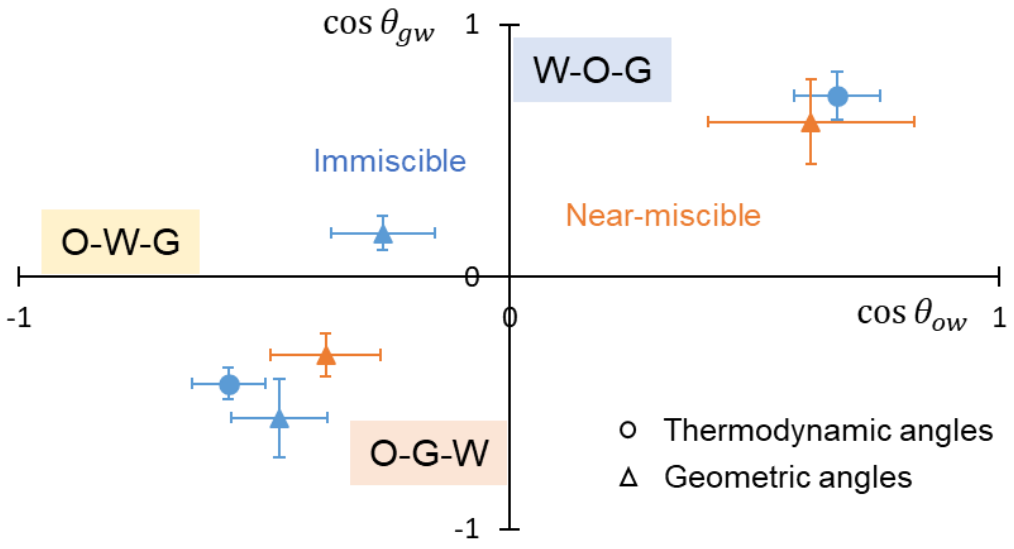

Figure 5. 2. Cosines of the geometric and thermodynamic gas-water and oil-water contact angles listed in Table 5.2. In orange are the angles measured in near-miscible gas-oil experiments, while in blue are the angles measured in immiscible experiments. The W-O-G, O-W-G, and O-G-W labels refer to the wettability order, from most to least wetting, in each quadrant, where W refers to water, O to oil, and G to gas.

5.1.2 Water-wet Systems

5.1.2.1 Immiscible conditions

In a water-wet porous medium at immiscible gas-oil conditions, the wettability order is water-oil-gas from most to least wetting [16, 42, 101, 142]. Water forms wetting layers occupying the corners, gas resides in the centres, while in most systems studied in the literature with fluids representative of subsurface conditions, oil spreads in layers sandwiched between gas and water, assuming a near-zero oil spreading coefficient, Eq. (2.8) [16, 42, 101]. An illustration of this wettability order *in situ* is shown in Fig. 5.3 [16].

The wettability order can also be indirectly inferred from pore-scale images by performing a statistical analysis of pore occupancy to obtain a relation between the dimension of the pores and the phase sitting in its centre. Fig. 5.3b quantifies the pore occupancy after immiscible gas injection in a water-wet carbonate rock [16]. Water resides in the smallest pores, gas the biggest, while oil occupies intermediate size pores confirming the water-oil-gas, from most to least wetting, wettability order in the system.

This wettability order is in line with *in situ* measurements of fluid-fluid contact angles, see Table 5.2 and Fig. 5.2. The thermodynamic contact angles are $\theta_{ow} = 48^o \pm 10^o$, $\theta_{go} = 0^o$, and $\theta_{gw} = 44^o \pm 10^o$; this is consistent with the geometrically measured $\theta_{ow} = 47^o \pm 5^o$ for a water-wet carbonate [33]. These results demonstrate that gas is non-wetting to both oil and water, oil is non-wetting to water and wetting to gas, while water is wetting to both oil and gas.

When gas is injected in a water-wet system after waterflooding, gas can only initially directly displace water before it contacts oil [101]. As soon as gas contacts oil, oil spreads in layers between gas and water preventing their frequent direct contact in the pore space. Further displacement of water by gas is only possible through gas-oil-water double displacement. This type of displacement is known as double drainage, which allows for the mobilization of trapped oil ganglia in the reservoir, increasing oil recovery [41], as seen by Scanziani et al. [16]. They reported that tertiary gas injection, after waterflooding, allows for the production of up to 40% of the waterflood residual oil saturation [16]. Furthermore, additional oil can be recovered through drainage of oil layers by continuous gas injection, albeit very slowly [101].

During chase water re-injection, after gas injection, the main displacement process is water-oil-gas double displacement which is known as double imbibition. Water imbibes into the corners of the pore space through wetting layers; this causes the wetting layers to swell, disconnecting the oil layers surrounding gas, which results in capillary trapping of gas in the centre of the pores. Fig. 5.4 shows an image of a trapped gas ganglion in the pore centre of a water-wet carbonate rock. Scanziani et al. [16] showed that, at immiscible conditions, 80% of the injected gas was trapped during chase water re-injection resulting in a residual gas saturation of 52% – the rest of the gas was displaced. The presence of spreading oil layers enhances the trapping of gas, since gas is strongly non-wetting to oil. This trapping mechanism – gas trapping by oil and oil trapping by water – is called double capillary trapping, which for gas storage applications can ensure that gas ganglia are immobilized by capillary and interfacial forces, especially as this gas is unlikely to dissolve in oil due to the immiscible conditions. Moreover, chase water re-injection can further increase oil recovery in the reservoir as seen by Scanziani et al. [16], where the oil saturation decreased from 30% to 18% after water re-injection.

Under three-phase conditions *more* gas can be trapped in the presence of both oil and water than in two-phase flow (for example, carbon dioxide storage in an aquifer). Rather than oil and gas competing to fill the larger pore spaces, oil in spreading layers is completely wetting to gas, which can result in more trapping than under two-phase conditions where the contact angle is not exactly zero [16, 18].

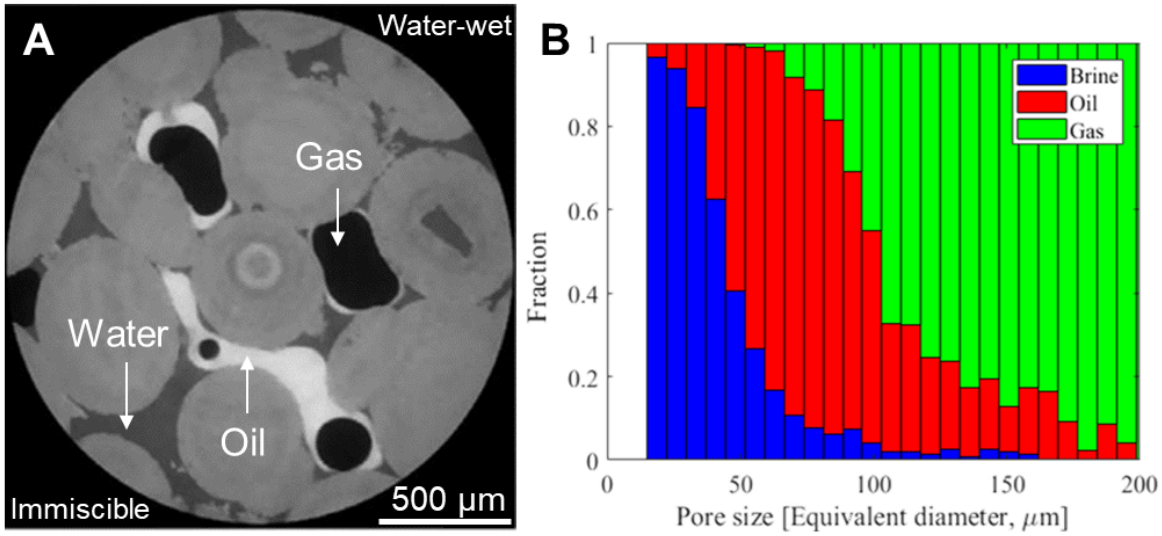

Figure 5. 3. (a) A 2 µm resolution two-dimensional raw pore-scale image showing the arrangement of gas, oil and water in the pore space of a water-wet carbonate rock at immiscible conditions. (b) A bar graph representing the pore occupancy of water, oil and gas in a water-wet rock after immiscible gas injection. In the grey-scale image (a) the order from brightest to darkest is oil, rock, water, gas. In (b), gas is shown in green, oil in red, while water (brine) in blue. Data from Scanziani et al. [16].

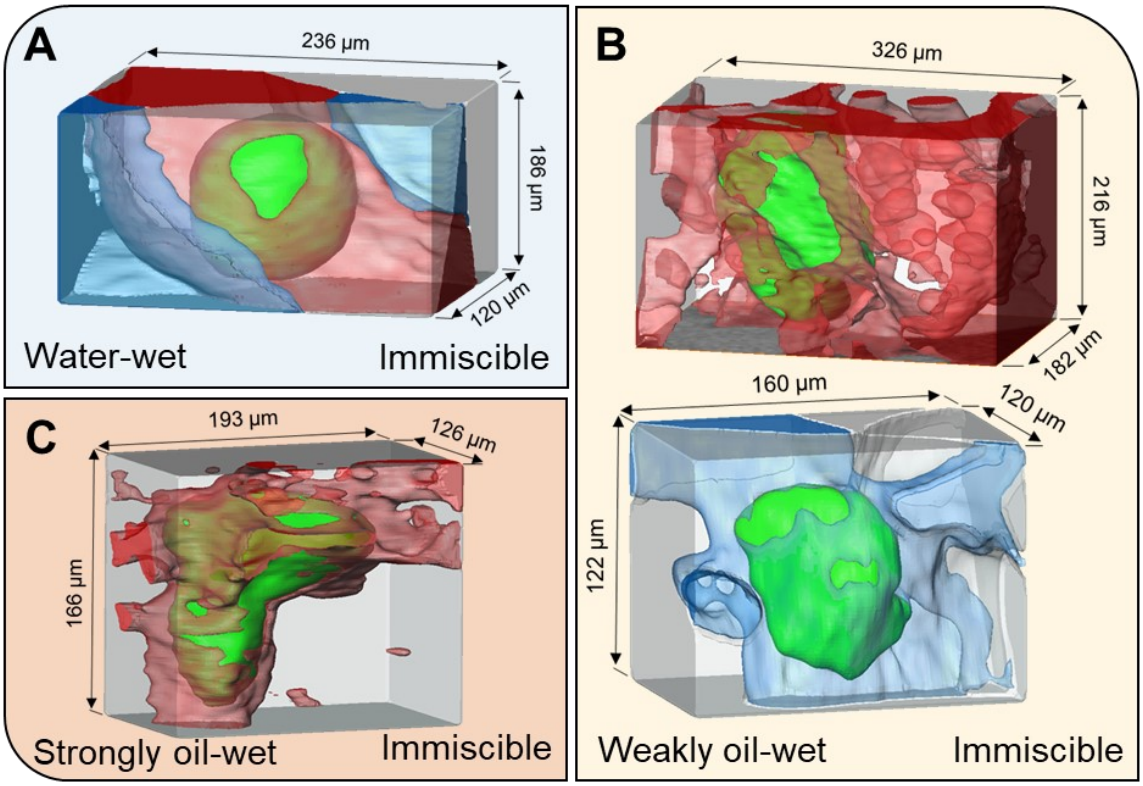

Figure 5. 4. Images of gas capillary trapping in a single pore of a carbonate rock at elevated temperatures and pressures for various surface wettabilities. Gas is shown in green, water in blue, oil in red, while the rock is rendered transparent. (a) In a water-wet rock, at immiscible conditions, gas gets double capillary trapped in the centre of large pores surrounded by oil spreading layers and water wetting layers [101]. (b) In a weakly oil-wet rock, at immiscible conditions, gas is capillary trapped in the centre of the pore space by both oil and water [38]. (c) In a strongly oil-wet rock, at immiscible conditions, gas can only be trapped in the centre of the pore space by oil wetting layers. The pore-scale images were acquired with a resolution of 2 µm.

5.1.2.2 Near-miscible conditions

The injection of gas, in a water-wet system, at near-miscible conditions efficiently displaces oil out of the pore space with a microscopic displacement efficiency close to 100%, see section 3.1. The low gas-oil interfacial tension, ≤ 1 mN/m, results in a small capillary pressure between gas and oil making near-miscible conditions extremely favourable for oil recovery applications. This was experimentally observed in section 3.1, where the injection of gas in a water-wet rock at near-miscible conditions resulted in an oil recovery factor of 80%, with the gas saturation reaching 76%. However, subsequent waterflooding, after gas injection, was not performed in this experiment, and hence the amount of gas trapping is unknown. Nevertheless, as discussed below, with little remaining oil, the behaviour is likely to be similar to a two-phase gas-water system.

In section 3.1 we observed that at near-miscible conditions oil and CO_2 became neutrally wetting to each other: the rock surface did not have a strong affinity to be preferentially coated by oil over gas. The strict wettability order, seen at immiscible conditions, where gas is distinctly more non-wetting than oil, breaks down as gas and oil compete to occupy the centre of the larger pores, while water remains connected in wetting layers in the corners of the pore space. This wettability order was observed directly from the pore-scale images acquired, see Fig 5.5. This was further confirmed by the measured fluid-fluid geometric contact angles, see Table 5.2 (the thermodynamic values have not been measured for this case), where oil and gas formed a large contact angle (θ_{go} = 73°), indicating that they are almost neutrally wetting to the surface, and had a similar contact angle with water (θ_{ow} = 52° and θ_{gw} = 52°). In terms of pore occupancy, after gas injection, gas, oil and water occupied pores of all sizes, see Fig. 5.5b. The unexpected result is that water appears to be pushed into some of the larger pores – this is explained below as a consequence of double displacement processes.

The experimental observation of a gas-oil contact angle approaching 90° as miscibility is reached contradicts the empirical assumption of Sorbie and van Dijke [115] and the experimental contact angle measurements of Al-Siyabi et al. [187], where they observed a gas-oil contact angle that stays almost constant down to low gas-oil interfacial tensions, before jumping to zero as miscibility is reached. We attribute this distinct behaviour in the gas-oil contact angle to the fluids used in the investigations as in section 3.1 we studied a CO_2-hydrocarbon system, while Al-Siyabi et al. [187] performed the gas-oil contact angle measurements on a hydrocarbon-hydrocarbon system. Furthermore, in our case, the angle was measured *in situ* inside a three-dimensional porous rock in three-phase equilibrium, whereas Al-Siyabi et al. [187] measured the gas-oil angle in a square capillary glass tube under two-phase equilibrium conditions [187]. It is possible though that oil does indeed form layers in the *in situ* experiments, and that the true contact angle with gas is close to zero, but that the layers are below the resolution of the images; gas displaces the oil efficiently leaving either no, or very little, oil remaining in the pore space whose presence cannot be detected. Moreover, the images were acquired at the end of the displacement – during gas injection there may be oil layers present with a near-zero effective contact angle between gas and oil. To sum up, it does remain an open question what the gas-oil contact angle is in the limit of a miscible system and whether or not this depends on the exact nature of the gaseous phase.

The other feature of near-miscible conditions is that oil is no longer confined to movement in spreading layers (oil does not form layers sandwiched between gas and water, since oil is no longer strongly wetting to gas) but instead flows rapidly in the centre of the pores; the residual oil saturation exists as disconnected clusters occupying the centre of the pore space rather than in layers, as seen under immiscible conditions. The absence of spreading oil layers can also be quantitatively assessed from a balance of the oil-water and gas-oil capillary pressures in the system. The capillary pressure analysis, shown in Fig. 5.5c, indicates that it is not possible for oil to spread in layers between gas and water in these experiments. Refer to section 3.1.3.2.5 for a detailed description of the methodology: a necessary

geometric condition for the formation of layers in the pore space is that $\kappa_{ow} > \kappa_{go}$, or, in terms of capillary pressure, Eq. (2.9) and Fig. 5.5c, $\sigma_{ow}P_{cgo} < \sigma_{go}P_{cow}$.

The absence of oil spreading layers allows gas to directly contact water in the pore space permitting the double displacement where gas displaces water that displaces oil during near-miscible gas injection. These double displacements allow water to enter some of the larger pores, as seen in Fig. 5.5b. Gas can remove water from some of the smaller pores, where it resides after oil injection; the water then has to shift to fill larger oil-filled elements through a local imbibition process. Nevertheless, since oil does not spread in layers surrounding gas, it is not possible to double capillary trap the gas phase during chase water re-injection; gas can only be capillary trapped by the water wetting layers. Therefore, in a water-wet system, we suggest that near-miscible conditions are less favourable for gas storage compared to immiscible conditions.

To recap this section: near-miscible conditions are favourable for oil recovery, as expected, since gas directly displaces oil. More surprising is the impact of miscibility on spreading layers and trapping. In a water-wet medium, oil can form spreading layers under immiscible conditions which facilitates gas trapping by a double imbibition mechanism during tertiary waterflooding. Under near-miscible conditions, oil layers are not seen while gas and oil compete to occupy the largest pores, with direct contact of gas by water. If there is very favourable oil displacement from gas injection, the subsequent injection of water will simply be a gas-water displacement with similar trapping as seen in two-phase flow: there is no enhanced trapping of gas thanks to snap-off by oil spreading layers, as seen in immiscible systems.

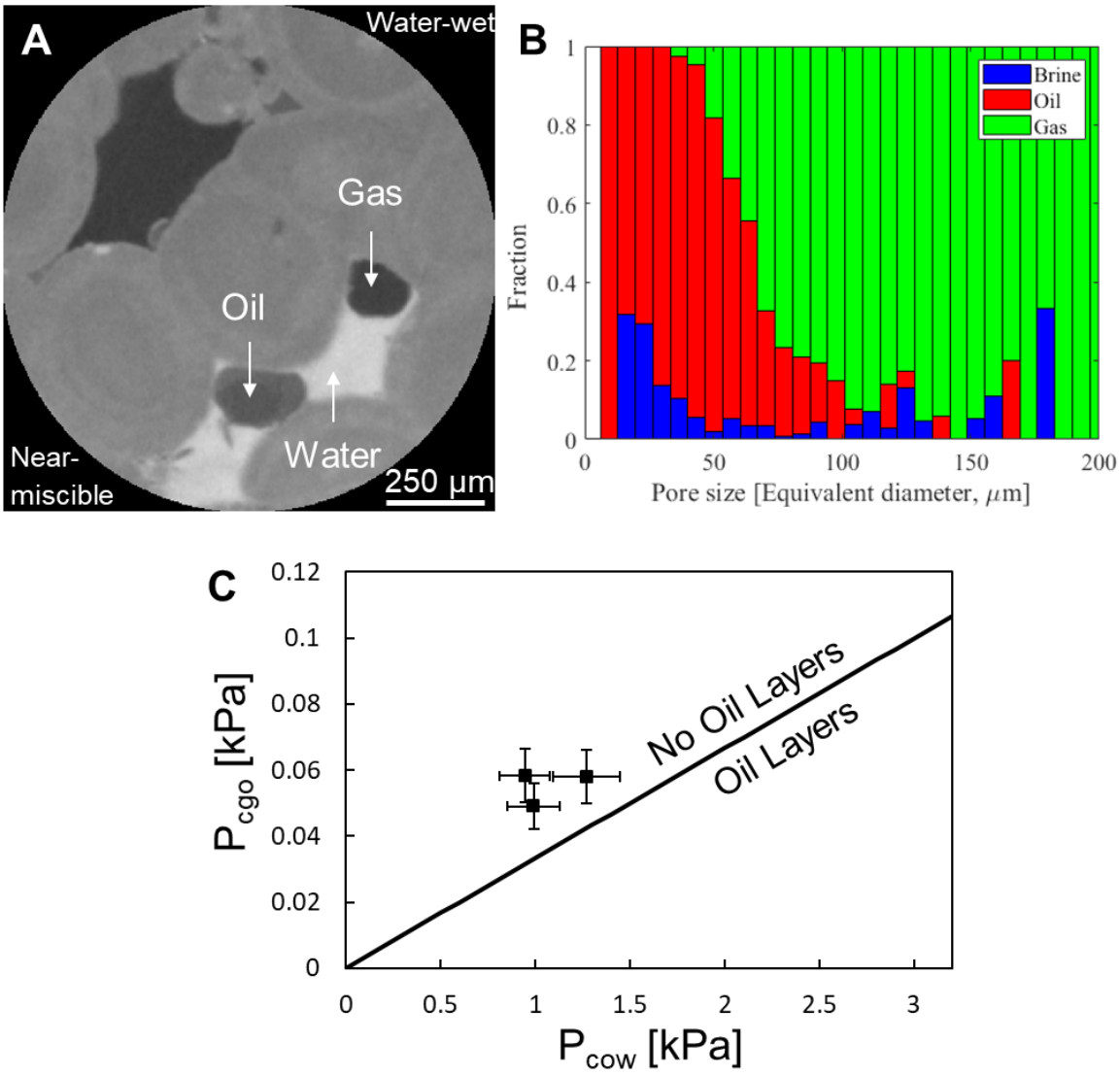

Figure 5. 5. (a) A 3.5 µm resolution two-dimensional raw pore-scale image showing the arrangement of gas, oil and water in the pore space of a water-wet carbonate rock at near-miscible conditions. (b) A bar graph representing the pore occupancy of water, oil and gas in a water-wet rock after near-miscible gas injection. (c) An analysis of the capillary pressures to assess the formation of spreading oil layers at near-miscible conditions in a water-wet system. In the grey-scale image (a) the order from brightest to darkest is water, rock, oil, gas. In (b), gas is shown in green, oil in red, while water (brine) in blue. In (c), P_c denotes the capillary pressure and subscripts w, o and g refer to water, oil and gas respectively. Data from section 3.1.

5.1.3 Weakly Oil-Wet Systems

5.1.3.1 Immiscible conditions

If a porous medium has undergone a severe wettability alteration, the system is referred to as strongly oil-wet; however, if its surfaces experience a moderate alteration in wettability, with oil-water contact angles θ_{ow} that are only slightly in excess of 90°, the porous medium is called weakly oil-wet [18]. In weakly oil-wet systems, at immiscible conditions, the wettability order is oil-water-gas from most to least wetting [17, 38]: this can be seen from the Bartell-Osterhof constraint, Eq. (2.11), where using the interfacial tension values, in Table 5.1, for immiscible conditions and assuming a gas-oil contact angle close to zero (oil is spreading) the contact angle between gas and water will be less than 90°, ($\cos\theta_{gw} > 0$) even if $\cos\theta_{ow} < 0$. This was experimentally confirmed by characterizing the geometric fluid-fluid

contact angles at these conditions for a carbonate sample that had been in prolonged contact with crude oil, which gave θ_{ow} = 105°, θ_{go} = 57°, and θ_{gw} = 80°, Table 5.2 [110].

Figs. 5.4b and 5.6 show pore-scale images of the distribution of oil, water and gas in the pore space of a weakly oil-wet rock at immiscible conditions [38]. Notice that gas bulges into water and water bulges into oil confirming that gas is the most non-wetting phase. This wettability order can further be inferred from the pore occupancy graph obtained by Scanziani et al. [38], where oil occupied the smallest pores, gas biggest, while water occupied medium-sized pores, see Fig. 5.6b. The existence of gas in the biggest pores is consistent with the conventional interpretation of weakly oil-wet core flood relative permeability measurements, where gas relative permeability is the highest for a given saturation, a function of gas saturation only and is independent of the relative amounts of water and oil [18].

Water, the intermediate-wet phase, has a very large and negative spreading coefficient, see Table 5.1, which prevents it from spreading in layers sandwiched between gas and oil. This pore-scale arrangement allows gas to directly contact oil and water in the pore space permitting its trapping by both phases. This is illustrated in Fig. 5.4b, where capillary trapping of gas in the centres by oil and water was imaged in a weakly oil-wet reservoir rock. Scanziani et al. [110] quantified the amount of residual gas trapped at these conditions after chase water re-injection and reported a gas saturation of 24%.

However, the amount of gas trapping is lower than in a strongly water-wet rock of similar structure with a spreading oil. The gas is no longer strongly non-wetting to oil.

To summarize this section, the injection of gas in weakly oil-wet systems facilitates the flow of oil which resides in thick wetting layers. During gas injection, oil is displaced through gas-oil-water double displacement events. Gas can also directly displace water in the centres of the pore space, leaving oil connected in the corners. For oil recovery and gas storage applications, chase water re-injection is important as (i) it can significantly increase oil recovery through water-oil-gas double displacement; and (ii) facilitate gas trapping by oil and water. Since gas is the most non-wetting phase, while connected, it can flow readily through the larger pores, which can result in excessive cycling of gas and insecure storage. Qin et al. [17] demonstrated the importance of chase water re-injection for oil recovery by performing water-alternating-gas (WAG) injection in weakly oil-wet samples. The authors reported a residual oil saturation of almost 30% after gas injection, which dropped down to 20% after chase water re-injection.

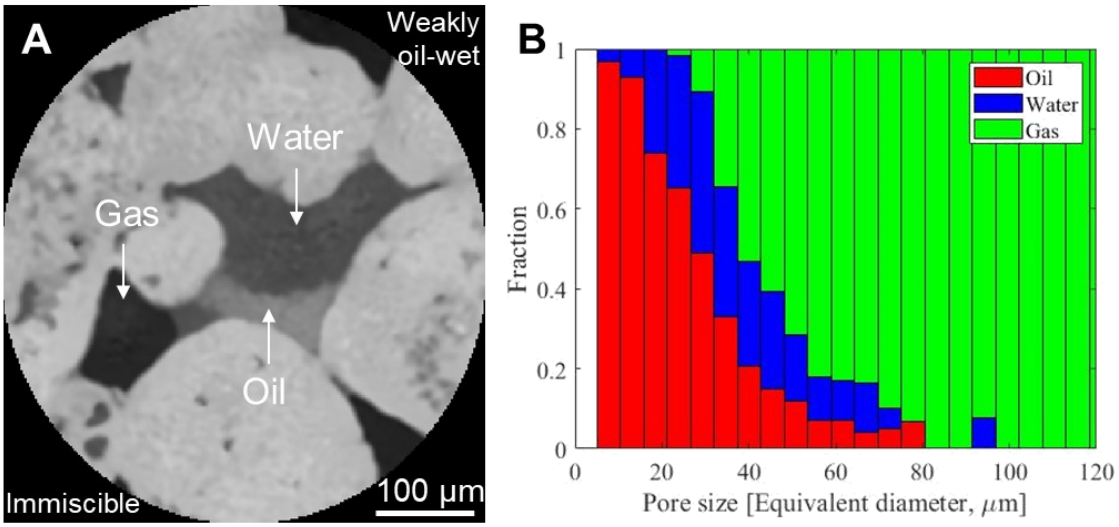

Figure 5. 6. (a) A 3.5 µm resolution two-dimensional raw pore-scale image showing the arrangement of gas, oil and water in the pore space of a weakly oil-wet carbonate rock at immiscible conditions. (b) A bar graph representing the pore occupancy of water, oil and gas in a weakly oil-wet rock after immiscible gas injection. In the grey-scale image (a) the order from brightest to darkest is rock, oil, water, gas. In (b), gas is shown in green, oil in red, while water in blue. Data from Scanziani et al. [38].

5.1.3.2 Near-miscible conditions

As gas and oil approach miscibility in a weakly oil-wet system, the wettability order is altered such that gas becomes unambiguously the intermediate-wet phase, water the most non-wetting phase, while oil remains the most wetting phase, see section 3.2. This can be seen from the Bartell-Osterhof relationship, Eq. (2.11): when σ_{go} tends to zero, we find $\sigma_{gw} \sim \sigma_{ow}$ (since oil and gas are similar – see Table 5.1) and hence $\cos\theta_{gw} \sim \cos\theta_{ow}$. Therefore, even if the system is only weakly oil-wet, gas will also be wetting (albeit also weakly) to water as it has similar properties to oil. This can be seen in Table 5.2, where the measured geometric contact angles between oil and water, and gas and water were 112° and 108° respectively at these conditions for a carbonate rock that had been in contact with crude oil.

If the gas-oil contact angle, θ_{go}, remains constant as the wettability – defined by the value of θ_{ow} – is varied, then from the Bartell-Osterhof relationship, Eq. (2.11), $\cos\theta_{gw}$ should be linearly related to $\cos\theta_{ow}$ [46, 115]. Using this linear relationship, the transition from gas being the most non-wetting phase in an immiscible system to water becoming most non-wetting at near-miscible conditions was first predicted by van Dijke and Sorbie [46]. This was later experimentally verified by Grate et al. [188] by measuring fluid-fluid contact angles on a flat surface using the static sessile drop method. While – as we show in Fig. 5.2 – there is not an obvious linear relationship between the cosines of the gas-water and oil-water contact angles, we do see a shift towards gas being more wetting to water as we lower the gas-oil interfacial tension. Nonetheless, we do not see the predicted linear trend because θ_{go} also changes with wettability. In addition, the Bartell-Osterhof relationship holds for contact angles measured at the same location in three-phase equilibrium. In our experiments, we measure contact angles between pairs of phases at different locations which means that Eq. (2.11) may not be strictly applicable to our measurements.

This wettability order – oil-gas-water, from most to least wetting – is typically associated with strongly oil-wet systems, where for immiscible conditions the Bartell-Osterhof Eq. (2.11) gives $\cos\theta_{gw} < 0$ only if $\cos\theta_{ow} \sim -1$; however, using pore-scale imaging we can see that gas becomes wetting to water in weakly oil-wet systems under near-miscible conditions, see Fig. 5.7. Performing the pore occupancy analysis on pore-scale images of a weakly oil-wet rock at near-miscible conditions indicates that oil resides in the smallest pores, water the biggest, while gas occupies the medium-sized pores (Fig. 5.7b).

This is consistent with the observed reduction in the gas relative permeability under weakly oil-wet near-miscible conditions [152]; this behaviour can now be explained using the wettability order.

This again confirms that although the surface wettability is the same, the pore-scale behaviour of fluids is different under near-miscible and immiscible conditions, as also seen in water-wet systems and described in sections 3.1 and 3.2.

Since gas is more wetting to the surface than water, it cannot be capillary trapped by water in the centres of the pore space. This may have an adverse impact on the security of gas storage applications. Furthermore, at these conditions, gas is present in spreading layers sandwiched between water and oil due to its spreading coefficient being close to zero, Table 5.1. Fig. 5.8 shows evidence of the existence of gas in layers at near-miscible weakly oil-wet conditions. The gas phase is disconnected except for thin layers of low flow conductivity which limits its mobility in the pore space making it difficult – but not impossible – for the gas to escape, and thus providing an alternative gas storage mechanism. Using direct numerical simulation, it was seen that the CO_2 conductance was reduced by a factor of 10 compared to an equivalent situation where it occupied the larger pores, see section 3.2.4.2. If gas is considered safely stored upon injection only, due to its limited mobility, this mitigates the need for chase water re-injection that reduces the gas storage capacity in the reservoir. This was demonstrated in section 3.2 as we showed that the stored gas saturation in a reservoir rock decreased from 33% to 21% after water re-injection. However, although spreading gas layers restrict flow, they can prevent the oil wetting layers from surrounding gas in the pore space disallowing capillary trapping of gas by oil.

Gas injection at these conditions is especially favourable for oil recovery applications. This was confirmed in section 3.2 where we reported an increase of up 30% in the oil recovery factor by near-miscible gas injection and another 33% by the subsequent water injection. The significant increase in oil recovery is attributed to two reasons: (i) the low gas-oil capillary pressure which results in a very efficient displacement of oil by gas; and (ii) during gas injection, gas, the intermediate-wet phase, displaces oil in the corners of the pore space, leaving water stranded in the centres which increases oil recovery and limits water production.

Two types of displacement occur when gas is injected at these conditions; gas-oil-water double displacement, and gas-water direct displacement. During chase water re-injection, water can displace oil directly in the pore space, or displace gas that further displaces oil out of the small sized pores.

To recap, as in a water-wet system, near-miscible gas injection is favourable for oil recovery. The miscibility also changes the wetting order in weakly oil-wet systems, unlike in a water-wet system: while oil remains the most wetting phase, when gas and oil are immiscible, gas is generally the most non-wetting phase, filling the largest pores, while gas becomes intermediate-wet under near-miscible conditions and forms spreading layers. Note the difference with the water-wet case, where no layers of the intermediate phase (oil) were seen under near-miscible conditions. When gas is the most non-wetting phase, tertiary water injection is needed to trap the gas effectively; instead, as an intermediate phase, the gas mobility is restricted and may be stored effectively after gas injection without the need to re-inject water.

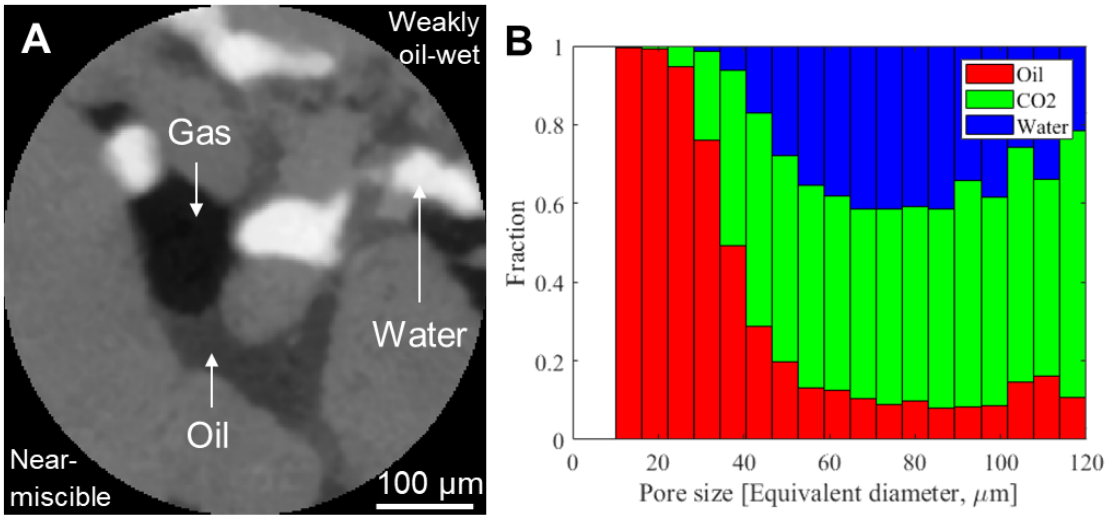

Figure 5. 7. (a) A 3.5 µm resolution two-dimensional raw pore-scale image showing the arrangement of gas, oil and water in the pore space of a weakly oil-wet carbonate rock at near-miscible conditions. (b) A bar graph representing the pore occupancy of water, oil and gas in a weakly oil-wet rock after near-miscible gas injection. In the grey-scale image (a) the order from brightest to darkest is water, rock, oil, gas. In (b), gas (CO_2) is shown in green, oil in red, while water in blue. Data from section 3.2.

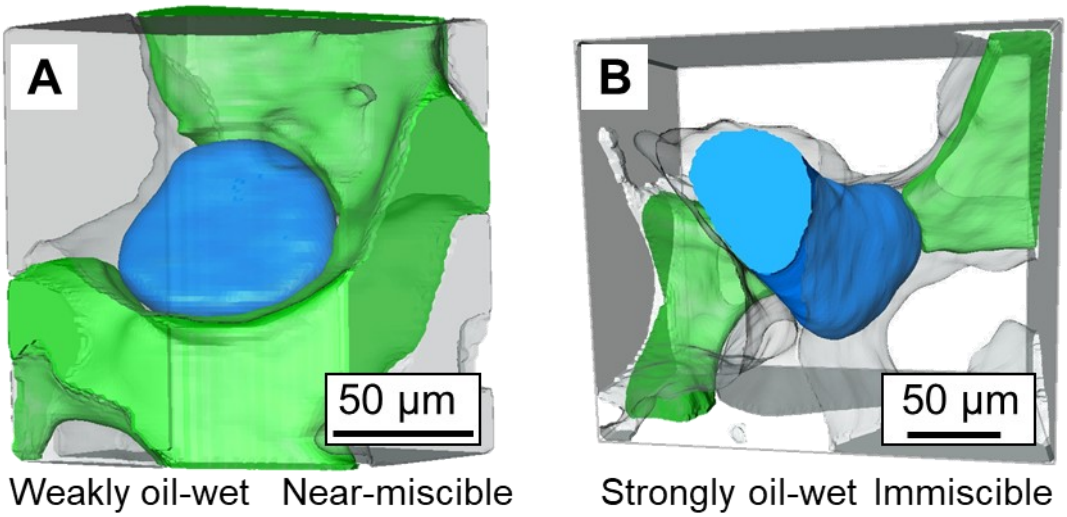

Figure 5. 8. Three-dimensional images of the configuration of gas and water in a single pore at (a) near-miscible weakly oil-wet conditions and (b) immiscible strongly oil-wet conditions. Gas is shown in green, while water in blue. Gas spreads in layers at near-miscible conditions, while it exists as disconnected clusters at immiscible conditions. The size of the three-dimensional subvolumes shown at immiscible and near-miscible conditions are 185×209×121 µm^3 and 109×134×152 µm^3 respectively. The pore-scale images were acquired at a resolution of 1.82 µm. From section 3.3.

5.1.4 Strongly Oil-Wet Systems

5.1.4.1 Immiscible conditions

For many years, it was believed that the theoretically predicted wettability order for strongly oil-wet systems – oil-gas-water from most to least wetting – does not occur in natural porous media. However, this wettability order is possible based on the Bartell-Osterhof relation, Eq. (2.11), as discussed previously, when $\cos\theta_{ow} \sim -1$ [116] and has been seen in micro-model experiments [47]. In section 3.3, we successfully altered the wettability of a reservoir rock towards strongly oil-wet conditions and

visualized, using pore-scale imaging, the hypothesized wettability order. To further confirm the wetting order in the system, we quantified the *in situ* fluid-fluid contact angles, see Table 5.2, which demonstrated that oil is wetting to both water and gas, gas is non-wetting to oil and wetting to water, while water is non-wetting to both oil and gas: this was the case for both the geometric and thermodynamic estimates of contact angles. Moreover, the pore occupancy statistics indicated that, on average, oil resides in the smallest pores and water the biggest, while gas occupies intermediate-sized pores, see Fig. 5.9.

Although the wettability order under strongly oil-wet immiscible conditions is the same as at weakly oil-wet near-miscible conditions, the pore-scale fluid configuration is different. While gas spreads in layers at near-miscible conditions, at immiscible conditions, gas exists in the pore space as disconnected ganglia, see Fig. 5.8b; gas, the intermediate-wet phase, does not spread in layers since it has a large and negative spreading coefficient, see Table 5.1. The existence of gas in disconnected clusters allows for the capillary trapping of gas by oil in the centre of the pores, see Fig. 5.4c. However, capillary trapping of gas by water is still not possible since gas is more wetting to the surface than water.

When gas is injected at immiscible conditions, it progresses through the pore space in disconnected clusters by gas-oil-water double and multiple displacements, combined with gas-water direct displacement. This was first observed in section 4.2 where we used time-resolved synchrotron imaging to capture the connectivity of gas during gas injection in a strongly oil-wet reservoir rock at immiscible conditions. Fig. 4.18 shows the connectivity of the gas phase during gas invasion at different time-steps – each colour represents a different gas cluster. We attributed this behaviour to the pore-scale events that govern the gas movement in the porous medium, which they termed three-phase Haines jumps. We observed that as gas displaces either oil or water, it rapidly progresses to fill several pores which causes it to retract from regions further away from the gas front to enable this fast filling. This retraction leads to a permanent disconnection of gas ganglia which fail to get reconnected as gas injection proceeds. While this is not seen in two-phase flow, the presence of double and multiple displacement mechanisms allows the gas to progress through the pore space while remaining discontinuous even under capillary-controlled conditions. The disconnected gas ganglia reach a new position of capillary equilibrium in the pore space and can only be displaced through double/multiple displacement events.

This type of advance is particularly favourable for gas storage applications since gas gets disconnected upon injection; the injection of large amounts of water to trap the gas is unnecessary. Therefore, gas injection alone should provide a favourable storage capacity. In section 3.3, we showed that the gas saturation can reach up to 25% in a strongly oil-wet rock at immiscible conditions.

However, the injection of water may be desirable to increase the oil recovery as the microscopic displacement efficiency of oil by gas is reduced under immiscible conditions due to the high gas-oil interfacial tension; gas injection only recovered 16% of the oil in place; by re-injecting water, after gas injection, an additional 31% of oil was recovered. During chase water re-injection, two types of displacement can occur, (i) water-oil direct displacement and (ii) water-gas-oil double displacement.

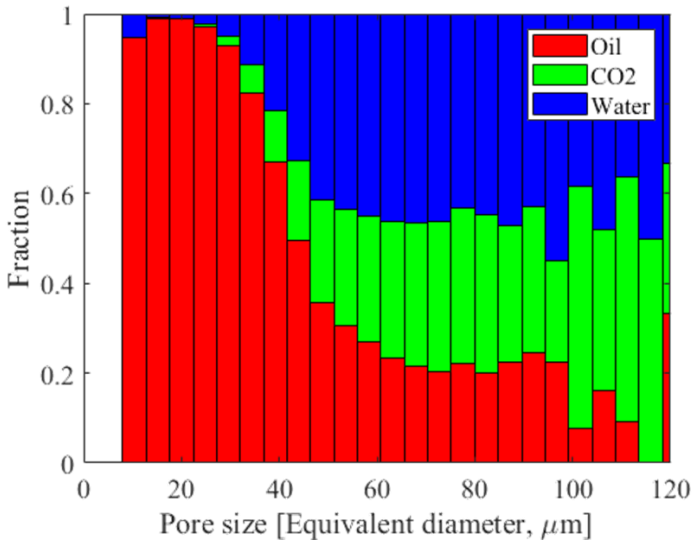

Figure 5. 9. A bar graph representing the pore occupancy of water, oil and gas in a strongly oil-wet rock after immiscible gas injection. Gas (CO_2) is shown in green, oil in red, while water in blue. From section 3.3.

5.1.4.2 Near-miscible conditions

No pore-scale imaging studies have been reported at near-miscible conditions in strongly oil-wet systems; however, we presume that the wettability order, wetting and spreading layers, and double displacement events will be similar to those observed under weakly oil-wet near-miscible conditions. In this case, the local displacement efficiency of oil will be favourable, with restricted flow of the gas in spreading layers.

5.1.5 Carbon Storage – EOR Implications

As mentioned in section 1.4 the initial rapid deployment of large-scale CO_2 sequestration is considered to be most feasible in oil and gas reservoirs [189-191]. This is attributed to many reasons including the: (i) large secure storage capacity of hydrocarbon reservoirs; (ii) geological knowledge of the reservoirs; (iii) built infrastructure and transportation routes; and (iv) a financial incentive from enhanced oil recovery (EOR).

In this section, we will suggest the optimum CO_2 injection strategy during CCS-EOR to improve the microscopic displacement efficiency in oil reservoirs under various wettability and miscibility conditions. Our discussion is limited to enhancing the microscopic displacement efficiency and does not consider the large-scale sweep efficiency and operational costs. We confine our discussion to immiscible and near-miscible conditions, but not fully miscible conditions, where oil and gas flow together as one phase in the reservoir. Although miscible conditions are favourable for local displacement efficiency, the high mobility contrast between the injected gas and resident oil can lead to channelling, while the hydrocarbon phase maintains a high mobility, which facilitates the recycling of CO_2 through the reservoir [8], and so is generally less favoured for secure storage. To optimize CO_2 injection during CCS-EOR, the goal is to store as much CO_2 as possible while maximizing oil production.

To optimize CCS-EOR in a water-wet oil reservoir, at immiscible conditions, we suggest a water-alternating-gas (WAG) injection strategy. When CO_2 is injected, it remains connected through the largest pores which allows it to flow rapidly in the pore space and potentially escape through any abandoned boreholes. Therefore, the injection of water is necessary to double capillary trap CO_2, as shown in Fig. 5.4a, immobilizing it in the pore space of the reservoir. Indeed the amount of trapping

can be larger than under equivalent two-phase conditions, since spreading oil is completely wetting to the gas. Furthermore, the injection of water can directly displace oil in the pore space, boosting oil recovery and facilitating drainage of oil through spreading layers.

Although double capillary trapping of CO_2 is not possible at near-miscible conditions, in a water-wet system, WAG is still the favourable injection strategy. The injection of water, after CO_2, at near-miscible conditions allows CO_2 to become trapped in the pore centres by water wetting layers, securing CO_2 storage. Nevertheless, it is recommended that CO_2 is injected alone at the beginning to maximize CO_2-oil contact in the reservoir, recovering large amounts of oil due to the high microscopic displacement efficiency of oil by CO_2.

The selected injection strategy is more pertinent in weakly oil-wet reservoirs, where CO_2 can go from residing in the centre of the pores to spreading in layers by switching from immiscible to near-miscible conditions. At immiscible conditions, the lower gas-oil displacement efficiency and the possibility of capillary trapping CO_2 in the centres by both oil and water, see Fig. 5.4b, suggest that WAG is the optimum injection strategy. However, as we show later, in section 6.2, from steady-state experiments, water injection in fact does not lead to trapping of CO_2 – instead it is displaced. Hence, while oil recovery may be improved, WAG is not recommended for CO_2 storage applications. On the other hand, at near-miscible conditions, where CO_2 is confined to movement in low mobility spreading layers, continuous CO_2 injection is definitely recommended for two reasons: (i) CO_2 can efficiently displace oil in the corners of the pore space significantly increasing oil recovery; and (ii) the injected CO_2 has very low flow conductivity in the reservoir which makes it highly improbable – but not impossible – for the stored CO_2 to flow towards abandoned wells and escape. Furthermore, an injection strategy of CO_2 injection only can maximize the CO_2 storage capacity in the reservoir as a lower fraction of the pore space is then occupied by water.

It is more difficult to predict the optimum injection strategy in strongly oil-wet reservoirs at immiscible conditions based on microscopic displacement efficiency insights only. At these conditions, CO_2 is disconnected upon injection, hence, an injection strategy of CO_2 injection only will produce oil while maximizing the storage capacity since the CO_2 remains poorly connected in the pore space. Nevertheless, at these conditions, the gas-oil displacement efficiency is reduced, and in some cases water injection may be necessary to boost oil recovery. Moreover, the injection of water at these conditions can promote capillary trapping of CO_2 by oil in the centres, see Fig. 5.4c. Therefore, there is an inevitable trade-off between storage capacity and oil recovery during the design of CCS-EOR in strongly oil-wet reservoirs at immiscible conditions. Additional knowledge, including the residual oil saturation and water availability may be needed to select the optimum injection strategy.

5.1.6 Final Remarks and Suggestions

This section has highlighted the recent insights into three-phase flow in porous media gained using three-dimensional pore-scale X-ray imaging. We provide *in situ* evidence of the different wettability orders, spreading and wetting layers, and double displacements at various conditions and discuss their impact on flow and trapping during the simultaneous flow of three fluid phases. We demonstrate that these pore-scale events are a function of wettability and miscibility.

This work has focussed on studying three-phase flow in porous rocks only, whereas the pore-scale behaviour of fluids may vary in different porous media, e.g., microfluidic devices, shales, or fractured rocks. The impact of using live oils on gas-oil miscibility must also be investigated since all the three-phase flow pore-scale imaging studies discussed used dead oils (that is oil with no dissolved natural gas at reservoir conditions). The scope of this study was confined to gas-oil-water three-phase systems; however, the use of pore-scale imaging can be extended to investigate the flow of liquid-liquid-solid and gas-liquid-solid systems which occur in chemical engineering applications. Furthermore, with pore-scale imaging the flow and impact of surfactants and foams can be investigated. Future work must also

focus on measuring three-phase relative permeabilities, which can be used to develop predictive models for three-phase flow in porous media; this is the subject of the following chapter.

With this, we conclude our discussion of unsteady-state three-phase flow in this thesis. In the next chapter, (6), will start investigating steady-state three-phase flow conditions using pore-scale X-ray imaging to determine relative permeability.

Chapter 6

In this chapter we will present the materials and methods, results, discussion, and conclusions of the steady-state experiments investigated with static imaging. Sections 6.1 and 6.2 will examine immiscible steady-state three-phase flow in a water-wet and a mixed-wet rocks respectively (*EXP6* and *EXP7*, see Table 1.1). Again, the heading of each section is given the title of the published manuscript.

6.1 Disconnected gas transport in steady-state three-phase flow

6.1.1 Summary

We use high-resolution three-dimensional X-ray imaging to investigate fluid displacement during steady-state three-phase flow in a cm-sized water-wet sandstone rock sample. The pressure differential across the sample is measured which enables the determination of relative permeability; capillary pressure is also estimated from the interfacial curvature. Though the measured relative permeabilities are consistent – to within experimental uncertainty – with values obtained without imaging on larger samples, we discover a unique flow dynamics. The most non-wetting phase (gas) is disconnected across the system: gas flows by periodically opening critical flow pathways in intermediate-sized pores. While this phenomenon has been observed in two-phase flow, here it is significant at low flow rates, where capillary forces dominate at the pore-scale. Gas movement proceeds in a series of double and multiple displacement events. Implications for the design of three-phase flow processes and current empirical models are discussed: the traditional conceptualization of three-phase dynamics based on analogies to two-phase flow vastly over-estimates the connectivity and flow potential of the gas phase.

6.1.2 Investigations

The motivation behind developing an experimental approach that combines steady-state three-phase flow with pore-scale X-ray imaging is highlighted in section 2.2.4. We show here how the development of such experimental systems allowed us to discover a unique three-phase flow dynamic at steady-state conditions.

Here, in *EXP* 6, we design a new flow cell that enables X-ray imaging at the pore-scale while simultaneously injecting three fluid phases into the rock. We conduct the experiment under capillary-dominated, immiscible gas-oil conditions. We measure three-phase relative permeability by monitoring the pressure drop across the sample, while saturations are obtained from the high-resolution (5.3 μm/voxel) images. We will investigate a saturation history, where the gas fractional flow is first increased and then decreased. We will compare our relative permeability measurements with core-scale data, obtained on the same rock type, and show that there is an agreement in the results, indicating the accuracy and applicability of our method. Furthermore, we will estimate the capillary pressures by extracting the fluid-fluid interfacial curvatures from the images. In addition, we will characterize fluid connectivity, pore occupancy, layer formation and contact angles at different fractional flows.

We show that contrary to the conventional assumption, gas flows in disconnected ganglia when injected simultaneously with oil and water under steady-state conditions in a water-wet rock. Gas progresses through the centre of the pores in the form of discrete blobs surrounded by oil and water layers; it is continuously displaced from the inlet to the outlet by double and multiple displacements. We observe intermittent flow regions, where gas and oil, and water and oil interchangeably occupy the same pores

during steady-state flow. This work suggests that in three-phase flow we may never genuinely attain steady-state conditions at the pore-scale, although we have, macroscopically, a constant saturation, since the fluid arrangement at the pore-scale is constantly fluctuating between locations of local capillary equilibrium.

6.1.3 Experimental Method

In this section, we first provide details of the rock sample and fluids used to perform the three-phase steady-state experiments. We then move on to describe the newly designed flow cell which permits the simultaneous injection of three fluid phases while allowing for the pressure drop to be recorded and high-resolution pore-scale images to be taken. Next, the set of gas, oil, and water fractional flows selected for the experiment are listed in detail. Finally, we describe the X-ray imaging parameters and image processing techniques implemented to analyze the pore-scale images obtained at different fractional flows.

6.1.3.1 Materials

The three-phase steady-state imaging experiment was performed on a Bentheimer sandstone of diameter 1.26 cm, and length 4.23 cm. Bentheimer sandstone has a unimodal pore radii distribution, with a mean pore radius of 30 μm, and consists of around 95% quartz with minor amounts of kaolinite and swellable clay minerals [192]. The pore size distribution is plotted in Fig. A6.1 in Appendix 6. The selected sample has a total porosity of 0.24 measured using the differential imaging method [127], see section 3.1.3.1 for more details. Fig. 6.1 shows the distribution of the image-based porosity across the length of the sample. The absolute permeability (k) of the sample, measured at the experimental conditions, is 1.75 ± 0.03 D ($1.73\times10^{-12} \pm 0.03\times10^{-12}$ m^2).

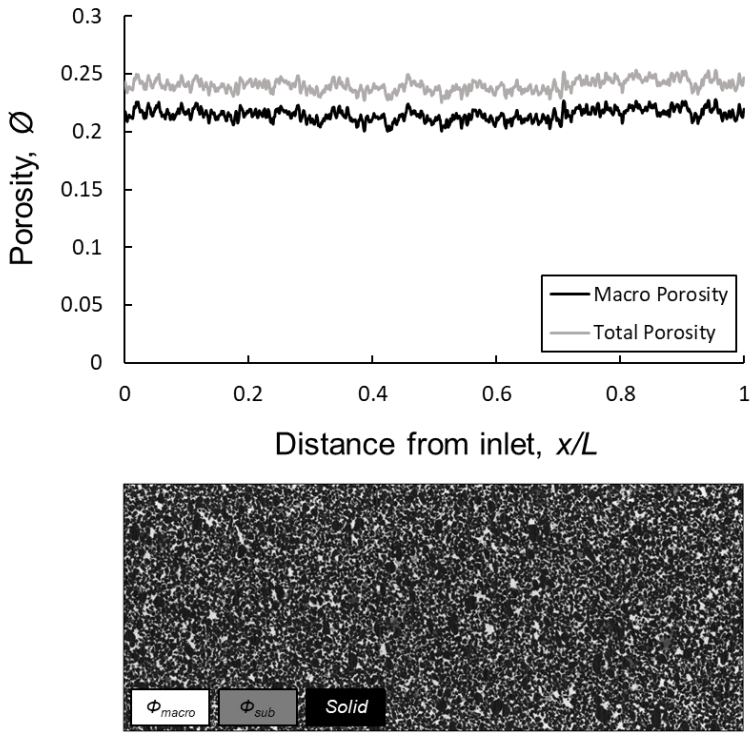

Figure 6. 1. Porosity distribution along the Bentheimer sample characterized using the differential imaging method [127]. Below is a two-dimensional image of the whole sample, highlighting the macro-pores, sub-resolution pores and the solid rock surface. Solid is shown in black, macro-pores in white, and sub-resolution pores in grey.

In terms of fluids, nitrogen (N_2) was used as the gas phase, *n*-decane ($C_{10}H_{22}$) as the oil phase, and deionized water (H_2O) as the water phase. To distinguish between the three fluid phases in the X-ray images, 17.5 wt.% Iododecane ($C_{10}H_{21}I$) and 25 wt.% sodium iodide (NaI) were added to the oil and water phases respectively.

The experimental pore pressure was maintained at 1 MPa, and the temperature at 30 ºC. At these conditions, gas and oil have dynamic viscosities of μ_g = 0.017 mPa·s [193] and μ_o = 4.27 mPa·s [130] respectively, with an interfacial tension of σ_{go} = 11.2 mN· m^{-1} [170]. Oil and gas are immiscible at the selected experimental conditions. Water has a dynamic viscosity of μ_w = 1.40 mPa·s with an interfacial tension of σ_{ow} = 52.1 mN· m^{-1} with oil, and σ_{gw} = 63.7 mN· m^{-1} with gas [130, 170].

The spreading coefficients (C_s) of the phases were calculated using Eq. (2.8). The only positive spreading coefficient is of oil (C_{so} = +0.4 mN·m^{-1}), indicating that it is only possible for oil to spread in layers sandwiched between the other two phases in the pore space.

6.1.3.2 Steady-state flow and imaging apparatus

To perform a three-phase steady-state flow experiment, three fluid phases must be simultaneously injected into the sample while recording the differential pressure drop across the system. While this can be achieved in the lab, the difficult part in our experiment is integrating this process with pore-scale imaging. Acquiring high-resolution, micro-scale images requires the X-ray source to be placed close to the sample. However, needing four injection ports (three ports for fluid injection and one for pressure measurement), would require a large fluid injection piece; therefore, the source must be pushed away from the sample, which reduces the spatial resolution of the images.

To overcome this issue, we designed, in-house, a new coreholder – flow cell – which consists of three primary components: (i) injection piece, (ii) production piece, and (iii) coreholder body, see Fig. 6.2. The injection piece was made of stainless steel and has four injection ports that are in direct contact with the sample inlet. Stainless steel was chosen since it is highly resistant to corrosion and can withstand high operating pressures and temperatures. There is an additional confining port which is used to inject a confining fluid into the coreholder annulus. Fig. 6.2a shows that there is a mixing groove that connects the four injection ports. This groove was placed to allow for the three fluid phases to mix before entering the sample, therefore, preventing the accumulation of the phases on the side of their injection port. The fourth port is needed to measure the pressure at the inlet of the sample. The injection rod is around 12 mm in diameter allowing for X-ray images to be acquired at a resolution of 5.3 μm per voxel which is sufficient to capture the pore-scale properties during steady-state three-phase flow.

The production piece has a single port to allow for the displaced fluid phases to be produced (Fig. 6.2b). The outlet pressure is measured downstream of the production piece, outside the coreholder assembly. The coreholder body is made of a thermoplastic polymer known as Polyether ether ketone (PEEK), as opposed to more conventional carbon fibre designs [138]; PEEK is X-ray transparent. The PEEK walls are around 3 mm thick which results in a stiff cylindrical design that shows no/little movement as it rotates when mounted with stainless steel end pieces at high pressure and temperature conditions. Minimizing movement during rotation is key to performing repeat X-ray imaging experiments.

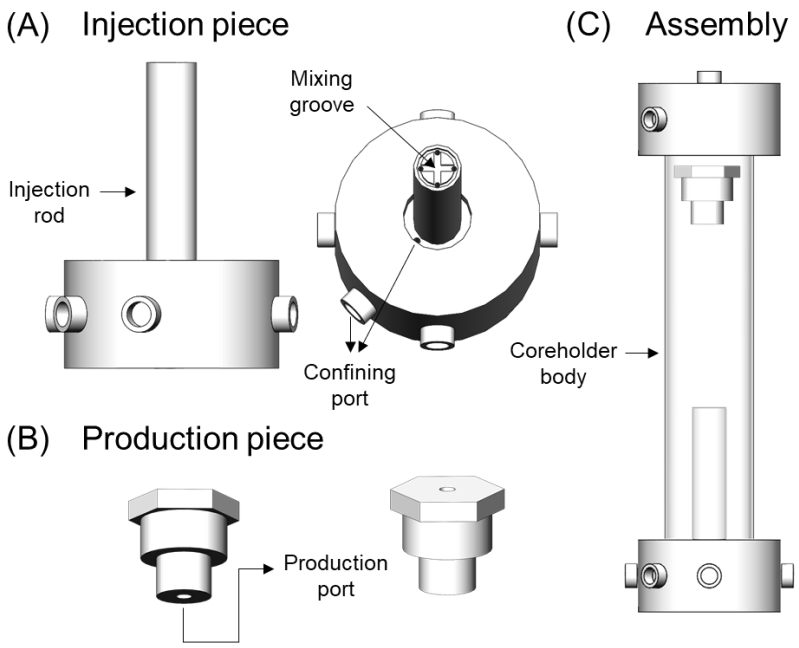

Figure 6. 2. A schematic of the new coreholder design which allows for combining steady-state three-phase relative permeability measurements with pore-scale imaging. The design assembly consists of three main components: (i) injection piece, (ii) production piece, and (iii) coreholder body. Refer to the text for a detailed description of the coreholder design.

The combined pore-scale imaging and steady-state three-phase flow apparatus is shown in Fig. 6.3. The apparatus consisted of five Teledyne Isco pumps, a Keller PD-33X differential pressure transducer, the newly designed PEEK coreholder and a Zeiss Xradia 510 micro-CT scanner.

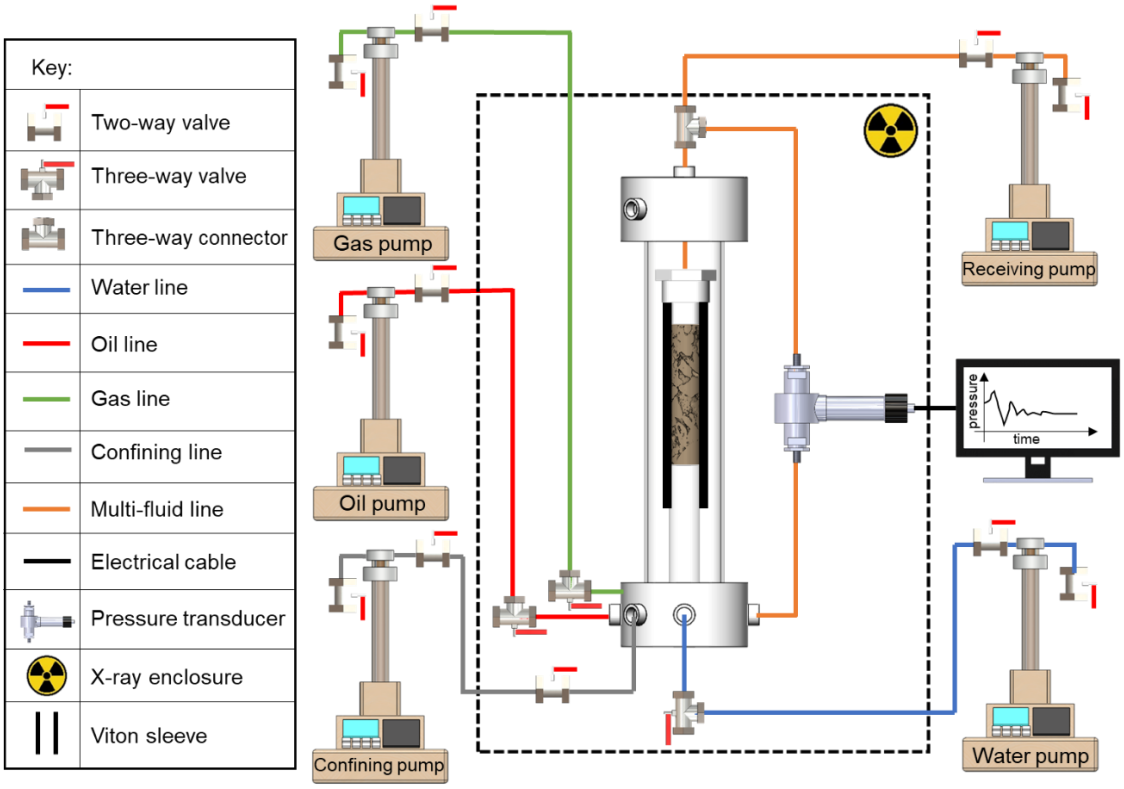

Figure 6. 3. The combined steady-state three-phase flow and pore-scale X-ray imaging apparatus. The dashed line represents the scanner enclosure. The coreholder, pumps, flow lines, valves, and pressure transducer in the experiment were assembled as shown in the schematic diagram.

6.1.3.3 Three-phase relative permeability experiment

The steady-state three-phase relative permeability experiment was performed with constant flow rates at 30 °C and 1 MPa pore back pressure. A net confining pressure of 2 MPa was applied at all fractional flows, and the differential pressure was measured with an accuracy of ±0.03 kPa. The fluids were always injected from the bottom of the sample as shown in Fig. 6.3. The impact of gravity on the flow of fluids during the experiment was assessed using the Bond number, shown in Appendix 6. The Bond number indicates that at the pore-scale, the gravitational forces are small compared to the capillary pressure and therefore are insignificant. However, they could have an effect on the macroscopic properties, such as saturation, at the full sample length-scale. Nonetheless, as shown later in section 6.1.4.5, we see almost constant fluid saturations in the experiment and no evidence of a capillary pressure gradient.

In this study, three-phase steady-state conditions were reached at various gas, oil, and water fractional flows (f_g, f_o, and f_w) by keeping constant fluid flow rates with a total flow rate of Q_t = 0.8 mL/min. The fractional flows selected for the experiment are listed in Table 6.1. The waiting time for each fractional flow to reach steady-state conditions was at least 12 hr. After that, we waited until the differential pressure was constant over a period of at least 1 hr, to record the pressure drop and start X-ray imaging to determine the fluid saturations.

Table 6. 1. The set of gas, oil and water fractional flows at which steady-state conditions were reached in the three-phase flow experiment. *f* and *Q* refer to the fractional flow and the flow rate respectively. Subscripts *w*, *o* and *g* refer to the water, oil and gas phases respectively. The total flow rate in the experiment was Q_t = 0.8 mL/min. Gas was introduced into the system in flooding step 4, with maximum gas fractional flow f_g = 1 reached in step 6.

Flooding step	f_w	f_o	f_g	Q_w mL/min	Q_o mL/min	Q_g mL/min
1	1	0	0	0.8	0	0
2	0	1	0	0	0.8	0
3	0.5	0.5	0	0.4	0.4	0
4	0.25	0.25	0.5	0.2	0.2	0.4
5	0.125	0.125	0.75	0.1	0.1	0.6
6	0	0	1	0	0	0.8
7	0.125	0.125	0.75	0.1	0.1	0.6
8	0.1875	0.1875	0.625	0.15	0.15	0.5
9	0.25	0.25	0.5	0.2	0.2	0.4
10	0.3125	0.3125	0.375	0.25	0.25	0.3
11	0.375	0.375	0.25	0.3	0.3	0.2

The experiment was performed under capillary-dominated conditions. As a characteristic of water-wet media with spreading oil layers surrounding the gas, we assume that gas and water can only displace oil, while oil can displace both gas and water; gas and water cannot directly displace each other as we will show later. Table 6.2 lists the possible displacement capillary numbers at different fractional flows during the experiment. The highest capillary number is 3.15×10^{-6} corresponding to a displacement of gas by oil in flooding step 11, see Table 6.2, which is still in the capillary-dominated flow regime; see Fig. A6.7 in Appendix 6.

Table 6. 2. The gas-oil, oil-gas, oil-water and water-oil capillary numbers calculated at different fractional flows during the steady-state three-phase flow experiment. Capillary numbers were calculated using $Ca_{ij} = \mu_i q_i/\sigma_{ij}$, where σ_{ij} is the interfacial tension between the phases, μ_i is the viscosity of the displacing fluid and q_i is its Darcy velocity. A gas-oil number represents the capillary number calculated when gas displaces oil in the pore space, as is the case for the other pairs. Refer to Table 6.1 for the fractional flows of each flooding step.

Flooding step	$Ca_{[go]}$	$Ca_{[og]}$	$Ca_{[ow]}$	$Ca_{[wo]}$
1	-	-	-	-
2	-	-	1.81×10^{-6}	-
3	-	-	9.05×10^{-7}	3.39×10^{-7}
4	1.79×10^{-8}	2.10×10^{-6}	4.52×10^{-7}	1.69×10^{-7}
5	2.68×10^{-8}	1.05×10^{-6}	2.26×10^{-7}	8.48×10^{-8}
6	3.57×10^{-8}	-	-	-
7	2.68×10^{-8}	1.05×10^{-6}	2.26×10^{-7}	8.48×10^{-8}
8	2.23×10^{-8}	1.57×10^{-6}	3.39×10^{-7}	1.27×10^{-7}
9	1.78×10^{-8}	2.10×10^{-6}	4.52×10^{-7}	1.69×10^{-7}
10	1.34×10^{-8}	2.63×10^{-6}	5.65×10^{-7}	2.12×10^{-7}
11	8.94×10^{-9}	3.15×10^{-6}	6.78×10^{-7}	2.54×10^{-7}

The selection of the set of fractional flows was done with special care to follow a certain saturation history and avoid any unwanted irreversible switch between drainage and imbibition displacement processes. In this experiment, we investigate the impact of a saturation history, where the gas fractional flow is first increased and then decreased, on three-phase relative permeability. To do so, we adopt an approach in which we keep the oil and water saturation changes in the same direction – while keeping oil and water flow rates the same (treating them as a single phase) – and change the gas saturation in the opposite direction [35, 194-197]. This can be seen in Table 6.1, where, first, the gas flow rate is increased and oil and water flow rates are decreased in steps 4, 5 and 6, and then gas rate is decreased and oil and water are increased in steps 7, 8, 9, 10 and 11.

The experimental protocol followed to initiate the steady-state three-phase flow X-ray imaging experiment is described below:

1. First, the sample was wrapped with aluminium foil and inserted in a Viton sleeve. The bottom and top ends of the Viton sleeve were mounted on the injection and production pieces respectively as shown in Fig. 6.3. The Viton sleeve sealed the rock sample from coming into contact with the confining fluid.
2. The coreholder was then placed inside the scanner and all the pumps and flow lines were connected as shown in Fig. 6.3. The differential pressure transducer was connected to the inlet and outlet to measure the pressure drop across the sample.
3. The empty annulus space between the Viton sleeve and the PEEK coreholder body was filled with the confining fluid, deionized water, and a net confining pressure of 2 MPa was applied. At this point a dry scan of the sample was acquired at 5.3 µm/voxel resolution.
4. 200 pore volumes (PV) of water (25 wt.% *NaI*) were injected into the sample to fully saturate the pore space and the pore pressure was raised to 1 MPa using a back-pressure pump. Water was injected at four flow rates (0.2, 0.4, 0.6 and 0.8 mL/min) while recording the stable pressure drop to calculate the absolute permeability of the sample, which was found to be $1.73\times10^{-12} \pm 0.03\times10^{-12}$ m^2 (k = 1.75 ± 0.03 D). A 5.3 µm/voxel water saturated scan was acquired at this point, which allowed for the characterization of the porosity distribution, including sub-resolution porosity, of the sample using the differential imaging method [127], see Fig. 6.1.
5. Oil (17.5 wt.% $C_{10}H_{21}I$) was injected into the sample at a flow rate of 2 mL/min to reach the irreducible water saturation. The flow rate was then dropped to 0.8 mL/min to measure the pressure drop and a scan was acquired.

6. Water and oil were then simultaneously injected at f_w = 0.5, with a total flow rate Q_t = 0.8 mL/min, to initiate the sample for the three-phase relative permeability experiment. After reaching steady-state conditions between oil and water, the pressure drop was recorded, and a scan of the sample was acquired.
7. Gas, oil and water were then simultaneously injected into the sample at the fractional flows listed in Table 6.1. The pressure drop was recorded and scans were taken once steady-state had been reached for each fractional flow to calculate the three-phase relative permeabilities. The gas flow rate was not pumped when f_g = 1 (flooding step 6, see Table 6.1).

After the experiment, the rock was taken out and cleaned using DI water to remove any residual gas and oil. The sample was then prepared for a repeat experiment, following the same steps mentioned here. In the repeat experiment, we only investigated one set of fractional flows (f_g = 0.5, $f_{w,o}$ = 0.25) during both increasing and decreasing gas flow paths. The repeat experiment was performed to verify if the gas phase was disconnected during steady-state injection, see section 6.1.4.4; therefore no pressure measurements were recorded.

6.1.3.4 X-ray image acquisition and processing

For every fractional flow, after reaching steady-state conditions, three-dimensional images of the sample and fluids within it were acquired using the ZEISS Xradia 510 Versa scanner. The photon energy and power were set to 80 keV and 7 W respectively at the X-ray source, with a 360° sample rotation angle. Air was the only filter used between the source and sample. A flat panel with a large field of view (12.45 mm × 12.45 mm × 10.23 mm) at a resolution of 5.3 µm/voxel was employed at the detector. The exposure time was set to 1.60 s with a total of 3,201 projections. Five images, with a 3.55 mm vertical overlap, were acquired during each scan to capture the length of the whole sample.

The images acquired were then reconstructed, normalized, registered, and stitched to obtain three-dimensional steady-state images of the rock and fluids at each fractional flow, see Figs. 6.4 and 6.5.

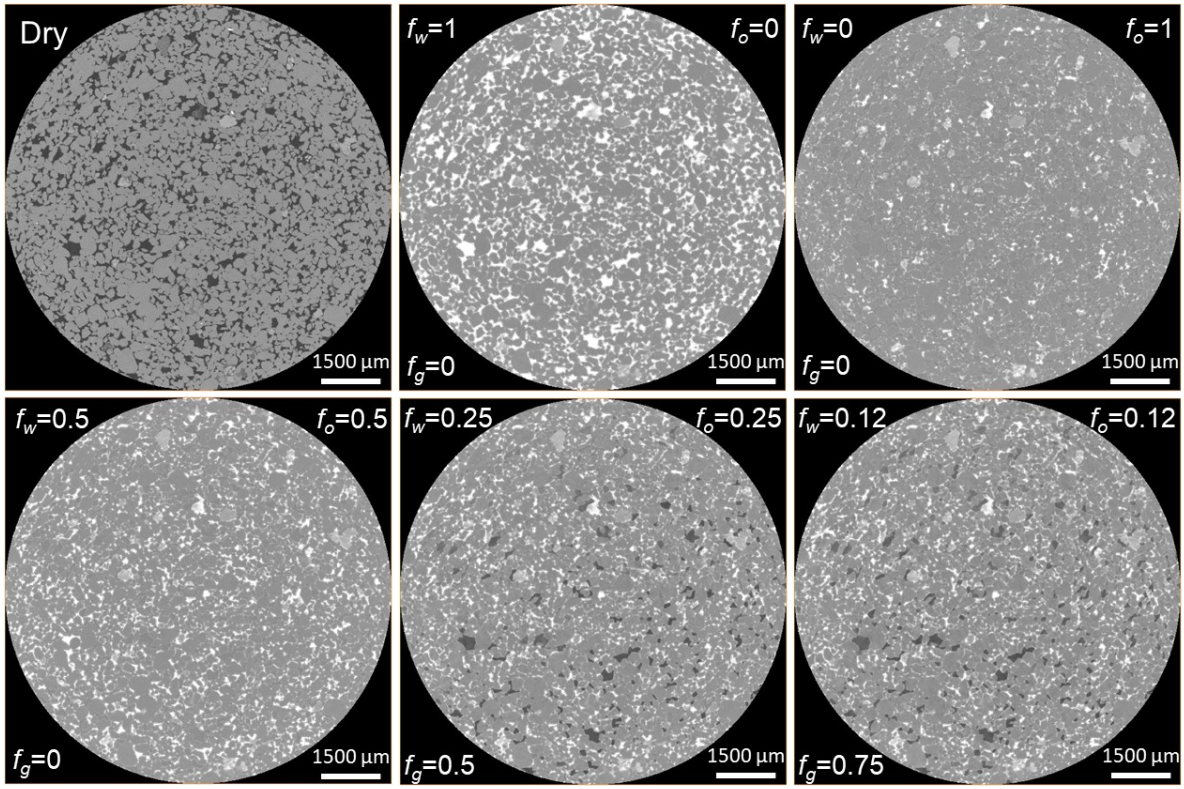

Figure 6. 4. Two-dimensional cross-sectional raw images of the sample acquired during the steady-state three-phase relative permeability experiment. In each image, the gas, oil and water fractional flows (f_g, f_o, and f_w) are stated. The rock, oil, gas, and water are shown in light grey, dark grey, black, and white respectively.

Image segmentation was then performed to obtain quantitative information, including saturations, fluid-fluid curvatures and surface areas. First, to make the segmentation process simpler we decided to ignore the fluid saturations in the sub-resolution porosity; sub-resolution porosity was segmented as a part of the rock phase – except when we characterized the porosity distribution along the sample in Fig. 6.1. This assumption is reasonable, as in water-wet systems, the sub-resolution porosity remains 100% water saturated.

As mentioned in section 6.1.2, we see some regions of the pore space with intermediate grey-scale values. We hypothesize that these are places where – during the time of the scan – the pore space was occupied for some time by oil and for some time by gas or water. In theory, therefore, the fluids in the macro-pores should be segmented into seven different phases: (i) water; (ii) oil; (iii) gas; (iv) gas from intermittent gas-oil regions; (v) oil from intermittent gas-oil regions; (vi) oil from intermittent oil-water regions; and (vii) water from intermittent oil-water regions. However, this is impractical, especially with our current image segmentation capabilities. Therefore, to simplify the segmentation process, while minimizing the impact on the quantitative results we decided to do the following: (1) ignore the oil-water intermittent flow regions, since oil-water intermittency does not occur very often – that is, ignore phases (vi) and (vii); (2) segment the gas from intermittent gas-oil regions as part of the gas phase – combining phases (iii) and (iv); and (3) segment the oil from intermittent gas-oil regions as part of the oil phase – combining phases (ii) and (v). This leaves us with three phases to segment from the pore-scale images.

To segment the images into these three phases, we used an approach that combines differential imaging with the interactive thresholding segmentation technique. Intermittent regions display a grey-scale value that is in-between the grey-scale values of the two intermittent phases. Therefore, using differential

imaging was needed to widen the grey-scale histograms between the intermittent phases, while thresholding was used to assign 50% of the intermittent region to each phase.

The segmentation procedure was as follows: (i) the rock phase was directly segmented from the dry scan, and was used subsequently in all the images; (ii) for each fractional flow, the image was subtracted from the high contrast water scan (f_w = 1), eliminating the water and rock phases, which leaves the oil and gas phases only in the differential image, with wide grey-scale histograms; (iii) the interactive thresholding technique was then used to directly segment the oil and gas phases from the differential images; finally (iv) the segmented oil and gas phases were then added to the segmented rock phase in step (i), and the rest of the unassigned voxels were considered as the water phase. The segmentation procedure is explained in more detail in Fig. A6.2 in Appendix 6.

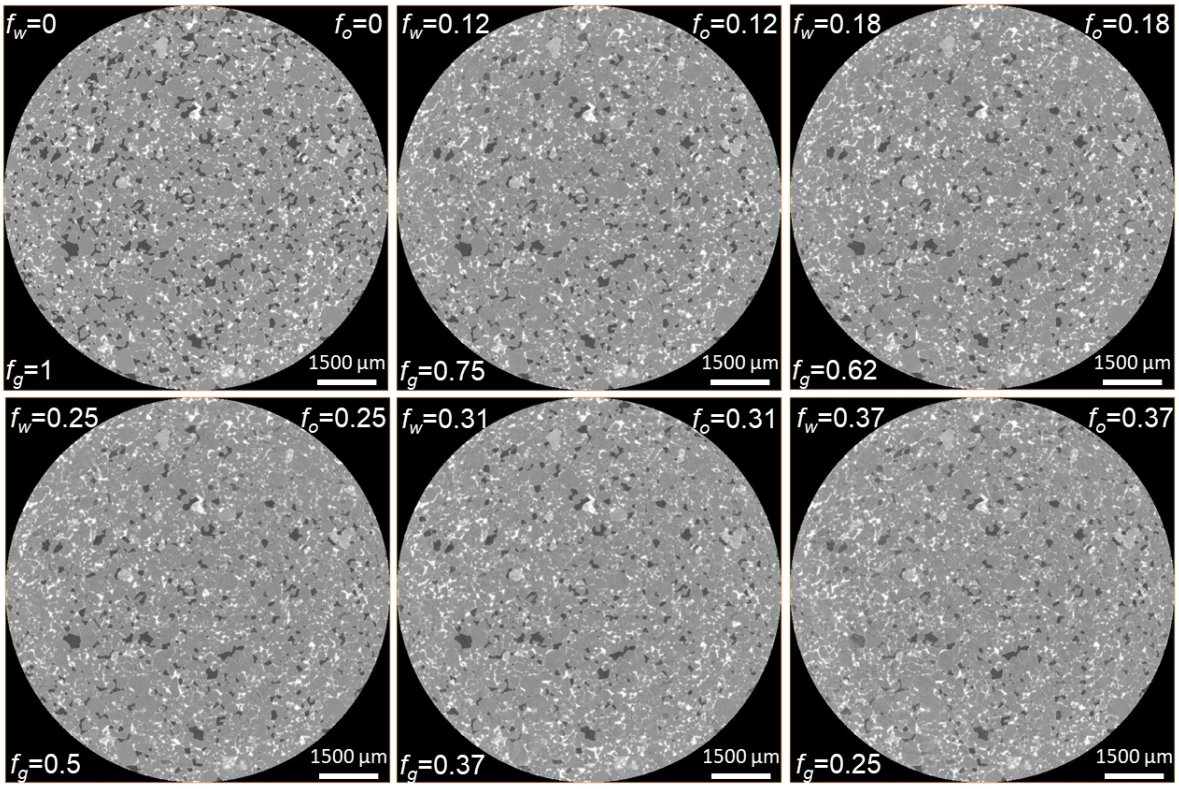

Figure 6. 5. Two-dimensional cross-sectional raw images of the sample acquired during the steady-state three-phase relative permeability experiment. In each image, the gas, oil and water fractional flows (f_g, f_o, and f_w) are stated. The rock, oil, gas, and water are shown in light grey, dark grey, black, and white respectively.

6.1.3.5 Data analysis

6.1.3.5.1 Relative permeability

The three-phase relative permeabilities were calculated using the multiphase flow Darcy equation, (2.6) [18]:

$$k_{rg} = \frac{q_g \mu_g L}{\Delta P k} \tag{6.1}$$

$$k_{ro} = \frac{q_o \mu_o L}{\Delta P k} \tag{6.2}$$

$$k_{rw} = \frac{q_w \mu_w L}{\Delta P k} \tag{6.3}$$

where k_r is the relative permeability, q is the Darcy velocity (flow rate per unit area), μ is the viscosity, k is the absolute permeability, ΔP is the pressure drop, and L is the sample length. Subscripts g, o and w refer to the gas, water and oil phases respectively.

While the pressure drop was measured using the differential pressure transducer, the fluid saturations at each fractional flow were measured on the segmented pore-scale images. Only fluid saturations in the macro-pore space were considered, see section 6.1.3.4 for more details.

6.1.4 Results and Discussion

Here we present the pore-scale findings obtained, using X-ray imaging, from the steady-state three-phase flow experiment. First, in section 6.1.4.1, we present measurements of the fluid-fluid contact angles to confirm the water-wet state of the rock, followed by a characterization of the pore occupancy in section 6.1.4.2. Then, in section 6.1.4.3, we display measurements of the fluid-fluid and fluid-solid specific interfacial areas. These results, alongside the fluid connectivity in section 6.1.4.4, are used to explain the three-phase relative permeability behaviour in section 6.1.4.5. Evidence of intermittent flow regions is presented in section 6.1.4.6. The measured local capillary pressures between the three fluid pairs are shown in section 6.1.4.7. Finally, in section 6.1.4.8, three-dimensional images illustrating the occurrence of double displacement processes are presented.

Fig. 6.6 shows the constructed three-dimensional images of the fluid configurations in the pore space at different fractional flows.

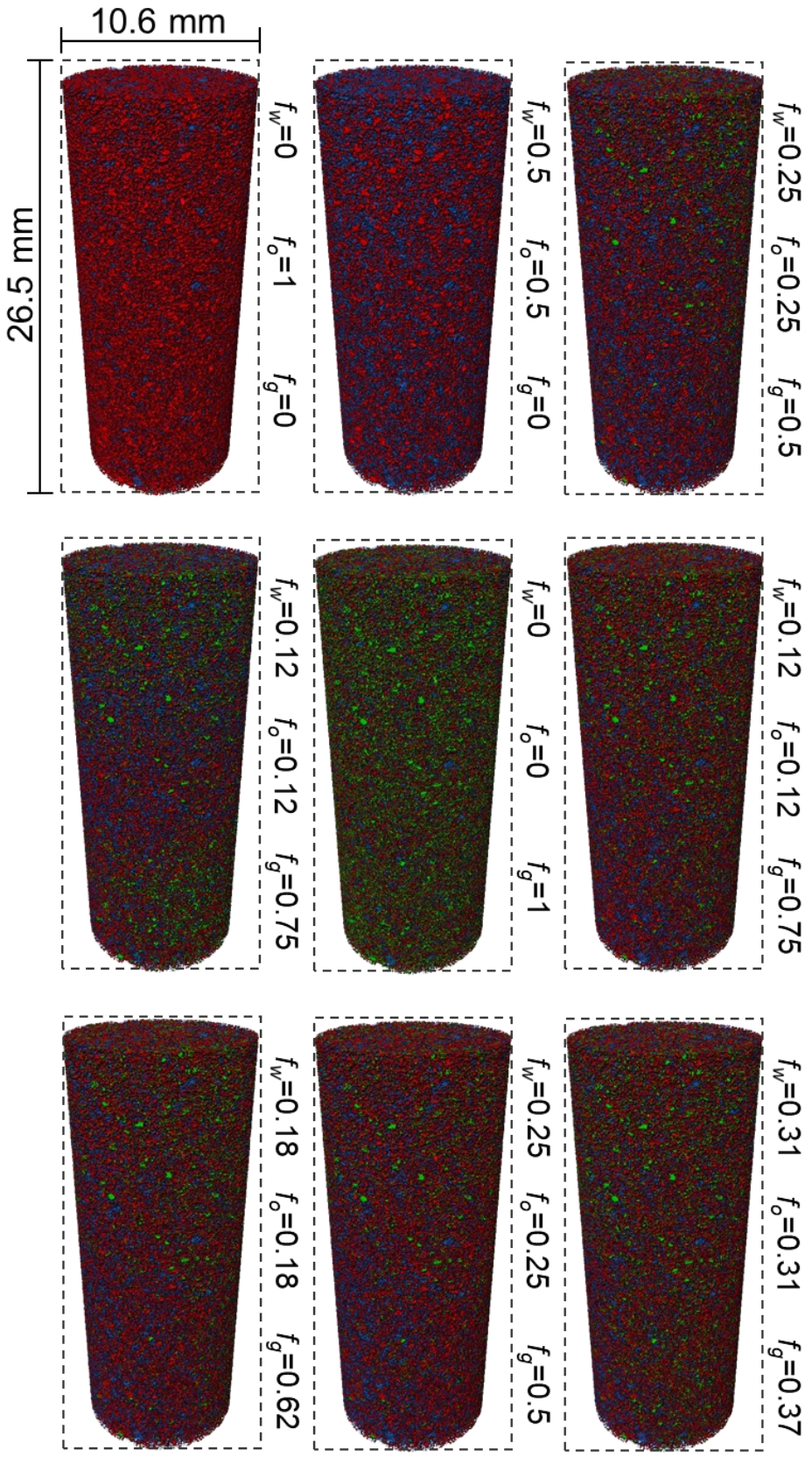

Figure 6. 6. Three-dimensional volume rendering of the fluid configurations in the pore space during the three-phase steady-state experiment at different fractional flows. Gas is shown in green, water in blue and oil in red. The rock is rendered transparent. Gas, oil, and water fractional flows (f_g, f_o, and f_w) are stated.

6.1.4.1 *In situ* wettability characterization

The oil-water, gas-oil, and gas-water contact angles were characterized on the same segmented subvolume, of size 2.65 mm × 2.65 mm × 2.65 mm, at different fractional flows using the same automated algorithm that measures the geometric angle on the three-phase contact line between each fluid pair as used previously in the thesis [30].

The geometric oil-water contact angles, measured through the denser phase (water), are shown in Fig. 6.7. The mean oil-water contact angle, for all fractional flows, is 61° ± 16°, confirming the water-wet nature of the sample. This is also evident from the two-phase pore-scale images shown in Fig. 6.7 (right), where oil resides in the centre of the pores surrounded by water wetting layers. Furthermore, Fig. 6.7 (left) illustrates that there was no wettability alteration throughout the flooding experiment; the contact angle between oil and water remains approximately constant. This also indicates that the geometric oil-water contact angle is independent of saturation history; the oil-water angle was not impacted by switching the saturation path.

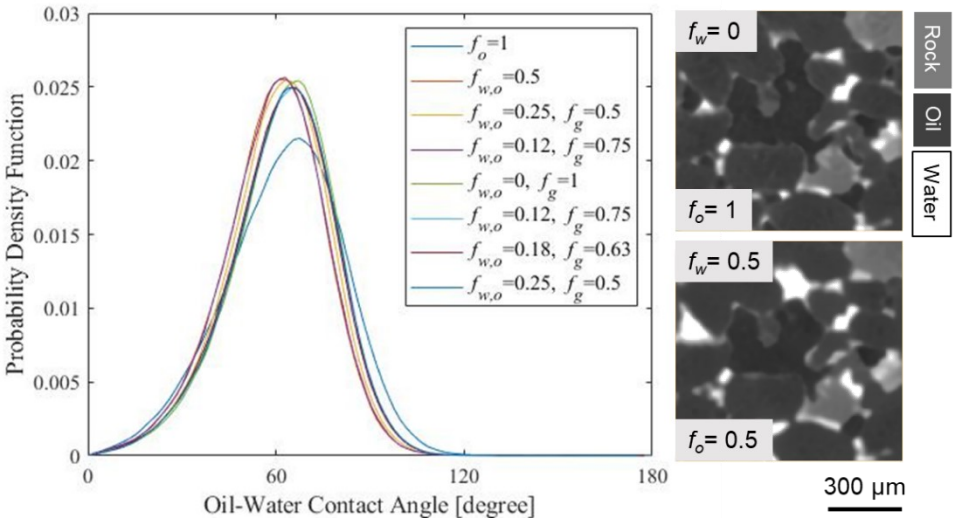

Figure 6. 7. (Left) Probability density function of the *in situ* measured oil-water contact angles throughout the steady-state three-phase flow experiment at different fractional flows. (Right) Two-dimensional pore-scale images of the same pore, at two different fractional flows, illustrating that oil resides in the centres in the presence of water, confirming the water-wet state of the rock sample. The contact angles were measured through the denser phase, water, using an automated algorithm developed by AlRatrout et al. [30]. f_w and f_o refer to water and oil fractional flows respectively.

As expected, due to the positive initial oil spreading coefficient (C_{so} = +0.4 mN·m^{-1}), see section 6.1.3.1, oil spreads in layers surrounding the gas phase which results in an effective gas-oil contact angle of zero; oil is strongly wetting to gas. This is evident from Fig. 6.8, where the three-dimensional arrangement of gas, oil and water in a single pore is presented; gas is shown in green, oil in red, water in blue, while the rock phase is rendered semi-transparent (grey). As soon as gas contacts oil, oil spreads in layers sandwiched between gas and water in the pore space. The presence of oil in layers prevents gas from directly contacting water in the pore space; therefore, we were unable to measure the geometric contact angle between gas and water. The measured contact angles are consistent with measurements previously made on water-wet rocks at immiscible gas-oil conditions [16, 29].

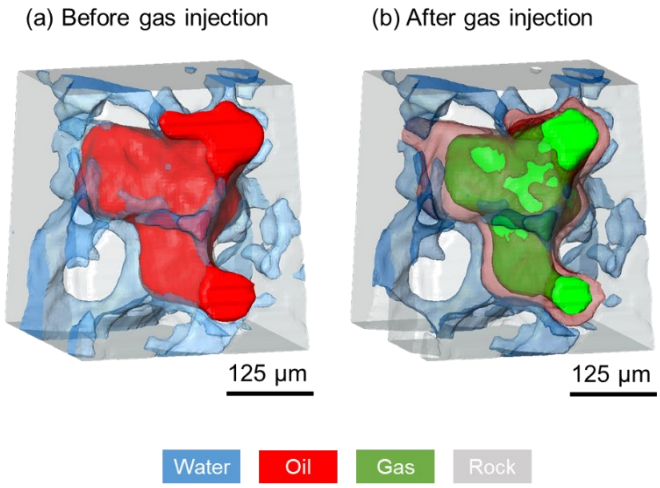

Figure 6. 8. Three-dimensional representation of the fluids arrangement in a single pore (a) before gas injection, and (b) after gas injection. Oil is shown in red, water in blue, gas in green, while the rock is rendered semi-transparent (grey).

6.1.4.2 Pore occupancy

The size of the pores occupied by the three fluid phases – also known as pore occupancy – was determined; we do not consider intermittency and assign a unique occupancy dependent on the average grey-scale level. Pore occupancy was characterized on images, of size 7.95 mm × 7.95 mm × 15.9 mm, located in the centre of the sample, for all fractional flows, where gas fractional flow (f_g) is first increased while oil and water (f_o and f_w) are decreased, and then gas is decreased while oil and water are increased, see Fig. 6.9.

Fig. 6.9a shows that when oil is first injected into the water-wet rock, it invades the largest pores confining water to smaller ones, as expected [16]. During the subsequent injection of oil and water, water imbibes into the corners in wetting layers, displacing oil in the smaller pores and restricting it to flow in the larger pores. Some oil gets trapped in the centre of the pores surrounded by water wetting layers, see Fig. 6.8a.

During the simultaneous injection of gas, oil and water, gas replaces oil in the larger pores, forcing it to flow in spreading layers in the medium sized pores, while water flow is restricted to smaller pores, see Fig. 6.9c. Some of the oil that was trapped during two-phase flow gets reconnected in regions of the pore space smaller than those occupied before as a consequence of oil spreading. As the gas fractional flow is increased – the oil and water flows decrease – Figs. 6.9d and 6.9e, gas squeezes more oil and water into smaller sized pores. From this we can establish a clear wettability order in the system, where water is the most-wetting phase, residing in the smallest pores, gas is the most non-wetting phase, occupying the biggest pores, while oil, is the intermediate-wet phase, spreading in layers sandwiched between gas and water, and filling medium sized pores; this wettability order is also evident from Fig. 8b. This is consistent with previous experiments conducted on water-wet media at immiscible gas-oil conditions [16, 41, 42].

However, we observe a unique pore occupancy behaviour as the saturation path is reversed, i.e., the gas fractional flow is decreased, while the oil and water fractional flows are increased. There is little/no change in the three-phase pore occupancy when f_g is decreased, as opposed to increasing f_g, which implies that pore occupancy is a function of saturation history, see Figs. 6.9f, 6.9g, 6.9h and 6.9i. This behaviour can be ascribed to double capillary trapping – gas trapping by oil and oil trapping by water – which can permanently trap gas in the pore centres. Therefore, regardless of the increase in oil and water fractional flows, they would not be able to displace the trapped gas phase; gas remains trapped in

the same pores. Also, since oil and water are injected at the same flow rate, they maintain their previously established pore occupancy. However, this can only be confirmed by looking at the fluid connectivity and saturations as we will show in sections 6.1.4.4 and 6.1.4.5. Furthermore, this can have an impact on the relative permeability of oil and water, as having a trapped gas phase can restrict their flow in the pore space.

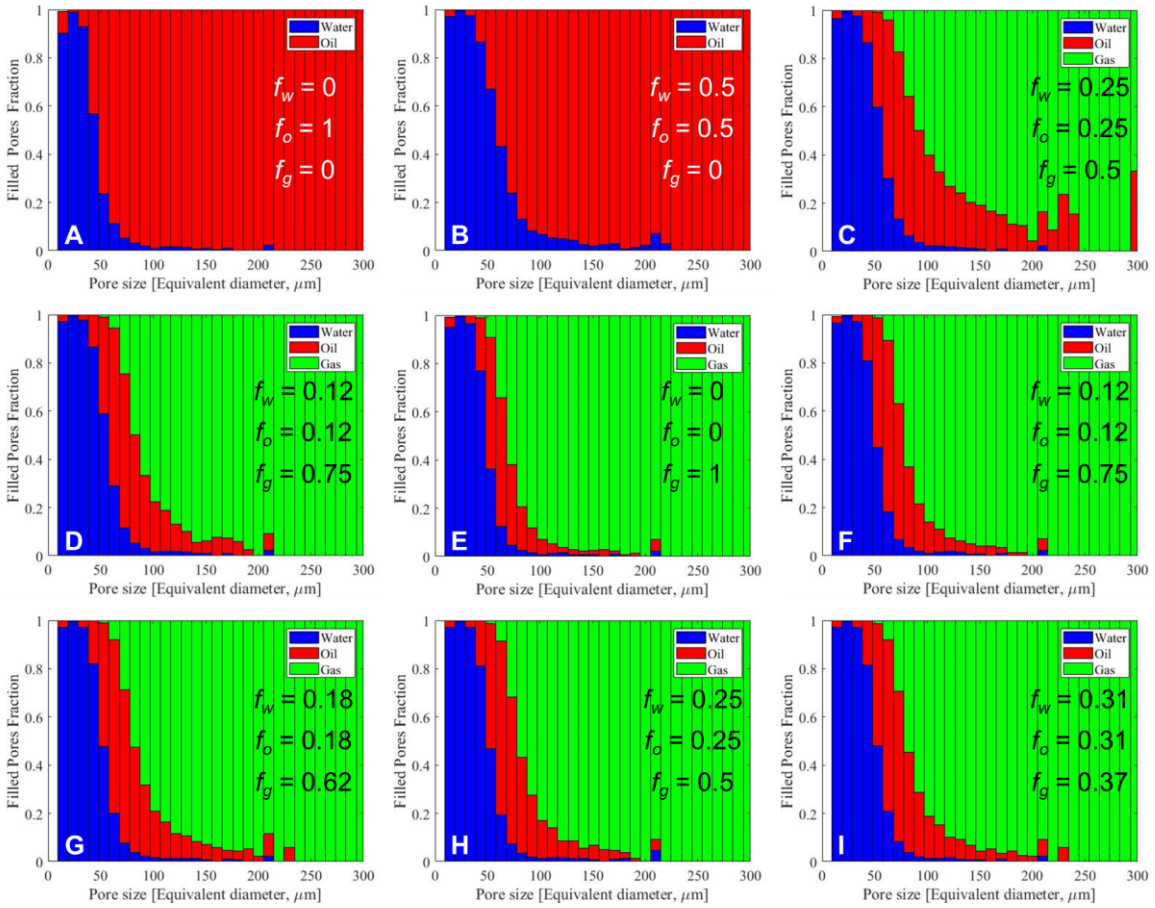

Figure 6. 9. Stacked bar charts showing the pore occupancy in the pore space of the rock at different fractional flows. The phase that occupies the centre of the pore is considered to occupy the pore. The size of the pores is determined by fitting them with inscribed spheres – the diameter of the sphere is the diameter of the pore. Pore occupancy was quantified on images of size 7.95 mm × 7.95 mm × 15.9 mm. Water is shown in blue, oil in red, and gas in green. Gas, oil, and water fractional flows (f_g, f_o, and f_w) are stated in the respective images.

6.1.4.3 Interfacial areas

Fig. 6.10 shows measurements of the specific interfacial areas – area per unit volume – between the fluids and the fluids and solid quantified on segmented images of the whole sample at different fractional flows: intermittency is not accounted for – instead a single-phase label was assigned to all voxels based on their grey-scale values. This meant that an intermittent voxel was either assigned to be gas or oil dependent on the nearest grey-scale value.

The oil-water specific interfacial area remains constant throughout the two- and three-phase steady-state displacements, with values around 1 mm^{-1}, see Fig. 6.10a. The specific interfacial area between oil and water is independent of saturation history under three-phase flow conditions, since the area is dominated by the contact between water in wetting layers close to the solid surface and oil either occupying medium-sized pores, or as a spreading layer surrounding gas. The gas-oil specific area, Fig. 6.10d, is slightly higher than the oil-water one, which can be ascribed to oil being more wetting to gas, than water is wetting to oil; this is reflected in the gas-oil and oil-water contact angles, where θ_{go} = 0°

compared to weakly wetting θ_{ow} = 61° ± 16° (section 6.1.4.1) as well as the lower gas-solid area compared to oil-solid. In contrast to the oil-water specific area, the gas-oil area appears to be a function of the saturation history; the gas-oil area remains roughly constant as the gas fractional flow is increased but shows a considerable change when it is decreased, even though the gas saturation is almost the same: as discussed below, this could be a result of intermittency. The gas-water interfacial area is zero since spreading oil layers prevent direct gas-water contact in the pore space. Oil spreading around gas also reduces the gas-solid specific area, see Fig. 6.10e.

Similar to the gas-oil specific area, the water-solid and oil-solid areas are impacted by the saturation history under three-phase conditions, see Figs. 6.10b and 6.10c. The huge variability in the gas-oil, gas-solid, and water-solid areas observed around the same saturation, when the gas fractional flow is decreased and oil and water fractional flows are increased can imply that the fluid configurations are constantly fluctuating between locations of local capillary equilibrium, despite having, macroscopically, constant saturations. This phenomenon is discussed in more detail in section 6.1.4.6. Water-solid and oil-solid areas are the highest in the pore space, with a slightly larger water-solid area due to water residing in wetting layers close to the solid surface.

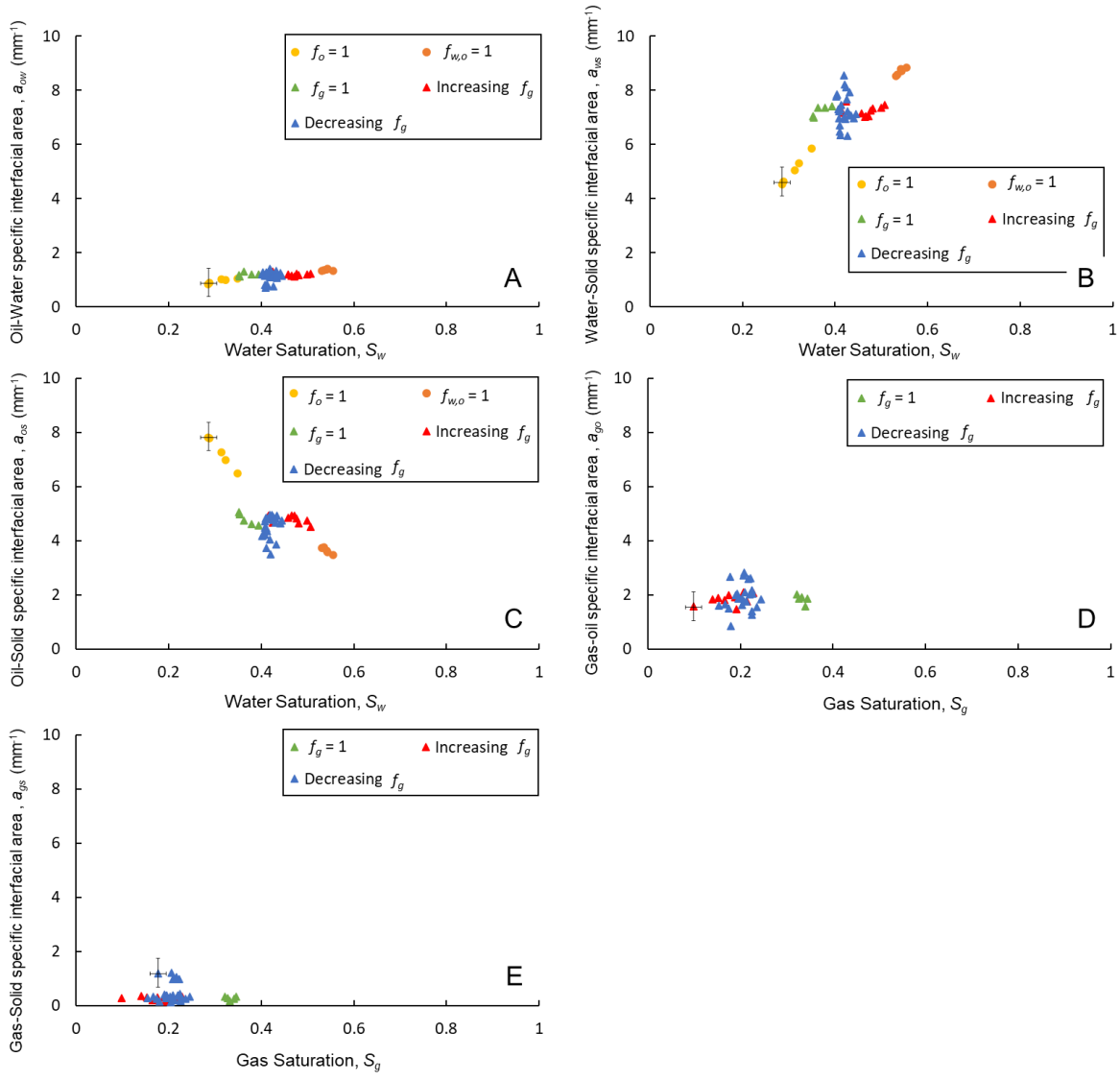

Figure 6. 10. Specific interfacial areas between (a) oil and water, (b) water and solid, (c) oil and solid, (d) gas and oil, and (d) gas and solid measured on segmented images of the whole sample throughout the flooding experiment. Error bars represent uncertainty in the measurements.

6.1.4.4 Fluid connectivity

Here, we assess the fluid connectivity in the pore space both qualitatively and quantitatively in Figs. 6.11 and 6.12, and Table 6.3. To qualitatively examine the connectivity, the fluids were first isolated from the segmented images, and each disconnected object, in the image of the isolated phase, is labelled with a distinct colour. Again, all voxels were given a unique phase label: intermittent regions were assigned to either gas or oil phases dependent on the nearest grey-scale value. Figs. 6.11 and 6.12 show in three-dimensions the *in situ* connectivity of the gas and oil phases respectively at different fractional flows – a large colour range represents a poorly connected phase, while a narrow colour distribution indicates better connectivity.

We observe a distinct gas flow pattern during the steady-state flow of gas, oil, and water in the water-wet rock, see Fig. 6.11. Gas, the most non-wetting phase, advances through the pore space in the form of disconnected ganglia; gas is not connected although it is continuously injected into the sample. This gas flow pattern contradicts the conventional assumption that the gas phase is connected in the larger pores in water-wet rocks at steady-state conditions, which is implemented in current three-phase flow models. Hence, by combining pore-scale imaging with steady-state three-phase flow, it has been discovered that gas, in fact, flows in disconnected clusters when injected simultaneously with oil and water in a water-wet system. Disconnected unsteady-state gas flow has been previously observed in a strongly oil-wet three-phase system, where gas was intermediate-wet, using synchrotron X-ray source, section 4.2, but not over a range of fractional flows in steady-state in a water-wet system.

Furthermore, we see that disconnected gas flow persists under both increasing gas fractional (f_g) – decreasing oil and water fractional flows (f_o and f_w) – and decreasing f_g (increasing f_o and f_w). This demonstrates that gas never connects across the sample, unless $f_g = 1$, when only gas is flowing, see Fig. 6.11. Therefore, we attribute the flow of gas in disconnected clusters when injected simultaneously with oil and water to the swelling of oil and water in the throats – the restrictions between the pores – continuously trapping gas in the pore centres. Since water and oil invade the pore space in an imbibition process, in the presence of gas, their layers thicken and coalesce in the throats disconnecting the gas phase. Gas is considered trapped in a double capillary trapping mechanism. Therefore, the only way for gas to progress through the pore space is through double and multiple displacement processes, as we will show in section 6.1.4.8. The disconnected flow pattern can have huge implications on the gas relative permeability as we will show in the next section. Moreover, it shows that subsequent water injection, after gas injection, to trap gas may be unnecessary in gas storage applications as gas naturally gets disconnected in the pore space [18]. However, intermittent pathways are not included in this analysis which, in theory, can improve the gas connectivity in the pore space.

As mentioned in section 6.1.3.3, we repeated the experiment in the same sample at one set of fractional flows (f_g = 0.5, $f_{w,o}$ = 0.25) during both increasing and decreasing gas flow paths to confirm this observation of disconnected gas flow at steady-state conditions. The connectivity results in the repeat experiment are shown in Fig. A6.3 in Appendix 6. We find that in the repeat experiment gas was also disconnected with positive normalized Euler characteristics of 31 mm^{-3} and 25 mm^{-3} during increasing and decreasing gas flow paths respectively. These values are even larger than the Euler characteristics measured in the main experiment at the same fractional flows in the two flow paths, 11 mm^{-3} and 16 mm^{-3} respectively and reinforce the main conclusion that the gas phase is disconnected.

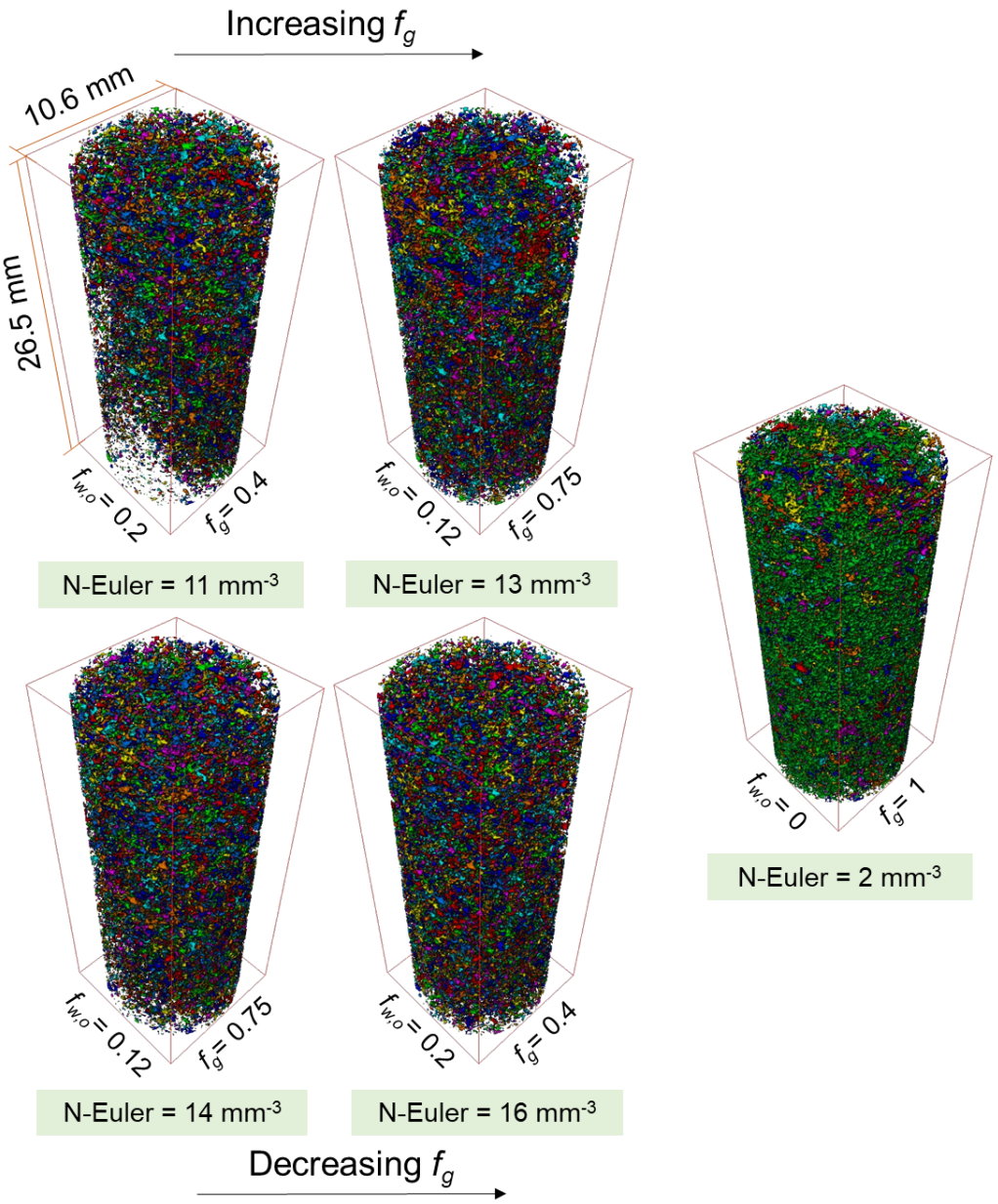

Figure 6. 11. Three-dimensional maps of the *in situ* gas connectivity in the pore space of the water-wet rock under three-phase steady-state conditions at different gas, oil, and water fractional flows. Each disconnected cluster is labelled with a different colour. Gas, oil and water fractional flows (f_g and $f_{w,o}$) are stated. N-Euler refers to the normalized Euler characteristic listed in Table 6.3. Images on top are acquired during the increasing gas fractional flow path – decreasing oil and water – while on the bottom are images acquired during decreasing gas fractional flow – increasing oil and water. On the right, is the image acquired at a gas fractional flow of 1 which is the only time the gas is connected across the sample.

Fig. 6.12 shows the three-dimensional connectivity of the oil at different fractional flows. Here we observe a unique trend in the oil connectivity: oil becomes more connected with increasing gas fractional flow, despite the simultaneous decrease in the oil flow; oil connectivity is enhanced as oil saturation decreases and gas saturation increases. The reason for this behaviour is the spreading of oil in connected layers in the presence of gas. As the gas saturation increases, it invades new pores, where oil could be previously trapped by water; the trapped oil is then connected to the spreading oil layer surrounding the invading gas phase. This justification can be supported by examining the oil connectivity at f_g = 1 – where the gas saturation is the highest – when oil is most connected, see Fig. 6.12. Conversely, oil becomes less connected as the gas fractional flow is decreased, and oil and water

fractional flows are increased with trapping of gas. This indicates that, unlike gas, oil connectivity is a function of saturation history.

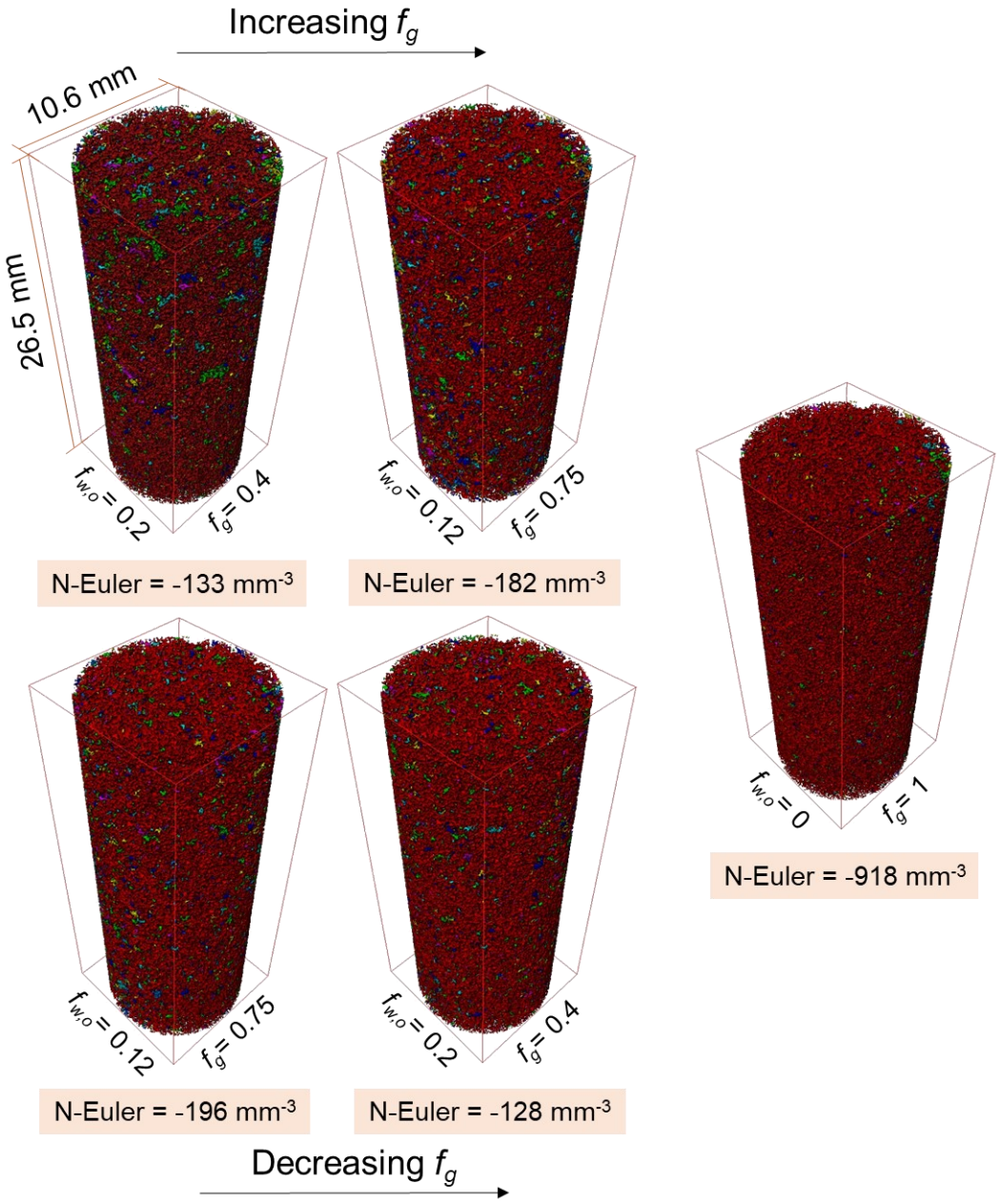

Figure 6. 12. Three-dimensional maps of the *in situ* oil connectivity in the pore space of the water-wet rock under three-phase steady-state conditions at different gas, oil, and water fractional flows. Each disconnected cluster is labelled with a different colour. Gas, oil and water fractional flows (f_g and $f_{w,o}$) are stated. N-Euler refers to the normalized Euler characteristic listed in Table 6.3. Images on top are acquired during the increasing gas fractional flow path – decreasing oil and water – while on the bottom are images acquired during decreasing gas fractional flow – increasing oil and water. On the right, is the image acquired at a gas fractional flow of 1.

Furthermore, we quantify the Euler characteristic of oil, water and gas on images of the whole sample to quantitatively assess their connectivity in the pore space at different fractional flows, see Table 6.3. We quote values per unit volume. Prior to measuring the Euler characteristic, the features smaller than 10 voxels in size were filtered out of the images.

The Euler characteristic results in Table 6.3 confirm that under steady-state three-phase flow conditions, oil and water are connected in spreading and wetting layers respectively, while gas is disconnected in

the pore space. Oil connectivity is better under three-phase flow conditions compared to two-phase flow. Again, we see that oil gets more connected as f_g is increased, and less connected as f_g is decreased with maximized connectivity when gas is injected alone (f_g = 1). The quantitative results support the qualitative observations that gas is disconnected when injected simultaneously with oil and water, and best connected when injected alone (f_g = 1). Water is largely connected in the pore space under both two and three-phase flow conditions, due to its existence in wetting layers.

Table 6. 3. Euler characteristic of water, oil, and gas during the steady-state three-phase experiment at different fractional flows. The Euler characteristic was measured on segmented images of the whole sample and normalized to the total volume. *f* refers to the fractional flow, while subscripts *w*, *o* and *g* refer to the water, oil and gas phases respectively.

Flooding step	f_w	f_o	f_g	Normalized Euler Characteristic [mm^{-3}]		
				Water	Oil	Gas
1	1	0	0	-	-	-
2	0	1	0	-4909	1	-
3	0.5	0.5	0	-3781	23	-
4	0.25	0.25	0.5	-3348	-133	11
5	0.125	0.125	0.75	-3149	-182	13
6	0	0	1	-3133	-918	1
7	0.125	0.125	0.75	-3491	-232	15
8	0.1875	0.1875	0.625	-3483	-196	14
9	0.25	0.25	0.5	-3476	-183	16
10	0.3125	0.3125	0.375	-3508	-128	16
11	0.375	0.375	0.25	-3542	-163	18

6.1.4.5 Three-phase relative permeability

The gas, oil, and water steady-state relative permeabilities were calculated using the multiphase Darcy equations, (6.1)-(6.3). The relative permeability of each phase is plotted as a function of its own saturation. As mentioned in section 6.1.3.4, only the fluid saturations in the macro-pores were considered in this study. The saturation profiles of the three fluid phases, at different fractional flows, are plotted in Fig. 6.13. Notice that Fig. 6.13 is divided into two columns, in the left column, are the saturation profiles for the increasing f_g, and decreasing f_o and f_w, flow path, while on the right are the saturation profiles for the decreasing f_g, and increasing f_o and f_w. The saturation profiles for f_g = 1 are plotted in both for reference. The averaged saturations, for all fractional flows, are plotted in a ternary diagram in Fig. A6.4 in Appendix 6.

Fig. 6.13a shows that the irreducible water saturation reached during two-phase flow, when f_o = 1, is around 0.32. The high irreducible water saturation is attributed to the water-wet nature of the rock and the low capillary pressure imposed at the end of primary drainage. Initial oil and water saturations at $f_{w,o}$ = 0.5, before gas injection, were 0.46 and 0.54 respectively, see Figs 6.13a and 6.13b.

At the first three-phase fractional flow, the gas saturation reached 0.15, with oil and water saturations of 0.38 and 0.47 respectively, see Figs. 6.13a, 6.13b and 6.13c. At the end of the increasing gas saturation flow path, f_g = 1, the gas saturation only reached 0.33, with 0.31 and 0.36 oil and water saturations. The water saturation is the highest as it remains connected in wetting layers in the corners of the pore space. Moreover, the gas rate was not increased at f_g = 1 which explains the low gas saturation – high remaining oil and water saturations – when gas is injected alone: once gas established a flow path through the sample there was no further displacement. During increasing f_g, and decreasing f_o and f_w, flow path, the gas saturation increased, while the oil and water saturations decreased as expected.

However, in contrast, during the subsequent saturation path – decreasing f_g and increasing f_o and f_w – the fluid saturations remained largely constant regardless of the change in the fluid flow rates, see Figs. 6.13d, 6.13e and 6.13f. This explains why the pore occupancy also remained constant in this saturation path (section 6.1.4.2). As discussed previously, this is due to gas trapping by oil and water layers. As gas gets trapped, it is immobilized in the pore space keeping the gas saturation constant, and since oil and water are injected at the same flow rate their saturations also remain constant. The high residual gas saturation observed indicates that water-wet reservoirs are ideal for gas storage applications; the stored gas is permanently immobilized once injection stops.

Nevertheless, since gas is continuously injected into the sample, although at lower flow rates than that reached at $f_g = 1$, then some of the apparently trapped gas is continuously displaced by double and multiple displacements. Therefore, we suspect that there are two types of trapped gas ganglia during the decreasing f_g and increasing f_o and f_w flow path: (i) trapped gas which can move at a given flow rate during decreasing f_g and increasing f_o and f_w; and (ii) trapped gas which is immobilized permanently unless gas is injected at a higher flow rate than that applied at $f_g = 1$ (higher than 0.8 mL/min). This indicates that fluid saturations are indeed a function of saturation history. The saturation profiles did not show any signs of capillary gradients – capillary end-effect.

Moreover, since we observe, macroscopically, constant fluid saturations but changing fluid-fluid and fluid-solid interfacial areas during decreasing f_g and increasing f_o and f_w, see Fig. 6.10, we hypothesize that during this saturation path we never genuinely attain steady-state conditions at the pore-scale, and that the fluid arrangement is constantly fluctuating between two or more locations of local capillary equilibrium. There is a small gradient in gas saturation with a slight tendency for gas to accumulate near the outlet – the top of the sample – due to the effects of gravitational forces; see the discussion in Appendix 6.

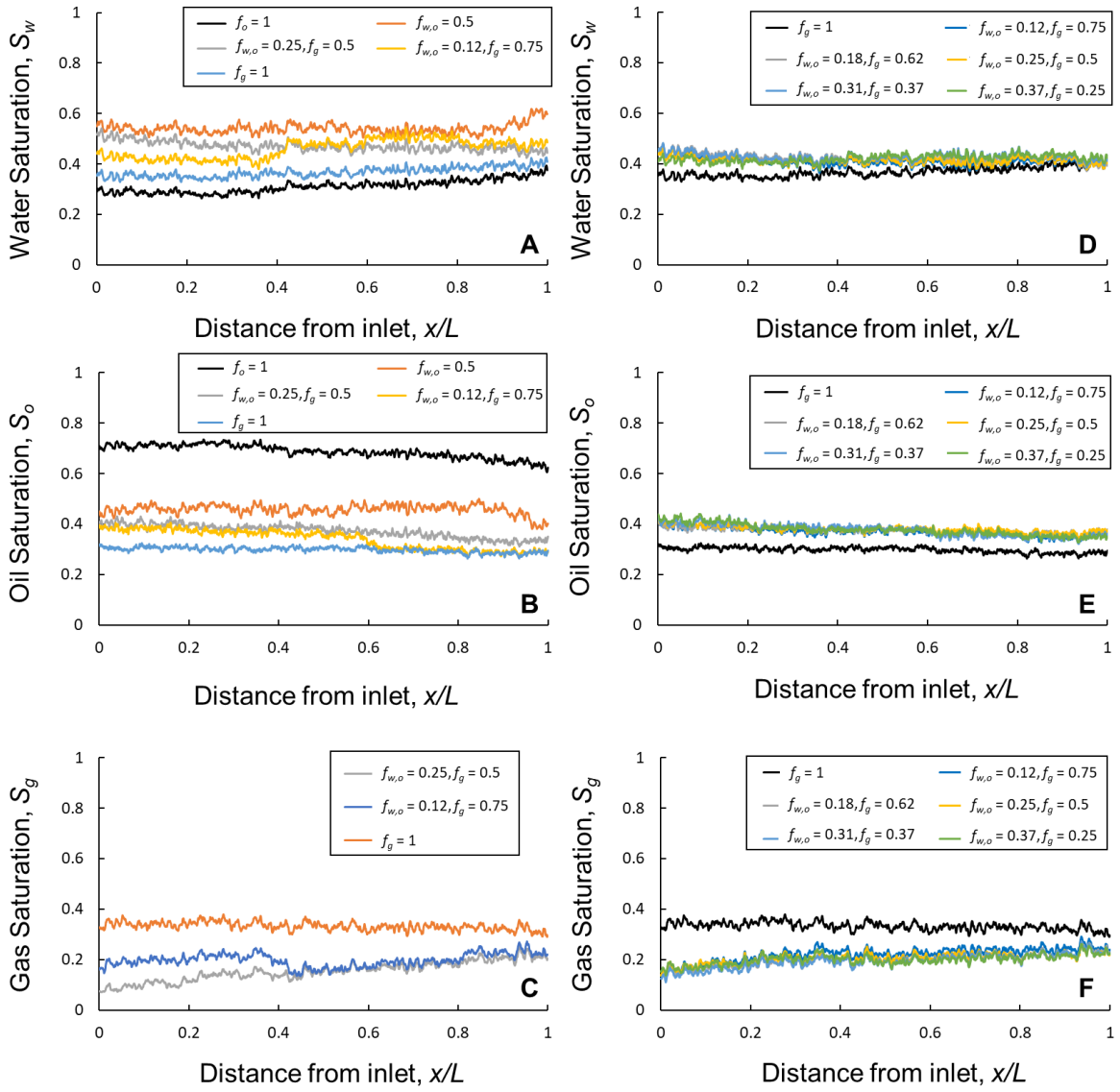

Figure 6. 13. Fluid saturation profiles of (a) water, (b) oil, and (c) gas during increasing gas fractional flow – decreasing oil and water fractional flows – and of (d) water, (e) oil, and (d) gas during decreasing gas fractional flow – increasing oil and water – plotted along the length of the whole sample. Fluid saturations in the macro-pores only are considered. Note that the saturation profiles are approximately constant with distance indicating that there is no noticeable capillary end effect. Gas, oil and water fractional flows (f_g and $f_{w,o}$) are stated.

To calculate the three-phase relative permeability, the pressure drop across the sample was measured. The measured differential pressures (ΔP), at all fractional flows are plotted in Fig. 6.14. The reported pressure is the stable differential pressure, at apparent steady-state conditions, measured over a period of 1 hr, after a minimum waiting time of at least 12 hr for each fractional flow. Reported in Fig. 6.14 are the mean pressure values used to calculate the three-phase relative permeabilities, with their corresponding standard deviations. Increasing the gas flow rate decreased the pressure drop which is consistent with the introduction of a less viscous phase in the sample [18]. The pressure drop in the flow lines was insignificant compared to that measured across the sample and hence was ignored.

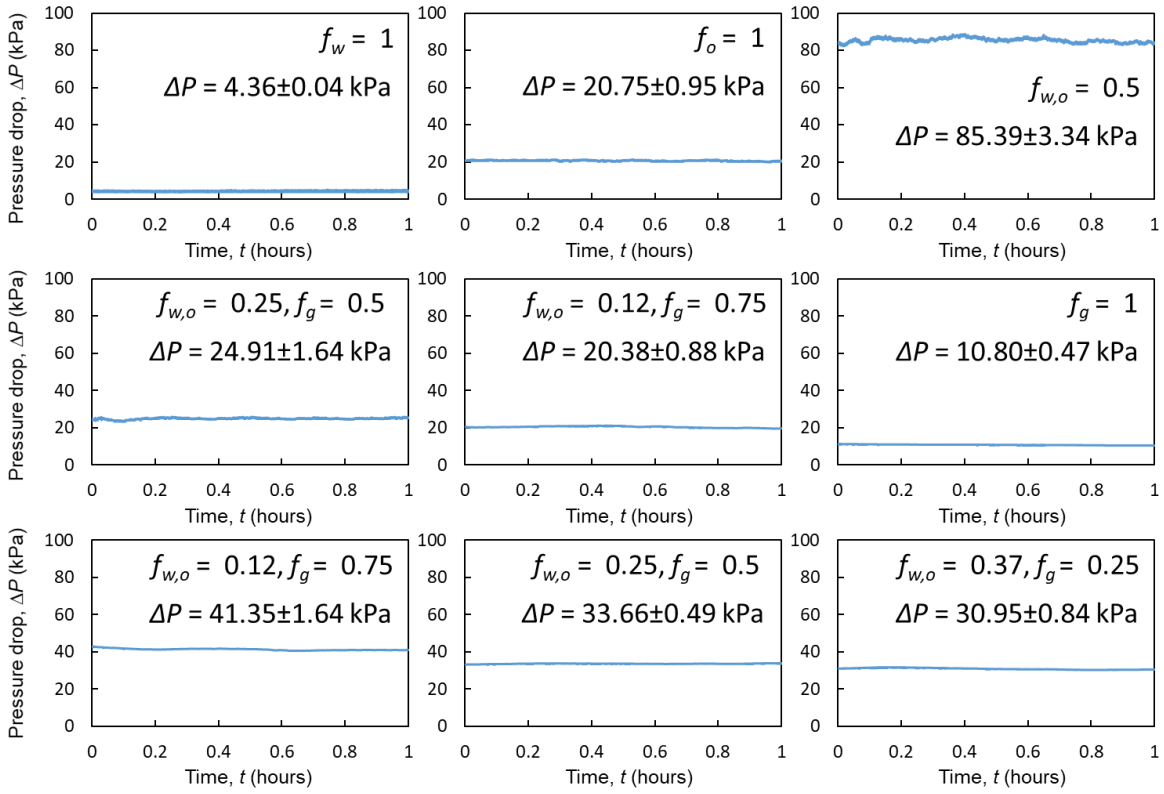

Figure 6. 14. The measured pressure drops across the sample using a differential pressure transducer for 1 hr when steady-state conditions are reached at different fractional flows. Gas, oil and water fractional flows (f_g and $f_{w,o}$) are stated. The mean pressure drop values, with their corresponding standard deviations are shown.

First, we compare our two-phase relative permeabilities, measured in flooding steps 1-3, see Table 6.1, with a two-phase relative permeability experiment conducted on a smaller water-wet Bentheimer sandstone sample of diameter 6.1 mm and length 25.8 mm [15, 140]. The two-phase relative permeabilities are shown in Fig. A6.5 in Appendix 6. The results show that the measurements are in agreement, and the only discrepancy is at irreducible water saturation which is larger in our experiment, since we imposed a lower capillary pressure and the end of primary drainage.

Fig. 6.15 shows the measured water, oil, and gas three-phase relative permeabilities at steady-state conditions. We compare our relative permeability with two three-phase relative permeability experiments – labelled as Exp A and Exp B – conducted by Alizadeh and Piri [197] on a larger sample of Bentheimer sandstone (3.81 cm in diameter and 15.24 cm in length). Fig. 6.15 is divided into two columns: in the left column, are the relative permeabilities measured during the increasing f_g, and decreasing f_o and f_w, flow path, while on the right are the permeabilities of the decreasing f_g, and increasing f_o and f_w path. Note that Exp B only investigates the increasing f_g flow path.

The dataset of Alizadeh and Piri [197] was chosen to validate our measurements against for a number of reasons: (i) the same rock type, Bentheimer sandstone, was used; (ii) similar initial oil and water saturations (before gas injection); and (iii) the same saturation path is investigated – first, increasing f_g, and decreasing f_o and f_w, and then decreasing f_g, and increasing f_o and f_w, with equal oil and water flow rates.

We observe that the water and oil relative permeabilities in our experiment, for increasing f_g, agree with the data of Alizadeh and Piri [197] which indicates the accuracy of our steady-state three-phase relative permeability measurement method. Furthermore, it shows that the sample size used in our experiment is well within the representative elementary volume (REV) for relative permeability, see Figs. 6.15a and 6.15c. However, Figs. 6.15b and 6.15d show that for decreasing f_g, the measured water and oil

relative permeabilities are in a different saturation range compared to the data of Alizadeh and Piri [197]. This is because they increased the gas flow rate at f_g = 1, which reduced the water and oil saturations further in the pore space, while we did not. Hence our permeability measurements are at lower gas saturation compared to Alizadeh and Piri [197], see Figs. 6.15e and 6.15f. However, we still see a match in the gas relative permeability at low gas saturations for increasing f_g, see Fig. 6.15e.

Fig. 6.15 shows that, in our experiment, the gas relative permeability is lower than the oil and water relative permeabilities, despite gas occupying the larger pores. This counter-intuitive behaviour can be explained by the disconnected gas flow observed in section 6.1.4.4. Although both oil and water flow in connected layers, the oil relative permeability is still higher than the water one, Figs. 6.15a, 6.15b, 6.15c, and 6.15d. This is attributed to oil flowing in medium-sized pores, while water flows in smaller pores and layers close to the solid surface.

Our results show that the saturation history has little impact on the water relative permeability, see Fig. A6.6a in Appendix 6. This is expected since water is the most wetting phase in the pore space. However, we observe a clear dependency of oil and gas relative permeabilities on the saturation history, see Figs. A6.6b and A6.6c in Appendix 6.

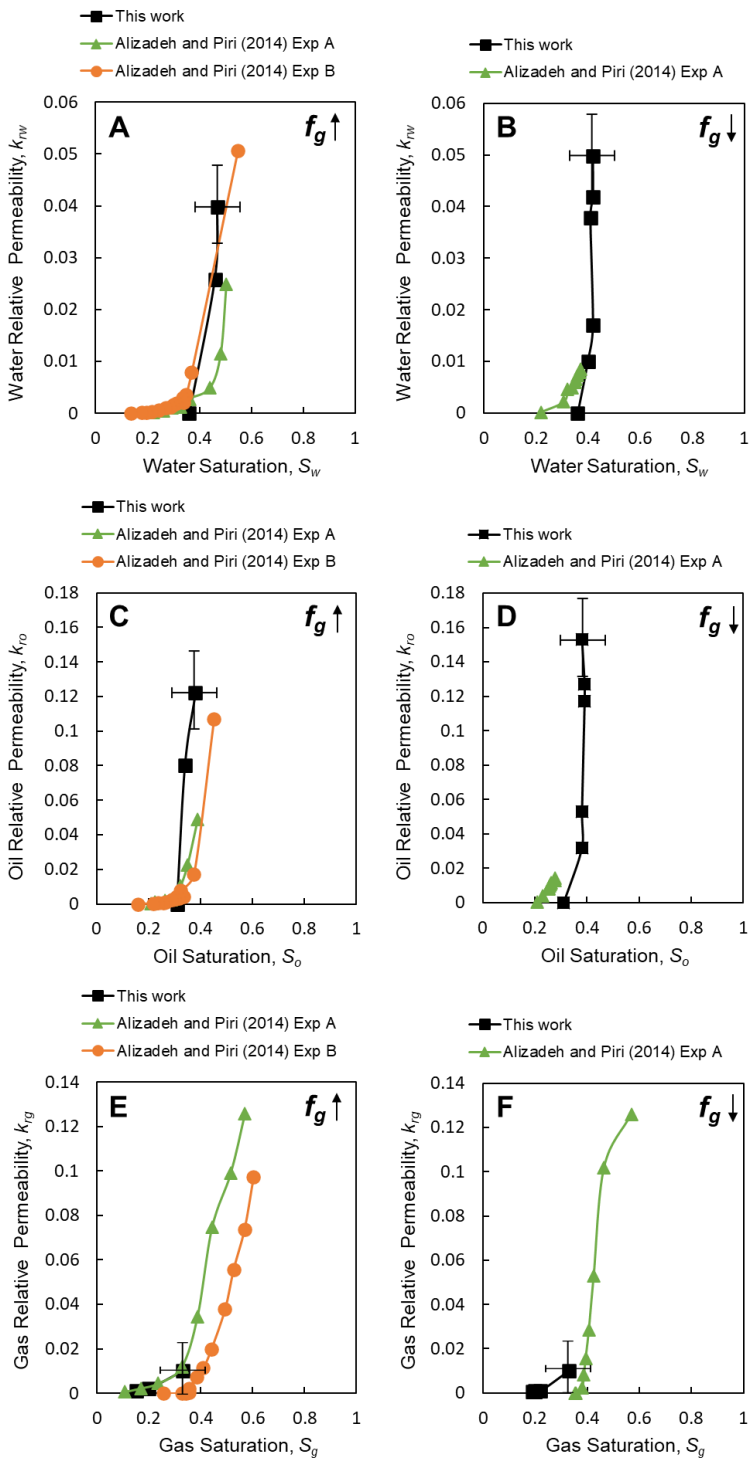

Figure 6. 15. The measured three-phase relative permeability of (a) water, (c) oil, and (e) gas during increasing gas fractional flow – decreasing oil and water fractional flows – and of (b) water, (d) oil, and (f) gas during decreasing gas fractional flow – increasing oil and water. Exp A and Exp B data from Alizadeh and Piri [197]. The upward and downward pointing arrows represent the saturation path where gas fractional flow (f_g) is increased and decreased respectively. Error bars indicate the uncertainty in the measurements.

6.1.4.6 Intermittency in three-phase flow

We observe that a significant fraction of the pore space is filled with two fluid phases during the scan time, identified by an intermediate grey-scale level, see Fig. 6.16. This pore-scale phenomenon, called intermittency, has been seen hitherto in two-phase flow and refers to the alternative filling of the same pore by two immiscible fluid phases [37, 113, 120, 121, 198, 199].

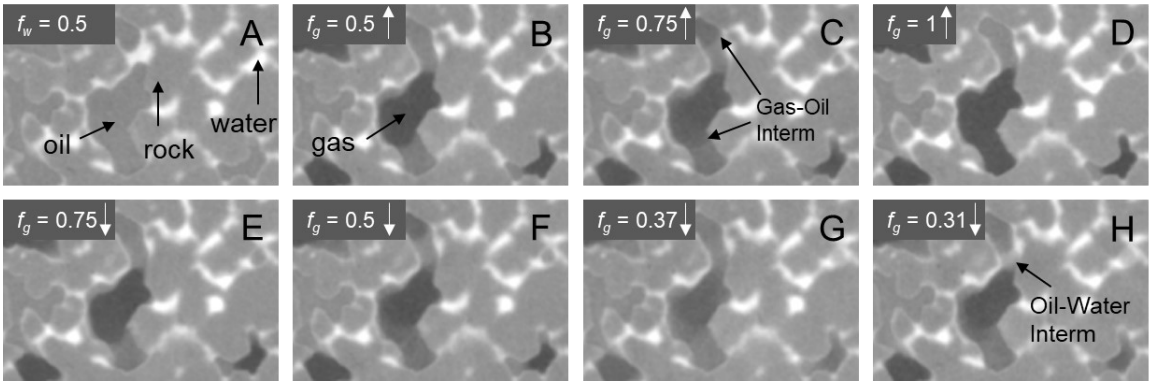

Figure 6. 16. Two-dimensional unfiltered pore-scale images showing the occurrence of gas-oil and oil-water intermittency under three-phase flow conditions in the same pore at different fractional flows. The upward and downward pointing arrows represent the saturation path where gas fractional flow (f_g) is increased and decreased respectively. Water is shown in white, rock in light grey, oil in dark grey, and gas in black. Intermittency appears with with a grey-scale value that is in between the grey-scale values of the two intermittent phases.

In two-phase flow, intermittency has only been observed at moderate to high flow rates [200], where the relationship between rate and pressure gradient is non-linear, far from the Darcy (capillary-dominated) regime. The onset of the transition from the Darcy regime to the viscous one was quantified by Zhang et al. [201] using a pore-scale energy balance. We use their approach, assuming two-phase flow between gas and oil, and oil and water, see Fig. A6.7 in Appendix 6. For oil-water displacement the flow is clearly in the Darcy capillary-dominated regime, whereas for gas-oil flow, because of the lower gas viscosity, the experiments are on the predicted boundary between Darcy-like and intermittent flow. This suggests that the intermittent flow regions observed in our three-phase experiment can occur even under capillary-controlled flow conditions. Since gas, the most non-wetting phase, is disconnected in the pore space, it can only progress through the intermittent opening and closing of critical flow paths facilitated by double and multiple displacement events.

We identify two intermittent regions in the pore-scale images: (i) a more dominant gas-oil region, and (ii) an oil-water region, see Fig. 6.16. No intermittent gas-water flow was observed since the two phases do not directly contact each other in the pore space. In Fig. 6.17 we quantify the intermittent gas-oil fraction of the pore space at different fractional flows and show that it occurs mostly in intermediate-sized pores, smaller than those occupied by gas, which indicates that gas forges temporary pathways to increases its conductance in the pore space.

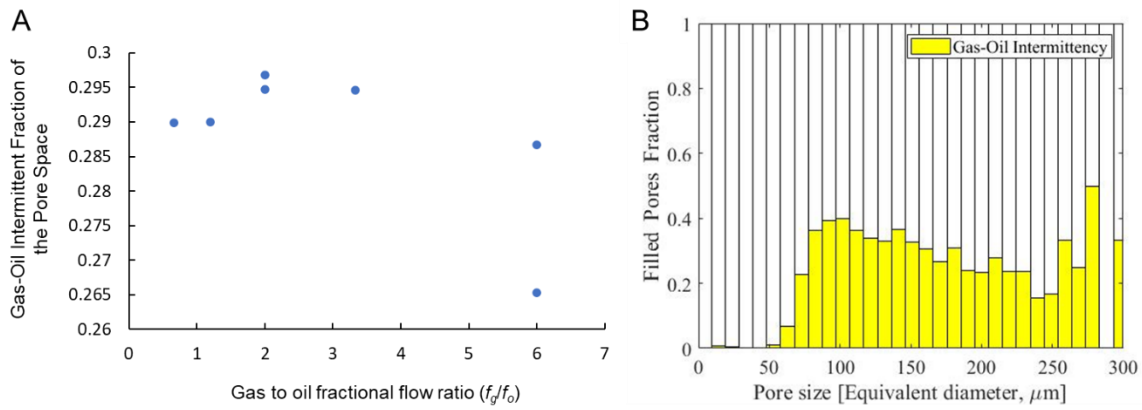

Figure 6. 17. (A) Quantification of the fraction of the pore space occupied by gas-oil intermittency at different gas to oil fractional flow ratios. (B) A bar chart showing the pore occupancy of gas-oil intermittency at flooding step 5, see Table 6.1.

6.1.4.7 Local capillary pressure

Using pore-scale imaging we were able to measure the local capillary pressures simultaneously with the steady-state three-phase relative permeability. Fig. 6.18 shows the measured oil-water and gas-oil pressures using the curvature-based approach. Again, intermittency was not considered in this analysis; we do not expect this to influence the trend of capillary pressure change with saturation.

The two-phase oil-water capillary pressure is compared with the pressure measurements of Lin et al. [140] obtained using two-phase flow imaging on a water-wet Bentheimer sandstone, see Fig. 6.18a. The measured oil-water capillary pressures are in the same range (+2.5 kPa ± 0.4 kPa) demonstrating the consistency of the curvature-based approach. A positive oil-water capillary pressure indicates that the rock surfaces are indeed water-wet. There is little change in the oil-water capillary pressure with water saturation in both experiments; this is due to the relatively narrow pore size distribution of the Bentheimer sandstone, see Fig. A6.1 in Appendix 6.

Under three-phase flow conditions – Fig. 6.18b – the oil-water capillary pressure decreased with increasing water saturation as expected. The gas-oil capillary pressure is also positive, with an average value of +0.26 kPa ± 0.4 kPa, indicating that oil is wetting to gas, see Fig. 6.18c. This confirms the expected wettability order, water-oil-gas from most to least wetting, for the water-wet system at immiscible conditions. The gas-oil capillary pressure increased slightly with gas saturation. Again, it was not possible to measure the gas-water capillary pressure due to oil spreading layers preventing their contact in the pore space.

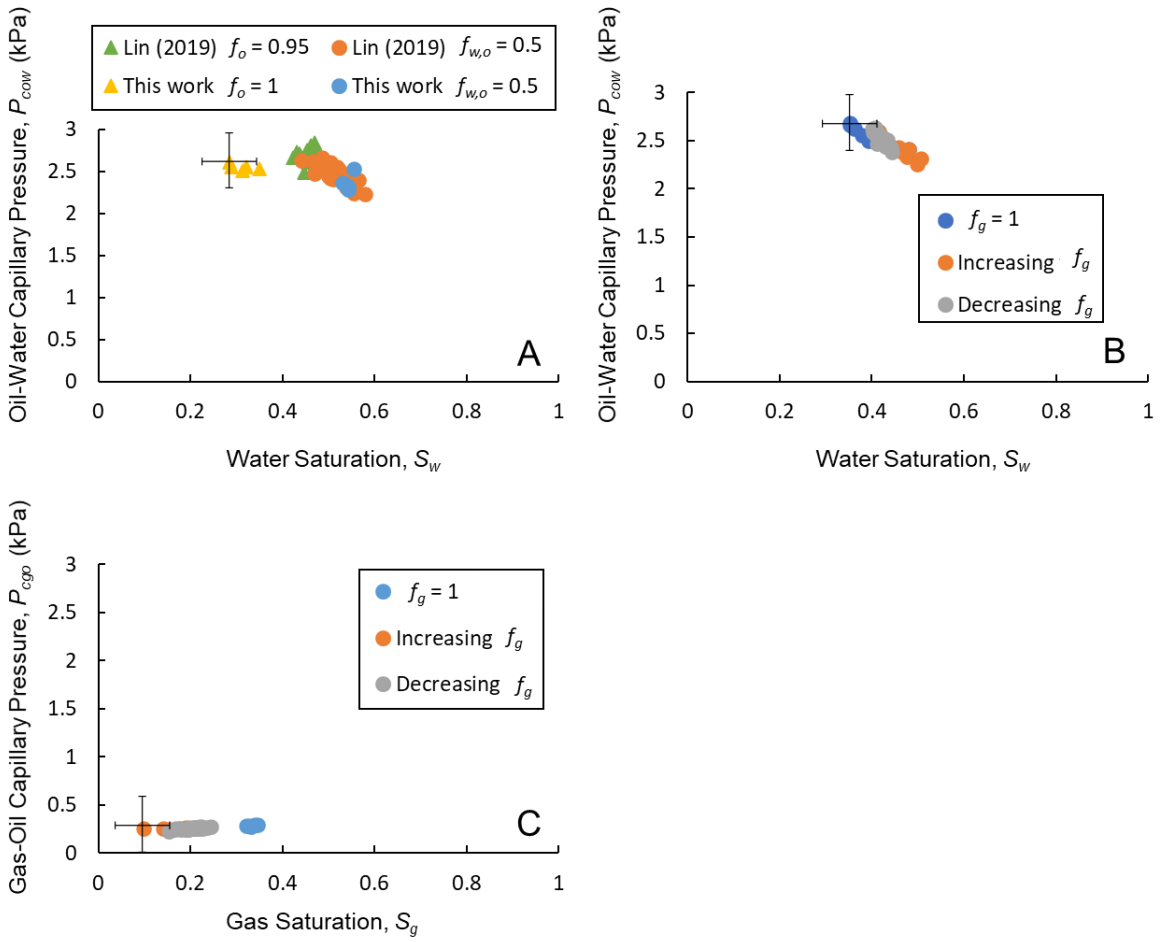

Figure 6. 18. The curvature-based (a) two-phase oil-water, (b) three-phase oil-water, and (c) three-phase gas-oil capillary pressures plotted as a function of water and gas saturations. Increasing f_g represents the pressures obtained during the increasing gas fractional flow – decreasing oil and water fractional flows – saturation path, while decreasing f_g is of the decreasing gas fractional flow – increasing oil and water – path. The two-phase oil-water capillary pressures are compared to the measurements of Lin et al. [140]. Error bars indicate the uncertainty in the measurements.

6.1.4.8 Double and multiple displacement

As gas exists in the form of disconnected ganglia, it can only propagate through the pore space by double and multiple displacement chains. These displacements will always involve oil as a mediator between gas and water as the two phases do not contact each other in the pore space.

Two double displacement processes were observed in the steady-state pore-scale images: (i) a gas-oil-water double displacement and (ii) a water-oil-gas displacement, see Fig. 6.19. The same double displacements were previously observed in water-wet unsteady-state experiments [39, 41]. Fig. 6.19a shows images of a gas-oil-water double displacement process in a single pore. Water was first displaced by oil in a drainage process which was then displaced by gas in another drainage process. Notice that during a gas-oil-water double displacement, gas does not completely displace oil and water out of the pore space; oil and water remain connected in spreading and wetting layers respectively. However, during a water-oil-gas displacement, where oil first displaces gas in an imbibition process followed by another imbibition process when oil is displaced by water, the displaced phases completely exit the pore space; there is no remaining oil and gas, see Fig. 6.19b.

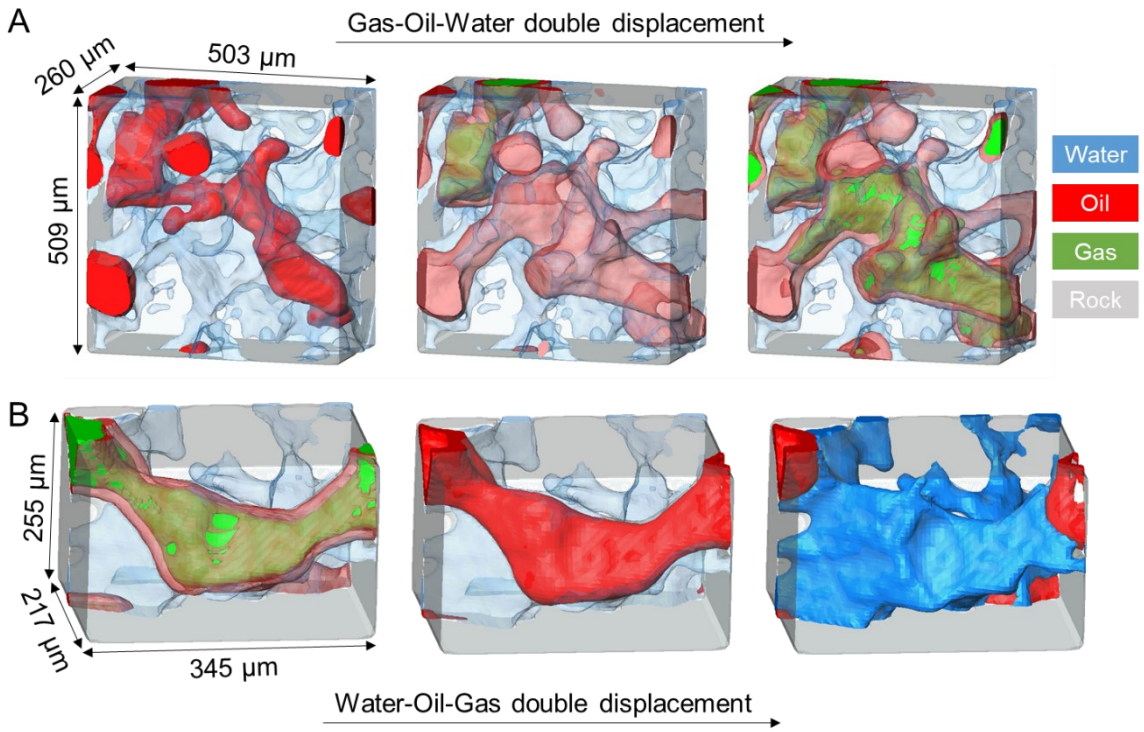

Figure 6. 19. Three-dimensional images showing the occurrence of (a) gas-oil-water double displacement, and (b) water-oil-gas double displacement in the water-wet rock under capillary-dominated conditions. Water is shown in blue, oil in red, gas in green, while the rock phase is rendered semi-transparent (grey).

6.1.5 Final Remarks and Suggestions

We have developed a methodology to couple steady-state three-phase relative permeability measurements with high-resolution pore-scale X-ray imaging (5.3 µm per voxel). Three-phase relative permeability was determined simultaneously with capillary pressure at different gas, oil, and water fractional flows in a water-wet sandstone rock under capillary dominated conditions. In our water-wet system, at immiscible conditions, water is the most wetting phase, residing in small pores and wetting layers, gas is the most non-wetting phase, occupying the large pores, while oil is the intermediate-wet phase, forming spreading layers in the medium-sized pores. Combining macroscopic measurements of flow properties with pore-scale imaging allowed the following discoveries to be made:

1. **Disconnected gas flow at steady-state conditions**: We observed a unique gas flow pattern at steady-state conditions, where gas advances through the pore space in the form of disconnected ganglia mediated by double and multiple displacement processes. This behaviour was attributed to the continuous swelling of water and oil layers in the throats, trapping gas in the pore centres. Gas was only connected in the pore space when injected at a gas fractional flow of one.
2. **Intermittent flow**: We identified intermittent gas-oil and gas-water regions, where both phases interchangeably occupied the same pores during the scan time. Gas-oil intermittency was more dominant. No gas-water intermittency was observed because the direct contact of the two phases is prevented by oil spreading layers. This intermittency is similar to that observed at moderate to high flow rates in two-phase flow but is observed in three-phase flow even under capillary-dominated displacement conditions. The periodic opening and closing of flow paths to gas facilitates its flow: gas ganglia are not advected through the pore space, but undergo a stop-start type transport, akin to cars controlled by traffic lights.
3. **High residual gas saturation**: A high residual gas saturation was observed in the flooding experiment; once gas invaded the pore space it was not possible to displace it, when water and oil fractional flows were subsequently increased. This is due to double capillary trapping, where

gas is trapped in the centre of the pores by oil and water layers; when more water and oil are injected, they imbibe in the corners of the pore space surrounding the gas phase in the centres, keeping it trapped, as discussed in section 5. This has huge implications for gas storage applications in water-wet oil reservoirs, as it ensures that once gas is injected it remains trapped and does not flow once injection ceases.

4. **Understanding three-phase relative permeability**: The low gas relative permeability seen in water-wet systems, albeit occupying the largest pores, can now be attributed to disconnected gas flow. Even though both water and oil exist in layers, oil has higher relative permeability which is ascribed to water occupying smaller pores than oil. The impact of saturation history on gas and oil relative permeabilities was larger than its impact on the water relative permeability. Our relative permeability results were in agreement with core-scale three-phase relative permeability measurements indicating the accuracy of our method.
5. **Capillary pressures**: The capillary pressure measurements displayed a positive oil-water and gas-oil capillary pressures consistent with a wettability order of water-oil-gas, from most to least wetting.
6. **Double displacements in steady-state flow**: Two double displacement processes were observed: (i) gas-oil-water, and (ii) water-oil-gas. The latter is essential for gas to progress through the pore space since it exists in disconnected ganglia.

This analysis uncovers several topics for future work. (a) We need to quantify the apparent relative permeability for different flow rates. Is there a linear relationship between flow rate and pressure gradient and for what range of capillary number? (b) The analysis could be extended to mixed-wet and oil-wet rocks, and for a wider range of rock types. (c) The implications for modelling need to be explored. It is evident that the current quasi-static assumption of pore network models that compute relative permeability based on the connected network of each phase through the pore space is flawed. For empirical models that use two-phase analogies to predict three-phase properties, again the predictions are likely to be significantly in error since they do not encapsulate the unique nature of three-phase flow.

In the next section, (6.2), we extended the steady-state three-phase X-ray imaging to study a mixed-wet reservoir rock.

6.2 Steady-state three-phase flow in a mixed-wet porous medium: A pore-scale X-ray microtomography study

6.2.1 Summary

We use three-dimensional X-ray imaging to investigate steady-state three-phase flow in a mixed-wet reservoir rock, while measuring both relative permeability and capillary pressure. This extends the work of the previous section to a mixed-wet (or weakly oil-wet) system. Here, oil occupied the smallest pores, gas the biggest, while water occupied medium-sized pores. We report a distinct flow pattern, where gas flows in the form of disconnected ganglia by periodically opening critical flow pathways, as seen in the water-wet case. Despite having capillary-controlled displacements, a significant fraction of the pore space was intermittently occupied by gas-oil and oil-water phases. Both types of intermittency (gas-oil and oil-water) occurred in intermediate-sized pores. Gas mainly displaces oil, and oil displaces water as the gas flow rate is increased, while oil displaces gas, and water displaces oil as gas flow is decreased. No gas was trapped in the rock due to its mixed-wettability which prevents either oil or water completely surrounding gas, suppressing snap-off and capillary trapping, which has significant implications for the design of gas storage in three-phase systems.

6.2.2 Investigations

The motivation behind this study is provided in section 2.2.4.

Here, we investigate three-phase steady-state flow in a mixed-wet reservoir rock extracted from a large producing field in the Middle East. We will study a saturation history similar to section 6.1, where the gas fractional flow is first increased and then decreased. This experiment is also performed under capillary-dominated, immiscible gas-oil conditions.

Similar to section 6.1, in *EXP* 7, we will measure three-phase relative permeabilities and capillary pressures. However, we will determine the saturations directly from the raw pore-scale images, without performing image segmentation, by extending the saturation analysis introduced by Lin et al. [202], from two to three phases. We present a new image analysis technique to quantify the displacement of each phase when moving from one steady-state condition to another. In addition, we determine pore occupancies, layer formation, interfacial areas, contact angles and fluid connectivity. We end with a discussion of the implications of this work on the design of carbon dioxide storage in oil reservoirs.

In this section, the pore occupancy results indicate that the wettability order in our mixed-wet reservoir rock is oil-water-gas from most to least wetting. We observe disconnected gas flow across the system at steady-state conditions, similar to the observations of section 6.1 for a water-wet rock. Although displacements were capillary-controlled, we identified intermittent gas-oil and oil-water regions, where the phases alternatively filled the same pores. Unlike the water-wet system, in section 6.1, the oil-water intermittency is more significant here. As the gas fractional flow was increased, gas only filled the pores that were previously occupied by oil, and gas was mostly displaced by oil as the fractional flow was decreased. This work further supports the finding of section 6.1 that pore-scale steady-state conditions may never be attained in three-phase flow, despite, macroscopically, having a constant averaged saturation.

More significantly, there was no gas trapping in this mixed-wet reservoir rock at the end of gas injection, when only water and oil were injected. This is different from the water-wet system, in section 6.1, where

a significant amount of gas was trapped in the pore centres surrounded by oil and water layers. This behaviour was ascribed to the mixed-wet nature of the surface which prevented either oil or water from completely surrounding the gas phase in the pore centres. This work suggests that a water-alternating-gas (WAG) injection strategy may not be favourable for carbon dioxide storage in mixed-wet oilfields since it can mobilize the gas possibly leading to its escape. This modifies the conclusions presented in section 5: while water injection may further improve oil recovery, it will not lead to more secure storage – CO_2 is displaced. Instead, an injection strategy of continuous gas injection is more effective since gas naturally gets disconnected upon injection, ensuring secure storage.

6.2.3 Materials and Methods

6.2.3.1 Rock and fluid properties

The same carbonate reservoir rock used in sections 3.2, 3.3, 4.1 and 4.2 was selected for this study. However, the sample was larger in size with a length of 42.9 mm and 12.3 mm diameter. The sample has a total porosity of 24.4%, characterised using differential imaging [127], and an absolute permeability (k) of 660 ± 30 mD ($6.60\times10^{-13} \pm 0.03\times10^{-13}$ m^2) – measured at the experimental conditions. The pore and throat size distributions of the sample are plotted in Fig. A7.1 in Appendix 7.

The experimental fluids were nitrogen (N_2), *n*-decane ($C_{10}H_{22}$), and deionized water (H_2O) respectively. The oil and water phases were mixed with 20 wt.% iododecane ($C_{10}H_{21}I$) and 30 wt.% sodium iodide (NaI) respectively.

At the experimental conditions, 1 MPa pore pressure and 30 ºC temperature, the dynamic viscosities of gas, oil and water were 0.017, 4.27, and 1.40 mPa·s respectively [130, 193]. Gas and oil were immiscible with an interfacial tension of 11.2 mN·m^{-1} [170]. The interfacial tensions between gas and water, and oil and water were 63.7 and 52.1 mN·m^{-1} respectively [130].

In our three-phase system, oil has a positive initial spreading coefficient (C_{so} = +0.4 mN·m^{-1}) which indicates that it will spread in layers sandwiched between gas and water in the rock pore space, as we will show later; gas and water both have a negative spreading coefficient.

6.2.3.2 Wettability alteration process

Prior to performing the steady-state experiment, the rock wettability was rendered mixed-wet. To alter the wettability of the reservoir rock, we first saturated the rock sample with formation brine – a brine solution prepared with the same salt composition as the reservoir brine from which the rock was extracted. Then, 100 pore volumes (PV) of crude oil, from the same reservoir, were injected at ambient conditions into the pore space with a flowrate of 0.1 mL/min. The injection of crude oil at a low flowrate is necessary to ensure that not all the formation brine is swept out and that some pores remain brine occupied, i.e., remain water-wet to achieve mixed-wettability. The sample was then taken out and placed in a crude oil bath at 80 ºC for two months. The crude oil properties are listed in Table 3.5. This wettability alteration protocol is different to that previously detailed in section 3.2.3.2 which has shown to render the samples strongly oil-wet.

6.2.3.3 Experimental procedure

The flow apparatus used in this study is similar to that used in section 6.1, however, the receiving pump was replaced with a back pressure regulator as shown in Fig. 6.20. A net confining pressure of 2 MPa was applied, while the back pressure was set to 1 MPa. The experiment was conducted at a temperature of 30 ºC.

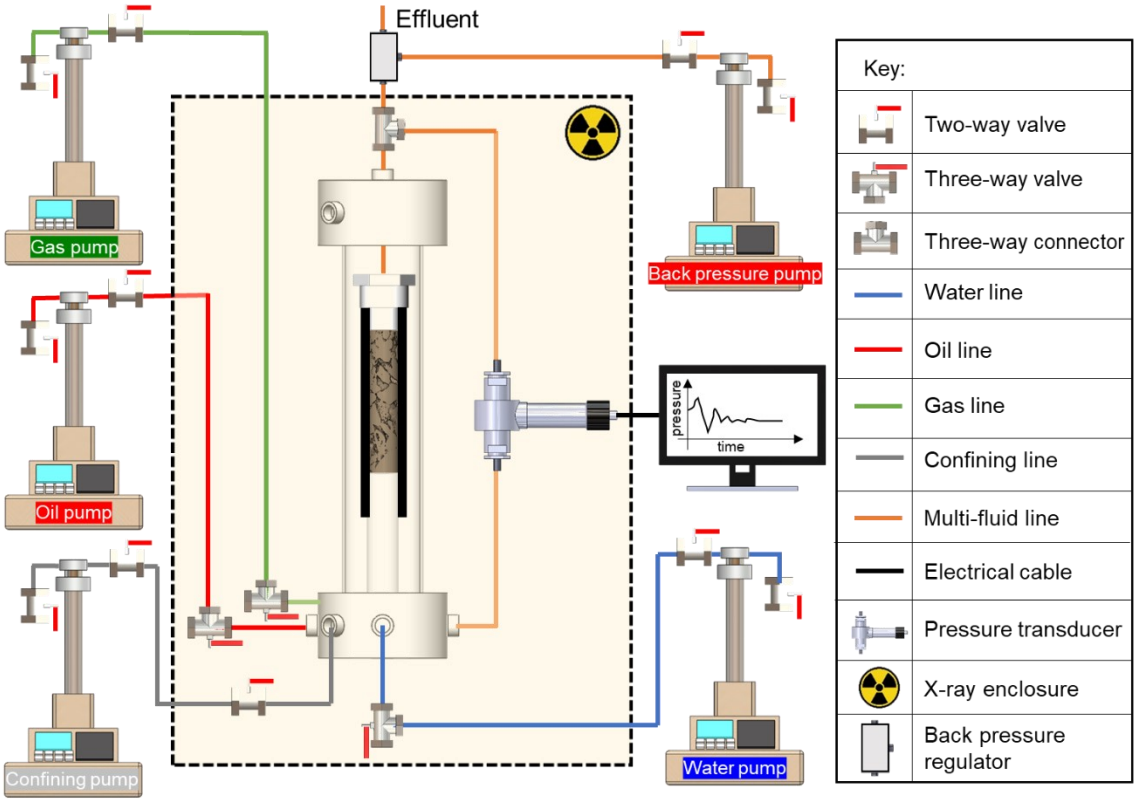

Figure 6. 20. A schematic diagram of the combined three-phase steady-state flow apparatus with the X-ray microtomography scanner. The black dashed line represents the X-ray scanner enclosure. The pumps, flow lines, valves, coreholder and pressure transducer were connected as shown in the diagram.

In the three-phase experiment, steady-state conditions were reached at various gas, oil, and water fractional flows (f_g, f_o and f_w) by keeping the fluid flow rates constant, with a total flow rate of $Q_t = 0.8$ mL·min^{-1}. The sets of fractional flows are listed in Table 6.4.

The selection of fractional flows was done prudently to investigate the impact of a saturation history, where the gas saturation is first increased and then decreased, on three-phase relative permeability. Similar to the water-wet experiment, we keep the oil and water saturation changes in the same direction – by keeping oil and water flow rates the same – and change the gas saturation in the opposite direction [35, 194-197]. The minimum waiting time for each set of fractional flows to reach steady-state conditions was at least 12 hr. After which, we waited for the differential pressure signal to stabilize over a period of 3 hr to record the pressure drop and start the X-ray imaging process. This is longer than the waiting time for the water-wet system since the pressure fluctuations were larger here.

In flow step 1, see Table 6.4, oil (80 wt.% *n*-decane and 20 wt.% iododecane) was injected into the sample to replace the crude oil introduced during the wettability alteration process. Water was then injected in step 2 to reach the residual or remaining oil saturation. In step 3, both oil and water were injected simultaneously ($f_w = 0.5$ and $f_o = 0.5$) to initialize the sample for the three-phase steady-state experiment.

Gas was first injected into the sample in step 4. Five three-phase steady-state conditions were reached as f_g was increased (steps 4, 5, 6, 7 and 8), while only three steady-state conditions were reached when f_g was decreased (steps 9, 10 and 11). At $f_g = 1$ (step 8), the gas flow rate was increased to 2 mL·min^{-1} to reach the maximum gas saturation.

The absolute permeability (k) = 668 ± 30 mD ($6.60\times10^{-13} \pm 0.03\times10^{-13}$ m^2) of the sample was measured using deionized water (H_2O) prior to altering the wettability of the rock at the experimental conditions.

A dry scan and a high contrast water saturated scan were also acquired at this point to characterize the porosity distribution, including sub-resolution porosity, of the sample using the differential imaging method [127].

Table 6. 4. The gas, oil, and water fractional flows at which steady-state conditions were reached in the three-phase flow experiment. Q and f refer to the flow rate and fractional flow respectively. Subscripts g, o and w refer to the gas, oil, and water phases respectively. The total flow rate (Q_t) was 0.8 mL·min^{-1}. Five steady-state conditions were reached as f_g was increased (steps 4, 5, 6, 7 and 8), while only three steady-state conditions were reached when f_g was decreased (steps 9, 10 and 11).

Flow Step	Q_g	Q_o	Q_w	f_g	f_o	f_w
	mL·min^{-1}	mL·min^{-1}	mL·min^{-1}			
1	0	0.8	0	0	1	0
2	0	0	0.8	0	0	1
3	0	0.4	0.4	0	0.5	0.5
4	0.3	0.25	0.25	0.375	0.3125	0.3125
5	0.4	0.2	0.2	0.5	0.25	0.25
6	0.5	0.15	0.15	0.625	0.1875	0.1875
7	0.6	0.1	0.1	0.75	0.125	0.125
8	0.8	0	0	1	0	0
9	0.6	0.1	0.1	0.75	0.125	0.125
10	0.4	0.2	0.2	0.5	0.25	0.25
11	0.2	0.3	0.3	0.25	0.375	0.375
12	0	0.4	0.4	0	0.5	0.5

The fluids were injected at low flow rates to ensure that displacements occur under capillary-dominated conditions. Table 6.5 lists the capillary numbers between the gas-oil and oil-water fluid pairs at each set of fractional flows. Since oil has an initial positive spreading coefficient (C_{so} = +0.4 mN·m^{-1}), see section 6.2.3.1, we expect it to spread in layers between gas and water preventing their direct displacement.

Table 6. 5. The capillary numbers between oil-water, water-oil, gas-oil and oil-gas fluid pairs at different fractional flows during the steady-state three-phase flow experiment. An oil-water capillary number represents the number calculated when oil displaces water, as is the case for the other pairs. Capillary numbers were calculated using $Ca_{ij} = \mu_i q_i/\sigma_{ij}$, where σ_{ij} is the interfacial tension between the phases, μ_i is the viscosity of the displacing fluid and q_i is its Darcy velocity. Refer to Table 6.4 for the fractional flows of each flow step.

Flow Step	$Ca_{[ow]}$	$Ca_{[wo]}$	$Ca_{[go]}$	$Ca_{[og]}$
1	-	-	-	-
2	-	6.34×10^{-7}	-	-
3	1.13×10^{-6}	3.17×10^{-7}	-	-
4	7.07×10^{-7}	1.98×10^{-7}	1.34×10^{-8}	5.26×10^{-6}
5	5.66×10^{-7}	1.58×10^{-7}	1.79×10^{-8}	3.29×10^{-6}
6	4.24×10^{-7}	1.19×10^{-7}	2.24×10^{-8}	2.63×10^{-6}
7	2.83×10^{-7}	7.92×10^{-8}	2.68×10^{-8}	1.97×10^{-6}
8	-	-	3.58×10^{-8}	-
9	2.83×10^{-7}	7.92×10^{-8}	2.68×10^{-8}	1.97×10^{-6}
10	5.66×10^{-7}	1.58×10^{-7}	1.79×10^{-8}	3.29×10^{-6}
11	8.49×10^{-7}	2.38×10^{-7}	8.95×10^{-8}	3.95×10^{-6}
12	1.13×10^{-6}	3.17×10^{-7}	-	5.26×10^{-6}

Three-dimensional images of the whole sample were acquired, with a voxel size of 5.36 μm, using the Zeiss Versa 510 scanner, after reaching steady-state conditions at each set of fractional flows. To capture the whole length, images, of size 12.45 mm × 12.45 mm × 10.23 mm, were taken at four different locations of the sample, with an overlap of 25%. The exposure time was set to 1.60 s with a total of 3,201 projections taken at all sets of fractional flows. All the pore-scale images were then reconstructed, normalized, registered, and stitched as shown in Figs. 6.21 and 6.22.

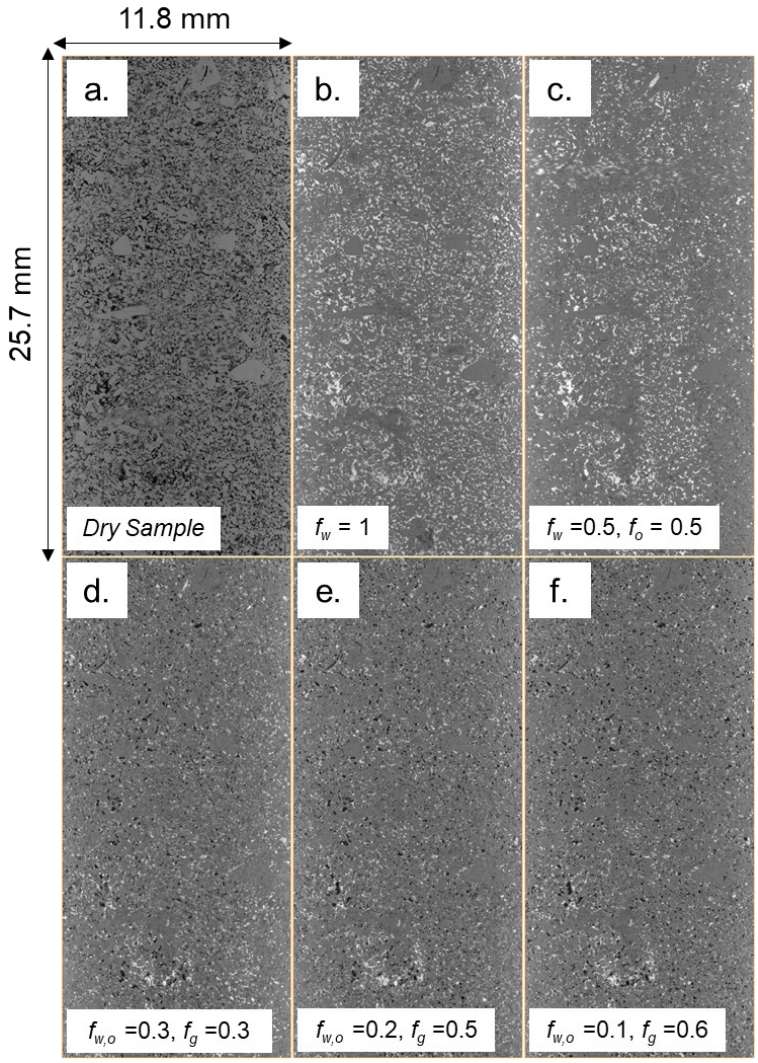

Figure 6. 21. Vertical cross-sectional raw images of the whole sample acquired at steady-state conditions for different gas, oil, and water fractional flows. The gas, oil and water fractional flows (f_g, f_o, and f_w) are stated in each image. The black phase is gas, dark grey is oil, light grey is rock, and white is water.

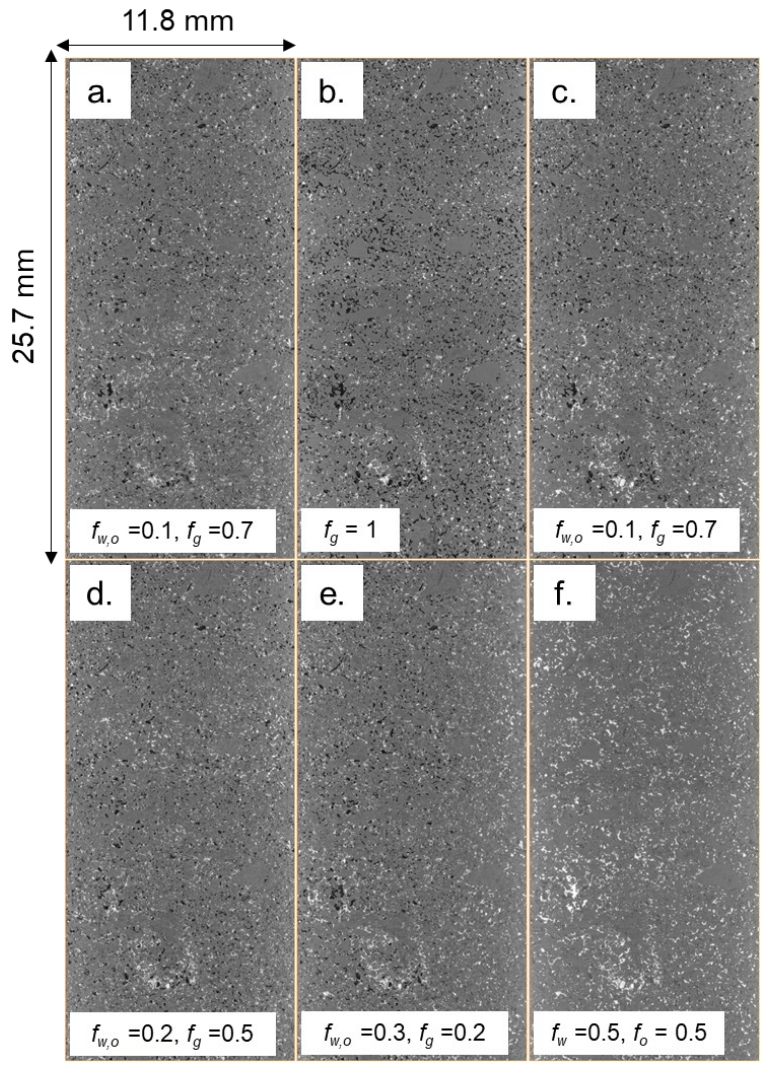

Figure 6. 22. Vertical cross-sectional raw images of the whole sample acquired at steady-state conditions for different gas, oil, and water fractional flows. The gas, oil and water fractional flows (f_g, f_o, and f_w) are stated in each image. The black phase is gas, dark grey is oil, light grey is rock, and white is water.

6.2.3.4 Image processing and analysis

As mentioned in section 6.2.2, we observe that a large fraction of the pore space is occupied by gas-oil and oil-water phases intermittently at three-phase steady-state conditions. Intermittency can take any grey-scale value in-between the grey-scale values of the two intermittent phases. This makes image segmentation almost impossible, and even if segmented there would be eight different phases in the image including rock, water, oil, gas, gas from gas-oil intermittency, oil from gas-oil intermittency, oil from oil-water intermittency, and water from oil-water intermittency.

Therefore, we decided not to segment the three-phase steady-state images with significant intermittency, and instead perform image analysis directly on the raw images. The analysis performed on the raw three-phase images includes saturation, pore occupancy and displacement analysis.

Nonetheless, there was no/little intermittency in the pore-scale images acquired in flow steps 2, 3, 8 and 12, see Table 6.4. Hence, these images were segmented using the seeded watershed algorithm and used for the analysis of contact angles, capillary pressures, interfacial areas and connectivity. We also characterize the saturations in the segmented images and compare them to the saturations obtained

directly from the raw images, see the next section. The segmentation procedure is detailed in Fig. A7.2 in Appendix 7.

6.2.3.4.1 Saturation from grey-scale values

Since it was not possible to segment the three-phase steady-state images, we used an approach, developed by Lin et al. [202], to find the fluid saturations directly from the raw (unsegmented) pore-scale images. We extend this approach from two to three fluid phases. Here, fluid saturations are determined using their grey-scale values in the pore-scale images. In this approach, the saturation of the intermittent region is added to the saturation of their respective phases, e.g., the contributions to the saturations of oil from gas-oil and oil-water intermittent regions are added to the oil saturation. We only considered the fluid saturations in the macro-porosity (porosity that was explicitly resolved in the images). Please refer to Lin et al. [202] for the calculation of two-phase saturations directly from the pore-scale images.

The saturations, in the macro-porosity, at each set of three-phase fractional flows were obtained as follows:

$$CT_{f_w,f_o,f_g} = S_w CT_w + S_o CT_o + S_g CT_g \tag{6.4}$$

where CT_{f_w,f_o,f_g} is the average grey-scale value in the macro-porosity of the three-phase steady-state image at each set of fractional flows, CT_w is the average grey-scale value in the macro-porosity of the water saturated image, CT_o is the average grey-scale value in the macro-porosity of the fully oil saturated image (acquired after flow step 1, see Table 6.4), and CT_g is the average grey-scale value in the macro-porosity of a fully gas saturated image (dry scan). S_w, S_o and S_g refer to the water, oil and gas saturations respectively.

Now, if we substitute S_o = 1- S_w - S_g, Eq. (6.4) can be re-written as:

$$S_w = \frac{CT_o - CT_{f_w,f_o,f_g} + S_g CT_g - S_g CT_o}{CT_o - CT_w} \tag{6.5}$$

While CT_w, CT_o, and CT_g, are constant, CT_{f_w,f_o,f_g} changes depending on the fluid saturations in the macro-porosity of each three-phase steady-state image. Eq. (6.5) can be solved linearly giving a range of S_w and S_g values; we limit this range by the minimum and maximum water and gas saturations that are obtained from the segmented images in flow steps 3, 8 and 12. Finally, the water and gas saturations are obtained by taking the mid-point of their narrowed ranges at each set of fractional flows; oil saturation is then found from S_o = 1- S_w - S_g.

6.2.3.4.2 Displacement analysis

To quantitatively assess the displacement processes in the three-phase mixed-wet system when moving from one steady-state condition to another, we developed an in-house algorithm that identifies the pores and throats occupied by a certain phase, at each set of fractional flows $f_g(i)$, $f_o(i)$ and $f_w(i)$, and then records the phases that occupy the same pores and throats at the next set of fractional flows $f_g(i+1)$, $f_o(i+1)$ and $f_w(i+1)$. Displacement is said to have taken place if the occupancy in the pore changes from one steady-state condition to another.

As in previous chapters, we use the network model code developed by Dong and Blunt [145] and Raeini et al. [146] to extract the pores and throats from the dry scan of the sample. Pores are defined as wide regions of the pore space, that are connected by narrower regions, the throats. The pore diameter is the diameter of the largest sphere that can fit entirely in the pore, while the throat diameter is the diameter of the largest sphere that sits on the throat centre. We assume that the macro pore space is occupied by five phases: (i) gas; (ii) oil; (iii) water; (iv) gas-oil intermittency; and (v) oil-water intermittency, at all

three-phase steady-state conditions. For simplicity, we consider the intermittent regions as a single phase.

To determine the occupancy in the pores, we first set a range of grey-scale values for each phase, as shown in Fig. A7.3 in Appendix 7. Then, we find the average grey-scale value in the sphere we have extracted from the pores. Depending on what range the average grey-scale value falls in, the occupancy is assigned.

6.2.4 Results and Discussion

First, in section 6.2.4.1, we measure the geometric fluid-fluid contact angles to confirm the mixed wettability state of the reservoir rock. Then, in section 6.2.4.2, we show evidence of intermittent gas-oil and oil-water flow at three-phase steady-state conditions. We quantify pore occupancy in section 6.2.4.3 to determine the wettability order in the system. In sections 6.2.4.4 and 6.2.4.5, the connectivity of the fluids and interfacial areas are examined respectively. Saturations are then quantified in section 6.2.4.6 and plotted against the measurements of three-phase relative permeabilities in section 6.2.4.7. Capillary pressures are characterized in section 6.2.4.8. In section 6.2.4.9, fluid-fluid displacements in the three-phase mixed-wet system are analyzed. Finally, in section 6.2.4.10, we examine gas trapping and discuss the implications of pore-scale properties on the design of field-scale CO_2 storage and oil recovery.

6.2.4.1 Wettability

The oil-water (θ_{ow}), gas-oil (θ_{go}) and gas-water (θ_{gw}) geometric contact angles were measured on subvolumes, of size 2.68 mm × 2.68 mm × 2.68 mm, on the segmented images (see section 6.2.3.4 and Table 6.4 for the fractional flows of the segmented images). The geometric angles were measured using the automated method developed by AlRatrout et al. [30], see Fig. 6.23.

Fig. 6.23a shows measurements of the oil-water contact angle at two-phase flow conditions (f_w = 0.5 and f_o = 0.5), measured before and after gas injection (at the end of the experiment), denoted by subscripts *b* and *a* respectively. We observe that θ_{ow} has a wide distribution with angles both lower and higher than 90º, indicating the local existence of both water-wet and oil-wet regions which is a predominant characteristic of mixed-wet media [18]. The mean oil-water contact angles, before and after gas injection, are 82º ± 42º and 84º ± 39º respectively. This confirms that the wettability alteration protocol successfully achieved mixed-wet conditions, as opposed to the dynamic ageing protocol, previously performed on the same reservoir rock in multiple studies, which resulted in more oil-wet conditions with mean oil-water contact angles of 112º ± 21º, 118º ± 25º and 110º ± 20º, see sections 3.2, 3.3 and 4.1.

At f_g = 1, the measured mean oil-water contact angle is 80º ± 41º, see Fig. 6.23b. The consistency of the values indicates that the contact angle does not change within the uncertainty of the measurements during and after gas injection. The gas-oil and gas-water contact angles are 66º ± 41º and 78º ± 40º respectively, suggesting that both oil and water are more wetting to the surface than gas. However, it is not possible to determine a clear wettability order in the system using the geometric contact angle measurements only.

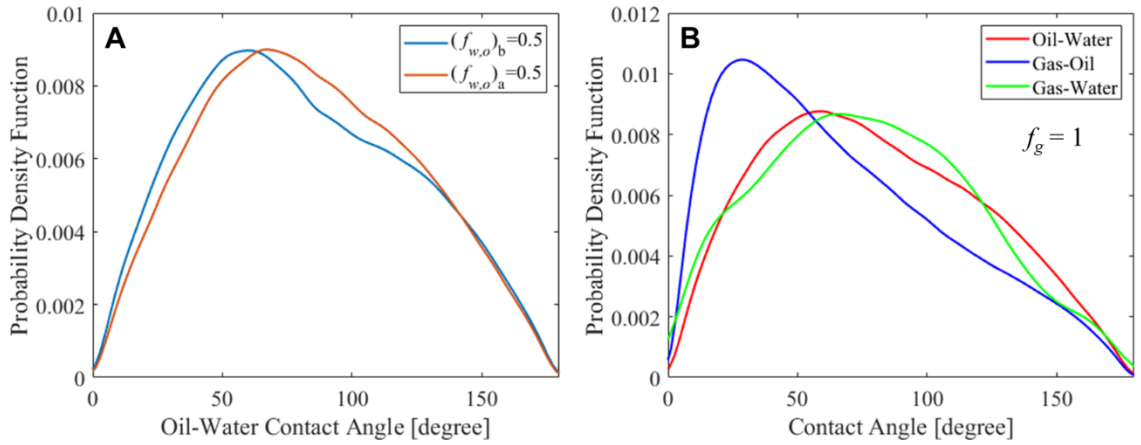

Figure 6. 23. Probability density function of the *in situ* measured geometric contact angles, at steady-state conditions, between (A) oil and water at f_w = 0.5 and f_o = 0.5, before and after gas injection (flow steps 3 and 12), and (B) oil and water, gas and oil, and gas and water at f_g = 1 (flow step 8). Refer to Table 6.4 for the details of each flow step. In (A), subscripts *b* and *a* refer to before and after gas injection (the end of the experiment) respectively. The contact angles were measured through the denser phase: water in the case of oil and water and gas and water, and oil in the case of gas and oil. f_w, f_o and f_g refer to the water, oil and gas fractional flows respectively.

6.2.4.2 Three-phase intermittency

As mentioned previously, a large fraction of the pore space becomes occupied by gas-oil and oil-water phases intermittently at three-phase steady-state conditions, during which the two intermittent phases alternatively occupy the same pores. Intermittency is manifested in an intermediate grey-scale value in-between the grey-scale values of the two intermittent phases as shown in Fig. 6.24. This pore-scale phenomenon has been previously observed in two-phase flow albeit in the non-linear flow regime [37, 113, 120, 121, 198, 199]. Nonetheless, it was also seen in a three-phase water-wet system under capillary-controlled conditions, see section 6.1.

Fig. 6.24 shows the existence of two intermittent regions in the mixed-wet pore space: (i) a gas-oil region, and (ii) an oil-water region. We do not observe intermittent gas-water regions since the two phases do not come in direct contact due to the presence of oil layers, as observed in the water-wet case, section 6.1. However, in contrast to the water-wet system, where gas-oil intermittency was clearly more dominant, the oil-water and gas-oil intermittencies both occupy significant fractions of the pore space in the mixed-wet system. This is supported by the pore occupancy analysis in the next section.

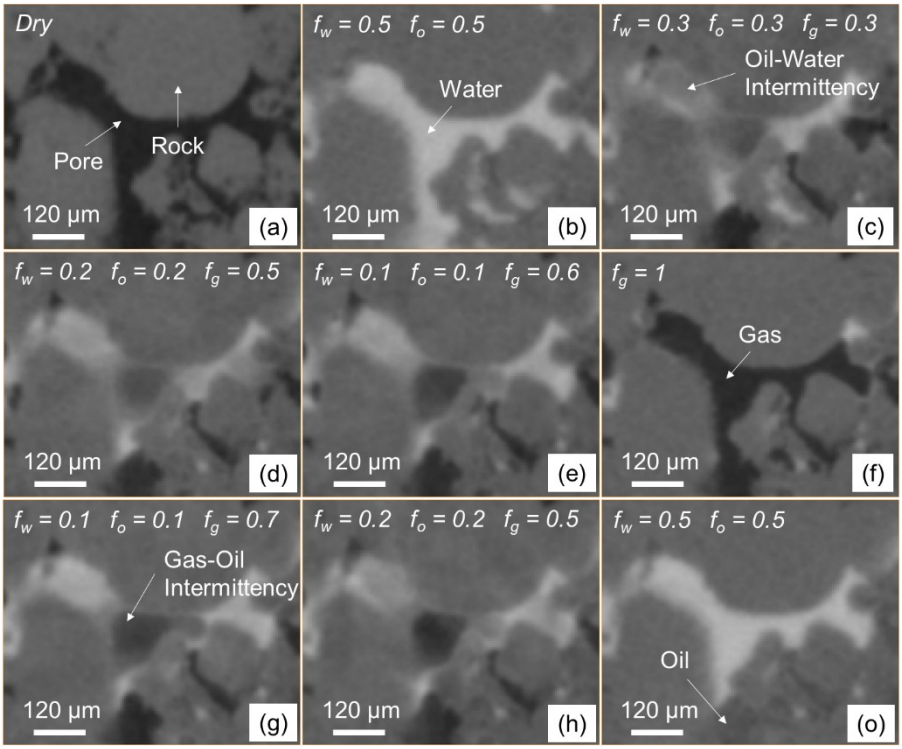

Figure 6. 24. Two-dimensional unfiltered pore-scale images showing the occurrence of intermittent gas-oil and oil-water flow in the same pore under different three-phase steady-state conditions despite flowing in a capillary-force dominated displacement regime. Water is shown in white, rock in light grey, oil in dark grey, and gas in black. Intermittency appears with a grey-scale value that is in between the grey-scale values of the two intermittent phases. f_w, f_o and f_g refer to the water, oil, and gas fractional flows respectively.

6.2.4.3 Pore occupancy

We characterized the pore occupancy – the size of the pores occupied by each fluid phase – directly from the raw two- and three-phase steady-state images of the whole sample, see Fig. 6.25. In two-phase flow, we divided the pore space into three phases: (i) oil; (ii) water; and (iii) oil-water intermittency, while we assigned five phases under three-phase steady-state conditions: (i) gas; (ii) oil; (iii) water; (iv) gas-oil intermittency; and (v) oil-water intermittency. We extract the pores using the pore-network model extraction [145, 146], as in previous sections, and then assign a unique occupancy dependent on the average grey-scale value in the pore; each phase is given a grey-scale value range and if the average value in the pore falls within this range then the pore is considered to be occupied by that phase, see section 6.2.3.4.2.

Fig. 6.25a shows that at f_w = 0.5 and f_o = 0.5, before gas injection, on average, oil flows in pores smaller than those occupied by water which suggests that oil is more wetting to the rock than water. Nonetheless, oil also flows in a large fraction of the big pores as well; this is ascribed to the mixed-wet nature of the surface. Furthermore, we notice that oil-water intermittency takes place mostly in the intermediate-sized pores as seen previously in two-phase flow experiments [37, 120].

At three-phase steady-state conditions, as f_g is increased, and f_o and f_w are decreased, Figs. 6.25b to 6.25f, gas flows in the largest pores, oil the smallest, while water flows in medium-sized pores. This suggests that the wettability order in the mixed-wet system is oil-water-gas from most to least wetting. This wettability order has been previously observed in weakly oil-wet rocks at immiscible gas-oil conditions

[38]. While one would expect more competition between oil and water to occupy the smallest pores, due to the mixed wettability, we believe that this is dictated by the filling order, since oil saturated the pore space first before water. We see that gas-oil and oil-water intermittency occurs in pores of similar, intermediate, size during the increasing f_g, and decreasing f_o and f_w, flow path. Gas tends to favour filling the larger pores, and oil the smaller ones, so they compete to occupy pores of intermediate size. Furthermore, as seen in two-phase flow, oil and water both occupy larger and smaller pores, since this is a mixed-wet system, and intermittency is seen in a range of pore sizes, and most commonly around the mode with intermediate radius.

The same wettability order persists during the decreasing f_g, and increasing f_o and f_w, flow path, see Figs. 6.25f to 6.25h. During this flow path, gas occupied increasingly smaller pores, while oil and water filled larger pores. This is expected since the gas saturation decreases, while the oil and water saturations increase as we will show in section 6.2.4.6. This pore occupancy behaviour is different to that observed in the water-wet system, see section 6.1, where limited displacement was observed during the decreasing f_g, and increasing f_o and f_w, flow path due to double capillary trapping of gas by oil and water. Hence, this suggests that there is less gas trapping in the mixed-wet system at three-phase steady-state conditions. Therefore, it implies that the saturation history has little impact on the pore occupancy in a mixed-wet rock.

Finally, we observe that at $f_w = 0.5$ and $f_o = 0.5$, after gas injection, Fig. 6.25i, only oil and water exist in the pore space – no gas. This will be discussed in more detail in section 6.2.4.6. Nonetheless, we notice that a large fraction of oil has now moved into larger pores compared to before gas injection (Fig. 6.25a). We attribute this to the preferential displacement of gas by oil as we will show in section 6.2.4.9.

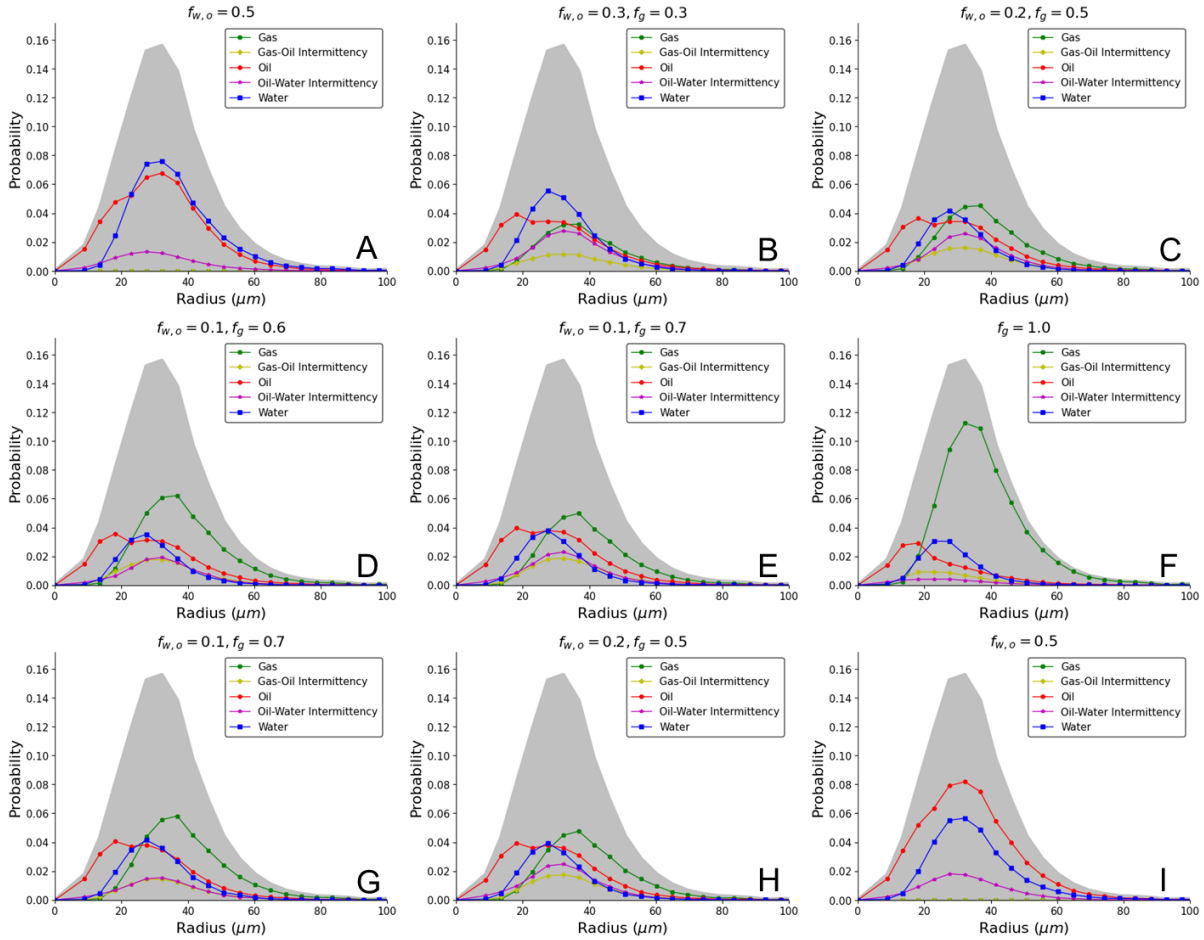

Figure 6. 25. Probability histograms showing the pore occupancy in the mixed-wet rock in three-phase steady-state conditions at different fractional flows. Gas, oil, and water fractional flows (*fg*, *fo*, and *fw*) are stated in the respective images. The grey-shaded area represents the size distribution of all the pores.

6.2.4.4 Connectivity

Here, we qualitatively and quantitatively assess the fluid connectivity on the segmented pore-scale images in flow steps 3, 8 and 12, see Table 6.4 for their respective fractional flows. It was impossible to examine the fluid connectivity in the three-phase steady-state images as they could not be segmented due to the frequent occurrence of intermittent gas-oil and oil-water flow, as explained in section 6.2.3.4.

Fig. 6.26 shows the *in situ* three-dimensional connectivity of water, oil, and gas – a wide range of colours represents a poorly connected phase, while a narrow colour distribution indicates that the phase is well connected. Furthermore, the volume-normalized Euler characteristic of each phase is quoted to quantitatively evaluate its connectivity [160-164].

We observe that at $f_w = 0.5$ and $f_o = 0.5$, before gas injection, oil is more connected than water, see Fig. 6.26a, supported by the negative Euler characteristic (-328 mm^{-3}). This implies that oil exists in thin wetting layers in the corners, and therefore, confirms that it is more wetting to the surface than water. However, the Euler characteristic of oil is still not in the range of Euler characteristic measured on weakly and strongly oil-wet rocks from the same reservoir, where the oil characteristic was much smaller than -1000 mm^{-3}, see section 3.3. This suggests that the rock surfaces are indeed mixed-wet.

At $f_g = 1$, see Fig. 6.26b, both water and gas appear disconnected, with positive Euler characteristic, while the oil connectivity is significantly improved. The enhanced oil connectivity under three-phase conditions is attributed to the spreading of oil in connected layers in the presence of gas as seen

previously in water-wet experiments, see section 6.1. In contrast, gas exists in disconnected clusters even when injected alone in the mixed-wet system unlike the water-wet case, see section 6.1. This behaviour has huge implications for gas storage applications; it means that the re-injection of water to trap gas is unnecessary. This gas behaviour has been previously observed in oil-wet rocks, extracted from the same reservoir, under unsteady-state conditions, see sections 3.3 and 4.2.

Furthermore, at three-phase steady-state conditions, we suspect that all three phases have a poor connectivity due to their intermittent behaviour. This can lead to each phase having a dynamic connectivity, where it is momentarily connected and then disconnected at steady-state conditions.

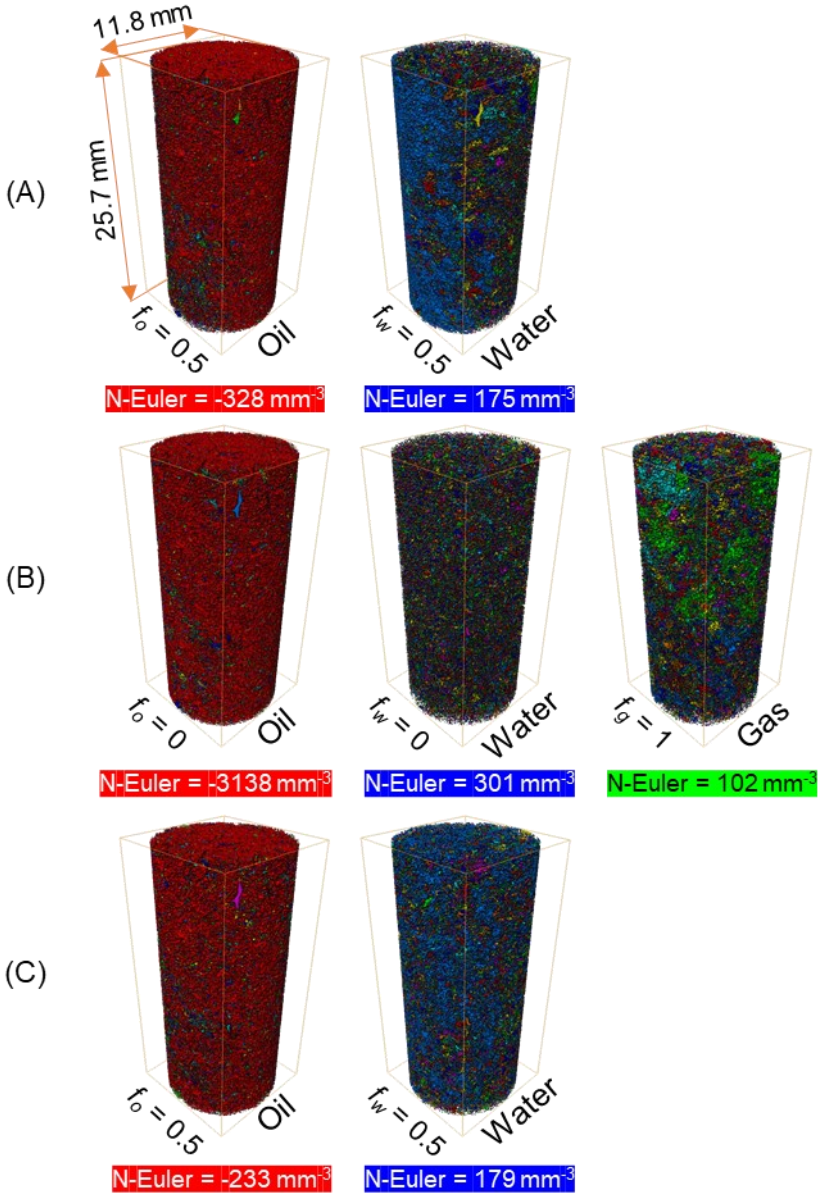

Figure 6. 26. Three-dimensional maps of oil, water, and gas connectivity in the pore-space of the mixed-wet rock at steady-state conditions. A wide range of colours represents a poorly connected phase, while a narrow colour distribution indicates that the phase is well connected. Gas, water and oil fractional flows (f_g, f_w, and f_o) are stated. N-Euler refers to the normalized Euler characteristic of each phase.

6.2.4.5 Specific interfacial areas

The fluid-fluid and fluid-solid specific interfacial areas – area per unit total volume (pore and grain) – were measured only on the segmented images of the sample, see Fig. 6.27.

The oil-water interfacial area remains almost constant under two- and three-phase conditions, with values around 1 mm^{-1}, see Fig. 6.27a. The same behaviour was observed for the area between oil and water in the water-wet system, see section 6.1. Oil and water are respectively the most and intermediate wetting phases in both systems; the oil-water area is dominated by their contact in the smaller sized pores next to the solid surface.

The water-solid and oil-solid interfacial areas are the largest, see Figs. 6.27b and 6.27c, with the oil-solid area being slightly higher. This indicates that there are more oil-wet regions compared to water-wet regions in the mixed-wet pore space. In contrast, the gas-solid area is much lower; oil spreading around gas reduces its contact with the solid surface. Furthermore, oil spreading prevents any direct contact between gas and water.

The gas-oil interfacial area is higher than that of the oil-water under three-phase conditions ($f_g = 1$), with values around 2 mm^{-1}, see Figs. 6.27a and 6.27e. This is a consequence of the spreading of oil in layers around gas in the large pores.

It was not possible to determine the dependence of fluid-fluid and fluid-solid interfacial areas on the saturation history since the three-phase steady-state images could not be segmented.

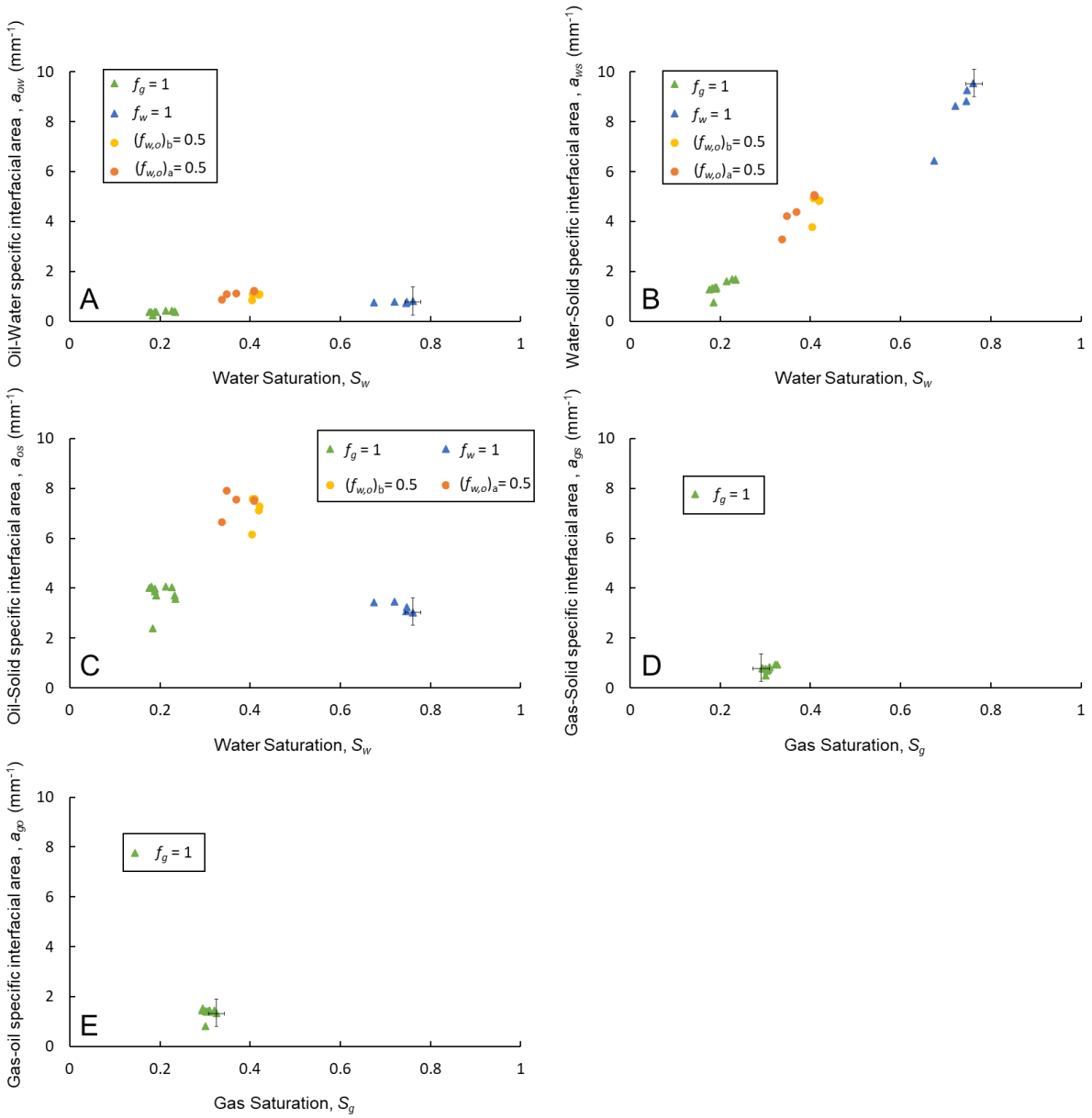

Figure 6. 27. Specific interfacial areas between (a) oil and water, (b) water and solid, (c) oil and solid, (d) gas and solid, and (e) gas and oil measured on the segmented images of the sample. f_g, f_w, and f_o refer to gas, water, and oil fractional flows respectively. Subscripts b and a in the legends of (a), (b) and (c) refer to before and after gas injection respectively. Error bars represent the uncertainty in the measurements.

6.2.4.6 Saturation

The gas, oil and water saturations, in the macro-pores, were quantified directly from the raw two- and three-phase steady-state images using the approach described in section 6.2.3.4.1, see Fig. 6.28. This calculation gives a range of gas and water saturations for each three-phase steady-state image (represented by the line connecting the black circles in Fig. 6.28); therefore, to obtain the average saturation across the whole sample we assume it is the mid-point of that range (shown in red circles). Fig. 6.28 is divided into two parts, in part (a), are the saturations for the increasing f_g, and decreasing f_o and f_w, flow path, while, in part (b), are the saturations for the decreasing f_g, and increasing f_o and f_w, path. The saturations from the segmented images in flow steps 2, 3, 8 and 12, see Table 6.4 for their fractional flows, are also plotted (shown in black squares).

On average, Fig. 6.28 displays that there is a good agreement between the saturations obtained from the raw and segmented images, with an uncertainty of ± 5%. However, for consistency, we will only quote the saturations obtained from the raw images in the text.

The first step of the experiment involved the injection of water into the oil-saturated sample, at $f_w = 1$, to reach the remaining oil saturation in the mixed-wet system. Fig. 6.28a shows that the remaining oil saturation reached only 0.34 despite increasing the water flow rate. While a value of 0.34 may seem high, it is still much lower than the values reached in the same reservoir rock but under oil-wet conditions, where the irreducible oil saturations were 0.54 and 0.61, sections 3.2 and 3.3. Again, this behaviour confirms that our system is a mixed-wet one. After that, oil and water were injected at $f_w = 0.5$ and $f_o = 0.5$, and the initial saturations of oil and water, before gas injection, were 0.58 and 0.42 respectively.

At the first three-phase steady-state condition, the gas saturation was 0.12, with oil and water saturations of 0.53 and 0.35 respectively, see Fig. 6.28a. As the gas fractional flow was increased, finally reaching $f_g = 1$, the maximum gas saturation only reached 0.32, with 0.49 and 0.19 oil and water saturations respectively. The first observation here is that the gas saturation never exceeds 0.32 despite increasing the gas flow rate. This has been previously seen in other unsteady-state and steady-state three-phase flow imaging studies, see sections 3.1, 3.2, 3.3, 4.2, and 6.1. Hence, we suggest that, under three-phase capillary-dominated conditions, with immiscible gas and oil phases, the maximum gas saturation that can be reached in this reservoir rock during core flooding is approximately 32-40% regardless of the rock wettability. The second observation at $f_g = 1$ is the high remaining oil saturation, see Fig. 6.28a. We note that gas mainly replaces water in this mixed-wet rock, which will be discussed in more detail in section 6.2.4.9.

As the flow path is reversed, decreasing f_g, and increasing f_o and f_w, the gas saturation decreases and the oil and water saturations increase, see Fig. 6.28b. This suggests that, unlike the water-wet system, see section 6.1, gas does not get trapped in the pore centres by oil and water; instead, it is produced as more oil and water are injected. While there is a little hysteresis in the saturation path of the two flow paths in the mixed-wet experiment, we conclude that fluid saturations are less impacted by the saturation history compared to the water-wet system.

More significantly, we observe that the gas saturation reaches zero when the gas injection is stopped (at $f_w = 0.5$ and $f_o = 0.5$), see Fig. 6.28b, i.e., no gas is trapped in the mixed-wet system. This implies that the stored gas can escape in the case of a water re-injection in mixed-wet reservoir. We will discuss this in more detail in section 6.2.4.10.

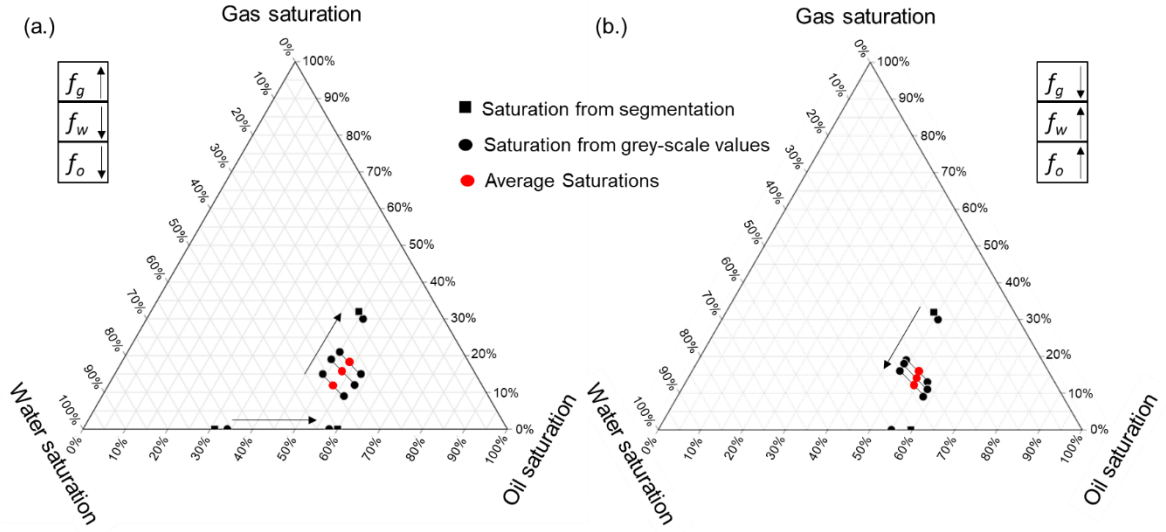

Figure 6. 28. Ternary diagrams showing the saturations obtained at (a) increasing gas fractional flow – decreasing oil and water flow – and (b) decreasing gas fractional flow – increasing oil and water – during the steady-state three-phase experiment in the mixed-wet reservoir rock. Black circles represent the saturations obtained directly from the raw images. Red circles are the averaged saturations obtained from the raw images. Black squares are the saturation obtained from the segmented images in flow steps 2, 3, 8 and 12, see Table 6.4 for their respective fractional flows. f_g, f_w, and f_o refer to gas, water, and oil fractional flows respectively.

Fig. 6.29 shows the saturation profiles across the sample obtained from the segmented images in flow steps 2, 3, 8 and 12, see Table 6.4 for their respective fractional flows. While a saturation gradient is seen in 3 of the 4 cases, there is no evidence for a significant capillary end-effect (retention of the wetting phase) at the outlet (x/L = 1).

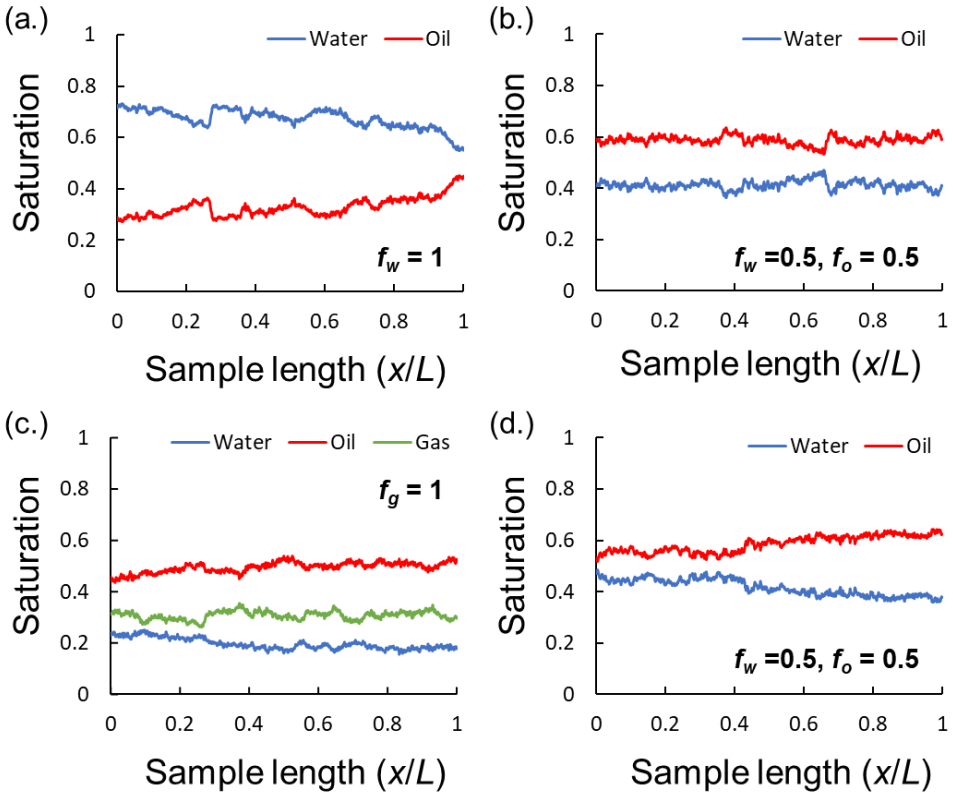

Figure 6. 29. Steady-state fluid saturation profiles obtained from the segmented images at (a) f_w = 1, (b) f_w = 0.5 and f_o = 0.5, (c) f_g = 1, and (d) f_w = 0.5 and f_o = 0.5 in the mixed-wet rock plotted along the length of the sample. Fluid saturations in the macro-pores only are considered. f_g, f_w, and f_o refer to gas, water, and oil fractional flows respectively.

6.2.4.7 Three-phase relative permeability

We recorded the pressure drop across the sample at two- and three-phase steady-state conditions to calculate the relative permeabilities in our mixed-wet reservoir rock, using Eqs. (6.1), (6.2) and (6.3). The measured pressures were stable in two-phase flow but continuously fluctuated between two pressure values under three-phase steady-state conditions. We believe that these fluctuations are caused by the intermittent behaviour of fluids which continuously altered the pressure needed for displacement at steady-state conditions.

The pressure fluctuations are significantly larger in the mixed-wet system compared to the water-wet one in section 6.1. We attribute this behaviour to the larger fraction of oil-water intermittency in the mixed-wet system. Furthermore, these observations imply that true steady-state conditions are never attained at the pore-scale in three-phase flow, and that the fluid arrangement is constantly fluctuating between locations of local capillary equilibrium.

Nonetheless, the average of the two pressure values, between which the pressure drop fluctuated, was used to calculate the three-phase relative permeabilities at all the fractional flows. Fig. 6.30 shows measurements of gas, oil, and water three-phase relative permeabilities in the mixed-wet system for the increasing f_g – decreasing f_o and f_w – and decreasing f_g – increasing f_o and f_w – flow paths. The relative permeability of each phase is plotted as a function of its own saturation; the fluid saturations in the macro-pores were obtained directly from the raw pore-scale images as described in section 6.2.4.6.

The water relative permeability is lower than that of oil, but higher than gas, see Fig. 6.30. The low water relative permeability consistent with the poor water connectivity shown in section 6.2.4.4; water

flow is limited to medium-sized pores as shown in the pore occupancy (section 6.2.4.3). In contrast, the oil relative permeability is highest due to its improved connectivity in wetting and spreading layers, see Fig. 6.30c.

Fig. 6.30b shows that the gas relative permeability is very low. This is ascribed to two reasons: (i) gas progresses in the form of disconnected clusters in the pore centres; and (ii) gas invasion is mostly limited to pores occupied by oil as we will show in section 6.2.4.9.

Fig. 6.30c shows that the saturation history has a little impact on the oil relative permeability. This is expected since oil is considered the most wetting phase in our system; oil flows in smaller pores and spreading layers regardless of the flow path. On the other hand, water and gas relative permeabilities show clear dependency on the saturation history since their flow is impacted by the relative presence of another phase in the medium- and large pores.

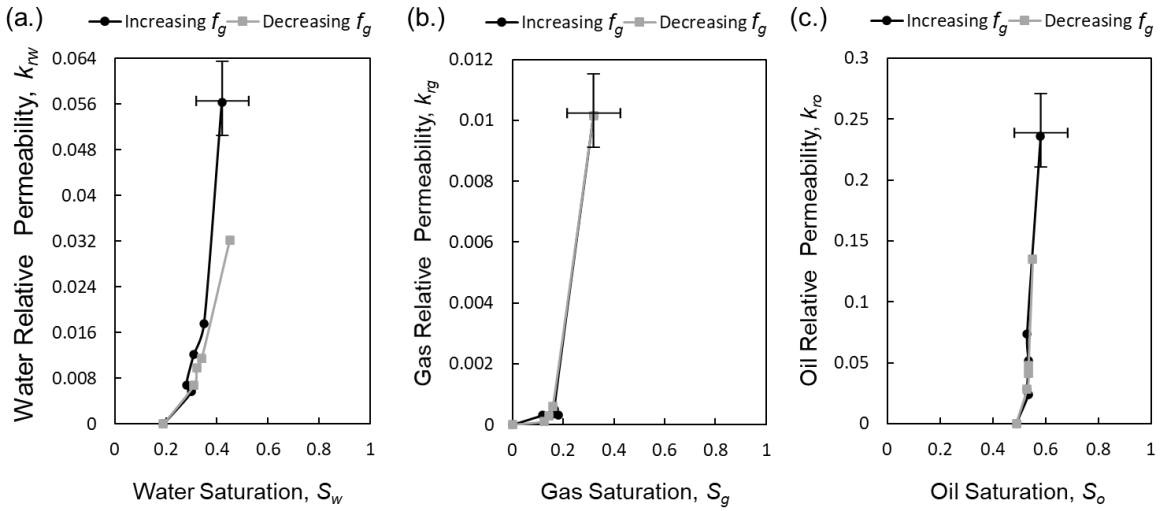

Figure 6. 30. Three-phase relative permeability of (a) water, (b) gas, and (c) oil during the increasing gas fractional flow – decreasing oil and water fractional flows – and decreasing gas fractional flow – increasing oil and water – in the mixed-wet reservoir rock. Error bars indicate the uncertainty in the measurements for all the points; both in the estimate of saturation and the determination of average pressure drop.

6.2.4.8 Capillary pressures

The capillary pressures (P_c) were calculated from the interfacial curvature (κ_{ij}) between the fluid pairs using the Young-Laplace law [18, 19, 141]: Eq. (2.9). The interfaces between the fluids were constructed and smoothed, kernel size = 5, from the segmented images in flow steps 3, 8 and 12, see Table 6.4, before measuring their curvatures. Fig. 6.31 shows the measured oil-water and gas-oil capillary pressures in the mixed-wet rock; it was not possible to measure the gas-water capillary pressure since spreading oil layers prevented direct gas-water contact.

The two- and three-phase oil-water capillary pressures are negative, with values around -0.5 kPa, demonstrating the dominance of oil-wet regions over water-wet regions in the mixed-wet reservoir sample, see Fig. 6.31a. The two-phase oil-water capillary pressure is slightly higher after gas injection, denoted by subscript *a* in Fig. 6.31a, compared to that from before, denoted by subscript *b*. We attribute this behaviour to the shift in oil pore occupancy to larger pores after gas injection as we have shown in section 6.2.4.3. As expected, the gas-oil capillary pressure is positive, with values around +0.25 kPa, indicating that oil is wetting to gas, see Fig. 6.31b.

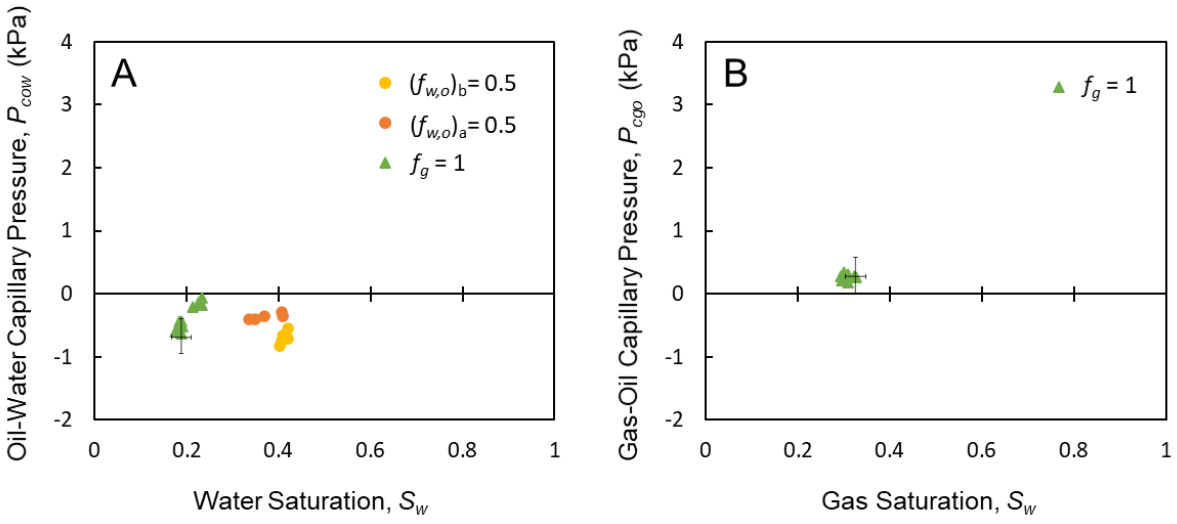

Figure 6. 31. The curvature-based capillary pressure between (a) oil and water, and (b) gas and oil measured on the segmented images and plotted as a function of water and gas saturations respectively. f_g, f_w, and f_o refer to gas, water, and oil fractional flows respectively. Subscripts *b* and *a* in the legend of (a) refer to before and after gas injection (at the end of the experiment) respectively. Error bars represent the uncertainty in the measurements.

6.2.4.9 Three-phase displacements

We quantify the fluid-fluid displacement when moving from one steady-state condition to another on the raw pore-scale images as described in section 6.2.3.4.2. Similar to pore occupancy, we consider the existence of five phases in the pores of the rock: gas, oil, water, gas-oil intermittency, and oil-water intermittency. Figs. 6.32, 6.33 and 6.34 show the displacement in the pores filled with gas, gas-oil intermittency, and oil at different fractional flows respectively.

Figs. 6.32a and 6.32b show that during the increasing f_g, and decreasing f_o and f_w, flow path, the gas-filled pores – represented by the dotted black line – remain mostly occupied by gas; there is very little displacement of gas as f_g increases.

In contrast, when f_g is decreased, and f_o and f_w are increased, Fig. 6.32c, we notice that gas is mostly displaced by oil, especially when gas injection stops (Fig. 6.32d). Gas is produced since it does not get trapped in the pore centres; the displacement of gas by oil is piston-like. While one would expect a percolation-like displacement, with snap-off, we suspect that it is suppressed by the mixed-wet nature of the surface which prevents continuous oil flow and snap-off of gas by oil. The preferential displacement of gas by oil shifts the oil occupancy towards larger pores as seen in section 6.2.4.3.

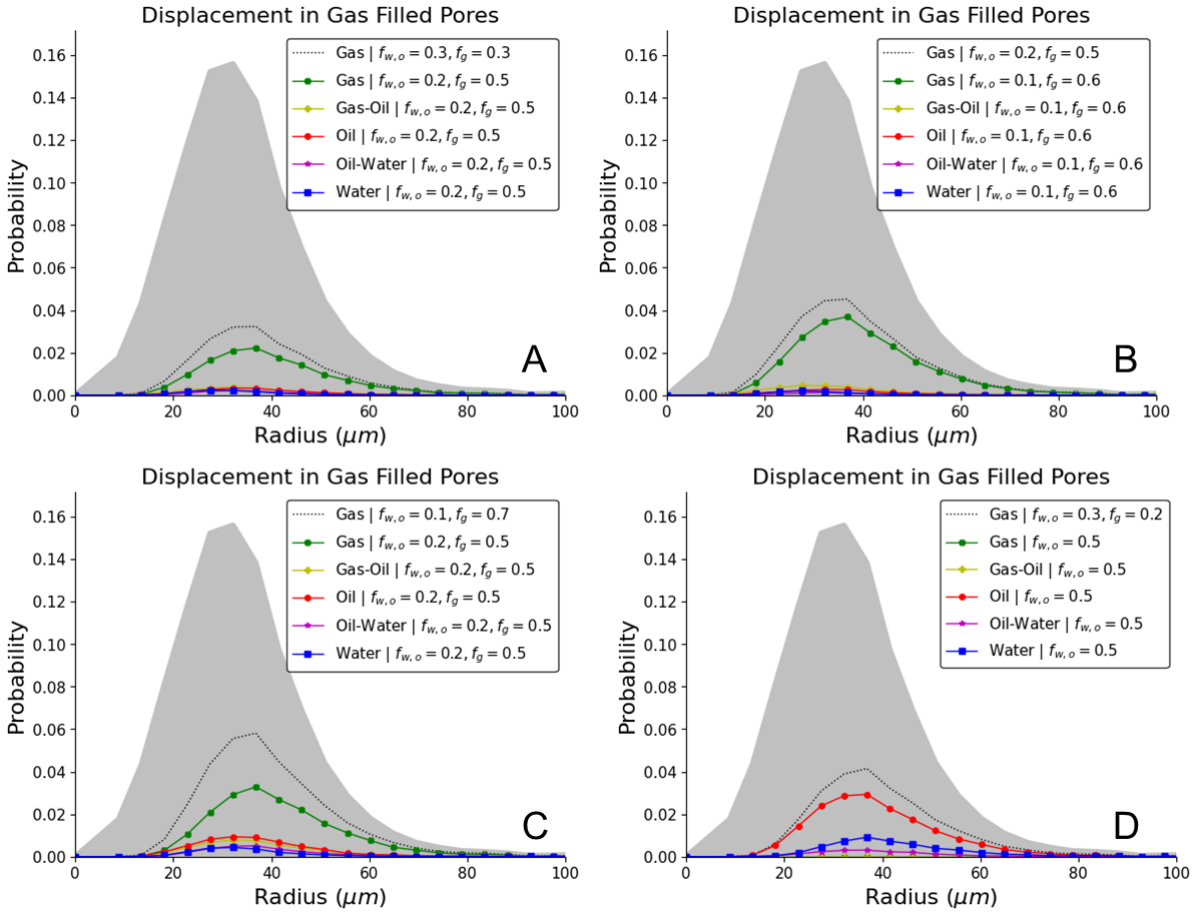

Figure 6. 32. Displacement in the gas-filled pores at different fractional flows in the mixed-wet rock during (a) and (b) increasing gas fractional flow, decreasing oil and water fractional flows, and (c) and (d) decreasing gas fractional flow, increasing oil and water plotted as a function of pore size. Displacement here refers to the change in pore occupancy from one fractional flow to another. Gas, oil and water fractional flows (f_g and $f_{w,o}$) are stated.

Fig. 6.33 shows the displacement in the gas-oil intermittency-filled pores at different fractional flows. We observe that as f_g is increased, and f_o and f_w are decreased, most of the gas-oil intermittency occupied pores are filled with gas, see Figs. 6.33a and 6.33b. In contrast, when f_g is decreased, and f_o and f_w are increased, the gas-oil intermittency occupied pores become filled with oil. This suggests that intermittent regions of the pore space are transitional occupancies waiting for displacement to occur in the direction of the phase with the increasing fractional flow.

In the case of oil-water intermittency, the intermittent pores were equally displaced by oil and water at different fractional flows, regardless of the flow path. This is because the oil and water flow rates were kept in the same direction and had the same value throughout the experiment; see Table 6.41 for the flow rates. The change in the oil-water intermittency-filled pores is shown in Fig. A7.4 in Appendix 7.

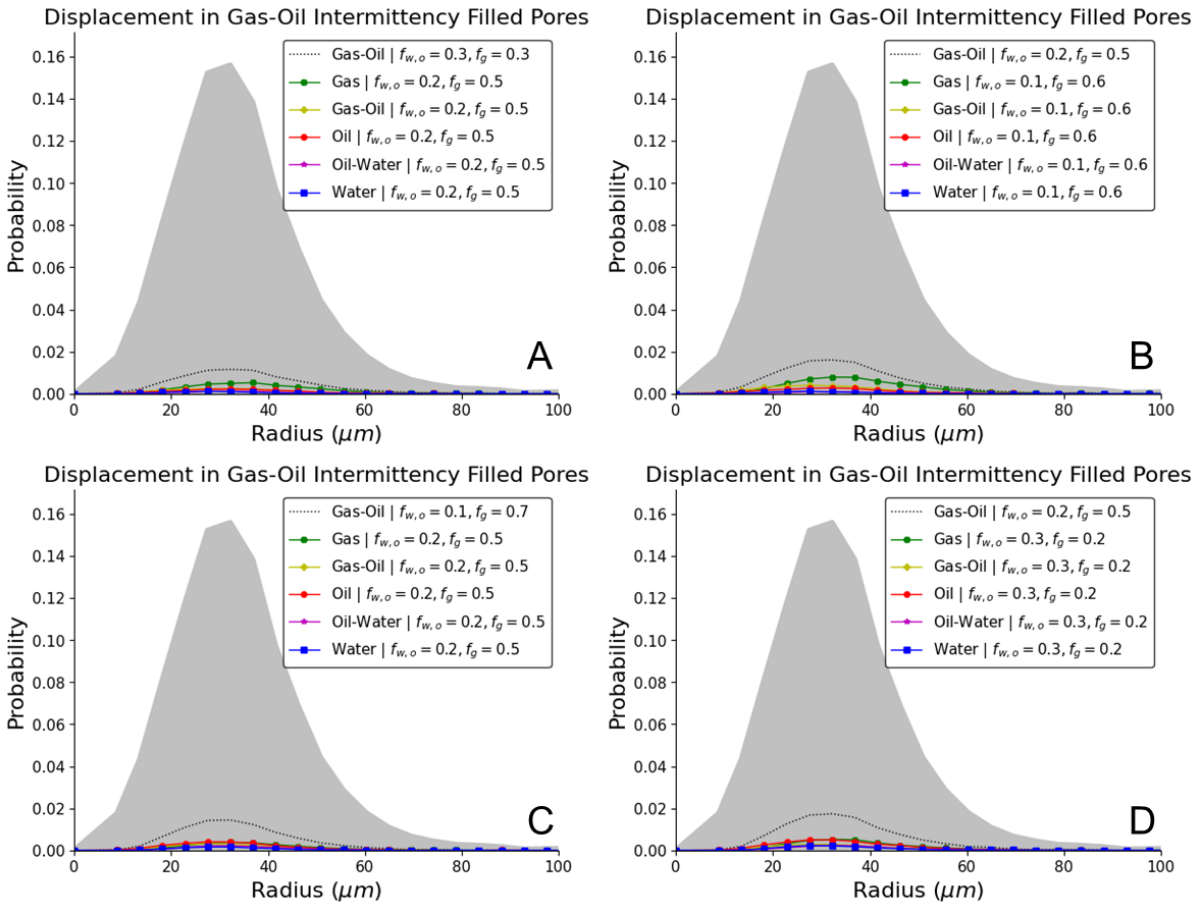

Figure 6. 33. Displacement in the gas-oil intermittency-filled pores at different fractional flows in the mixed-wet rock during (a) and (b) increasing gas fractional flow, decreasing oil and water fractional flows, and (c) and (d) decreasing gas fractional flow, increasing oil and water plotted as a function of pore size. Displacement here refers to the change in pore occupancy from one fractional flow to another. Gas, oil and water fractional flows (f_g and $f_{w,o}$) are stated.

The displacement in oil-filled pores during the increasing f_g, and decreasing f_o and f_w, flow path is shown in Figs. 6.34a and 6.34b. Oil is mostly displaced by gas. However, this contradicts the saturation results in section 6.2.4.6, where mostly the water saturation decreased as the gas saturation increased. This phenomenon will be explained later in this section. Furthermore, we note that most of the oil displacement occurs in the bigger pores; there is a little displacement of oil in the smallest pores. This is due to the strongly oil-wet nature of the smaller pores that are filled with oil in our mixed-wet system, where a very high capillary pressure is needed to displace the oil out.

As f_g is decreased, and f_o and f_w are increased, oil is mostly displaced now by water or oil-water intermittency, see Fig. 6.34c and 6.34d.

On the other hand, water is mostly displaced by oil or oil-water intermittency regardless of the flow path direction as shown in Fig. A7.5 in Appendix 7.

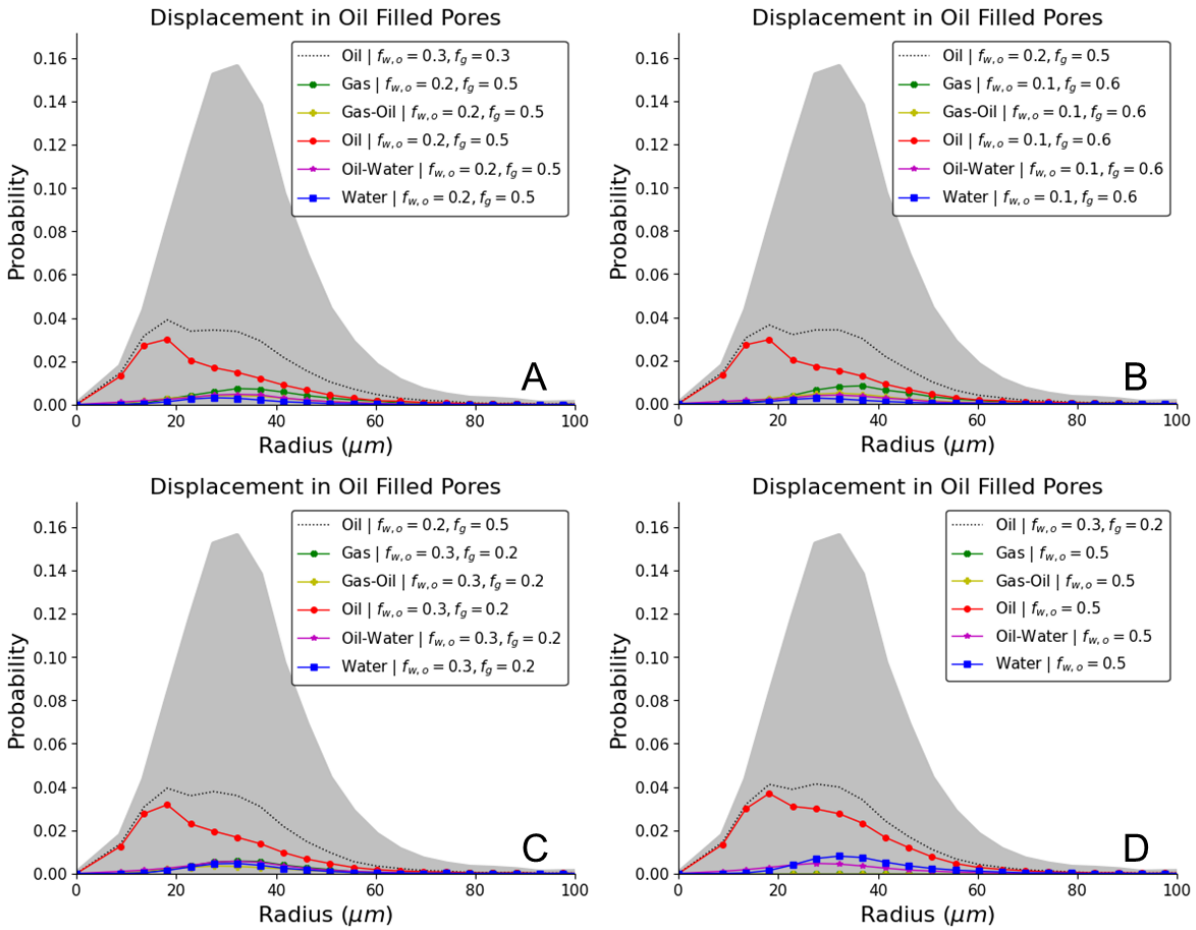

Figure 6. 34. Displacement in the oil-filled pores at different fractional flows in the mixed-wet rock during (a) and (b) increasing gas fractional flow, decreasing oil and water fractional flows, and (c) and (d) decreasing gas fractional flow, increasing oil and water plotted as a function of pore size. Displacement here refers to the change in pore occupancy from one fractional flow to another. Gas, oil and water fractional flows (f_g and $f_{w,o}$) are stated.

To summarize this section, when f_g is increased, and f_o and f_w are decreased, oil is mostly displaced by gas, and water is displaced by oil, whereas when f_g is decreased, and f_o and f_w are increased, gas is mostly displaced by oil, oil is displaced by water, and water is displaced by oil.

From this we can explain why, as f_g is increased, and f_o and f_w are decreased, the water saturation decreases considerably as the gas saturation is increased, although gas mostly displaces oil. As gas invades the pore space, it mainly displaces oil in the largest pores. The displaced oil then moves to mobilize water in smaller pores. The mobilized water then gets produced. At the next fractional flow, gas invades the newly invaded pores by oil, displacing oil out and forcing it to mobilize water in even smaller pores until the irreducible water saturation is reached at a gas fractional flow of one.

This process is reversed when f_g is decreased, and f_o and f_w are increased. Now, oil displaces gas from the smaller pores first. This is accompanied by displacement of oil by water either in intermediate-sized pores, or large pores where oil displaced gas. The displaced gas gets produced flowing through the largest pores. This continues until there is no more gas in the pore space.

While gas can directly displace oil and vice versa, water and gas can only displace each other in a double displacement process mediated by oil, i.e., gas-oil-water and water-oil gas double displacement processes.

6.2.4.10 Trapping and implications for CO_2 storage

Fig. 6.35 shows the fluid arrangements in a single pore before, during, and after gas injection in the mixed-wet rock. Before gas injection, oil existed in thin wetting layers in the corners of the pores, as expected for mixed-wet media, see Fig. 6.35a. Once gas was injected, Fig. 6.35b, the oil connectivity significantly improved as seen in section 6.2.4.4; the thickness of oil layers increased as it spread between gas and water. Once gas injection was stopped, at $f_w = 0.5$ and $f_o = 0.5$, oil and water completely displaced gas from the pore centre; there is no gas trapping. This is due to the mixed-wet nature of the surface which prevents oil or water completely surrounding the gas phase, suppressing snap-off and capillary trapping.

In previous work, which have studied gas trapping during water injection under unsteady-state conditions in weakly oil-wet or mixed-wet rock [17, 38], the amount of gas trapped was lower than under equivalent water-wet conditions; however, some gas was trapped. See section 5.1.5 for a further discussion of these results. In this experiment, the gas appears to be completely displaced. Further work is required to understand why this is the case and how pore structure and wettability combine to control the residual saturation. Overall though, less gas trapping is seen in weakly oil-wet and mixed-wet rocks since there is less trapping by snap-off by swelling water and oil layers.

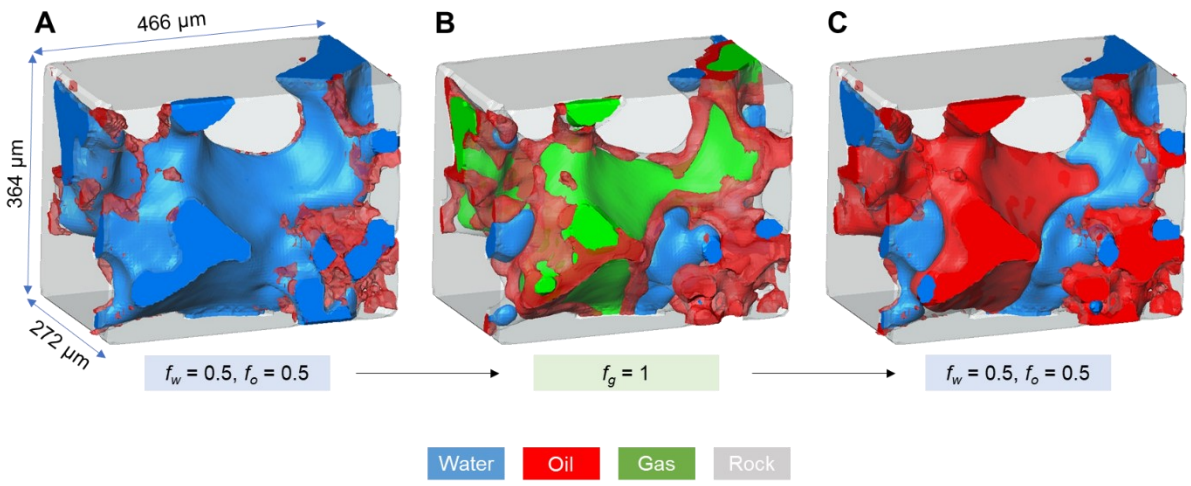

Figure 6. 35. Three-dimensional representation of the fluids arrangement in a single pore (a) before, (b) during and (c) after gas injection in the mixed-wet rock. Oil is shown in red, water in blue, gas in green, while the rock is rendered semi-transparent (grey). f_g, f_w, and f_o refer to gas, water, and oil fractional flows respectively.

This work illustrates the impact that pore-scale displacement can have on field-scale carbon dioxide storage. The observation of little or no gas trapping has huge implications on the design of CO_2 storage in depleted oil reservoirs with a mixed wettability state. It shows that the widely implemented water-alternating-gas (WAG) injection strategy in oil reservoirs may not be ideal for secure CO_2 storage. While the strategy is well known for increasing the oil recovery, this work shows that it can lead to recycling of the injected CO_2 as it continuously gets produced.

We suggest that an injection strategy of continuous CO_2 injection is in fact better for secure storage in mixed-wet reservoirs, as suggested previously in chapter 5. This is for two reasons: (i) CO_2 naturally gets disconnected when injected as we have shown in section 6.2.4.4; this restricts its flow conductance in the reservoir; and (ii) the injection of large amounts of water, after CO_2 injection, mobilizes CO_2 in the reservoir, producing significant quantities of the stored CO_2.

6.2.5 Final Remarks and Suggestions

We have presented steady-state measurements of three-phase relative permeability combined with high-resolution pore-scale X-ray imaging, 5.36 μm per voxel, for a carbonate reservoir rock with a mixed wettability state. The experiment was performed under capillary-dominated, immiscible gas-oil conditions. We investigated the impact of a saturation history, where the gas fractional flow is first increased and then decreased on flow properties; oil and water fractional flows were kept the same and changed in the opposite direction to gas. The use of pore-scale imaging allowed us to characterize simultaneously, with relative permeability, the *in situ* contact angles, pore occupancy, connectivity, interfacial areas, capillary pressures, saturations, displacement processes, and trapping.

The mixed-wet nature of the rock surfaces – achieved through contact with crude oil at conditions of high temperature and pressure – was confirmed by calculating the two-phase geometric oil-water contact angle which had a value of $82^o \pm 42^o$. Post gas injection, the gas-oil, oil-water and gas-water contact angles were $66^o \pm 41^o$, $80^o \pm 41^o$, and $78^o \pm 40^o$ respectively. While it was not possible to determine a clear wettability order from the contact angle measurements, the pore occupancy results demonstrated that, at different fractional flows, oil occupied the smallest pores, water intermediate pores, and gas the largest pores, suggesting an oil-water-gas wettability order, from most to least wetting.

This wettability order was further supported by the negative oil-water and positive gas-oil local capillary pressures. A negative oil-water pressure illustrates that there are more oil-wet regions compared to water-wet regions in the pore space. No gas-water capillary was calculated since oil spread in layers between gas and water preventing their direct contact.

We observed intermittent flow regions between gas and oil, and oil and water at three-phase steady-state flow despite having capillary-dominated conditions. The pores that were intermittently occupied were filled with the phase with the increasing fractional flow at the next steady-state condition. While intermittent flow at capillary-conditions was previously observed in a three-phase water-wet system, section 6.1, here, it is more frequent and occupies a larger fraction of the pore space; in particular, the oil-water intermittency is significant. Both oil-water and gas-oil intermittently occupied pores of similar size, i.e., intermediate-sized pores.

We identify a distinct gas flow pattern, where gas advances in the form of disconnected ganglia mediated by double and multiple displacement processes. Oil was the only connected phase since it forms connected wetting and spreading layers; water existed in disconnected clusters. The oil relative permeability was the highest in the pore space followed by water, then gas. The high oil relative permeability is attributed to its improved connectivity. In contrast, gas has a low relative permeability given that it is disconnected and its flow in the larger pores is blocked by water. The impact of saturation history on gas and water relative permeabilities was larger than its impact on the oil relative permeability.

As the gas fractional flow was increased – oil and water flows decreased – gas mainly displaced oil, and oil displaced water. When the flow path was reversed oil replaced gas in the larger pores and water displaced oil in the medium-sized pores. Oil was shifted to larger pores after gas injection. While gas can directly displace oil and vice versa, water and gas can only displace each other in a double displacement process mediated by oil, i.e., gas-oil-water and water-oil gas double displacement processes.

Surprisingly, there was no gas trapped when gas injection was stopped. We attributed this behaviour to the mixed-wet nature of the surface which prevents either oil or water from completely surrounding gas and capillary trapping it in the pore centres. These outcomes suggest that the subsequent water injection,

after gas, is not ideal for gas storage applications. Instead, a continuous injection of gas only can ensure safe trapping as gas is naturally disconnected upon injection in the reservoir.

Future work should focus on quantifying the steady-state three-phase relative permeability, combined with imaging, in strongly oil-wet rocks to examine the impact of an oil-gas-water, from most to least wetting, wettability order on relative permeability. This will also provide insights into intermittency showing whether intermittent flow is as frequent as it is in a mixed-wet system. Future experiments should consider investigating the impact of different flow paths to have a comprehensive understanding of the relationship between saturation history and relative permeability. Furthermore, the impact of reaching near-miscible gas-oil conditions could be investigated.

Chapter 7

In this chapter we will summarize the novel findings and insights of our work as well as suggest topics for future studies to further improve our understanding of three-phase flow in porous media.

7.1 Conclusions and Future Work

7.1.1 Conclusions

This thesis presents a novel approach to investigate – *in situ* – three-phase flow in porous media using X-ray microtomography. Specifically, we studied the impact of surface wettability and gas-oil miscibility – immiscible and near-miscible conditions – on micro-scale flow and trapping mechanisms. We examined three-phase flow under unsteady-state and steady-state conditions and employed both laboratory and synchrotron X-ray sources in our investigations. While the insights from this PhD thesis can be used to understand three-phase flow in any porous medium, we focus on its importance for the optimization of CO_2 sequestration in hydrocarbon reservoirs as a vital component of efforts to prevent climate change.

The use of X-ray imaging in our experiments offers the advantage of accessing a range of pore-scale properties otherwise inaccessible through conventional experimental techniques. The set of novel experiments performed in this PhD thesis are outlined in Table 1.1. Furthermore, we developed a suite of image analysis techniques to characterize three-phase flow phenomena that provide a complete description of the pore-scale physics that control the conductance and trapping of each phase which are:

1. **Wettability order**
2. **Spreading and wetting layers**
3. **Double/multiple displacements**

Alongside these unique three-phase processes, our experimental and analysis methods allowed for the characterization of key petrophysical properties that are pertinent to subsurface applications such as:

1. **Fluid saturation**
2. **Capillary pressure**
3. **Relative permeability**
4. **Interfacial areas**
5. **Connectivity (Euler characteristic)**
6. **Pore occupancy**

Now, we will list the new insights obtained from each of the seven experiments in the order they are described in the thesis.

Firstly, in section 3.1, we proved that the pore-scale properties underlying three-phase flow exhibit a different behaviour under near-miscible conditions compared to immiscible conditions, suggesting that it is a unique process and cannot be represented by models developed for immiscible conditions. We showed that under **unsteady-state** three-phase flow in a **water-wet** porous medium at **near-miscible conditions**:

i. Gas and oil become neutrally wetting to the surface which facilitates their flow along the same path in the pore space; the strict wettability order – water-oil-gas, from most to least wetting – seen at immiscible conditions breaks down.

ii. Oil does not form spreading layers sandwiched between water and gas at near-miscible conditions as opposed to the immiscible case.
iii. The microscopic displacement of oil by gas at near-miscible conditions is very efficient due to the low gas-oil interfacial tension.
iv. Both gas-oil-water and gas-water-oil double displacements can occur in the pore space during gas injection at near-miscible conditions, whereas only a gas-oil-water displacement is possible at immiscible conditions.

Secondly, in section 3.2, we investigated **near-miscible conditions** in a **weakly oil-wet** system during **unsteady-state** flow. We demonstrated that the traditional assumption that CO_2 is always the most non-wetting phase is incorrect implying that flow of CO_2 in reality is impeded by an order of magnitude or more compared to conventional models. We showed that under near-miscible conditions:

i. The wettability order is oil-CO_2-water, from most to least wetting as opposed to an oil-water-CO_2 one at immiscible conditions.
ii. CO_2, the intermediate-wet phase, forms spreading layers in the pore space which impedes its flow in the pore space although connectivity is maintained.
iii. CO_2 displaces oil efficiently from the corners of the pore space leaving water stranded in the centres.
iv. At these conditions, a continuous CO_2 injection strategy is recommended to improve oil recovery and boost CO_2 storage capacity.

Next, in section 3.3, we provided the first experimental evidence of the anticipated wettability order – oil-gas-water from most to least wetting – in **strongly oil-wet** rocks at **immiscible conditions**. We compared the results with those obtained in section 3.2, at near-miscible conditions, where the same wettability order was observed. We noticed the following at **unsteady-state** conditions:

i. CO_2 as the intermediate-wet phase forms layers surrounding water at near-miscible conditions, while, at immiscible conditions, it exists as disconnected ganglia in the pore space.
ii. CO_2 is more connected at near-miscible conditions, albeit with a low flow conductance.
iii. Capillary trapping of CO_2 by water in the centres is not possible at both immiscible and near-miscible conditions.
iv. Capillary trapping of CO_2 by oil is only possible at immiscible conditions.
v. Near-miscible conditions are more favourable for oil recovery.
vi. To maximize the amount of oil recovered and CO_2 stored at immiscible conditions, a water-alternating-gas injection strategy is suggested as opposed to continuous gas injection in the near-miscible case.

In section 4.1, we investigated, for the first time, using synchrotron imaging, the pore-scale dynamics during **unsteady-state** water injection in an **oil-wet** reservoir rock (**two-phase flow**). We observed the following:

i. Water displaces oil in a drainage-like process, where water advances as a connected front displacing oil in the centre of the pores, confining it to wetting layers.
ii. The displacement is an invasion percolation process, where throats, the restrictions between pores, fill in order of size, with the largest available throats filled first.
iii. The displacement is predominantly size-controlled; wettability has a smaller effect, due to the wide range of pore and throat sizes, as well as largely oil-wet surfaces.
iv. Haines jumps occur on single- and/or multiple-pore levels accompanied by the rearrangement of water in the pore space to allow the rapid filling.
v. Snap-off events are observed both locally and distally and the capillary pressure of the trapped water ganglia is shown to reach a new capillary equilibrium state.
vi. Both water and oil are well-connected in the pore space.

In section 4.2, we extended the pore-scale dynamics study described in section 4.1 to three-phase flow. Gas, at **immiscible conditions** with the oil, was introduced into a **strongly oil-wet** system and **unsteady-state** pore-scale displacement events were captured using synchrotron X-ray imaging. We observed, for the first time, a unique gas invasion pattern, where gas progresses through the pore space in the form of disconnected clusters mediated by double and multiple displacement events. Gas advances in a process we name three-phase Haines jumps, during which gas re-arranges its configuration in the pore space, retracting from some regions to enable the rapid filling of multiple pores. The gas retraction leads to a permanent disconnection of gas ganglia, which do not reconnect as gas injection proceeds. Our main conclusions and implications from this work are:

i. The wettability order is oil–gas–water from most to least wetting in a strongly oil-wet system where the gas phase is nitrogen.
ii. Thermodynamic contact angles derived from energy balance provide a better estimate of displacement angles compared to the geometric approach consistent with the measured pore occupancy and capillary pressure.
iii. Gas being the intermediate-wet phase is apparently disconnected in the pore space.
iv. As gas invaded the pore space, it displaced oil and water in direct gas–water and gas–oil displacements, as well as double and multiple gas–oil–water displacement.
v. During gas injection, water maintains its connectivity through the larger pores, while oil remains hydraulically connected through wetting layers and spreading oil layers.

Chapter 5 provided a synthesized review of the latest pore-scale insights into unsteady-state three-phase flow achieved with three-dimensional X-ray imaging. The review included insights from our work and other three-phase flow X-ray imaging studies in the literature. We ended the section by suggesting the optimum CO_2 injection strategy during CCS-EOR to improve the microscopic displacement efficiency in hydrocarbon reservoirs under various wettability and miscibility conditions.

Next, in section 6.1, we developed a novel experimental approach to combine steady-state three-phase flow techniques with pore-scale X-ray imaging for the first time. This involved the design of a new flow cell that allows for the simultaneous injection of three fluid phases while recording the pressure drop across the system, enabling the simultaneous determination of three-phase relative permeability and capillary pressure on the same sample. We tested the **steady-state** approach first on a **water-wet** sample at **immiscible conditions** where the wettability order is water-oil-gas from most to least wetting. Though the measured relative permeabilities were consistent, to within experimental uncertainty, with values obtained without X-ray imaging on larger samples, we discovered a unique flow dynamics. The most non-wetting phase (gas) is disconnected across the system: gas flows by periodically opening critical flow pathways in intermediate-sized pores. Combining macroscopic measurements of flow properties with pore-scale imaging allowed for the following discoveries to be made:

i. Gas was continuously trapped in the centres by spreading oil and wetting water layers despite being continuously injected.
ii. Intermittent gas-oil and oil-water flow occurs in three-phase flow even under capillary-dominated displacement conditions; this is different to the intermittent flow observed in two-phase flow at high flow rates.
iii. Once gas invaded the pore space it was not possible to displace it since it was trapped by double capillary trapping.
iv. The gas relative permeability was the lowest since it was disconnected in the pore space and oil the highest as it was connected in medium-sized pores.
v. Two double displacement processes were observed: (i) gas-oil-water, and (ii) water-oil-gas during the two flow paths.

Finally, in section 6.2, we investigated **steady-state** three-phase flow in a **mixed-wet** (or weakly oil-wet) system at **immiscible** conditions. The main conclusions from this work were:

i. The wettability order in the mixed-wet system is oil-water-gas, from most to least wetting.
ii. Oil existed in both wetting layers, in the oil-wet regions, and spreading layers.
iii. Intermittency was more pronounced in the mixed-wet system compared to the water-wet one.
iv. The pores that were intermittently occupied, were filled with the phase with the increasing fractional flow at the next steady-state condition.
v. Both oil-water and gas-oil intermittently occupied pores of similar size, i.e., intermediate-sized pores.
vi. Gas advances in the form of disconnected ganglia mediated by double and multiple displacement processes.
vii. The oil relative permeability was the highest in the pore space followed by water, then gas similar to the water-wet system.
viii. The impact of saturation history on gas and water relative permeabilities was larger than its impact on the oil relative permeability.
ix. As the gas fractional flow was increased – oil and water flows decreased – gas mainly displaced oil, and oil displaced water. When the flow path was reversed oil replaced gas in the larger pores and water displaced oil in the medium-sized pores.
x. Surprisingly, there was no gas trapping in the system due to its mixed-wet nature which prevents oil and water from completely surrounding the gas phase.

To sum up, we have advised a methodology to describe three-phase flow in porous media using pore-scale X-ray imaging. We extended the scope of the imaging work on three-phase flow to near-miscible gas-oil conditions in systems with different wettabilities. We also tapped into the hitherto unproven wettability state – strongly oil-wet – at immiscible conditions, not only using static but also dynamic imaging. Furthermore, we vastly expanded the X-ray imaging work on three-phase flow by combining it with steady-state techniques at various wettability conditions. Nonetheless, there is a plenty of work yet to be done in this area.

7.1.2 Future Work

Despite covering a wide range of topics in this thesis, more research is most certainly required to disentangle the pore-scale complexities underlying three-phase flow in porous media. We believe that the use of micro-scale X-ray imaging is the way forward to gain a comprehensive understanding of this phenomena as we have shown from this work.

While the experimental methodologies and image analysis techniques developed were strictly applied to investigate three-phase flow in permeable rocks, it can in fact be used as a standard procedure to study multiphase flow in a broad range of porous media. More specifically, the techniques could be adapted for various applications, other than carbon dioxide storage and enhanced oil recovery, including the design of microfluidic devices, batteries, fuel cells as well as contaminant transport in soils.

The first suggestion for future work – which naturally arises from reading this thesis – would be a simple repetition of the experiments performed to confirm the novel findings; this could help strengthen the results by proving their reproducibility. These experiments are rather time consuming, where including the preliminary preparation – e.g., drilling, cleaning, and wettability alteration – a single experiment requires few months let alone the limited lab accessibility. Hence, in the interest of exploring different areas of three-phase flow, the experiments were not repeated in this thesis.

The second recommendation is to perform a series of three-phase experiments for a range of gas-oil interfacial tensions to exactly delineate the transition zone from immiscible to near-miscible conditions under which a unique set of pore-scale physics can be used to describe the flow and trapping of fluids.

Thirdly, for **unsteady-state conditions**, there are few cases that are yet to be investigated with X-ray imaging. Hence, rather than giving a general future topic, below we list the potential experiments that can be investigated using the methodologies developed in this thesis:

1. Static imaging of tertiary near-miscible gas injection in a water-wet system.
2. Stating imaging of secondary near-miscible gas injection in a weakly oil-wet system.
3. Static imaging of tertiary and secondary near-miscible gas injection in a strongly oil-wet system.
4. Static imaging of tertiary and secondary near-miscible gas injection in a mixed-wet system.
5. Dynamic imaging of secondary and tertiary near-miscible gas injection in water-wet, weakly oil-wet, strongly oil-wet, and mixed-wet systems.
6. Dynamic imaging of secondary immiscible gas injection in water-wet, weakly oil-wet, strongly oil-wet, and mixed-wet systems.
7. Dynamic imaging of tertiary immiscible gas injection in a weakly oil-wet system.

In addition to studying the influence of wettability and miscibility, for each of the experiments listed above, the impact of different: (i) rock types; (ii) temperatures and pressures; (iii) gas phase, e.g., CO_2, nitrogen, or hydrogen; and (iv) flow rates; can be investigated.

These experiments, alongside the work from this thesis and the literature, could serve as the foundation stone to pore-scale modelling and field simulations of immiscible and near-miscible unsteady-state gas injection processes. Moreover, future modelling studies should focus on finding a way to simulate the disconnected progression of gas when it is the intermediate-wet phase at unsteady-state conditions. This can only be achieved through the incorporation of double and multiple displacements as well as the concept of gas Haines jumps which we discovered in our work.

On the other hand, at **steady-state conditions**, there is even a larger number of studies that can be performed. Therefore, it would be more practical to use X-ray imaging to characterize the impact of a certain three-phase pore-scale phenomena on the flow behaviour. This can be achieved by changing one property while fixing all the other variables. The main phenomena that must be investigated include:

1. Intermittent flow.
2. Saturation history.
3. Surface wettability.
4. Spreading and layer flow.
5. Interfacial tensions.

The major finding at steady-state conditions was the occurrence of intermittent flow at what we believed was a capillary-dominated flow regime. This implied that in three-phase flow we may never genuinely attain steady-state conditions at the pore-scale, although we have, macroscopically, a constant saturation, since the fluid arrangement at the pore-scale is constantly fluctuating between locations of local capillary equilibrium. This must be thoroughly investigated by performing X-ray imaging of steady-state flow at very low flow rates since it can have huge implications for current empirical three-phase flow models. This also poses the question whether or not there is an apparent relative permeability that must be quantified in three-phase flow for different flow rates. Furthermore, it is evident that the current quasi-static assumption of pore network models that compute relative permeability based on the connected network of each phase through the pore space is flawed. For empirical models that use two-phase analogies to predict three-phase properties, again the predictions are likely to be significantly in error since they do not encapsulate this unique nature of three-phase flow.

Moreover, our work has shown that the use of the same three-phase pore-scale assumptions interchangeably between steady-state and unsteady-state conditions can result in significant errors. For example, in a water-wet system, at immiscible conditions, gas was connected at unsteady-state conditions while it was disconnected at steady-state conditions. Therefore, to have accurate field-scale

simulations of carbon dioxide storage, future work should focus on characterizing the locations in the reservoir where steady-state and unsteady-state flows take place.

In this thesis, the role of micro or sub-resolution porosity in assisting the flow of fluids was ignored due to the added segmentation difficulty in three-phase flow. Micro-porosity plays a major role in providing flow paths for water, especially at lower saturations. Hence, in the future a better segmentation method must be developed to account for the contribution of micro-porosity.

Moreover, the average *in situ* measured geometric contact angle was taken as the mean of the distribution which was wide and varied in individual pores due to surface roughness and complex pore geometry. While this can often provide a good indication of the surface wettability, it is not representative of displacement angles which are needed for pore-scale modelling. On the other hand, the introduction of the thermodynamic contact angle, obtained from energy balance, provided better estimates of displacement angles since it depended on less sensitive parameters such as the local change in volume, interfacial curvature and areas rather than a pinned three-phase contact line. Nonetheless, this was still not enough to satisfy the Bartell-Osterhof relationship which holds at one location in equilibrium. One way to overcome this issue would be to measure the thermodynamic contact angle on a pore-by-pore basis.

Finally, the impact of using live oils on gas–oil miscibility must also be investigated since all the three-phase flow pore-scale imaging studies discussed used dead oils (that is oil with no dissolved natural gas at reservoir conditions). Also, with pore-scale imaging the flow and impact of surfactants and foams can be studied. Finally, as mentioned previously, the same techniques could be used to study other flow in porous media problems, including micro-fluidic devices, batteries, and fuel cells.

References

[1] M. Roser. "Future Population Growth." OurWorldInData. https://ourworldindata.org/future-population-growth (accessed 2021).

[2] BP Statistical Review of World Energy. "BP Statistical Review of World Energy." https://www.bp.com/en/global/corporate/energy-economics/statistical-review-of-world-energy.html (accessed 28/09/2021).

[3] H. Ritchie and M. Roser. "CO_2 and Greenhouse Gas Emissions." OurWorldInData. https://ourworldindata.org/co2-and-other-greenhouse-gas-emissions (accessed 2021.

[4] NASA/GISS. "Global Land-Ocean Temperature Index." https://climate.nasa.gov/vital-signs/global-temperature/ (accessed 2021).

[5] M. Allen *et al.*, "Technical Summary: Global warming of 1.5° C. An IPCC Special Report on the impacts of global warming of 1.5° C above pre-industrial levels and related global greenhouse gas emission pathways, in the context of strengthening the global response to the threat of climate change, sustainable development, and efforts to eradicate poverty," 2019.

[6] IEA, "The Role of CO2 Storage," *Interantional Energy Agency,* 2019. [Online]. Available: https://www.iea.org/reports/the-role-of-co2-storage

[7] L. Irlam, "Global costs of carbon capture and storage," *Global CCS institute,* 2017.

[8] L. W. Lake, "Enhanced oil recovery," 1989.

[9] EIA. "SHORT-TERM ENERGY OUTLOOK." U.S. Energy Information Administration https://www.eia.gov/outlooks/steo/report/global_oil.php (accessed 22/07/2019).

[10] SCCS. "Global CCS Map." Scotish Carbon Capture and Storage. https://www.sccs.org.uk/expertise/global-ccs-map (accessed 11/2021).

[11] M. J. Blunt *et al.*, "Pore-scale imaging and modelling," *Advances in Water Resources,* vol. 51, pp. 197-216, 2013/01/01/ 2013, doi: https://doi.org/10.1016/j.advwatres.2012.03.003.

[12] D. Wildenschild and A. P. Sheppard, "X-ray imaging and analysis techniques for quantifying pore-scale structure and processes in subsurface porous medium systems," *Advances in Water Resources,* vol. 51, pp. 217-246, 2013/01/01/ 2013, doi: https://doi.org/10.1016/j.advwatres.2012.07.018.

[13] A. M. Alhammadi, A. AlRatrout, K. Singh, B. Bijeljic, and M. J. Blunt, "In situ characterization of mixed-wettability in a reservoir rock at subsurface conditions," *Scientific Reports,* vol. 7, no. 1, p. 10753, 2017/09/07 2017, doi: 10.1038/s41598-017-10992-w.

[14] A. M. Alhammadi, Y. Gao, T. Akai, M. J. Blunt, and B. Bijeljic, "Pore-scale X-ray imaging with measurement of relative permeability, capillary pressure and oil recovery in a mixed-wet micro-porous carbonate reservoir rock," *Fuel,* vol. 268, p. 117018, 2020/05/15/ 2020, doi: https://doi.org/10.1016/j.fuel.2020.117018.

[15] Q. Lin, B. Bijeljic, R. Pini, M. J. Blunt, and S. Krevor, "Imaging and Measurement of Pore-Scale Interfacial Curvature to Determine Capillary Pressure Simultaneously With Relative Permeability," *Water Resources Research,* vol. 54, no. 9, pp. 7046-7060, 2018/09/01 2018, doi: 10.1029/2018WR023214.

[16] A. Scanziani, K. Singh, T. Bultreys, B. Bijeljic, and M. J. Blunt, "In situ characterization of immiscible three-phase flow at the pore scale for a water-wet carbonate rock," *Advances in Water Resources,* vol. 121, pp. 446-455, 2018/11/01/ 2018, doi: https://doi.org/10.1016/j.advwatres.2018.09.010.

[17] Z. Qin, M. Arshadi, and M. Piri, "Micro-scale experimental investigations of multiphase flow in oil-wet carbonates. II. Tertiary gas injection and WAG," *Fuel,* vol. 257, p. 116012, 2019/12/01/ 2019, doi: https://doi.org/10.1016/j.fuel.2019.116012.

[18] M. J. Blunt, *Multiphase flow in permeable media: A pore-scale perspective*. Cambridge University Press, 2017.

[19] R. T. Armstrong, M. L. Porter, and D. Wildenschild, "Linking pore-scale interfacial curvature to column-scale capillary pressure," *Advances in Water Resources,* vol. 46, pp. 55-62, 2012/09/01/ 2012, doi: https://doi.org/10.1016/j.advwatres.2012.05.009.

[20] R. M. El-Maghraby and M. J. Blunt, "Residual CO2 Trapping in Indiana Limestone," *Environmental Science & Technology,* vol. 47, no. 1, pp. 227-233, 2013/01/02 2013, doi: 10.1021/es304166u.
[21] C. H. Pentland, R. El-Maghraby, A. Georgiadis, S. Iglauer, and M. J. Blunt, "Immiscible Displacements and Capillary Trapping in CO2 Storage," *Energy Procedia,* vol. 4, pp. 4969-4976, 2011/01/01/ 2011, doi: https://doi.org/10.1016/j.egypro.2011.02.467.
[22] W. R. Purcell, "Capillary Pressures - Their Measurement Using Mercury and the Calculation of Permeability Therefrom," *SPE-949039-G,* vol. 1, no. 02, pp. 39-48, 1949/2/1/ 1949, doi: 10.2118/949039-G.
[23] R. Pini, S. C. M. Krevor, and S. M. Benson, "Capillary pressure and heterogeneity for the CO2/water system in sandstone rocks at reservoir conditions," *Advances in Water Resources,* vol. 38, pp. 48-59, 2012/03/01/ 2012, doi: https://doi.org/10.1016/j.advwatres.2011.12.007.
[24] A. W. Adamson and A. P. Gast, *Physical chemistry of surfaces*. Interscience New York, 1967.
[25] A. Georgiadis *et al.*, "Interfacial tension measurements and modelling of (carbon dioxide+n-alkane) and (carbon dioxide+water) binary mixtures at elevated pressures and temperatures," *The Journal of Supercritical Fluids,* vol. 55, no. 2, pp. 743-754, 2010/12/01/ 2010, doi: https://doi.org/10.1016/j.supflu.2010.09.028.
[26] E. Amott, "Observations Relating to the Wettability of Porous Rock," ed: Society of Petroleum Engineers, 1959, p. 7.
[27] E. C. Donaldson, R. D. Thomas, and P. B. Lorenz, "Wettability Determination and Its Effect on Recovery Efficiency," *SPE-2338-PA,* vol. 9, no. 01, pp. 13-20, 1969/3/1/ 1969, doi: 10.2118/2338-PA.
[28] A. Cassie and S. J. T. o. t. F. s. Baxter, "Wettability of porous surfaces," vol. 40, pp. 546-551, 1944.
[29] M. Andrew, B. Bijeljic, and M. J. Blunt, "Pore-scale contact angle measurements at reservoir conditions using X-ray microtomography," *Advances in Water Resources,* vol. 68, pp. 24-31, 2014/06/01/ 2014, doi: https://doi.org/10.1016/j.advwatres.2014.02.014.
[30] A. AlRatrout, A. Q. Raeini, B. Bijeljic, and M. J. Blunt, "Automatic measurement of contact angle in pore-space images," *Advances in Water Resources,* vol. 109, pp. 158-169, 2017/11/01/ 2017, doi: https://doi.org/10.1016/j.advwatres.2017.07.018.
[31] A. Scanziani, K. Singh, M. J. Blunt, and A. Guadagnini, "Automatic method for estimation of in situ effective contact angle from X-ray micro tomography images of two-phase flow in porous media," *Journal of Colloid and Interface Science,* vol. 496, pp. 51-59, 2017/06/15/ 2017, doi: https://doi.org/10.1016/j.jcis.2017.02.005.
[32] M. J. Blunt, Q. Lin, T. Akai, and B. Bijeljic, "A thermodynamically consistent characterization of wettability in porous media using high-resolution imaging," *Journal of Colloid and Interface Science,* vol. 552, pp. 59-65, 2019/09/15/ 2019, doi: https://doi.org/10.1016/j.jcis.2019.05.026.
[33] M. J. Blunt, A. Alhosani, Q. Lin, A. Scanziani, and B. Bijeljic, "Determination of contact angles for three-phase flow in porous media using an energy balance," *Journal of Colloid and Interface Science,* vol. 582, pp. 283-290, 2021/01/15/ 2021, doi: https://doi.org/10.1016/j.jcis.2020.07.152.
[34] M. Muskat and M. W. Meres, "The Flow of Heterogeneous Fluids Through Porous Media," *Physics,* vol. 7, no. 9, pp. 346-363, 1936/09/01 1936, doi: 10.1063/1.1745403.
[35] A. H. Alizadeh and M. Piri, "Three-phase flow in porous media: A review of experimental studies on relative permeability," *Reviews of Geophysics,* vol. 52, no. 3, pp. 468-521, 2014/09/01 2014, doi: 10.1002/2013RG000433.
[36] D. G. Avraam and A. C. Payatakes, "Flow regimes and relative permeabilities during steady-state two-phase flow in porous media," *Journal of Fluid Mechanics,* vol. 293, pp. 207-236, 1995, doi: 10.1017/S0022112095001698.
[37] C. A. Reynolds, H. Menke, M. Andrew, M. J. Blunt, and S. Krevor, "Dynamic fluid connectivity during steady-state multiphase flow in a sandstone," *Proceedings of the National Academy of Sciences,* vol. 114, no. 31, p. 8187, 2017, doi: 10.1073/pnas.1702834114.
[38] A. Scanziani, A. Alhammadi, B. Bijeljic, and M. J. Blunt, "Three-Phase Flow Visualization and Characterization for a Mixed-Wet Carbonate Rock," presented at the Abu Dhabi International

Petroleum Exhibition & Conference, Abu Dhabi, UAE, 2018/11/12/, 2018. [Online]. Available: https://doi.org/10.2118/192666-MS.

[39] M. Sohrabi, D. H. Tehrani, A. Danesh, and G. D. Henderson, "Visualization of Oil Recovery by Water-Alternating-Gas Injection Using High-Pressure Micromodels," *SPE-60767-PA,* vol. 9, no. 03, pp. 290-301, 2004/9/1/ 2004, doi: 10.2118/89000-PA.

[40] G. J. Hirasaki, "Structural interactions in the wetting and spreading of van der Waals fluids," *Journal of Adhesion Science and Technology,* vol. 7, no. 3, pp. 285-322, 1993/01/01 1993, doi: 10.1163/156856193X00718.

[41] P. E. Oren, J. Billiotte, and W. V. Pinczewski, "Mobilization of Waterflood Residual Oil by Gas Injection for Water-Wet Conditions," *SPE-20185-PA,* vol. 7, no. 01, pp. 70-78, 1992/3/1/ 1992, doi: 10.2118/20185-PA.

[42] M. Feali *et al.*, "Qualitative and Quantitative Analyses of the Three-Phase Distribution of Oil, Water, and Gas in Bentheimer Sandstone by Use of Micro-CT Imaging," *SPE-151609-PA,* vol. 15, no. 06, pp. 706-711, 2012/12/1/ 2012, doi: 10.2118/151609-PA.

[43] A. Kantzas, I. Chatzis, and F. A. L. Dullien, "Mechanisms of Capillary Displacement of Residual Oil by Gravity-Assisted Inert Gas Injection," presented at the SPE Rocky Mountain Regional Meeting, Casper, Wyoming, 1988/1/1/, 1988. [Online]. Available: https://doi.org/10.2118/17506-MS.

[44] P. E. Oren and W. V. Pinczewski, "The Effect of Wettability and Spreading Coefficients on the Recovery of Waterflood Residual Oil by Miscible Gasflooding," *SPE-20185-PA,* vol. 9, no. 02, pp. 149-156, 1994/6/1/ 1994, doi: 10.2118/24881-PA.

[45] A. A. Keller, M. J. Blunt, and A. P. V. Roberts, "Micromodel Observation of the Role of Oil Layers in Three-Phase Flow," *Transport in Porous Media,* vol. 26, no. 3, pp. 277-297, 1997/03/01 1997, doi: 10.1023/A:1006589611884.

[46] M. I. J. van Dijke and K. S. Sorbie, "Pore-scale modelling of three-phase flow in mixed-wet porous media: multiple displacement chains," *Journal of Petroleum Science and Engineering,* vol. 39, no. 3, pp. 201-216, 2003/09/01/ 2003, doi: https://doi.org/10.1016/S0920-4105(03)00063-9.

[47] M. Sohrabi, D. H. Tehrani, A. Danesh, and G. D. Henderson, "Visualisation of Oil Recovery by Water Alternating Gas (WAG) Injection Using High Pressure Micromodels - Oil-Wet & Mixed-Wet Systems," presented at the SPE Annual Technical Conference and Exhibition, New Orleans, Louisiana, 2001/1/1/, 2001. [Online]. Available: https://doi.org/10.2118/71494-MS.

[48] M. Sohrabi, G. D. Henderson, D. H. Tehrani, and A. Danesh, "Visualisation of Oil Recovery by Water Alternating Gas (WAG) Injection Using High Pressure Micromodels - Water-Wet System," presented at the SPE Annual Technical Conference and Exhibition, Dallas, Texas, 2000/1/1/, 2000. [Online]. Available: https://doi.org/10.2118/63000-MS.

[49] F. E. Bartell and H. J. Osterhof, "Determination of the Wettability of a Solid by a Liquid: Relation of Adhesion Tension to Stability of Color Varnish and Lacquer Systems," *Industrial and Engineering Chemistry,* Article vol. 19, no. 11, pp. 1277-1280, 1927, doi: 10.1021/ie50215a026.

[50] M. J. Blunt, "Constraints on Contact Angles for Multiple Phases in Thermodynamic Equilibrium," *Journal of Colloid and Interface Science,* vol. 239, no. 1, pp. 281-282, 2001/07/01/ 2001, doi: https://doi.org/10.1006/jcis.2001.7534.

[51] B. P. Flannery, H. W. Deckman, W. G. Roberge, and K. L. Amico, "Three-Dimensional X-ray Microtomography," *Science,* vol. 237, no. 4821, p. 1439, 1987, doi: 10.1126/science.237.4821.1439.

[52] V. Cnudde and M. N. Boone, "High-resolution X-ray computed tomography in geosciences: A review of the current technology and applications," *Earth-Science Reviews,* vol. 123, pp. 1-17, 2013/08/01/ 2013, doi: https://doi.org/10.1016/j.earscirev.2013.04.003.

[53] J.-H. Lambert, *JH Lambert,... Photometria, sive de Mensura et gradibus luminis, colorum et umbrae*. sumptibus viduae E. Klett, 1760.

[54] J. G. J. Shyeh-Yung, "Mechanisms of Miscible Oil Recovery: Effects of Pressure on Miscible and Near-Miscible Displacements of Oil by Carbon Dioxide," presented at the SPE Annual Technical Conference and Exhibition, Dallas, Texas, 1991/1/1/, 1991. [Online]. Available: https://doi.org/10.2118/22651-MS.

[55] H. Chen *et al.*, "Study on pressure interval of near-miscible flooding by production gas Re-injection in QHD offshore oilfield," *Journal of Petroleum Science and Engineering,* vol. 157, pp. 340-348, 2017/08/01/ 2017, doi: https://doi.org/10.1016/j.petrol.2017.07.045.

[56] D. S. Schechter, R. Grigg, B. Guo, and B. Schneider, "Wellman Unit CO2 Flood: Reservoir Pressure Reduction and Flooding the Water/Oil," presented at the SPE Annual Technical Conference and Exhibition, New Orleans, Louisiana, 1998/1/1/, 1998. [Online]. Available: https://doi.org/10.2118/48948-MS.

[57] R. B. Grigg and D. S. Schechter, "State of the Industry in CO2 Floods," presented at the SPE Annual Technical Conference and Exhibition, San Antonio, Texas, 1997/1/1/, 1997. [Online]. Available: https://doi.org/10.2118/38849-MS.

[58] J. E. Burger, B. Rao, and K. K. Mohanty, "Effect of Phase Behavior on Bypassing in Enriched Gasfloods," *SPE-25254-PA,* vol. 9, no. 02, pp. 112-118, 1994/5/1/ 1994, doi: 10.2118/25254-PA.

[59] K. K. Pande, "Effects of Gravity and Viscous Crossflow on Hydrocarbon Miscible Flood Performance in Heterogeneous Reservoirs," presented at the SPE Annual Technical Conference and Exhibition, Washington, D.C., 1992/1/1/, 1992. [Online]. Available: https://doi.org/10.2118/24935-MS.

[60] F. B. Thomas, N. Holowach, X. Zhou, D. B. Bennion, and D. W. Bennion, "Miscible or Near-Miscible Gas Injection, Which Is Better?," presented at the SPE/DOE Improved Oil Recovery Symposium, Tulsa, Oklahoma, 1994/1/1/, 1994. [Online]. Available: https://doi.org/10.2118/27811-MS.

[61] M. Sohrabi, A. Danesh, D. H. Tehrani, and M. Jamiolahmady, "Microscopic Mechanisms of Oil Recovery By Near-Miscible Gas Injection," *Transport in Porous Media,* vol. 72, no. 3, pp. 351-367, 2008/04/01 2008, doi: 10.1007/s11242-007-9154-z.

[62] M. Jamiolahmady, A. Danesh, D. H. Tehrani, and D. B. Duncan, "A Mechanistic Model of Gas-Condensate Flow in Pores," *Transport in Porous Media,* vol. 41, no. 1, pp. 17-46, 2000/10/01 2000, doi: 10.1023/A:1006645515791.

[63] J. K. Williams and R. A. Dawe, "Photographic observations of unusual flow phenomena in porous media at interfacial tensions below 0.1 mN m−1," *Journal of Colloid and Interface Science,* vol. 124, no. 2, pp. 691-696, 1988/08/01/ 1988, doi: https://doi.org/10.1016/0021-9797(88)90209-3.

[64] L. H. Bui, J.-S. Tsau, and G. P. Willhite, "Laboratory Investigations of CO2 Near Miscible Application in Arbuckle Reservoir," presented at the SPE Improved Oil Recovery Symposium, Tulsa, Oklahoma, USA, 2010/1/1/, 2010, SPE 129710. [Online]. Available: https://doi.org/10.2118/129710-MS.

[65] P. Wylie and K. K. Mohanty, "Effect of Water Saturation on Oil Recovery by Near-Miscible Gas Injection," *SPE-25254-PA,* vol. 12, no. 04, pp. 264-268, 1997/11/1/ 1997, doi: 10.2118/36718-PA.

[66] D. G. Longeron, "Influence of Very Low Interfacial Tensions on Relative Permeability," *SPE-2338-PA,* vol. 20, no. 05, pp. 391-401, 1980/10/1/ 1980, doi: 10.2118/7609-PA.

[67] L. Moghadasi, A. Guadagnini, F. Inzoli, M. Bartosek, and D. Renna, "Characterization of two- and three-phase relative permeability of water-wet porous media through X-Ray saturation measurements," *Journal of Petroleum Science and Engineering,* vol. 145, pp. 453-463, 2016/09/01/ 2016, doi: https://doi.org/10.1016/j.petrol.2016.05.031.

[68] H. L. Stone, "Probability Model for Estimating Three-Phase Relative Permeability," *SPE-949039-G,* vol. 22, no. 02, pp. 214-218, 1970/2/1/ 1970, doi: 10.2118/2116-PA.

[69] H. L. Stone, "Estimation of Three-Phase Relative Permeability And Residual Oil Data," *PETSOC-73-04-06,* vol. 12, no. 04, p. 10, 1973/10/1/ 1973, doi: 10.2118/73-04-06.

[70] A. AlRatrout, M. J. Blunt, and B. Bijeljic, "Wettability in complex porous materials, the mixed-wet state, and its relationship to surface roughness," *Proceedings of the National Academy of Sciences,* vol. 115, no. 36, p. 8901, 2018, doi: 10.1073/pnas.1803734115.

[71] R. N. Wenzel, "RESISTANCE OF SOLID SURFACES TO WETTING BY WATER," *Industrial & Engineering Chemistry,* vol. 28, no. 8, pp. 988-994, 1936/08/01 1936, doi: 10.1021/ie50320a024.

[72] R. A. Salathiel, "Oil Recovery by Surface Film Drainage In Mixed-Wettability Rocks," *SPE-949039-G,* vol. 25, no. 10, pp. 1216-1224, 1973/10/1/ 1973, doi: 10.2118/4104-PA.

[73] G. Gompper and D. A. Fedosov, "Modeling microcirculatory blood flow: current state and future perspectives," (in eng), *Wiley Interdiscip Rev Syst Biol Med,* vol. 8, no. 2, pp. 157-68, Mar-Apr 2016, doi: 10.1002/wsbm.1326.

[74] P. V. Trusov, N. V. Zaitseva, and M. R. Kamaltdinov, "A Multiphase Flow in the Antroduodenal Portion of the Gastrointestinal Tract: A Mathematical Model," (in eng), *Comput Math Methods Med,* vol. 2016, pp. 5164029-5164029, 2016, doi: 10.1155/2016/5164029.

[75] A. Mularczyk *et al.*, "Droplet and Percolation Network Interactions in a Fuel Cell Gas Diffusion Layer," *Journal of The Electrochemical Society,* vol. 167, no. 8, p. 084506, 2020/05/01 2020, doi: 10.1149/1945-7111/ab8c85.

[76] J. M. Matter and P. B. Kelemen, "Permanent storage of carbon dioxide in geological reservoirs by mineral carbonation," *Nature Geoscience,* vol. 2, no. 12, pp. 837-841, 2009/12/01 2009, doi: 10.1038/ngeo683.

[77] S. Krevor *et al.*, "Capillary trapping for geologic carbon dioxide storage – From pore scale physics to field scale implications," *International Journal of Greenhouse Gas Control,* vol. 40, pp. 221-237, 2015/09/01/ 2015, doi: https://doi.org/10.1016/j.ijggc.2015.04.006.

[78] N. Morrow and J. Buckley, "Improved Oil Recovery by Low-Salinity Waterflooding," *SPE-949039-G,* vol. 63, no. 05, pp. 106-112, 2011/5/1/ 2011, doi: 10.2118/129421-JPT.

[79] C. Sanchez, H. Arribart, and M. M. Giraud Guille, "Biomimetism and bioinspiration as tools for the design of innovative materials and systems," *Nature Materials,* vol. 4, no. 4, pp. 277-288, 2005/04/01 2005, doi: 10.1038/nmat1339.

[80] T. Sun, L. Feng, X. Gao, and L. Jiang, "Bioinspired Surfaces with Special Wettability," *Accounts of Chemical Research,* vol. 38, no. 8, pp. 644-652, 2005/08/01 2005, doi: 10.1021/ar040224c.

[81] J. A. Nychka and M. M. Gentleman, "Implications of wettability in biological materials science," *JOM,* vol. 62, no. 7, pp. 39-48, 2010/07/01 2010, doi: 10.1007/s11837-010-0107-6.

[82] L. Bromberg *et al.*, "Control of human skin wettability using the pH of anionic surfactant solution treatments," (in eng), *Colloids Surf B Biointerfaces,* vol. 157, pp. 366-372, Sep 1 2017, doi: 10.1016/j.colsurfb.2017.06.009.

[83] D. Wilkinson and J. F. Willemsen, "Invasion percolation: a new form of percolation theory," *Journal of Physics A: Mathematical and General,* vol. 16, no. 14, pp. 3365-3376, 1983/10/01 1983, doi: 10.1088/0305-4470/16/14/028.

[84] R. Lenormand and S. Bories, "Description d'un mécanisme de connexion de liaison destiné à l'étude du drainage avec piégeage en milieu poreux," 1980.

[85] W. B. Haines, "Studies in the physical properties of soil. V. The hysteresis effect in capillary properties, and the modes of moisture distribution associated therewith," *The Journal of Agricultural Science,* vol. 20, no. 1, pp. 97-116, 1930, doi: 10.1017/S002185960008864X.

[86] J. G. Roof, "Snap-Off of Oil Droplets in Water-Wet Pores," *SPE-2338-PA,* vol. 10, no. 01, pp. 85-90, 1970/3/1/ 1970, doi: 10.2118/2504-PA.

[87] S. Berg *et al.*, "Real-time 3D imaging of Haines jumps in porous media flow," *Proceedings of the National Academy of Sciences,* vol. 110, no. 10, p. 3755, 2013, doi: 10.1073/pnas.1221373110.

[88] M. Andrew, H. Menke, M. J. Blunt, and B. Bijeljic, "The Imaging of Dynamic Multiphase Fluid Flow Using Synchrotron-Based X-ray Microtomography at Reservoir Conditions," *Transport in Porous Media,* vol. 110, no. 1, pp. 1-24, 2015/10/01 2015, doi: 10.1007/s11242-015-0553-2.

[89] J. J. Pickell, B. F. Swanson, and W. B. Hickman, "Application of Air-Mercury and Oil-Air Capillary Pressure Data In the Study of Pore Structure and Fluid Distribution," *SPE-2338-PA,* vol. 6, no. 01, pp. 55-61, 1966/3/1/ 1966, doi: 10.2118/1227-PA.

[90] R. Lenormand, C. Zarcone, and A. Sarr, "Mechanisms of the displacement of one fluid by another in a network of capillary ducts," *Journal of Fluid Mechanics,* vol. 135, pp. 337-353, 1983, doi: 10.1017/S0022112083003110.

[91] K. Singh *et al.*, "Dynamics of snap-off and pore-filling events during two-phase fluid flow in permeable media," *Scientific Reports,* vol. 7, no. 1, p. 5192, 2017/07/12 2017, doi: 10.1038/s41598-017-05204-4.

[92] M. Rücker *et al.*, "From connected pathway flow to ganglion dynamics," *Geophysical Research Letters,* vol. 42, no. 10, pp. 3888-3894, 2015/05/28 2015, doi: 10.1002/2015GL064007.

[93] S. S. Datta, T. S. Ramakrishnan, and D. A. Weitz, "Mobilization of a trapped non-wetting fluid from a three-dimensional porous medium," *Physics of Fluids,* vol. 26, no. 2, p. 022002, 2014/02/01 2014, doi: 10.1063/1.4866641.

[94] T. Bultreys, W. De Boever, and V. Cnudde, "Imaging and image-based fluid transport modeling at the pore scale in geological materials: A practical introduction to the current state-of-the-art," *Earth-Science Reviews,* vol. 155, pp. 93-128, 2016/04/01/ 2016, doi: https://doi.org/10.1016/j.earscirev.2016.02.001.

[95] K. Singh, B. Bijeljic, and M. J. Blunt, "Imaging of oil layers, curvature and contact angle in a mixed-wet and a water-wet carbonate rock," *Water Resources Research,* vol. 52, no. 3, pp. 1716-1728, 2016/03/01 2016, doi: 10.1002/2015WR018072.

[96] T. Pak, I. B. Butler, S. Geiger, M. I. J. van Dijke, and K. S. Sorbie, "Droplet fragmentation: 3D imaging of a previously unidentified pore-scale process during multiphase flow in porous media," *Proceedings of the National Academy of Sciences,* vol. 112, no. 7, p. 1947, 2015, doi: 10.1073/pnas.1420202112.

[97] M. Andrew, B. Bijeljic, and M. J. Blunt, "Pore-scale imaging of trapped supercritical carbon dioxide in sandstones and carbonates," *International Journal of Greenhouse Gas Control,* vol. 22, pp. 1-14, 2014/03/01/ 2014, doi: https://doi.org/10.1016/j.ijggc.2013.12.018.

[98] M. Kumar, M. A. Knackstedt, T. J. Senden, A. P. Sheppard, and J. P. Middleton, "Visualizing And Quantifying the Residual Phase Distribution In Core Material," *SPWLA-2010-v51n5a4,* vol. 51, no. 05, p. 10, 2010/10/1/ 2010. [Online]. Available: https://doi.org/.

[99] R. T. Armstrong, A. Georgiadis, H. Ott, D. Klemin, and S. Berg, "Critical capillary number: Desaturation studied with fast X-ray computed microtomography," *Geophysical Research Letters,* vol. 41, no. 1, pp. 55-60, 2014/01/16 2014, doi: 10.1002/2013GL058075.

[100] R. T. Armstrong and S. Berg, "Interfacial velocities and capillary pressure gradients during Haines jumps," *Physical Review E,* vol. 88, no. 4, p. 043010, 10/22/ 2013, doi: 10.1103/PhysRevE.88.043010.

[101] A. Scanziani, K. Singh, H. Menke, B. Bijeljic, and M. J. Blunt, "Dynamics of enhanced gas trapping applied to CO2 storage in the presence of oil using synchrotron X-ray micro tomography," *Applied Energy,* p. 114136, 2019/11/23/ 2019, doi: https://doi.org/10.1016/j.apenergy.2019.114136.

[102] A. Scanziani, Q. Lin, A. Alhosani, M. J. Blunt, and B. Bijeljic, "Dynamics of fluid displacement in mixed-wet porous media," *Proceedings of the Royal Society A: Mathematical, Physical and Engineering Sciences,* vol. 476, no. 2240, p. 20200040, 2020/08/26 2020, doi: 10.1098/rspa.2020.0040.

[103] A. R. Kovscek, H. Wong, and C. J. Radke, "A pore-level scenario for the development of mixed wettability in oil reservoirs," *AIChE Journal,* vol. 39, no. 6, pp. 1072-1085, 1993/06/01 1993, doi: 10.1002/aic.690390616.

[104] J. S. Buckley, "Effective wettability of minerals exposed to crude oil," *Current Opinion in Colloid & Interface Science,* vol. 6, no. 3, pp. 191-196, 2001/06/01/ 2001, doi: https://doi.org/10.1016/S1359-0294(01)00083-8.

[105] M. I. J. van Dijke, K. S. Sorbie, M. Sohrabi, and A. Danesh, "Three-Phase Flow WAG Processes in Mixed-Wet Porous Media: Pore-Scale Network Simulations and Comparison With Water-Wet Micromodel Experiment," *SPE-60767-PA,* vol. 9, no. 01, pp. 57-66, 2004/3/1/ 2004, doi: 10.2118/87822-PA.

[106] M. I. J. van Dijke, M. Lorentzen, M. Sohrabi, and K. S. Sorbie, "Pore-Scale Simulation of WAG Floods in Mixed-Wet Micromodels," *SPE-60767-PA,* vol. 15, no. 01, pp. 238-247, 2010/3/1/ 2010, doi: 10.2118/113864-PA.

[107] I. Chatzis, Ioannis, Morrow, N. R, Lim, and H. T, "Magnitude and Detailed Structure of Residual Oil Saturation," *SPE-2338-PA,* vol. Volume 23, pp. 311-326, 04/01 1983, doi: 10.2118/10681-PA.

[108] A. S. Mayer and C. T. Miller, "An experimental investigation of pore-scale distributions of nonaqueous phase liquids at residual saturation," *Transport in Porous Media,* vol. 10, no. 1, pp. 57-80, 1993/01/01 1993, doi: 10.1007/BF00617511.

[109] M. Rücker *et al.*, "The Effect of Mixed Wettability on Pore-Scale Flow Regimes Based on a Flooding Experiment in Ketton Limestone," *Geophysical Research Letters,* vol. 46, no. 6, pp. 3225-3234, 2019/03/28 2019, doi: 10.1029/2018GL081784.

[110] A. Scanziani *et al.*, "In Situ Characterization of Three-Phase Flow in Mixed-Wet Porous Media Using Synchrotron Imaging," *Water Resources Research,* https://doi.org/10.1029/2020WR027873 vol. 56, no. 9, p. e2020WR027873, 2020/09/01 2020, doi: https://doi.org/10.1029/2020WR027873.

[111] H. Schott, "Contact angles and wettability of human skin," (in eng), *J Pharm Sci,* vol. 60, no. 12, pp. 1893-5, Dec 1971, doi: 10.1002/jps.2600601233.

[112] R. D. Wyckoff and H. G. Botset, "The Flow of Gas-Liquid Mixtures Through Unconsolidated Sands," *Physics,* vol. 7, no. 9, pp. 325-345, 1936/09/01 1936, doi: 10.1063/1.1745402.

[113] Y. Gao, Q. Lin, B. Bijeljic, and M. J. Blunt, "X-ray Microtomography of Intermittency in Multiphase Flow at Steady State Using a Differential Imaging Method," *Water Resources Research,* https://doi.org/10.1002/2017WR021736 vol. 53, no. 12, pp. 10274-10292, 2017/12/01 2017, doi: https://doi.org/10.1002/2017WR021736.

[114] M. A. Gjennestad, M. Winkler, and A. Hansen, "Pore Network Modeling of the Effects of Viscosity Ratio and Pressure Gradient on Steady-State Incompressible Two-Phase Flow in Porous Media," *Transport in Porous Media,* vol. 132, no. 2, pp. 355-379, 2020/03/01 2020, doi: 10.1007/s11242-020-01395-z.

[115] K. S. Sorbie and M. I. van Dijke, "The Mechanism of Oil Recovery by Water-Alternating-Gas Injection at Near-Miscible Conditions in Mixed Wet Systems," 2010. [Online]. Available: https://doi.org/10.2118/129837-MS.

[116] M. I. J. van Dijke and K. S. Sorbie, "An Analysis of Three-Phase Pore Occupancies and Relative Permeabilities in Porous Media with Variable Wettability," *Transport in Porous Media,* vol. 48, no. 2, pp. 159-185, 2002/08/01 2002, doi: 10.1023/A:1015692630733.

[117] M. M. Honarpour, F. Koederitz, and A. Herbert, *Relative permeability of petroleum reservoirs*. United States: CRC Press Inc,Boca Raton, FL (in English), 1986.

[118] A. L. Herring, J. Middleton, R. Walsh, A. Kingston, and A. Sheppard, "Flow rate impacts on capillary pressure and interface curvature of connected and disconnected fluid phases during multiphase flow in sandstone," *Advances in Water Resources,* vol. 107, pp. 460-469, 2017/09/01/ 2017, doi: https://doi.org/10.1016/j.advwatres.2017.05.011.

[119] S. Zou, R. T. Armstrong, J.-Y. Arns, C. H. Arns, and F. Hussain, "Experimental and Theoretical Evidence for Increased Ganglion Dynamics During Fractional Flow in Mixed-Wet Porous Media," *Water Resources Research,* https://doi.org/10.1029/2017WR022433 vol. 54, no. 5, pp. 3277-3289, 2018/05/01 2018, doi: https://doi.org/10.1029/2017WR022433.

[120] Y. Gao, A. Qaseminejad Raeini, M. J. Blunt, and B. Bijeljic, "Pore occupancy, relative permeability and flow intermittency measurements using X-ray micro-tomography in a complex carbonate," *Advances in Water Resources,* vol. 129, pp. 56-69, 2019/07/01/ 2019, doi: https://doi.org/10.1016/j.advwatres.2019.04.007.

[121] Y. Gao, A. Q. Raeini, A. M. Selem, I. Bondino, M. J. Blunt, and B. Bijeljic, "Pore-scale imaging with measurement of relative permeability and capillary pressure on the same reservoir sandstone sample under water-wet and mixed-wet conditions," *Advances in Water Resources,* vol. 146, p. 103786, 2020/12/01/ 2020, doi: https://doi.org/10.1016/j.advwatres.2020.103786.

[122] S. Iglauer, A. Paluszny, T. Rahman, Y. Zhang, W. Wülling, and M. Lebedev, "Residual Trapping of CO2 in an Oil-Filled, Oil-Wet Sandstone Core: Results of Three-Phase Pore-Scale Imaging," *Geophysical Research Letters,* vol. 46, no. 20, pp. 11146-11154, 2019/10/28 2019, doi: 10.1029/2019GL083401.

[123] M. Piri and M. J. Blunt, "Three-dimensional mixed-wet random pore-scale network modeling of two- and three-phase flow in porous media. I. Model description," *Physical Review E,* vol. 71, no. 2, p. 026301, 02/04/ 2005, doi: 10.1103/PhysRevE.71.026301.

[124] M. Piri and M. J. Blunt, "Three-dimensional mixed-wet random pore-scale network modeling of two- and three-phase flow in porous media. II. Results," *Physical Review E,* vol. 71, no. 2, p. 026302, 02/04/ 2005, doi: 10.1103/PhysRevE.71.026302.

[125] L. E. Baker, "Three-Phase Relative Permeability Correlations," 1988. [Online]. Available: https://doi.org/10.2118/17369-MS.

[126] B. Bijeljic, P. Mostaghimi, and M. J. Blunt, "Insights into non-Fickian solute transport in carbonates," *Water Resources Research,* vol. 49, no. 5, pp. 2714-2728, 2013/05/01 2013, doi: 10.1002/wrcr.20238.

[127] Q. Lin, Y. Al-Khulaifi, M. J. Blunt, and B. Bijeljic, "Quantification of sub-resolution porosity in carbonate rocks by applying high-salinity contrast brine using X-ray microtomography differential imaging," *Advances in Water Resources,* vol. 96, pp. 306-322, 2016/10/01/ 2016, doi: https://doi.org/10.1016/j.advwatres.2016.08.002.

[128] X. Li, E. Boek, G. C. Maitland, and J. P. M. Trusler, "Interfacial Tension of (Brines + CO2): (0.864 NaCl + 0.136 KCl) at Temperatures between (298 and 448) K, Pressures between (2 and 50) MPa, and Total Molalities of (1 to 5) mol·kg–1," *Journal of Chemical & Engineering Data,* vol. 57, no. 4, pp. 1078-1088, 2012/04/12 2012, doi: 10.1021/je201062r.

[129] E. Heidaryan, T. Hatami, M. Rahimi, and J. Moghadasi, "Viscosity of pure carbon dioxide at supercritical region: Measurement and correlation approach," *The Journal of Supercritical Fluids,* vol. 56, no. 2, pp. 144-151, 2011/03/01/ 2011, doi: https://doi.org/10.1016/j.supflu.2010.12.006.

[130] NIST. "Reference Fluid Thermodynamic and Transport Properties Database (REFPROP)." https://www.nist.gov/srd/refprop (accessed July 3, 2019.

[131] T. R. Jones, A. Carpenter, and P. Golland, "Voronoi-Based Segmentation of Cells on Image Manifolds," in *Computer Vision for Biomedical Image Applications*, Berlin, Heidelberg, Y. Liu, T. Jiang, and C. Zhang, Eds., 2005// 2005: Springer Berlin Heidelberg, pp. 535-543.

[132] K. Brown, S. SchlÜTer, A. Sheppard, and D. Wildenschild, "On the challenges of measuring interfacial characteristics of three-phase fluid flow with x-ray microtomography," *Journal of Microscopy,* vol. 253, no. 3, pp. 171-182, 2014/03/01 2014, doi: 10.1111/jmi.12106.

[133] A. P. Sheppard, R. M. Sok, and H. Averdunk, "Techniques for image enhancement and segmentation of tomographic images of porous materials," *Physica A: Statistical Mechanics and its Applications,* vol. 339, no. 1, pp. 145-151, 2004/08/01/ 2004, doi: https://doi.org/10.1016/j.physa.2004.03.057.

[134] M. I. J. van Dijke and K. S. Sorbie, "Three-phase capillary entry conditions in pores of noncircular cross-section," *Journal of Colloid and Interface Science,* vol. 260, no. 2, pp. 385-397, 2003/04/15/ 2003, doi: https://doi.org/10.1016/S0021-9797(02)00228-X.

[135] M. I. J. van Dijke, M. Lago, K. S. Sorbie, and M. Araujo, "Free energy balance for three fluid phases in a capillary of arbitrarily shaped cross-section: capillary entry pressures and layers of the intermediate-wetting phase," *Journal of Colloid and Interface Science,* vol. 277, no. 1, pp. 184-201, 2004/09/01/ 2004, doi: https://doi.org/10.1016/j.jcis.2004.05.021.

[136] M. I. J. van Dijke and K. S. Sorbie, "Consistency of three-phase capillary entry pressures and pore phase occupancies," *Advances in Water Resources,* vol. 30, no. 2, pp. 182-198, 2007/02/01/ 2007, doi: https://doi.org/10.1016/j.advwatres.2005.03.024.

[137] D. H. Fenwick and J. M. Blunt, "Pore Level Modelling of Three Phase Flow in Porous Media," presented at the IOR 1995 - 8th European Symposium on Improved Oil Recovery Vienna, Aastree,, 15 May 1995, 1995.

[138] M. Andrew, B. Bijeljic, and M. J. Blunt, "Pore-by-pore capillary pressure measurements using X-ray microtomography at reservoir conditions: Curvature, snap-off, and remobilization of residual CO2," *Water Resources Research,* vol. 50, no. 11, pp. 8760-8774, 2014/11/01 2014, doi: 10.1002/2014WR015970.

[139] T. Li, S. Schlüter, M. I. Dragila, and D. Wildenschild, "An improved method for estimating capillary pressure from 3D microtomography images and its application to the study of disconnected nonwetting phase," *Advances in Water Resources,* vol. 114, pp. 249-260, 2018/04/01/ 2018, doi: https://doi.org/10.1016/j.advwatres.2018.02.012.

[140] Q. Lin, B. Bijeljic, S. Berg, R. Pini, M. J. Blunt, and S. Krevor, "Minimal surfaces in porous media: Pore-scale imaging of multiphase flow in an altered-wettability Bentheimer sandstone," *Physical Review E,* vol. 99, no. 6, p. 063105, 06/10/ 2019, doi: 10.1103/PhysRevE.99.063105.

[141] T. Akai, Q. Lin, A. Alhosani, B. Bijeljic, and J. M. Blunt, "Quantification of Uncertainty and Best Practice in Computing Interfacial Curvature from Complex Pore Space Images," *Materials,* vol. 12, no. 13, 2019, doi: 10.3390/ma12132138.

[142] S. Iglauer, A. Paluszny, and M. J. Blunt, "Simultaneous oil recovery and residual gas storage: A pore-level analysis using in situ X-ray micro-tomography," *Fuel,* vol. 103, pp. 905-914, 2013/01/01/ 2013, doi: https://doi.org/10.1016/j.fuel.2012.06.094.

[143] T. Hildebrand and P. Rüegsegger, "A new method for the model-independent assessment of thickness in three-dimensional images," *Journal of Microscopy,* vol. 185, no. 1, pp. 67-75, 1997/01/01 1997, doi: 10.1046/j.1365-2818.1997.1340694.x.

[144] T. Bultreys, L. Van Hoorebeke, and V. Cnudde, "Multi-scale, micro-computed tomography-based pore network models to simulate drainage in heterogeneous rocks," *Advances in Water Resources,* vol. 78, pp. 36-49, 2015/04/01/ 2015, doi: https://doi.org/10.1016/j.advwatres.2015.02.003.

[145] H. Dong and M. J. Blunt, "Pore-network extraction from micro-computerized-tomography images," *Physical Review E,* vol. 80, no. 3, p. 036307, 09/14/ 2009, doi: 10.1103/PhysRevE.80.036307.

[146] A. Q. Raeini, B. Bijeljic, and M. J. Blunt, "Generalized network modeling: Network extraction as a coarse-scale discretization of the void space of porous media," *Physical Review E,* vol. 96, no. 1, p. 013312, 07/20/ 2017, doi: 10.1103/PhysRevE.96.013312.

[147] I. Arganda-Carreras *et al.*, "Trainable Weka Segmentation: a machine learning tool for microscopy pixel classification," *Bioinformatics,* vol. 33, no. 15, pp. 2424-2426, 2017, doi: 10.1093/bioinformatics/btx180.

[148] V. Kaynig, T. Fuchs, and J. M. Buhmann, "Neuron geometry extraction by perceptual grouping in ssTEM images," in *2010 IEEE Computer Society Conference on Computer Vision and Pattern Recognition*, 13-18 June 2010 2010, pp. 2902-2909, doi: 10.1109/CVPR.2010.5540029.

[149] R. D. Rudyanto *et al.*, "Comparing algorithms for automated vessel segmentation in computed tomography scans of the lung: the VESSEL12 study," *Medical Image Analysis,* vol. 18, no. 7, pp. 1217-1232, 2014/10/01/ 2014, doi: https://doi.org/10.1016/j.media.2014.07.003.

[150] A. Q. Raeini, M. J. Blunt, and B. Bijeljic, "Modelling two-phase flow in porous media at the pore scale using the volume-of-fluid method," *Journal of Computational Physics,* vol. 231, no. 17, pp. 5653-5668, 2012/07/01/ 2012, doi: https://doi.org/10.1016/j.jcp.2012.04.011.

[151] M. I. J. van Dijke, K. S. Sorbie, M. Sohrabi, and A. Danesh, "Simulation of WAG floods in an oil-wet micromodel using a 2-D pore-scale network model," *Journal of Petroleum Science and Engineering,* vol. 52, no. 1, pp. 71-86, 2006/06/01/ 2006, doi: https://doi.org/10.1016/j.petrol.2006.03.014.

[152] S. M. Fatemi and M. Sohrabi, "Recovery Mechanisms and Relative Permeability for Gas/Oil Systems at Near-Miscible Conditions: Effects of Immobile Water Saturation, Wettability, Hysteresis, and Permeability," *Energy & Fuels,* vol. 27, no. 5, pp. 2376-2389, 2013/05/16 2013, doi: 10.1021/ef301059b.

[153] S. Iglauer, M. A. Fernø, P. Shearing, and M. J. Blunt, "Comparison of residual oil cluster size distribution, morphology and saturation in oil-wet and water-wet sandstone," *Journal of Colloid and Interface Science,* vol. 375, no. 1, pp. 187-192, 2012/06/01/ 2012, doi: https://doi.org/10.1016/j.jcis.2012.02.025.

[154] M. Andrew, B. Bijeljic, and M. J. Blunt, "Pore-scale imaging of geological carbon dioxide storage under in situ conditions," *Geophysical Research Letters,* vol. 40, no. 15, pp. 3915-3918, 2013/08/16 2013, doi: 10.1002/grl.50771.

[155] J. Alcalde *et al.*, "Estimating geological CO2 storage security to deliver on climate mitigation," *Nature Communications,* vol. 9, no. 1, p. 2201, 2018/06/12 2018, doi: 10.1038/s41467-018-04423-1.

[156] G. F. Teletzke, P. D. Patel, and A. Chen, "Methodology for Miscible Gas Injection EOR Screening," presented at the SPE International Improved Oil Recovery Conference in Asia

Pacific, Kuala Lumpur, Malaysia, 2005/1/1/, 2005. [Online]. Available: https://doi.org/10.2118/97650-MS.

[157] CDP. "Carbon Dioxide Properties Calculator " https://www.carbon-dioxide-properties.com/default.aspx (accessed 27/02/2020.

[158] E. Toolbox. "Carbon Dioxide - Dynamic and Kinematic Viscosity." https://www.engineeringtoolbox.com/carbon-dioxide-dynamic-kinematic-viscosity-temperature-pressure-d_2074.html (accessed 28/08/2020.

[159] M. I. J. van Dijke, K. S. Sorbie, and S. R. McDougall, "Saturation-dependencies of three-phase relative permeabilities in mixed-wet and fractionally wet systems," *Advances in Water Resources,* vol. 24, no. 3, pp. 365-384, 2001/02/01/ 2001, doi: https://doi.org/10.1016/S0309-1708(00)00062-2.

[160] A. L. Herring, E. J. Harper, L. Andersson, A. Sheppard, B. K. Bay, and D. Wildenschild, "Effect of fluid topology on residual nonwetting phase trapping: Implications for geologic CO2 sequestration," *Advances in Water Resources,* vol. 62, pp. 47-58, 2013/12/01/ 2013, doi: https://doi.org/10.1016/j.advwatres.2013.09.015.

[161] A. L. Herring, L. Andersson, S. Schlüter, A. Sheppard, and D. Wildenschild, "Efficiently engineering pore-scale processes: The role of force dominance and topology during nonwetting phase trapping in porous media," *Advances in Water Resources,* vol. 79, pp. 91-102, 2015/05/01/ 2015, doi: https://doi.org/10.1016/j.advwatres.2015.02.005.

[162] K. R. Mecke and H. Wagner, "Euler characteristic and related measures for random geometric sets," *Journal of Statistical Physics,* vol. 64, no. 3, pp. 843-850, 1991/08/01 1991, doi: 10.1007/BF01048319.

[163] H. J. Vogel and A. Kretzschmar, "Topological characterization of pore space in soil — sample preparation and digital image-processing," *Geoderma,* vol. 73, no. 1, pp. 23-38, 1996/09/01/ 1996, doi: https://doi.org/10.1016/0016-7061(96)00043-2.

[164] H.-J. Vogel, "Topological Characterization of Porous Media," in *Morphology of Condensed Matter: Physics and Geometry of Spatially Complex Systems*, K. Mecke and D. Stoyan Eds. Berlin, Heidelberg: Springer Berlin Heidelberg, 2002, pp. 75-92.

[165] A. L. Herring, V. Robins, and A. P. Sheppard, "Topological Persistence for Relating Microstructure and Capillary Fluid Trapping in Sandstones," *Water Resources Research,* vol. 55, no. 1, pp. 555-573, 2019/01/01 2019, doi: 10.1029/2018WR022780.

[166] M. I. J. van Dijke, S. R. McDougall, and K. S. Sorbie, "Three-Phase Capillary Pressure and Relative Permeability Relationships in Mixed-Wet Systems," *Transport in Porous Media,* vol. 44, no. 1, pp. 1-32, 2001/07/01 2001, doi: 10.1023/A:1010773606657.

[167] Y. Zheng, X. Gao, and L. Jiang, "Directional adhesion of superhydrophobic butterfly wings," *Soft Matter,* 10.1039/B612667G vol. 3, no. 2, pp. 178-182, 2007, doi: 10.1039/B612667G.

[168] S. Zhang, J. Huang, Z. Chen, S. Yang, and Y. Lai, "Liquid mobility on superwettable surfaces for applications in energy and the environment," *Journal of Materials Chemistry A,* 10.1039/C8TA09403A vol. 7, no. 1, pp. 38-63, 2019, doi: 10.1039/C8TA09403A.

[169] A. Elkhyat, P. Agache, H. Zahouani, and P. Humbert, "A new method to measure in vivo human skin hydrophobia," *International Journal of Cosmetic Science,* vol. 23, no. 6, pp. 347-352, 2001/12/01 2001, doi: 10.1046/j.0412-5463.2001.00108.x.

[170] T. Jianhua, "Density and intefacial tension of nitrogen-hydrocarbon systems at elevated pressures," *中国化学工程学报,* vol. 1, no. 4, pp. 223-231, 1993.

[171] G. Garfi, C. M. John, S. Berg, and S. Krevor, "The Sensitivity of Estimates of Multiphase Fluid and Solid Properties of Porous Rocks to Image Processing," *Transport in Porous Media,* vol. 131, no. 3, pp. 985-1005, 2020/02/01 2020, doi: 10.1007/s11242-019-01374-z.

[172] K. A. Klise, D. Moriarty, H. Yoon, and Z. Karpyn, "Automated contact angle estimation for three-dimensional X-ray microtomography data," *Advances in Water Resources,* vol. 95, pp. 152-160, 2016/09/01/ 2016, doi: https://doi.org/10.1016/j.advwatres.2015.11.006.

[173] L. E. Dalton, K. A. Klise, S. Fuchs, D. Crandall, and A. Goodman, "Methods to measure contact angles in scCO2-brine-sandstone systems," *Advances in Water Resources,* vol. 122, pp. 278-290, 2018/12/01/ 2018, doi: https://doi.org/10.1016/j.advwatres.2018.10.020.

[174] M. Khishvand, A. H. Alizadeh, and M. Piri, "In-situ characterization of wettability and pore-scale displacements during two- and three-phase flow in natural porous media," *Advances in Water Resources,* vol. 97, pp. 279-298, 2016/11/01/ 2016, doi: https://doi.org/10.1016/j.advwatres.2016.10.009.
[175] N. R. Morrow, "Physics and Thermodynamics of Capillary Action in Porous Media," *Industrial & Engineering Chemistry,* vol. 62, no. 6, pp. 32-56, 1970/06/01 1970, doi: 10.1021/ie50726a006.
[176] T. Akai, A. Alhammadi, M. Blunt, and B. Bijeljic, "Modeling Oil Recovery in Mixed-Wet Rocks: Pore-Scale Comparison Between Experiment and Simulation," *Transport in Porous Media,* 11/23 2018, doi: 10.1007/s11242-018-1198-8.
[177] C. H. Arns, M. A. Knackstedt, and N. S. Martys, "Cross-property correlations and permeability estimation in sandstone," *Physical Review E,* vol. 72, no. 4, p. 046304, 10/05/ 2005, doi: 10.1103/PhysRevE.72.046304.
[178] C. H. Arns, M. A. Knackstedt, and K. R. Mecke, "Boolean reconstructions of complex materials: Integral geometric approach," *Physical Review E,* vol. 80, no. 5, p. 051303, 11/30/ 2009, doi: 10.1103/PhysRevE.80.051303.
[179] H.-J. Vogel, U. Weller, and S. Schlüter, "Quantification of soil structure based on Minkowski functions," *Comput. Geosci.,* vol. 36, no. 10, pp. 1236–1245, 2010, doi: 10.1016/j.cageo.2010.03.007.
[180] K. Culligan, D. Wildenschild, B. Christensen, W. Gray, M. Rivers, and A. Tompson, "Interfacial area measurements for unsaturated flow through a porous medium," *Water Resour. Res,* vol. 40, 12/01 2004, doi: 10.1029/2004WR003278.
[181] K. K. Mohanty, H. T. Davis, and L. E. Scriven, "Physics of oil entrapment in water-wet rock," (in English), 1987-02-01 1987, doi: 10.2118/9406-PA.
[182] T. C. Ransohoff, P. A. Gauglitz, and C. J. Radke, "Snap-off of gas bubbles in smoothly constricted noncircular capillaries," *AIChE Journal,* vol. 33, no. 5, pp. 753-765, 1987/05/01 1987, doi: 10.1002/aic.690330508.
[183] A. C. Payatakes, K. M. Ng, and R. W. Flumerfelt, "Oil ganglion dynamics during immiscible displacement: Model formulation," *AIChE Journal,* vol. 26, no. 3, pp. 430-443, 1980/05/01 1980, doi: 10.1002/aic.690260315.
[184] A. Buades, B. Coll, and J.-M. Morel, "Nonlocal Image and Movie Denoising," *International Journal of Computer Vision,* vol. 76, no. 2, pp. 123-139, 2008/02/01 2008, doi: 10.1007/s11263-007-0052-1.
[185] M. J. Blunt, A. Alhosani, Q. Lin, A. Scanziani, and B. Bijeljic, "Determination of contact angles for three-phase flow in porous media using an energy balance," *Journal of Colloid and Interface Science,* 2020.
[186] A. Scanziani *et al.*, "In situ characterisation of three-phase flow in mixed-wet porous media using synchrotron imaging," *Water Resources Research,* vol. n/a, no. n/a, p. e2020WR027873, 2020/08/11 2020, doi: 10.1029/2020WR027873.
[187] Z. Al-Siyabi, A. Danesh, B. Tohidi, and A. Todd, "Variation of gas-oil-solid contact angle with interfacial tension," *Petroleum Geoscience,* vol. 5, no. 1, pp. 37-40, 1999.
[188] J. W. Grate *et al.*, "Correlation of Oil–Water and Air–Water Contact Angles of Diverse Silanized Surfaces and Relationship to Fluid Interfacial Tensions," *Langmuir,* vol. 28, no. 18, pp. 7182-7188, 2012/05/08 2012, doi: 10.1021/la204322k.
[189] P. Brownsort *et al.*, "CO_2 storage and Enhanced Oil Recovery in the North Sea: Securing a low-carbon future for the UK," SCCS, 2015.
[190] S. Melzer, "Optimization of CO2 Storage in CO2 Enhanced Oil Recovery Projects," *Advanced Resources International,* 2010.
[191] D. Kramer, "Negative carbon dioxide emissions," *Physics today,* vol. 73, no. 1, pp. 44-51, 2020.
[192] A. E. Peksa, K.-H. A. A. Wolf, and P. L. J. Zitha, "Bentheimer sandstone revisited for experimental purposes," *Marine and Petroleum Geology,* vol. 67, pp. 701-719, 2015/11/01/ 2015, doi: https://doi.org/10.1016/j.marpetgeo.2015.06.001.
[193] E. ToolBox. "Nitrogen - Dynamic and Kinematic Viscosity." https://www.engineeringtoolbox.com/nitrogen-N2-dynamic-kinematic-viscosity-temperature-pressure-d_2067.html (accessed 18/05/2021.

[194] M. J. Oak, "Three-Phase Relative Permeability of Water-Wet Berea," presented at the SPE/DOE Enhanced Oil Recovery Symposium, Tulsa, Oklahoma, 1990/1/1/, 1990. [Online]. Available: https://doi.org/10.2118/20183-MS.

[195] M. J. Oak, L. E. Baker, and D. C. Thomas, "Three-Phase Relative Permeability of Berea Sandstone," *SPE-949039-G,* vol. 42, no. 08, pp. 1054-1061, 1990/8/1/ 1990, doi: 10.2118/17370-PA.

[196] D. N. Saraf, J. P. Batycky, C. H. Jackson, and D. B. Fisher, "An Experimental Investigation of Three-Phase Flow of Water-Oil- Gas Mixtures Through Water-Wet Sandstones," presented at the SPE California Regional Meeting, San Francisco, California, 1982/1/1/, 1982. [Online]. Available: https://doi.org/10.2118/10761-MS.

[197] A. Alizadeh and M. J. W. R. R. Piri, "The effect of saturation history on three-phase relative permeability: An experimental study," vol. 50, no. 2, pp. 1636-1664, 2014.

[198] C. Spurin, T. Bultreys, B. Bijeljic, M. J. Blunt, and S. Krevor, "Intermittent fluid connectivity during two-phase flow in a heterogeneous carbonate rock," *Physical Review E,* vol. 100, no. 4, p. 043103, 10/08/ 2019, doi: 10.1103/PhysRevE.100.043103.

[199] C. Spurin, T. Bultreys, B. Bijeljic, M. J. Blunt, and S. Krevor, "Mechanisms controlling fluid breakup and reconnection during two-phase flow in porous media," *Physical Review E,* vol. 100, no. 4, p. 043115, 10/29/ 2019, doi: 10.1103/PhysRevE.100.043115.

[200] Y. Gao, Q. Lin, B. Bijeljic, and M. J. Blunt, "Pore-scale dynamics and the multiphase Darcy law," *Physical Review Fluids,* vol. 5, no. 1, p. 013801, 01/16/ 2020, doi: 10.1103/PhysRevFluids.5.013801.

[201] Y. Zhang, B. Bijeljic, Y. Gao, Q. Lin, and M. J. Blunt, "Quantification of Nonlinear Multiphase Flow in Porous Media," *Geophysical Research Letters,* https://doi.org/10.1029/2020GL090477 vol. 48, no. 5, p. e2020GL090477, 2021/03/16 2021, doi: https://doi.org/10.1029/2020GL090477.

[202] Q. Lin, B. Bijeljic, S. Foroughi, S. Berg, and M. J. Blunt, "Pore-scale imaging of displacement patterns in an altered-wettability carbonate," *Chemical Engineering Science,* vol. 235, p. 116464, 2021/05/18/ 2021, doi: https://doi.org/10.1016/j.ces.2021.116464.

Appendices

9.1 Appendix 1

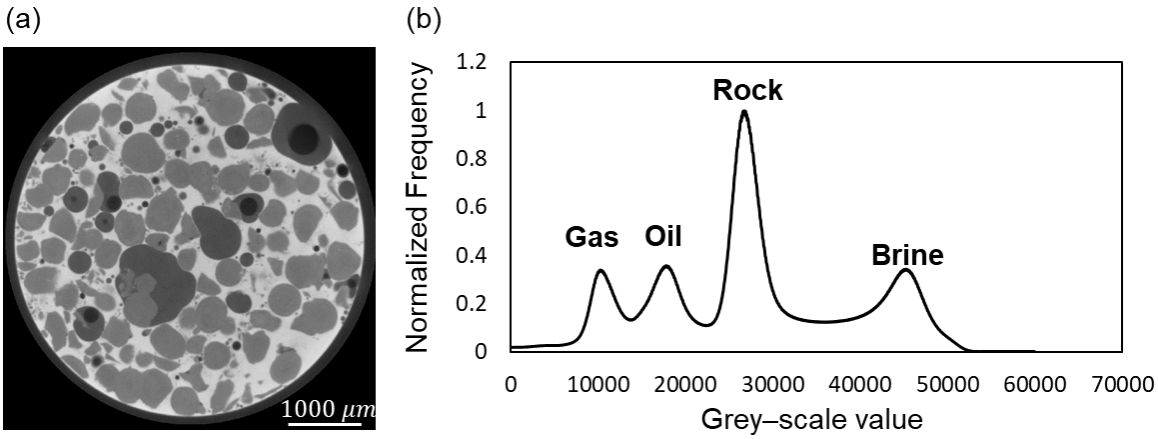

Figure A1. 1. (a) A phase contrast scan of four phases: (i) oil (20% iododecane + 80% decane); (ii) water (70% brine + 30% NaI); (iii) air; and (v) rock (99% calcite). (b) A signal-to-noise ratio histogram of the different phases, showing that the phases are clearly distinguishable from the grey-scale image with no large overlapping regions.

Table A1. 1. Interfacial tension measurements between the gas phase (scCO2) and the oil phase (80%wt decane and 20%wt iododecane mixture) as a function of pressure at 70 °C.

p [MPa]	T [°C]	$\Delta\rho$ [kg·m^{-3}]	σ [mN· m^{-1}]
1.42	70	0.73	16.72
2.85	70	0.71	14.30
3.43	70	0.69	13.62
4.27	70	0.68	12.22
5.02	70	0.66	10.63
6.00	70	0.64	9.07

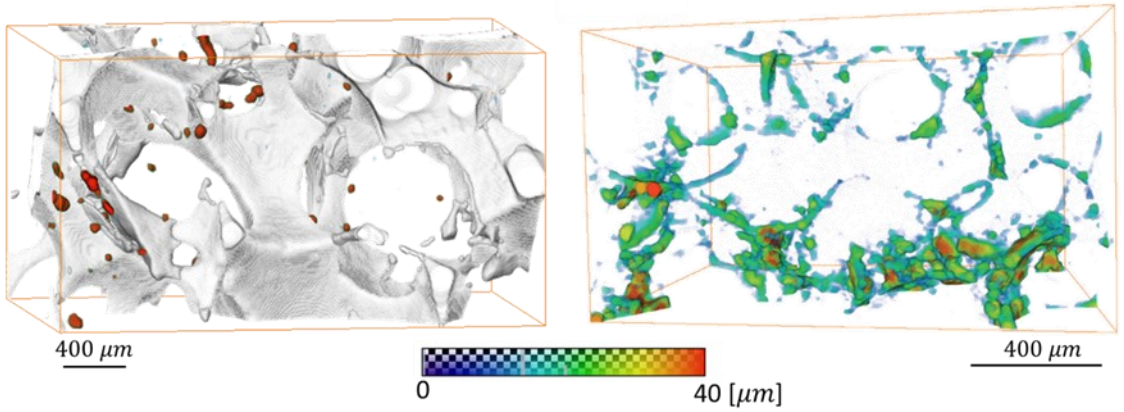

Figure A1. 2. The local thickness of the wetting water phase was computed in immiscible (right) and near-miscible (left) conditions. The water phase was isolated and maximal balls were fitted to its structure to obtain the thickness maps in both conditions. Water layer thickness map at immiscible conditions (right) from Scanziani et al. [16].

9.2 Appendix 2

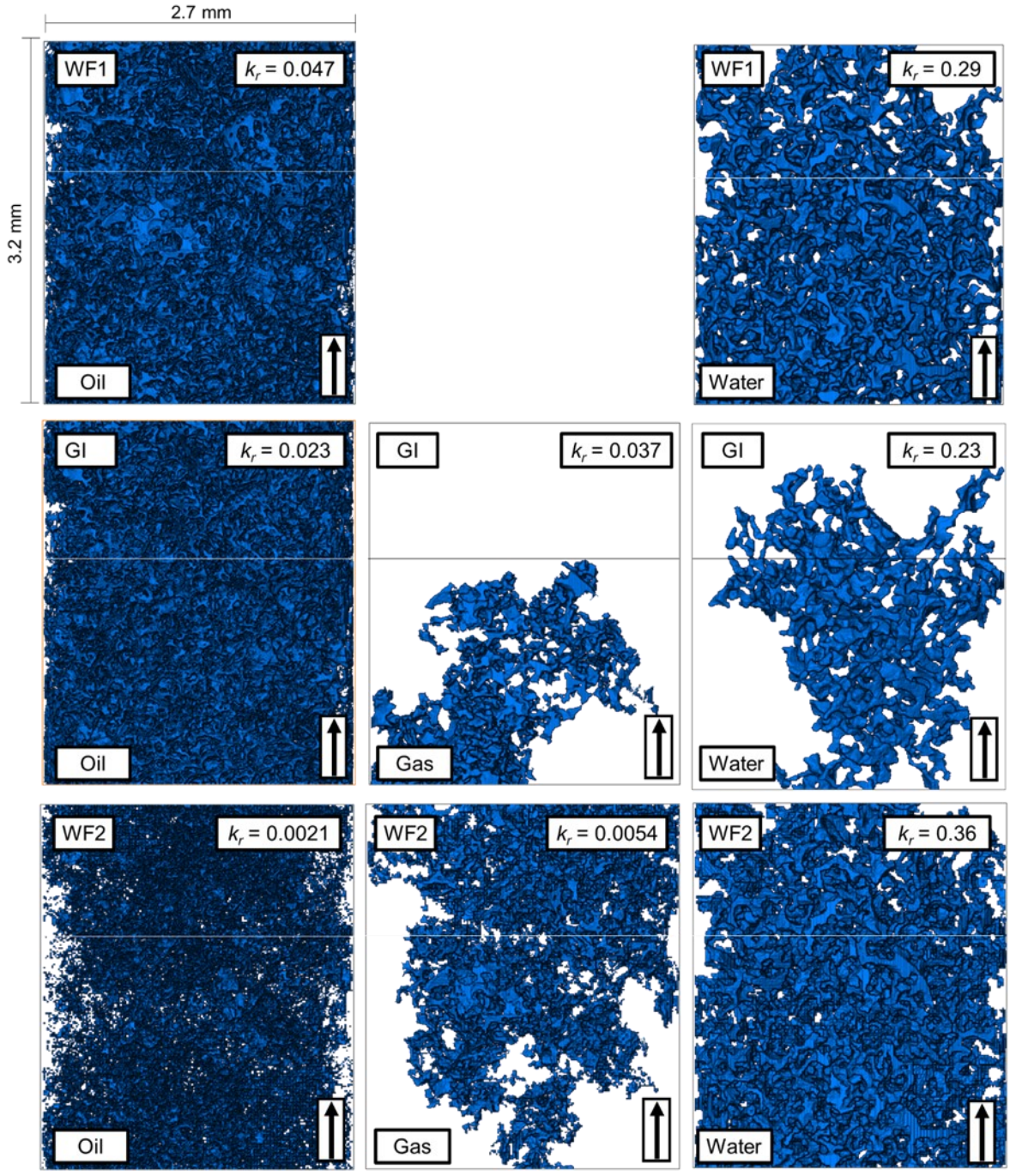

Figure A2. 1. A series of 2D images showing the connected clusters of oil, gas and water phases for which the relative permeability was measured during: (first row) first waterflooding (WF1); (second row) gas injection (GI); and (third row) second waterflooding (WF2). The relative permeabilities were quantified on images of resolution of 1.82 µm/voxel and size of 1483×1483×1000 voxels: the region beneath the horizontal line was used to quantify the relative permeability. The clusters were plotted using Avizo 9.5 software (https://www.fei.com/software/amira-avizo/).

9.3 Appendix 3

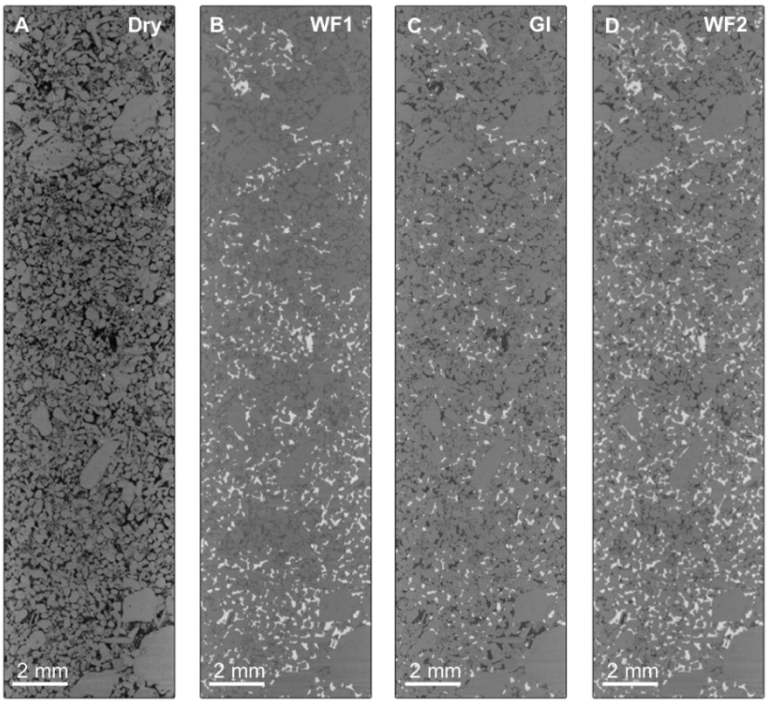

Figure A3. 1. A series of raw images with a 3.57 µm/voxel resolution of the whole sample after each injection sequence. From left to right: (i) A dry scan of the rock; (ii) After first waterflooding (WF1); (iii) After gas injection (GI); and (iv) after second waterflooding (WF2). In the dry scan, the rock is shown in grey and the pore space is in black. In the wet images, water is white, rock is light grey, oil is dark grey, and gas is black.

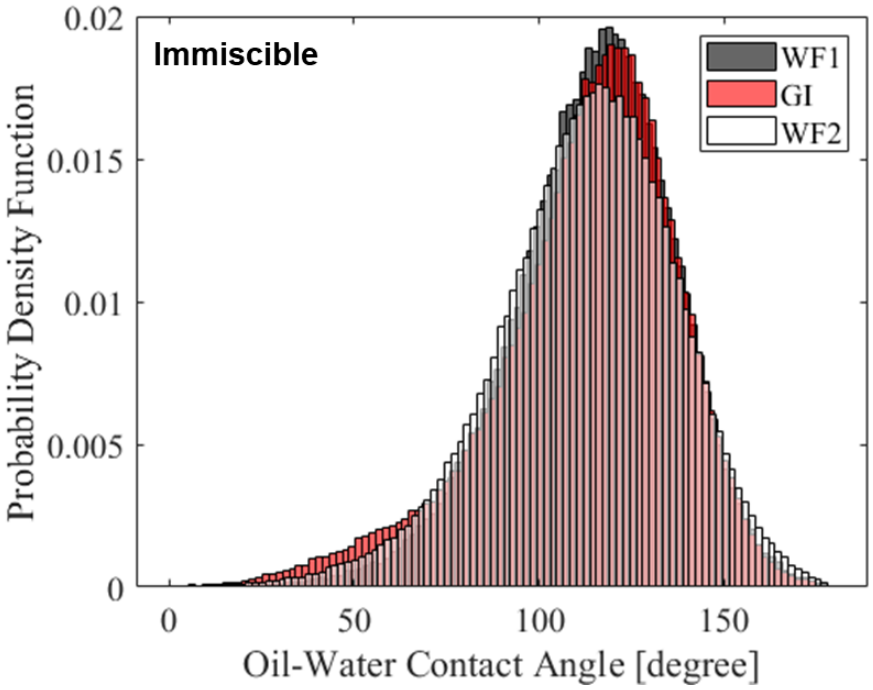

Figure A3. 2. Normalized histograms of the *in situ* measured oil-water contact angles in the aged rock at immiscible conditions after the first waterflooding (WF1), Gas injection (GI) and second waterflooding (WF2). The contact angles were measured through the water phase. The consistent oil-water contact distribution shows that there was wettability alteration throughout the injection sequence.

9.4 Appendix 4

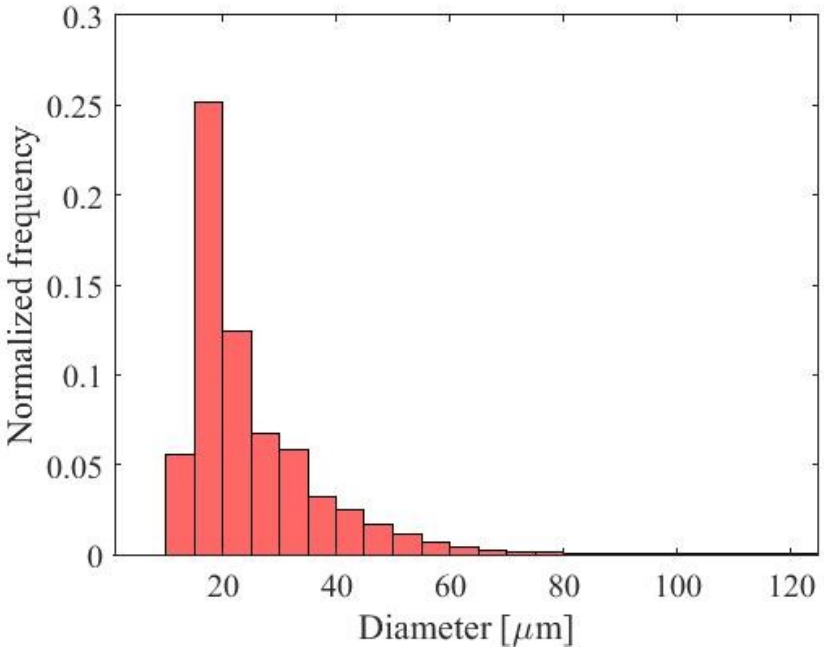

Figure A4. 1. A normalized histogram showing the pore size distribution of the reservoir rock used in the water injection experiment.

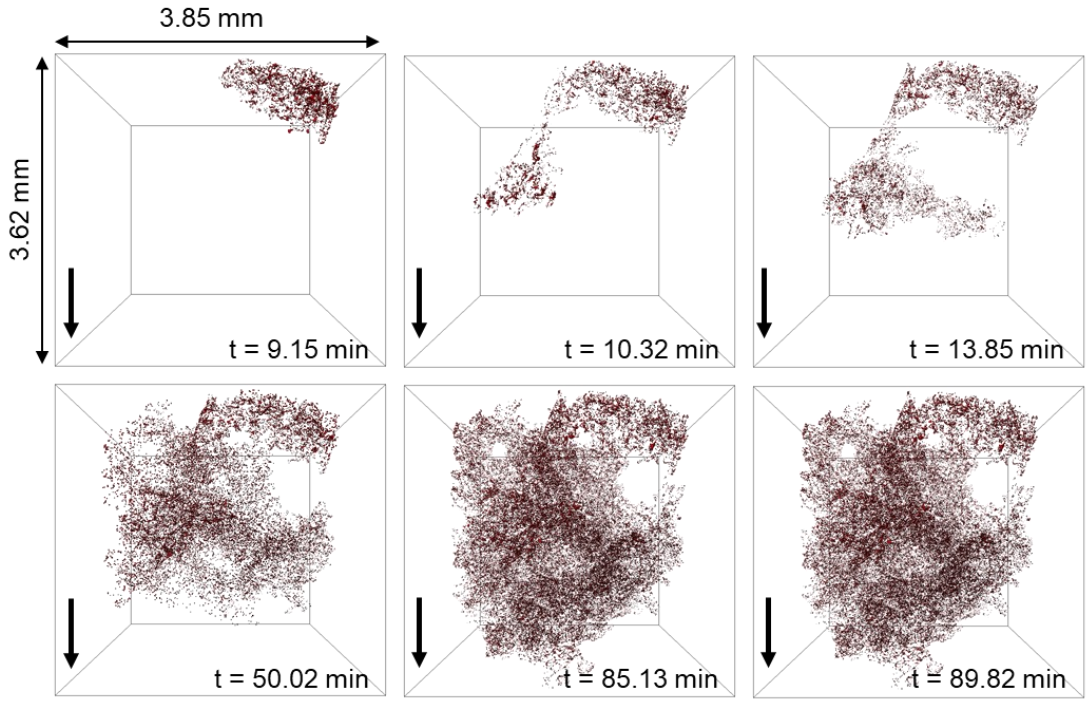

Figure A4. 2. Three-dimensional maps showing the volume and location of the oil displaced in the wetting layers at different time steps. The black arrow points towards the direction of flow.

9.5 Appendix 5

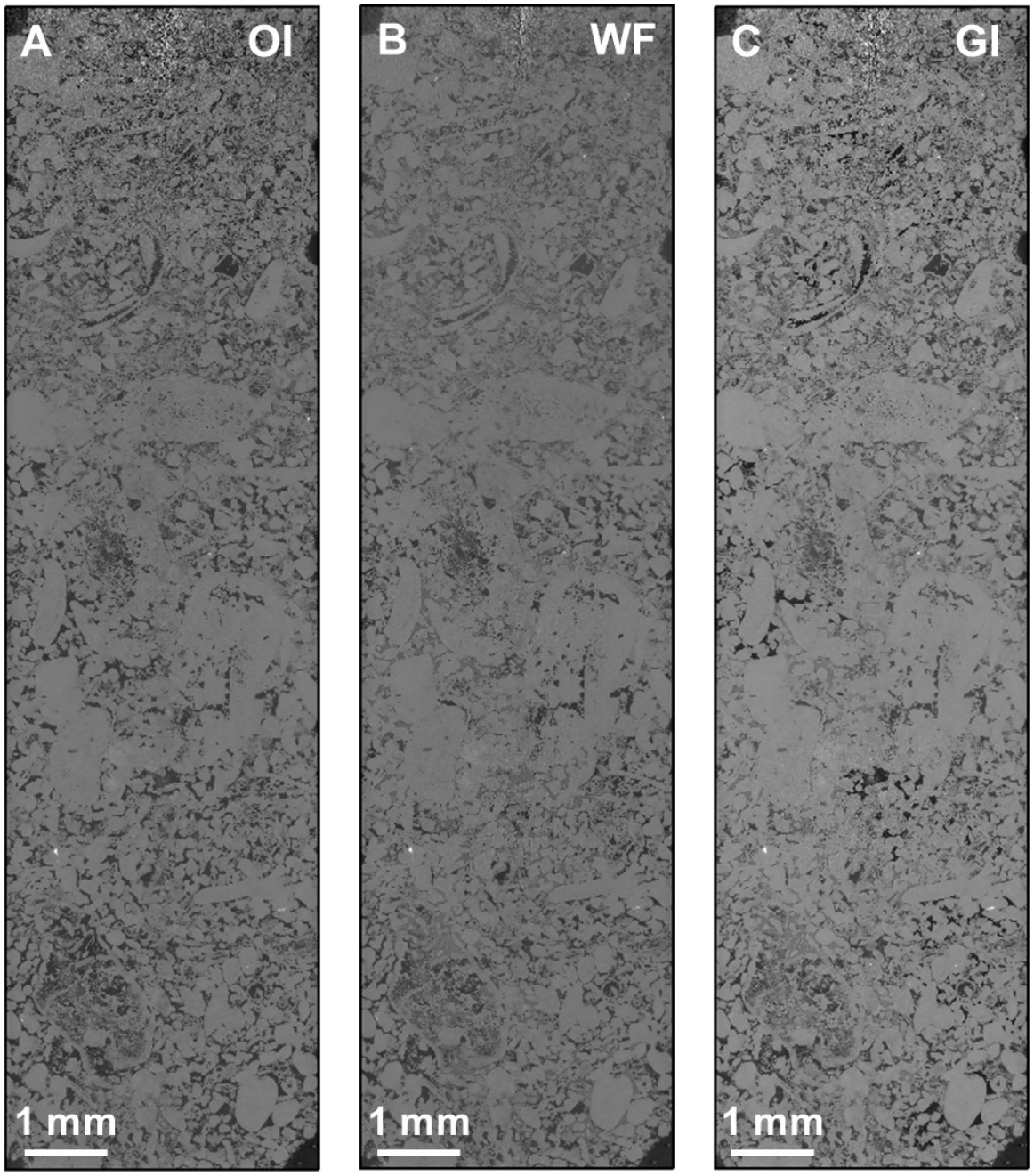

Figure A5. 1. Raw static images with a 3.57 µm/voxel resolution of the whole sample after each injection sequence: (a) after oil injection [OI]; (b) after waterflooding [WF]; and (c) after gas injection [GI]. In (a), rock is the light phase and oil is the dark phase. In (b) and (c), the order from darkest to brightest is: oil-water-rock; and gas-oil-water-rock respectively.

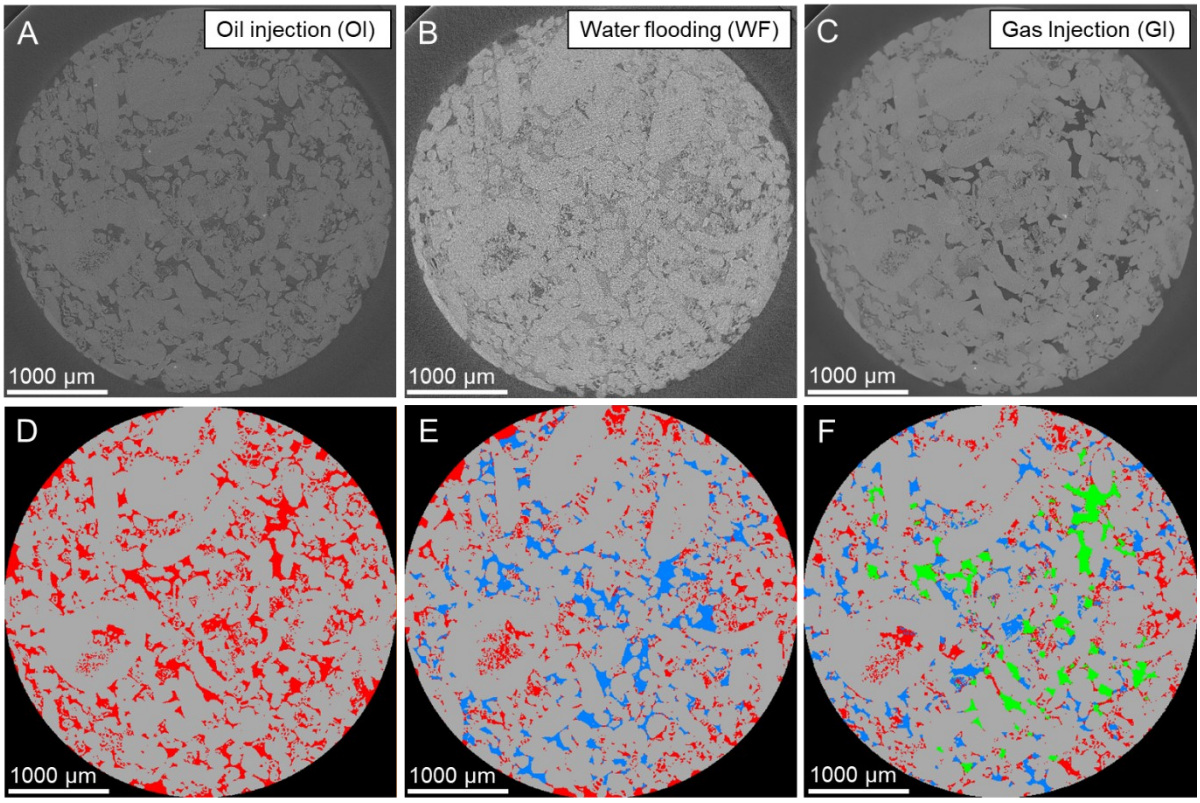

Figure A5. 2. Image segmentation. (Top row) raw images of the sample with a 3.57 µm/voxel resolution after: (a) oil injection [OI]; (b) waterflooding [WF]; and (c) gas injection [GI]. (Bottom row) Segmentation of the images in the top row using WEKA segmentation method with mean and variance texture filters. These images were selected to show the accuracy of segmentation for two, three and four phases. In (a), rock is the light phase and oil is the dark phase. In (b) and (c), the order from darkest to brightest is: oil-water-rock and gas-oil-water-rock respectively. In the segmented images, gas is shown in green, rock in grey, oil in red and water in blue.

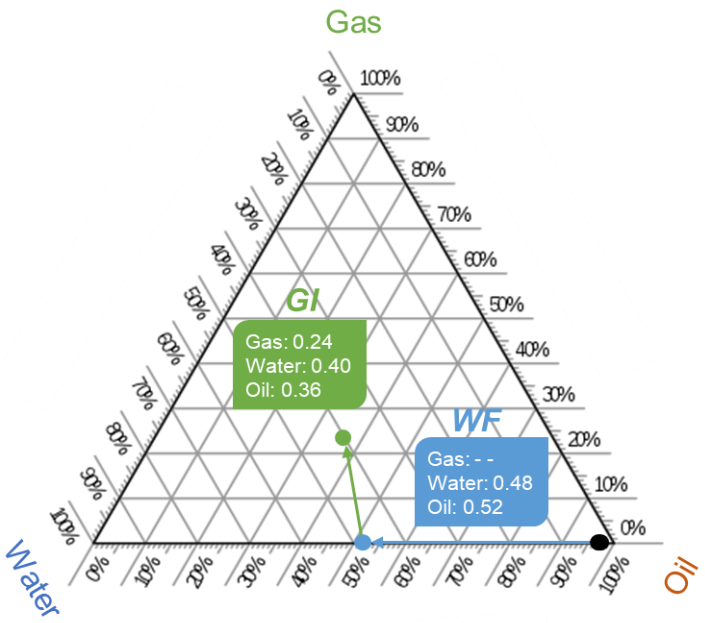

Figure A5. 3. A ternary diagram showing the end-point saturations of oil, water and gas after waterflooding [WF] and gas injection [GI]. Initially, the rock is almost fully saturated with oil in the macro pores (black point), then water is injected during WF resulting in the end saturations shown in the blue point, followed by gas injection during GI (green point).

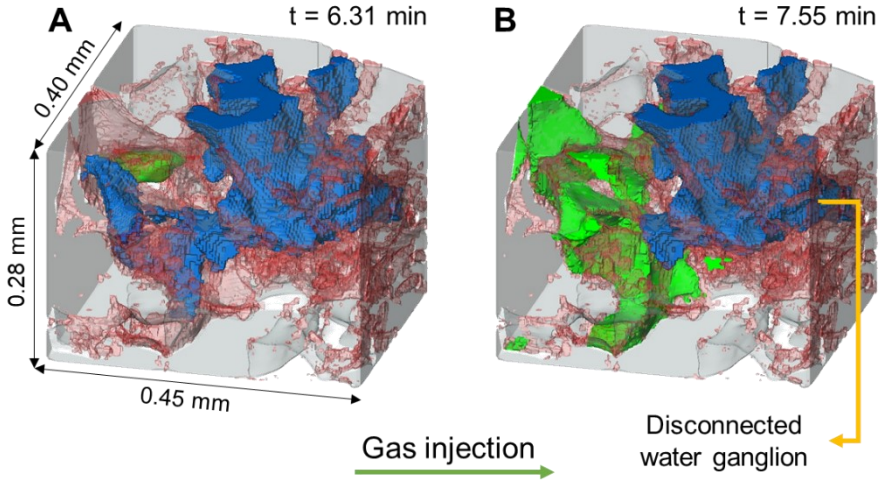

Figure A5. 4. Three-dimensional images of a small section of the pore space showing the trapping of water during gas injection in the oil-wet rock. Oil is shown in red, water in blue, gas in green while the rock is rendered transparent to permit the visualization of fluid configurations in the pore space.

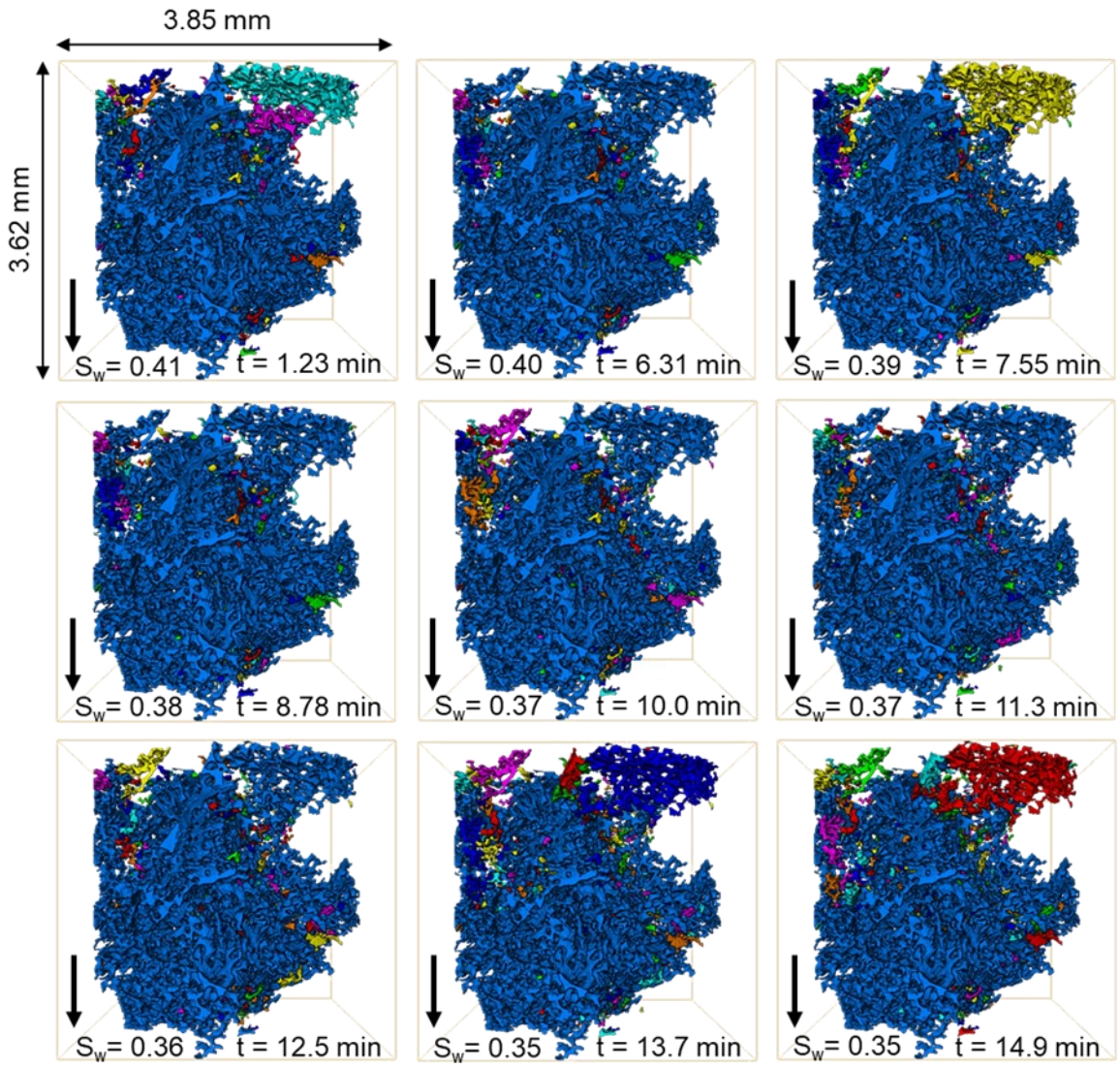

Figure A5. 5. Three-dimensional maps of the water connectivity in the pore space during GI shown at different time-steps. Each disconnected water cluster is labeled with a different color. The black arrow points towards the direction of flow. S_w is the gas saturation in the imaged section, while t is time.

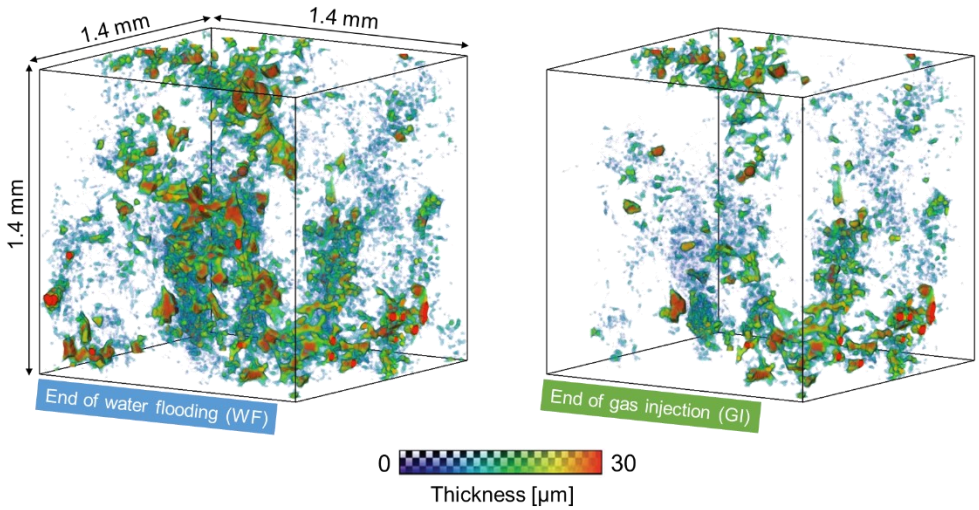

Figure A5. 6. Three-dimensional thickness maps of oil layers shown at the end of (left) waterflooding [WF] and (right) gas injection [GI]. The oil phase was isolated and maximal balls were fitted to its structure to obtain the thickness maps.

Three-phase thermodynamic contact angle: data from segmented images

Time [s]	S_w	S_g	a_{ow} [mm^{-1}]	a_{gw} [mm^{-1}]	a_{go} [mm^{-1}]	a_{ws} [mm^{-1}]	a_{gs} [mm^{-1}]	κ_{ow} [mm^{-1}]	κ_{go} [mm^{-1}]
1.2333333	0.41112	0.0059708	1.094409938	0.096543823	0.019870807	4.625258799	0.089184265	-81.71428571	45.41714286
3.85	0.41581	0.0080891	1.134023464	0.104833678	0.024655625	4.788405797	0.108662526	-81.71428571	50.98285714
5.0833333	0.41076	0.0101	1.14084196	0.104400276	0.041289165	4.746445825	0.128146308	-78.8	65.31428571
6.3166667	0.40444	0.019939	1.112574189	0.102539683	0.099254658	4.661973775	0.193195307	-79.65714286	62.22857143
7.55	0.39758	0.027043	1.100096618	0.103765355	0.132938578	4.605383023	0.250009662	-80.22857143	62
8.7833333	0.38331	0.039855	1.115638371	0.102777088	0.171641132	4.459627329	0.336645963	-80.45714286	58.4
10.016667	0.37657	0.050954	1.09294686	0.100436163	0.238694272	4.382332643	0.419296066	-81.31428571	61.77142857
11.25	0.37634	0.057936	1.086625259	0.101741891	0.290545204	4.376535542	0.45915804	-81.2	62.11428571
12.483333	0.36884	0.059263	1.094271912	0.099922705	0.283395445	4.305590062	0.472574189	-79.02857143	60.68571429
13.716667	0.35851	0.071233	1.076935818	0.100132505	0.31094548	4.251207729	0.549868875	-81.2	60.68571429
14.95	0.35608	0.076298	1.083395445	0.101013112	0.335983437	4.223878537	0.585866115	-80.8	61.25714286
16.183333	0.34824	0.084622	1.057612146	0.099743271	0.36389234	4.132229124	0.650655625	-81.48571429	60.97142857
17.416667	0.34464	0.08947	1.059820566	0.098824017	0.417860594	4.091373361	0.684030366	-81.65714286	62.34285714
18.65	0.34344	0.0934	1.052891649	0.096300897	0.438178054	4.072325742	0.718067633	-81.42857143	62.85714286
19.883333	0.34029	0.095393	1.047011732	0.099986197	0.451704624	4.053830228	0.739627329	-81.42857143	62.22857143
21.116667	0.34015	0.096611	1.044223602	0.099204969	0.436521739	4.049137336	0.748240166	-81.65714286	63.02857143
22.35	0.33944	0.097581	1.045327812	0.099064182	0.440138026	4.038647343	0.759337474	-81.48571429	62.68571429
23.583333	0.33785	0.097655	1.040717736	0.097416149	0.451290545	4.029537612	0.748985507	-81.42857143	63.25714286
24.816667	0.3374	0.098019	1.043119393	0.097783299	0.449744651	4.010766046	0.748295376	-82.05714286	63.14285714
26.05	0.33741	0.09758	1.045548654	0.098271912	0.446321601	4.010489993	0.74252588	-82.05714286	63.08571429
27.283333	0.33715	0.098558	1.04173913	0.099149758	0.452505176	4.006073154	0.756549344	-82	63.25714286
28.516667	0.33675	0.098128	1.043146998	0.09794617	0.448833678	3.994478951	0.750089717	-81.88571429	63.65714286
29.75	0.33675	0.098551	1.039392685	0.099514148	0.447867495	3.998067633	0.758095238	-82	63.31428571
30.983333	0.33629	0.097977	1.038426501	0.098570048	0.44621118	3.98426501	0.748378192	-81.54285714	63.42857143
32.216667	0.3355	0.098218	1.039889579	0.097659075	0.451511387	3.965217391	0.750117322	-81.88571429	62.97142857

Three-phase thermodynamic contact angle: differences

Time [s]	ΔS_w	ΔS_g	Δa_{ow} [mm^{-1}]	Δa_{gw} [mm^{-1}]	Δa_{go} [mm^{-1}]	Δa_{ws} [mm^{-1}]	Δa_{gs} [mm^{-1}]	$\Delta \kappa_{ow}$ [mm^{-1}]	$\Delta \kappa_{go}$ [mm^{-1}]
1.2333333									
3.85	0.00469	0.002118	0.039614	0.00829	0.004785	0.163147	0.019478	-81.7143	48.2
5.0833333	-0.00505	0.002011	0.006818	-0.00043	0.016634	-0.04196	0.019484	-80.2571	58.14857
6.3166667	-0.00632	0.009839	-0.02827	-0.00186	0.057965	-0.08447	0.065049	-79.2286	63.77143
7.55	-0.00686	0.007104	-0.01248	0.001226	0.033684	-0.05659	0.056814	-79.9429	62.11429
8.7833333	-0.01427	0.012812	0.015542	-0.00099	0.038703	-0.14576	0.086636	-80.3429	60.2
10.016667	-0.00674	0.011099	-0.02269	-0.00234	0.067053	-0.07729	0.08265	-80.8857	60.08571
11.25	-0.00023	0.006982	-0.00632	0.001306	0.051851	-0.0058	0.039862	-81.2571	61.94286
12.483333	-0.0075	0.001327	0.007647	-0.00182	-0.00715	-0.07095	0.013416	-80.1143	61.4
13.716667	-0.01033	0.01197	-0.01734	0.00021	0.02755	-0.05438	0.077295	-80.1143	60.68571
14.95	-0.00243	0.005065	0.00646	0.000881	0.025038	-0.02733	0.035997	-81	60.97143
16.183333	-0.00784	0.008324	-0.02578	-0.00127	0.027909	-0.09165	0.06479	-81.1429	61.11429
17.416667	-0.0036	0.004848	0.002208	-0.00092	0.053968	-0.04086	0.033375	-81.5714	61.65714
18.65	-0.0012	0.00393	-0.00693	-0.00252	0.020317	-0.01905	0.034037	-81.5429	62.6
19.883333	-0.00315	0.001993	-0.00588	0.003685	0.013527	-0.0185	0.02156	-81.4286	62.54286
21.116667	-0.00014	0.001218	-0.00279	-0.00078	-0.01518	-0.00469	0.008613	-81.5429	62.62857
22.35	-0.00071	0.00097	0.001104	-0.00014	0.003616	-0.01049	0.011097	-81.5714	62.85714
23.583333	-0.00159	7.4E-05	-0.00461	-0.00165	0.011153	-0.00911	-0.01035	-81.4571	62.97143
24.816667	-0.00045	0.000364	0.002402	0.000367	-0.00155	-0.01877	-0.00069	-81.7429	63.2
26.05	1E-05	-0.00044	0.002429	0.000489	-0.00342	-0.00028	-0.00577	-82.0571	63.11429
27.283333	-0.00026	0.000978	-0.00381	0.000878	0.006184	-0.00442	0.014023	-82.0286	63.17143
28.516667	-0.0004	-0.00043	0.001408	-0.0012	-0.00367	-0.01159	-0.00646	-81.9429	63.45714
29.75	0	0.000423	-0.00375	0.001568	-0.00097	0.003589	0.008006	-81.9429	63.48571
30.983333	-0.00046	-0.00057	-0.00097	-0.00094	-0.00166	-0.0138	-0.00972	-81.7714	63.37143
32.216667	-0.00079	0.000241	0.001463	-0.00091	0.0053	-0.01905	0.001739	-81.7143	63.2

Three-phase thermodynamic contact angle: equation solver

ϕ	σ_{ow} [mN/m]	σ_{gw} [mN/m]	σ_{go} [mN/m]
0.123889	52.1	63.7	11.2

Equation:

$$\left(\Delta a_{gs}\cos\theta_{go} + \Delta a_{go} - \kappa_{go}\phi\Delta S_g\right)\sigma_{go} + \Delta a_{gw}\sigma_{gw} - \left(\Delta a_{ws}\cos\theta_{ow} + \Delta a_{ow} - \kappa_{ow}\phi\Delta S_w\right)\sigma_{ow} = 0$$

Time [s]	θ_{ow} [°]	θ_{go} [°]	θ_{gw} [°]	Equation	Equation squared
1.2333333	125.9768329	73	115.4087976	5.09	25.88093523451830000
3.85	125.9768329	73	115.4087976	1.75	3.05298877984986000
5.0833333	125.9768329	73	115.4087976	-0.95	0.90836656155230100
6.3166667	125.9768329	73	115.4087976	1.19	1.40834661377316000
7.55	125.9768329	73	115.4087976	3.33	11.10774383811860000
8.7833333	125.9768329	73	115.4087976	-0.08	0.00671078735413993
10.016667	125.9768329	73	115.4087976	-0.19	0.03679307468710450
11.25	125.9768329	73	115.4087976	1.84	3.38638496442581000
12.483333	125.9768329	73	115.4087976	2.34	5.48097016963061000
13.716667	125.9768329	73	115.4087976	0.80	0.63432533576156900
14.95	125.9768329	73	115.4087976	-0.30	0.09256067287663450
16.183333	125.9768329	73	115.4087976	1.00	1.00092845126223000
17.416667	125.9768329	73	115.4087976	-0.48	0.22606144946790200
18.65	125.9768329	73	115.4087976	1.07	1.13864927673410000
19.883333	125.9768329	73	115.4087976	-0.51	0.26282364794079400
21.116667	125.9768329	73	115.4087976	0.09	0.00875389020084656
22.35	125.9768329	73	115.4087976	0.30	0.08793812863086740
23.583333	125.9768329	73	115.4087976	-0.24	0.05764097266186590

24.816667	125.9768329	73	115.4087976	0.13	0.01566457594811580		
26.05	125.9768329	73	115.4087976	-0.11	0.01223900821404890		
27.283333	125.9768329	73	115.4087976	-0.17	0.02924958605362340		
28.516667	125.9768329	73	115.4087976	-0.01	0.00006007891454337		
29.75	125.9768329	73	115.4087976	-0.29	0.08412078332074550		
30.983333	125.9768329	73	115.4087976	-0.10	0.01085526366843400	Sum of squares	Solver
32.216667	125.9768329	73	115.4087976	5.09	25.88093523451830000	54.9	Change θ_{wo} and θ_{og} to minimize the sum

9.6 Appendix 6

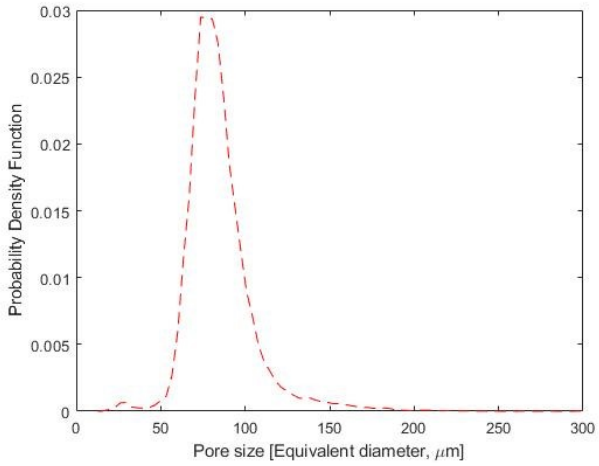

Figure A6. 1. Probability density function of the pore size distribution in the Bentheimer sample used in the steady-state three-phase experiment.

Gravitational Force Analysis:

The impact of gravity on the flow of fluids can in fact be assessed using the Bond number (*Bo*), which is the ratio of the pressure change due to buoyancy to the capillary pressure [18]:

$$Bo = \frac{\Delta\rho g l}{P_c}$$

where $\Delta\rho$ is density difference between the fluid pairs, g is the acceleration due to gravity (9.81 m/s^2), l is the characteristic length, and P_c is the measured capillary pressure.

At the pore-scale, l is around 60 μm (average pore diameter – see the pore size distribution, Fig. A6.1). This alongside the density data in section 6.1.3.1 of the main manuscript and capillary pressures section 6.1.4.7 give approximate oil-water and gas-oil Bond numbers of 7.2×10^{-5} and 7.2×10^{-4} respectively. Gravity has little to no impact on the flow of fluids at the pore-scale, since the gravitational forces are small compared to the capillary pressure.

On the other hand, at the experimental-scale, where l is assumed to be the length of the sample (40 mm), the oil-water and gas-oil Bond numbers are 0.048 and 0.48 respectively. This implies that gravitational forces could affect some of the macroscopic properties such as saturation. Nonetheless, as shown in section 6.1.4.5, we see almost constant fluid saturations in the experiment and no evidence of a capillary pressure gradient.

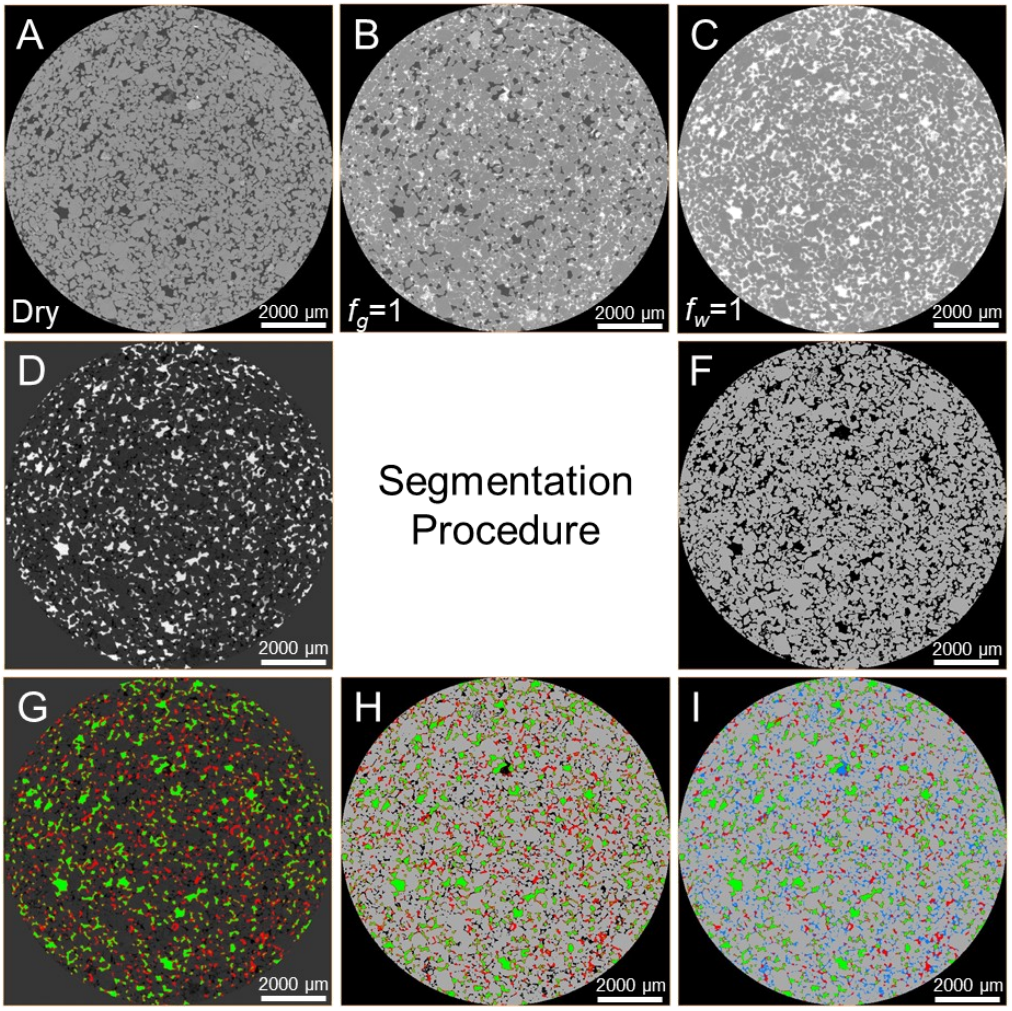

Figure A6. 2. Image segmentation workflow. (a) A 5.3 µm/voxel raw cross-sectional image of the dry scan used to segment the rock phase directly with the interactive thresholding technique as shown in (f). To segment the three-phase scan, in (b), it was first subtracted from the water saturated scan, in (c), to clearly distinguish the oil and gas phases, as shown in light grey and white respectively in (d). The oil and gas phases in (d) were then segmented with the interactive thresholding technique, as shown in (g); using direct thresholding allowed us to assign the intermittent phases, with intermediate grey-scale values, to the phase, either oil or gas, with the closest grey-scale value. The segmented rock phase in (f) was then added to the segmented oil and gas phases in (g) as shown in (h). The unassigned voxels in (h) were then added as the water phase giving the final segmented three-phase image in (i).

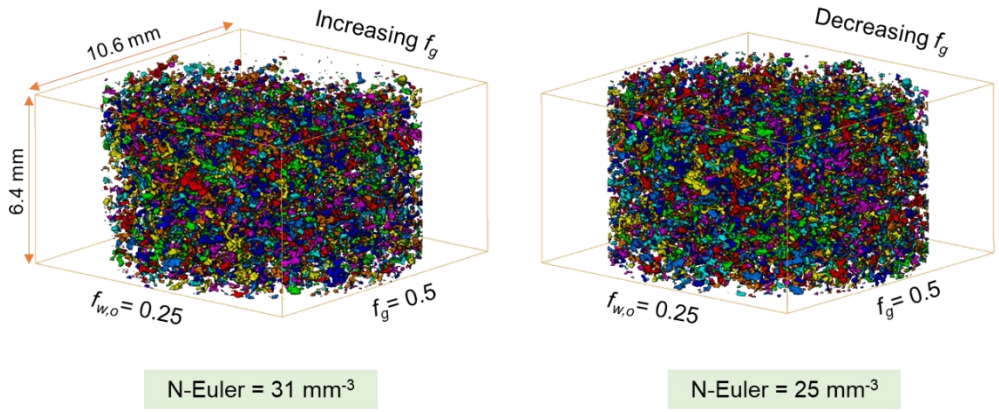

Figure A6. 3. Three-dimensional maps of the *in situ* connectivity of gas in the repeat experiment conducted in the same water-wet sample as the original experiment under three-phase steady-state conditions at a gas fractional flow of 0.5 and oil and water fractional flows of 0.25 during increasing (left) and decreasing (right) gas flow path. Only the middle part of the sample is shown here as opposed to showing the whole sample in the main manuscript. Each disconnected cluster is labelled with a different colour. f_g and $f_{w,o}$ refer to gas, oil and water fractional flows. N-Euler refers to the normalized Euler number.

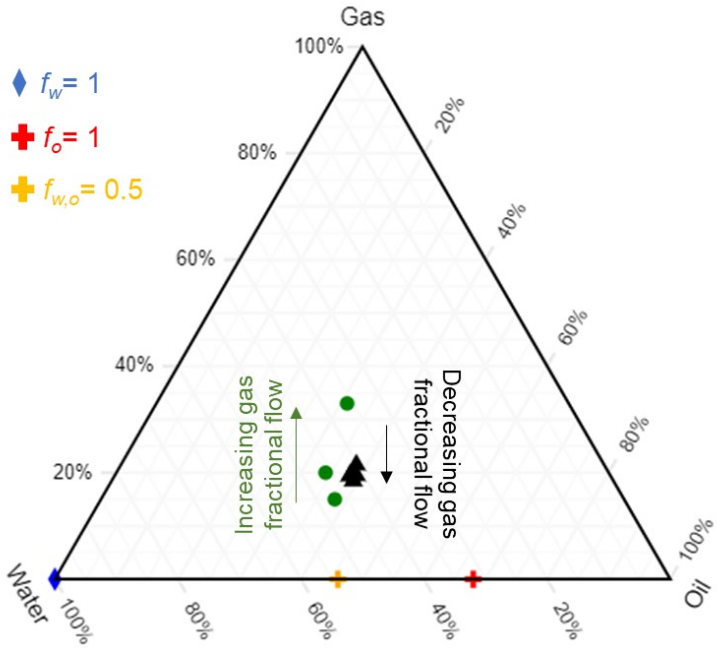

Figure A6. 4. A ternary diagram showing the averaged saturations at each fractional flow in the steady-state three-phase experiment.

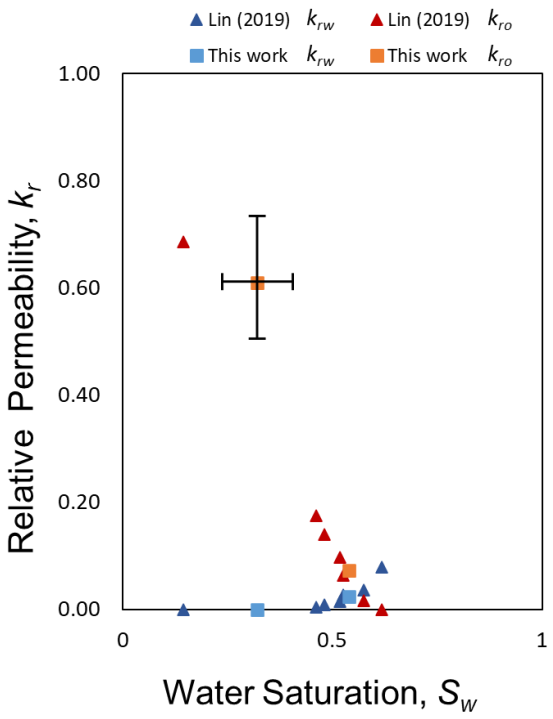

Figure A6. 5. Two-phase water and oil relative permeability measured before gas injection in the steady-state experiment. The relative permeabilities are compared with the measurements of Lin et al. [140]. The error bar indicates the uncertainty in the measurements.

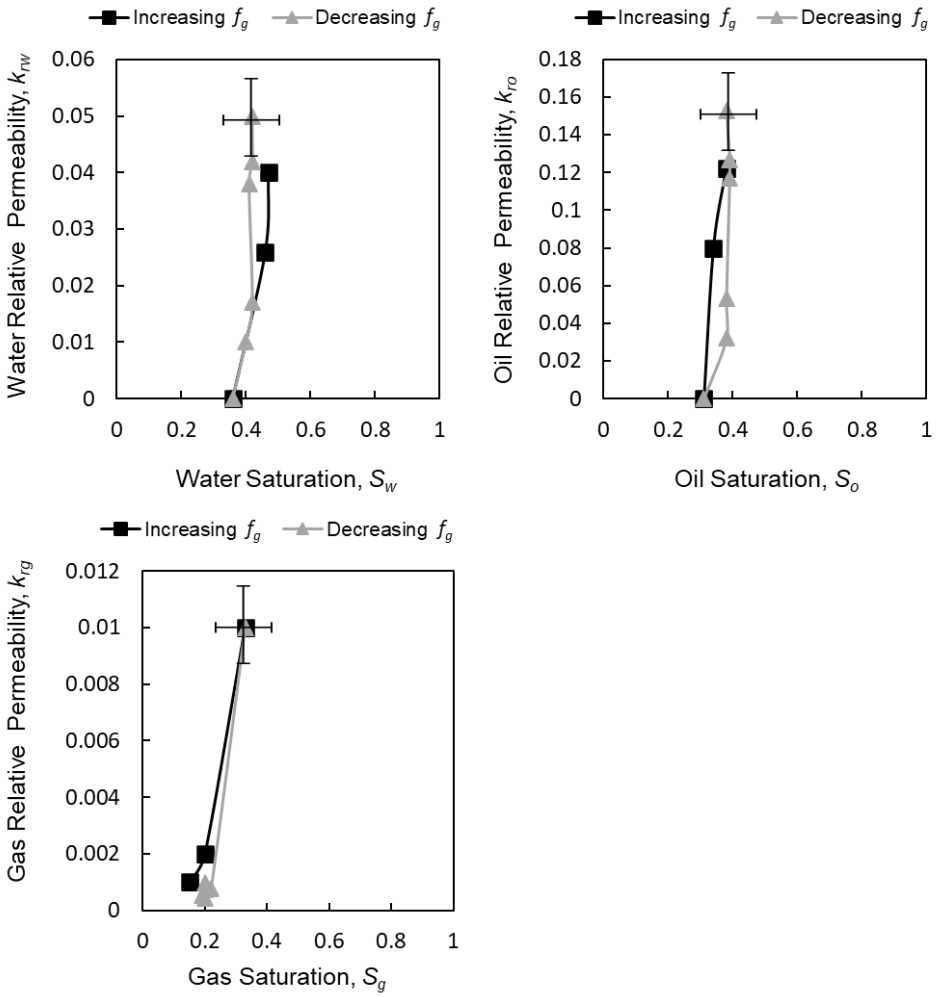

Figure A6. 6. Steady-state three-phase relative permeability of (a) water, (b) oil, and (c) gas measured during increasing gas fractional flow – decreasing oil and water fractional flows – and decreasing gas fractional flow – increasing oil and water. Error bars indicate the uncertainty in the measurements.

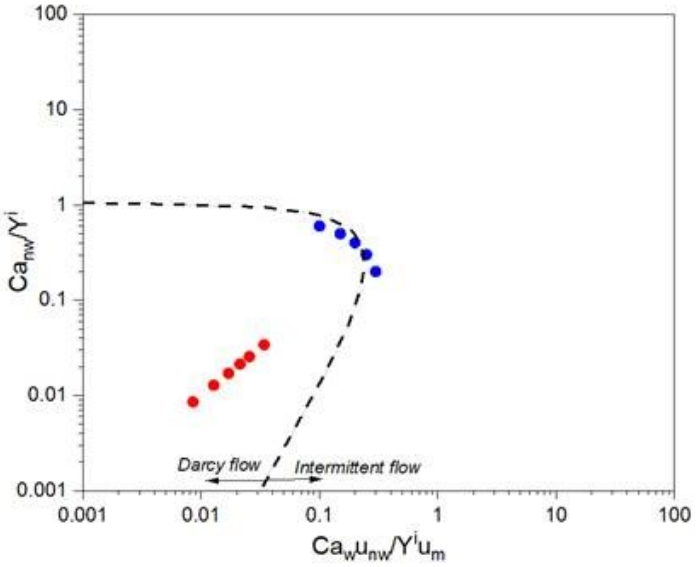

Figure A6. 7. The phase diagram of the transition from Darcy regime to the viscous regime for the two fluid pairs, oil and water (red) and gas and oil (blue), used in the experiment plotted as a function of the non-wetting phase capillary number (Ca_{nw}), gas in the case of gas and oil, and oil in the case of oil and water, wetting phase capillary number (Ca_w), non-wetting phase viscosity (u_{nw}), wetting viscosity (u_m), and Y number (Y^i) [201].

9.7 Appendix 7

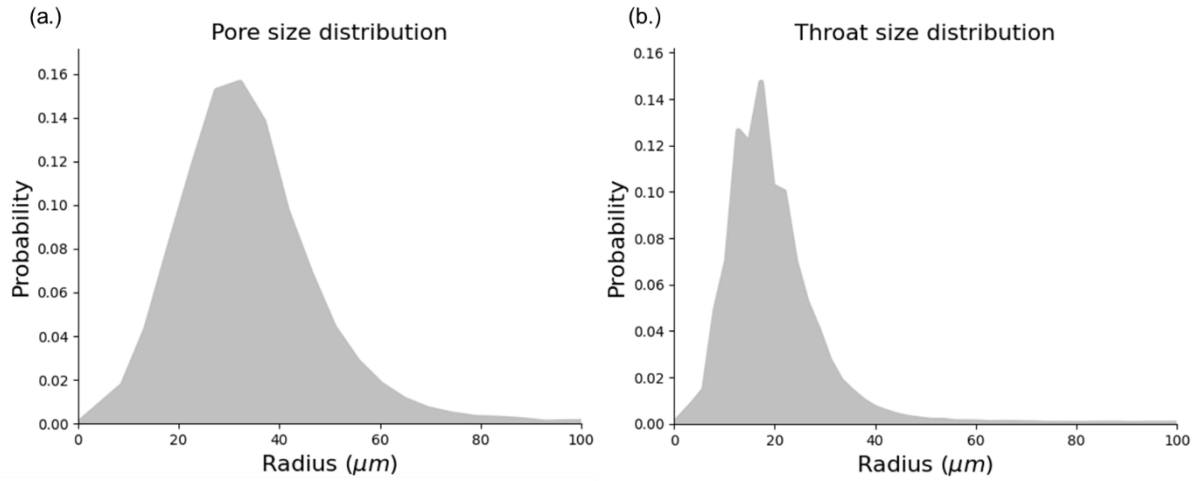

Figure A7. 1. Probability density function of the (a) pore and (b) throat size distribution in the reservoir rock sample used in the mixed-wet experiment.

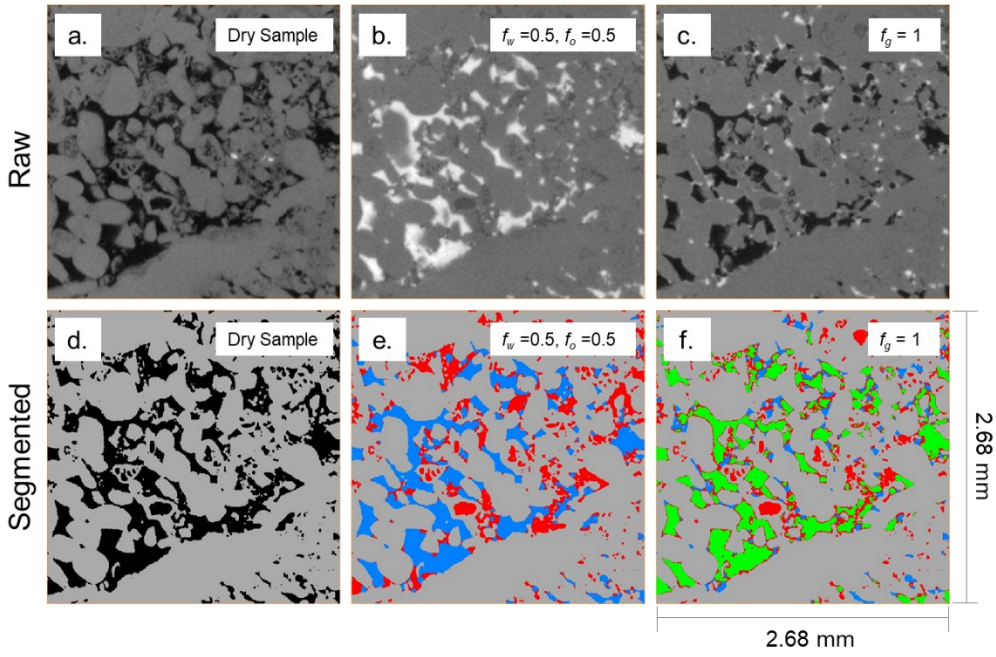

Figure A7. 2. Image segmentation workflow. (a) A 5.3 µm/voxel raw cross-sectional image of the dry scan used to segment the rock phase directly with watershed segmentation, shown in (d). In (b) is a raw two-phase image, with oil and water, acquired at f_w = 0.5 and f_o = 0.5. To segment (b), the watershed algorithm was first used to isolate the water phase, and then it was added to the rock phase segmented in (d), the unassigned voxels were then considered to be oil and used to give the final segmentation in (e). In (c) is a raw three-phase image, with gas, oil, and water, acquired at f_g = 1. To segment (c), the watershed algorithm was first used to isolate the water and gas phases, and then it was added to the rock phase segmented in (d), the unassigned voxels were then considered to be oil and used to give the final segmentation in (f). In the raw images, gas is shown in black, rock in light grey, oil in dark grey and water in white. In the segmented images, gas is shown in green, rock in grey, oil in red and water in blue.

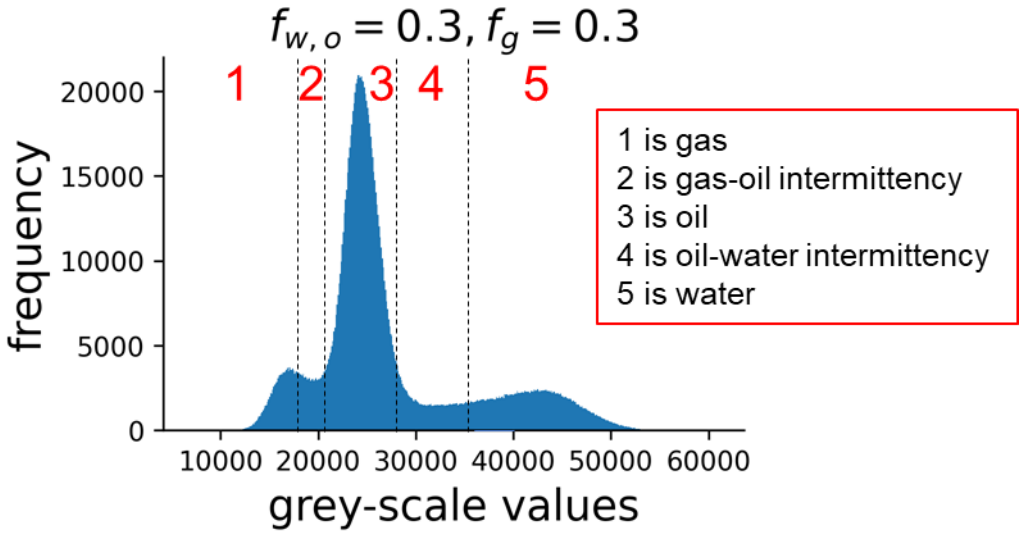

Figure A7. 3. A histogram of the grey-scale values in macro pore space of the reservoir rock at three-phase steady-state conditions, where gas, oil and water fractional flows are 0.375, 0.3125, and 0.3125 respectively. This example histogram is shown to illustrate the grey-scale value range set for each phase. We assume the existence of five phases at three-phase steady-state conditions. Gas, oil and water fractional flows (f_g and $f_{w,o}$) are stated.

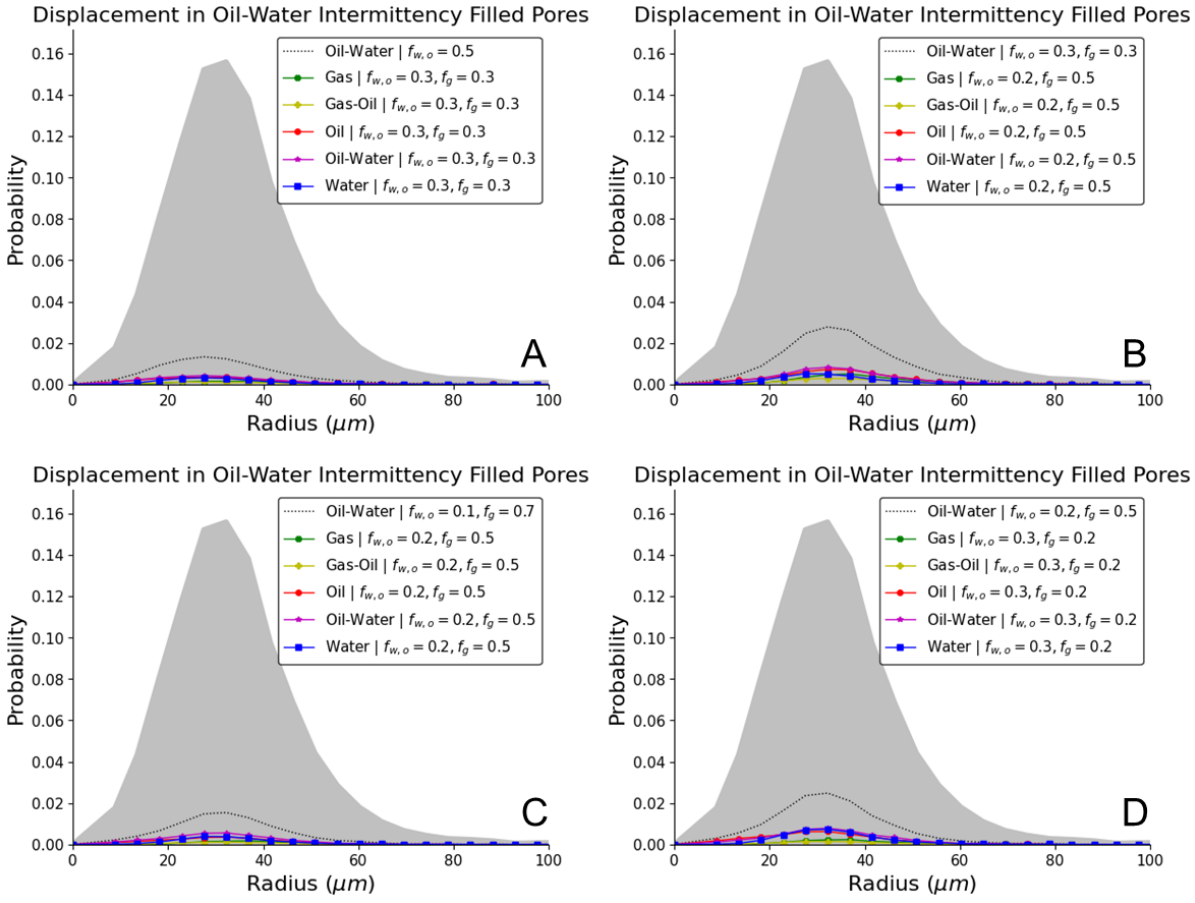

Figure A7. 4. Displacement in the oil-water intermittency-filled pores at different fractional flows in the mixed-wet rock during (a) and (b) increasing gas fractional flow, decreasing oil and water fractional flows, and (c) and (d) decreasing gas fractional flow, increasing oil and water, plotted as a function of pore size. Displacement here refers to the change in pore occupancy from one fractional flow to another. Gas, oil and water fractional flows (f_g and $f_{w,o}$) are stated.

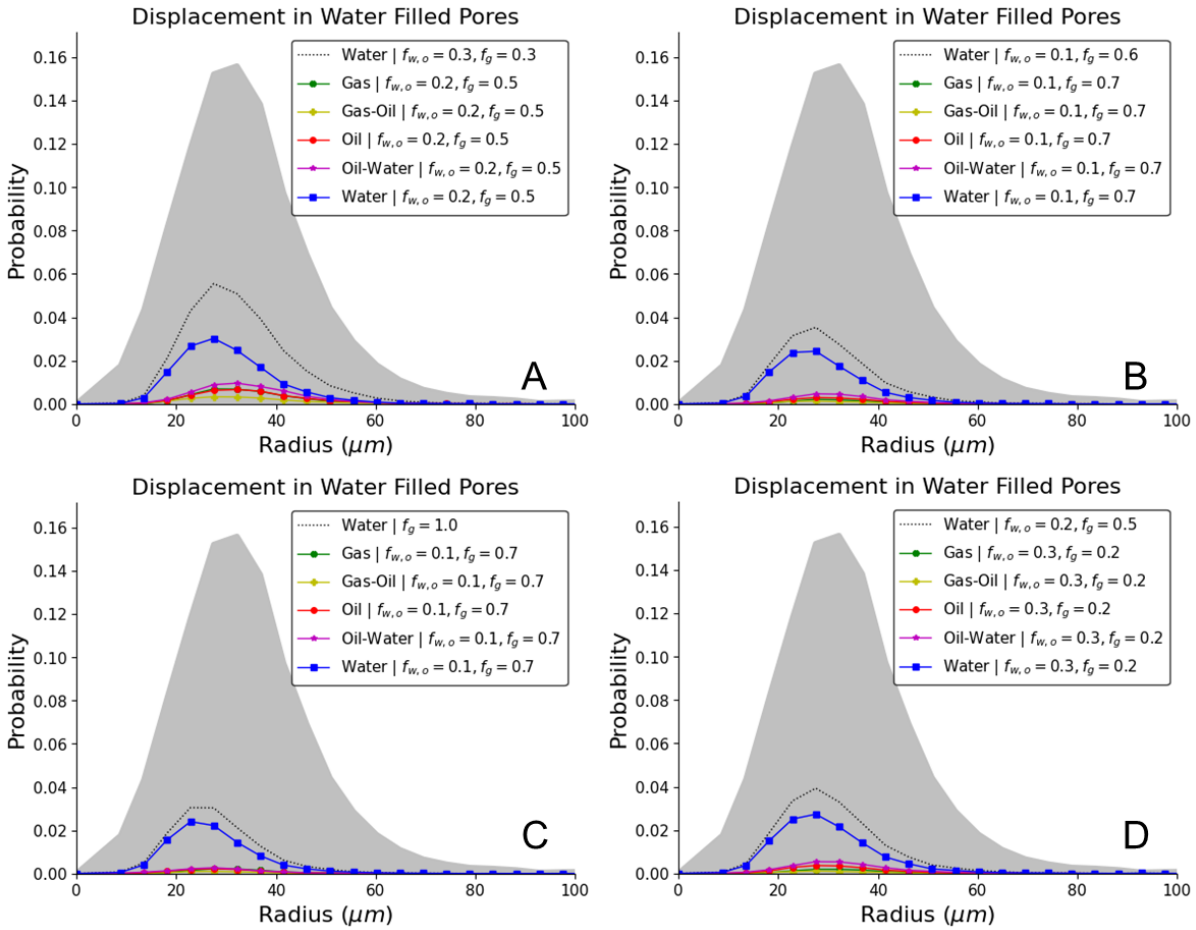

Figure A7. 5. Displacement in the water-filled pores at different fractional flows in the mixed-wet rock during (a) and (b) increasing gas fractional flow, decreasing oil and water fractional flows, and (c) and (d) decreasing gas fractional flow, increasing oil and water, plotted as a function of pore size. Displacement here refers to the change in pore occupancy from one fractional flow to another. Gas, oil and water fractional flows (f_g and $f_{w,o}$) are stated.